Development and calibration of wavelength scanning interferometry for surface topography measurement

Giuseppe Moschetti

A thesis submitted to The University of Huddersfield in partial fulfilment of the requirements for the degree of Doctor of Philosophy

The University of Huddersfield in collaboration with
the National Physical Laboratory

May 2016

Copyright Statement

i. The author of this thesis (including any appendices and/or schedules to this thesis) owns any copyright in it (the "Copyright") and s/he has given The University of Huddersfield the right to use such copyright for any administrative, promotional, educational and/or teaching purposes.

ii. Copies of this thesis, either in full or in extracts, may be made only in accordance with the regulations of the University Library. Details of these regulations may be obtained from the Librarian. This page must form part of any such copies made.

iii. The ownership of any patents, designs, trademarks and any and all other intellectual property rights except for the Copyright (the "Intellectual Property Rights") and any reproductions of copyright works, for example graphs and tables ("Reproductions"), which may be described in this thesis, may not be owned by the author and may be owned by third parties. Such Intellectual Property Rights and Reproductions cannot and must not be made available for use without the prior written permission of the owner(s) of the relevant Intellectual Property Rights and/or Reproductions.

Acknowledgment

I would like to thank (in order of appearance) all my supervisors for helping and directing me in the hostile and frustrating path that can be achieving a PhD degree. Thanks to Prof. Richard Leach for selecting me after the interview for the PhD project and for sharing your knowledge and expertise. Prof. Jane Xiang, thanks for providing guidance and supervision during my first year in Huddersfield and all the way to the end of my PhD (and beyond). Thanks to Dr. Feng Gao for sharing his experience and expertise. Thanks to Dr. Daniel O'Connor for the endless discussions and explanations that increased my understanding of optics and physics.
Thanks to Hussam Muhamedsalih for sharing his knowledge of the WSI and for the endless hours spent in the lab together, in the darkness, making his third and my first baby…
I would like to thank everyone in Huddersfield to have made it such a fantastic place, of which I have many beautiful memories.
Thanks to Mothana and Prashant for their help, support and for the dinners and the salsa moves. Thanks to QQ, Hongyu and Howard for the basketball games and for being amazing office mates. Thanks to the members of the Huddersfield Uni juggling society for the enjoyable afternoon at the parks and thanks to the members of the Italian society for the unbeatable dinners. Thanks to Rekaya Vincent Balang for being my cheekiest friend. Thanks to Etzali Ernandez for being "mi amica del corazon".

I would like to thank my research group at NPL for creating the environment where I could learn, work and increase my understanding of metrology; thanks to Claudiu Giusca, Christopher Jones, Andrew Henning, James Claverly, and Anuar Ismail.
A special thanks to Massimiliano Ferrucci who went from being an awesome office mate to being an amazing friend and for having had the patience to read through all of this thesis. Thanks to Adam Krisinsky, the good giant, for being a smart troll and a wise man.

Thanks to my parents, Leonardo and Annagrazia for telling me to copy from whoever was doing better than me, and for providing encouragement even when I saw no hope. Thanks to my brothers, Giovanni and Lorenzo, for letting me learn from their mistakes and for being there or not when I needed it.
This thesis is dedicated to my grandma Maria, for all her teachings and for having provided that little bit of extra training in all possible fields which contributed to make who I am.

For whomever checks whether his/her name is in the acknowledgement of this thesis: thanks to you too!
Finally thanks to Joanna Zimmerli for proofing reading this acknowledgment section.

Abstract

Modern advanced manufacturing is capable of generating complex structures on large area substrates while maintaining high feature resolution and small defects. Examples of these products include photovoltaic cells, OLED displays, and printed sensors, manufactured at high speed on roll-to-roll (R2R) processes. A challenge for manufacturers is to ensure that the quality of products is not compromised by the faster manufacturing process, therefore inspection should be in-line, fast, and should meet the accuracy needs of the product. A possible candidate for nanoscale surface measurement on large areas in an industrial environment is the wavelength scanning interferometer (WSI) technique for its higher speed when compared to other surface topography measurement techniques.

In this thesis, traceability for a WSI instrument is established, *i.e.* a procedure is defined to estimate the measurement uncertainty according to recent development in ISO standards for surface texture measurement. An estimation of measurement uncertainties associated with each of the metrological characteristics (MCs) and combined uncertainty is reported. It is shown that the WSI instrument is capable of measuring surface height with an uncertainty in the order of tens of nanometres. The larger uncertainty contribution is due to the linearity deviation of the vertical axis due to variable performance of the phase demodulating algorithm to fringe patterns with a large range of frequencies.

And alternative method is proposed to estimate the amplification factor and the linearity deviation which are usually estimated with the step height standard (SHS) method. The amplification factor can be estimated which lower uncertainty via the wavelength standard (WS) method and the linearity deviation *via* the measurement of a tilted-flat.

A technique variation, namely 'phase WSI' is proposed that improves the measurement performance of the WSI. Rather than determining the conventional fringe frequency-derived height directly, the method uses the frequency to resolve the fringe order ambiguity, and combine this information with the more accurate and repeatable fringe phase derived z height. A theoretical model to evaluate the method's performance in the presence of additive noise is derived and shown to be in good agreement with experiments. The linearity deviation is reduced by approximately an order of magnitude, reaching amplitudes of few nanometres. The measurement noise is also reduced by an order of magnitude, reaching the sub-nanometre range.

A complementary technique, quadrature WSI (QWSI), is also proposed which extends the measurement range by more than double, allowing positive and negative optical path differences (OPD) to be distinguished and making accessible for measurement the range around the zero OPD position. A theoretical explanation of the achieved improvement and the origin of possible phase estimation error is also provided.

Page intentionally left blank

Table of Contents

List of Figure

List of Table

List of Abbreviations

ACG	Areal cross grating
AFM	Atomic force microscopy
AOTF	Acousto-optics tuneable filter
ASG	Areal star groove
ASP	Areal star pattern
BE	Beam expander
BS	Beam splitter
CCD	Charge coupled display
CL	Collimating lens
CMOS	Complementary metal-oxide-semiconductor
CRB	Cramer-Rao bound
CSI	Coherence scanning interferometry
DHM	Digital holography microscopy
DM	Dichroic mirror
DMI	Displacement measuring interferometry
DOF	Depth of focus
DSCM	Disc scanning confocal microscope
EM	Electro magnetic
FFT	Fast Fourier transform
FT	Fourier transform
FWHM	Full width half maximum
GUM	Guide to the expression of uncertainty in measurement
IL	Imaging lens
IR	Infrared
IRP	Instrument response profile
ISO	International standard organisation
LSCM	Laser scanning confocal microscope
MC	Metrological characteristic
MO:	Microscope objective
MPE	Maximum permissible error
MTF	Modulus transfer function
NA	Numerical aperture
NPL	National Physical Laboratory
OCT	Optical coherence tomography
OL	Objective lens

OLED	Organic light emitting diode
OPD	Optical path difference
OPR	Optical path retarder
OTF	Optical Transfer function
PACM	Programmable array confocal microscope
PD	Photodetector
PI	Proportional-Integrative
PSI	Phase shifting interferometry
PTF	Phase transfer function
Q-WSI	quadrature wavelength scanning interferometry
R2R	Roll to Roll
RF	Radio frequency
RMSE	Root mean squared error
sCMOS	scientific Complementary metal-oxide-semiconductor
SHS	Step height standard
SLED	Super luminescence light-emitting diode
SNR	Signal to noise ratio
SPM	Scanning probe microscopySTM Scanning tunnel microscopy
STR	Surface topography repeatability VIM: International vocabulary of metrology
WS:	Wavelength standard
WSI:	wavelength scanning interferometer
WLI:	White light interferometry

1 Introduction

1.1 Motivation and aim

Modern advanced manufacturing is capable of generating complex and novel structures on large area substrates while maintaining high feature resolution and small defects. Examples of these products include photovoltaic cells, OLED displays, and printed sensors [1].

A common trend in manufacturing is the increased throughput by optimising and parallelising the production process, for example roll-to-roll (R2R) manufacturing processes. A challenge for manufacturers is to ensure that the quality of products is not compromised by the faster manufacturing process. For this task, quality control methods must be adapted to the changing production line; that is, inspection should be in-line, fast, and should meet the accuracy needs of the product. Without adequate inspection, the practical application of a manufactured product for its intended purpose cannot be verified. In other words, the quality of manufactured products is only as good as the instruments used to measure it.

A possible candidate for nanoscale surface measurement on large areas in an industrial environment is the wavelength scanning interferometer (WSI), which was developed at the University of Huddersfield [2], [3].

Under the European FP7 Nanomend project [4], research has been funded to fully integrate a WSI system into a R2R manufacturing process for detection of manufacturing defects. Detection of defects is an important step in the post-manufacturing, since it has been shown that defects can reduce the lifetime of organic solar cells [5].

Work performed towards the calibration of the WSI for surface topography measurement is described in this thesis. The **Thesis Aim** is provided by the statement below.

"To establish traceability of surface topography measurements from a wavelength scanning interferometer".

In this thesis, a dedicated calibration procedure is introduced. The application of this calibration procedure quantifies the WSI measurement uncertainty, and therefore assesses the performance of the WSI instrument.

1.2 Thesis objectives

Within the scope of the **Thesis Aim**, there are several specific **Thesis Objectives**, which will be further described in the following chapters.

- **Thesis Objective 1**: Acquire knowledge in the field of optical interferometry and build a WSI instrument at University of Huddersfield based on an existing design;
- **Thesis Objective 2**: To validate a procedure to estimate the WSI measurement uncertainty at the National Physical Laboratory (NPL).
- **Thesis Objective 3:** To identify limiting factors in the instrument and to develop methods to improve the instrument performance by reducing measurement uncertainty.

1.3 Approach and thesis structure

The main motive behind the work presented in this thesis is given in Chapter 1; the **Thesis Aim** and the **Thesis Objectives** were also introduced in Chapter 1. In Chapter 2, background information is given to provide context to the work. State-of-the-art surface measurement techniques are described and their benefits and challenges are discussed. Additional details are provided on optical surface measurement techniques, with an emphasis on interferometry and, ultimately, focusing on the WSI that was built at University of Huddersfield. The concept of measurement traceability and uncertainty determination are described in the context of surface texture measurements. Measurement uncertainties are reported for commercially available surface topography instruments and good practice methods for evaluating instrument performance are presented.

The WSI calibration method and results from its practical application are given in Chapters 3, 4 and 5. The calibration results are categorised in terms of measurement axis and metrological characteristics (MCs, which are defined for surface topography instruments in Chapter 2). Chapters 3 and 4 are dedicated to measurement uncertainty along the vertical measurement axis (z-axis), *i.e.* the measured surface height. Measurement noise and flatness deviation are covered in Chapter 3, while amplification and linearity deviation of the vertical axis are covered in Chapter 4. Chapter 5 is dedicated to the methods and results from the calibration of the lateral axes, *i.e.* the position in the instrument field of view (FOV). More specifically, the measurement uncertainty due to the amplification coefficient, linearity deviation and instrument resolution of the lateral axes are covered in Chapter 5. Two techniques to improve the WSI instrument performance are proposed in Chapter 6. A theoretical background for both techniques is reported and the modelled results are compared with real data measurements to validate the efficacy of the methods. In Chapter 7, thesis results are summarised, a conclusion is provided, and potential topics of further research are discussed.

Several appendices are provided in the thesis document, containing more detailed information and code developed.

1.4 Major contribution

The work in this thesis has produced two peer reviewed journal papers and two conference papers. A full publication list may be found in the Publication section at the end of this thesis.

2 Context and literature review

The aim of this chapter is to review the field of surface metrology and to present the variety of available surface measuring instruments. Further insight is given into the exploitation of light interference and, in particular, to the operating principles of interferometers to extract dimensional information of surfaces. The concept of traceability of a measurement is also described.

2.1 Surface metrology

Surface metrology is the study of measuring surface characteristics to ensure that a manufactured workpiece is able to fulfil the tasks it has been designed for [6]. Surfaces are manufactured to be used for a variety of purposes: mechanical contact (both static and dynamic), for instance engine parts; interaction with light, for example the surface of a lens; or for their properties when in contact with a liquid, such as hydro repellent surfaces, to cite a few applications. To be able to predict the workpiece performance, a fundamental step is to define what are we aiming to measure and therefore being able to answer the question: "How do you define a surface?" or "What is a surface?". One possible answer to this question is provided in reference [7], where it is stated that there is no universal definition of a surface. Instead, the authors of reference [7] argue that the definition of a surface is dependent on the method and instrument with which it is measured. Therefore, the surface measurement results and associated uncertainty from a given measuring procedure are, in themselves, the definition of the surface. Common measuring methodologies for extracting surface information are:

1. Mechanical contact,
2. Electromagnetic (EM) reflection or transmission,
3. Electric Field, and
4. Atomic forces.

A surface measured by mechanical contact or 'mechanical surface' is defined in ISO14406 [8] as the "boundary of the erosion, by a sphere of radius *r*, of the locus of the centre of an ideal tactile sphere, also with radius *r*, rolled over the model of the physical interface of the workpiece with its environment". The definition is a result of the measurement principle of contact-stylus instruments, which move a stylus tip over the surface to provide an estimation of the mechanical surface. The 'electromagnetic surface' can be defined as "the position where a detectable change in the electromagnetic properties occurs at the interface between media" [7]. Typical optical surface measurement instruments achieve measurement of the electromagnetic surface by illuminating the surface with set of planar waves of a known wavelength and detecting the scattered field. The electrical surface is defined as "the position at an interface where a measureable change in the current density at the interface between media" [7]. The

first instrument able to measure the electrical surface was developed by Young *et al.* [9]. Its measurement principle is based on the quantum mechanical tunnelling effect [10] and the technique is known as scanning tunnelling microscopy (STM). The tunnelling electric current measured between the non-contacting probe tip and the conductive surface is proportional to the distance between the tip and the surface [11]. The STM belongs to a wider class of surface topography measuring instrument called scanning probe microscope (SPM); another example of SPM is the atomic force microscope (AFM), which measures surfaces by scanning a cantilevered probing tip along the surface. Surface forces cause the cantilever to flex depending on the distance from the surface: by measuring the cantilever flex, the distance to the surface can be determined. An AFM can be used in different modes, such as "contact mode", "non-contact mode" and "tapping mode" [12], [13]. In contact mode, the scanning tip is in contact with the surface and the cantilever deflection is proportional to the change in surface height. The definition of surface measurements by contact AFM is similar to that of mechanical surfaces; however, the probing force of contact AFM is typically lower, usually in the range of tens of nanonewton. In non-contact mode, the cantilever is actively oscillated at a certain nominal distance from the measured surface. An observed change in the frequency oscillation can be related to surface forces interacting with the tip; from this observation, surface height can be inferred. In tapping mode, the tip oscillates and the amplitude of the oscillation is monitored to measure the surface distance and to keep the tip at the same distance from the sample whilst scanning the surface.

Instruments with differing measurement principles measure different measurands. The measuring instrument is therefore chosen according to the desired surface definition, which is related to its function. For example, if friction due to surface roughness is to be determined, then the surface is typically measured by mechanical contact. However, in some cases, the size of the contact probes in mechanical contact instruments exceeds the size of the desired features of interest on the surface. The previous scenario serves as an example of the considerations that should be given when selecting an instrument for a certain measurement task.

2.2 Surface measuring instruments

In section 2.1, various surface definitions are presented to describe how different instrument measure different surfaces. Other considerations are needed to determine the most suitable measuring instrument; for example, instruments can vary in their spatial frequency and vertical measurement range. A height-spatial period diagram (also known as amplitude-wavelength plot [14], [15]) is presented in figure 2.1; the height axis in this diagram corresponds to the achievable vertical measurement range and the spatial period axis corresponds to the size of

measurable features. Such a diagram provides a comparison of the measurement domains achievable by different instruments.

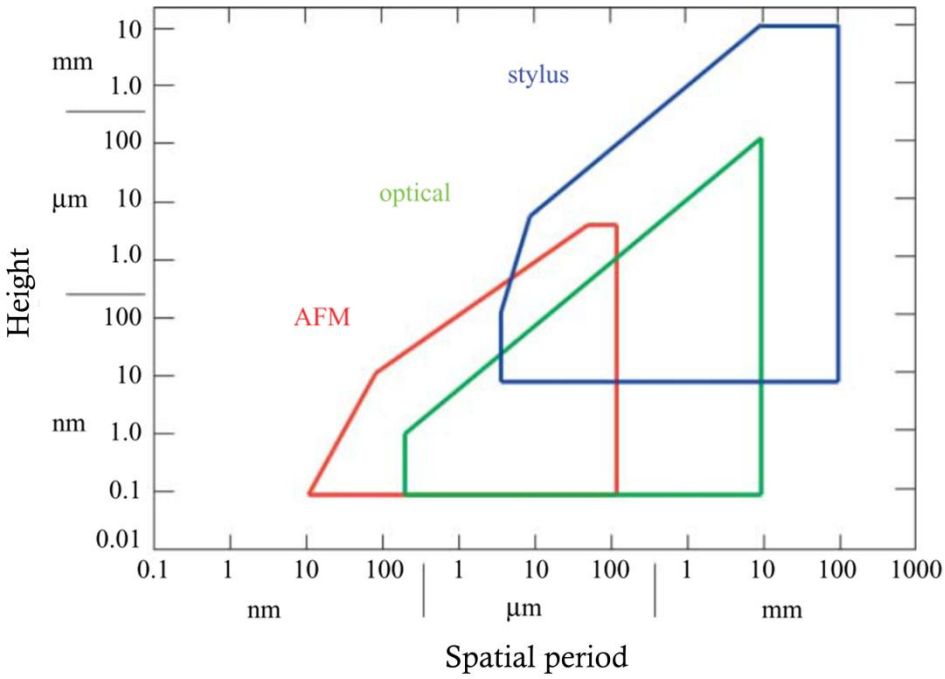

Figure 2.1: Amplitude-wavelength diagram of surface topography measuring instruments (adapted from [16]**).**

The surface feature size that is possible to measure by stylus instruments depends on the probe radius. Smaller tip radii can be used to measure smaller feature size (therefore shorter spatial periods); however, smaller radii are also more likely to damage the surface with the same measurement force. The probing force applied to smaller probes should therefore be carefully controlled.

Optical measuring instruments can typically measure shorter spatial periods than stylus instruments since they are not limited by the stylus tip size. Instead, the lower limit for the measurable spatial period is dependent on the diffractive nature of light and the finite numerical aperture (NA) of the objective lens. It is possible to achieve vertical measurements of heights of one thousandth of the light wavelength. For instance, for visible light the measurable height is in the sub-nanometre range [17].

For AFM, the sensing principle is based on the interaction of surface forces with the tip; therefore, smaller probing forces than in stylus instruments are achieved. Use of smaller tip radii allows measurement of shorter spatial period wavelengths than optical instruments. Also, AFM can achieve sub-nanometre surface height repeatability [12]. The main disadvantages of stylus instruments and AFMs are the need to contact or achieve nanometre proximity to the surface and the need to raster the surface point by point to obtain an areal surface

measurement. Optical instruments do not require contact or the same proximity to the surface; instead, the working distance of optical instruments depends on the instrument's optics. Most optical instruments employ 2D array sensors that provide an areal sampling of the surface, *i.e.* remove the need to raster the surface thereby decreasing measurement time. However, the performances of optical instruments are affected by the light scattered on the surface, which depends on the surface reflectivity, absorption, material composition and orientation. The decrease in measurement time makes optical instruments suitable for fast measurement of nanoscale defect detection [4]. More details about optical measuring instruments for surface topography measurement are discussed in section 2.3 since the research performed falls under this category.

2.3 Optical areal surface topography measuring techniques

Some of the more common optical areal surface topography measuring techniques are described in this section. The techniques described can be separated into two categories: non-interferometric and interferometric techniques. Non-interferometric techniques can measure surface topography by means of optical focus, light intensity or wavelength detection. Interferometric techniques, instead, exploits the physical phenomenon of interference of light (see appendix A) to compare the wavefront of the light scattered from a surface with a reference wavefront to reconstruct the surface. Three types of non-interferometric techniques are described: focus variation, confocal, and chromatic confocal. Five interferometric techniques are then described: digital holography microscopy (DHM), phase shifting interferometry (PSI), coherence scanning interferometry (CSI), wavelength scanning interferometry (WSI) and optical coherence tomography (OCT).

2.3.1 Non-interferometric techniques

2.3.1.1 Focus variation microscope

Focus variation is a method of extracting surface height information by detecting the position at which the image of a surface is at the sharpest focus. A typical optical setup for focus variation is shown in Figure 2.2.

In the measurement process, relative vertical position of the sample with respect to the optical system is scanned. Changes in vertical position can be achieved by either moving the sample or moving the optical head. For each vertical position of the sample, an image of the surface is acquired. The measurement process returns a stack of images and image processing algorithms are then applied to each image to identify regions of greatest image sharpness. The position of sharpest focus is estimated as the peak of a calculated merit function [18]. For example, a sharp image area can be defined as the set of pixels with highest contrast. Image sharpness can be

plotted as a function of vertical position for each pixel in the image. From this plot, the vertical position of maximum sharpness is used to extrapolate surface height information for the surface region defined by the pixel.

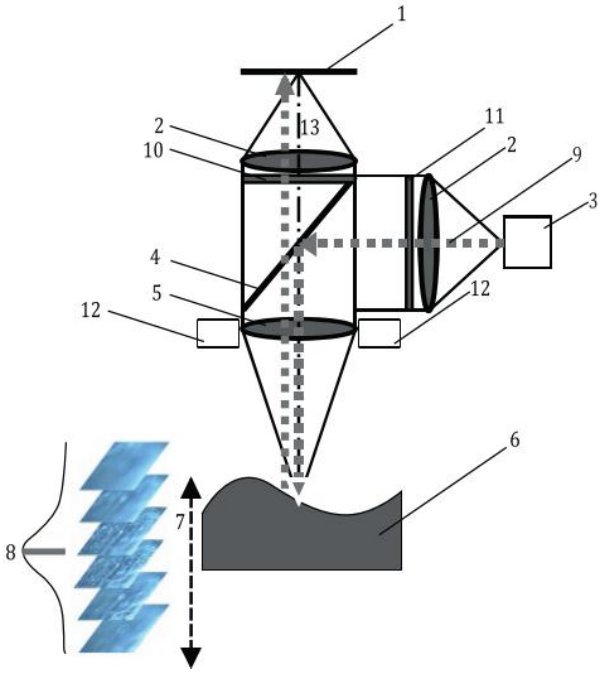

Figure 2.2. Optical setup of focus variation instrument. 1: Array detector. 2: imaging lens. 3: white light source. 4: Beam splitter. 5: Objective lens. 6: Specimen. 7: Vertical scan. 8: Focus information curve with maximum position. 9: Light beam. 10: Analyser. 11: Polariser. 12: Ring light. 13: Optical axis. Image reproduced from reference [19].

Vertical measurement resolution of a focus variation instrument is limited by the stepping intervals of the motion stage. Sub-sampling resolution is possible by applying curve-fitting algorithms and interpolating between image steps [18]. Typical specifications from commercially available instruments claim vertical resolutions from a few micrometres to 10 nm [20]. Lateral resolution is dependent on the number of adjacent pixels used to assess the image sharpness. Sharpness measuring algorithms are typically proprietary; it is therefore difficult to determine the relationship between lateral resolution and the number of pixels used. Measurement speed is limited by the mechanical motion for achieving multiple vertical positions of the sample. Higher throughput is possible by increasing the mechanical scan speed; however, vertical resolution is typically compromised for increased mechanical speed. Focus variation is a well-established technique with an associated ISO standard [19]. Typical measurement time depends on the vertical measurement range and the required accuracy; a full scan can therefore last from several seconds to few minutes.

2.3.1.2 Confocal microscope

Confocal microscopy is a sectioning imaging technique whose measuring principle is also the detection of the optical focus. The determination of best focus is obtained by measuring the intensity of the reflected light, which reaches a maximum when the surface is in focus [21]. In figure 2.3, a typical optical setup for a confocal instrument is shown. A laser light is filtered by the illuminating pinhole and its image is formed on the focal plane of the objective lens. The light reflected from the surface is collected from the objective lens and focused on a confocal aperture, which is located at a conjugate plane to the illuminating pinhole. When the surface is out of focus, the light reflected by the surface is dilated at the confocal aperture. As a result, less light enters through the aperture and a lower intensity is recorded by the detector. When the surface is in focus, the light incident on the aperture is focused to a smaller cross-sectional area. As a result, more light enters through the aperture and a higher intensity is recorded by the detector. A maximum in the observed intensity profile corresponds to the surface being in focus and the surface height can be estimated.

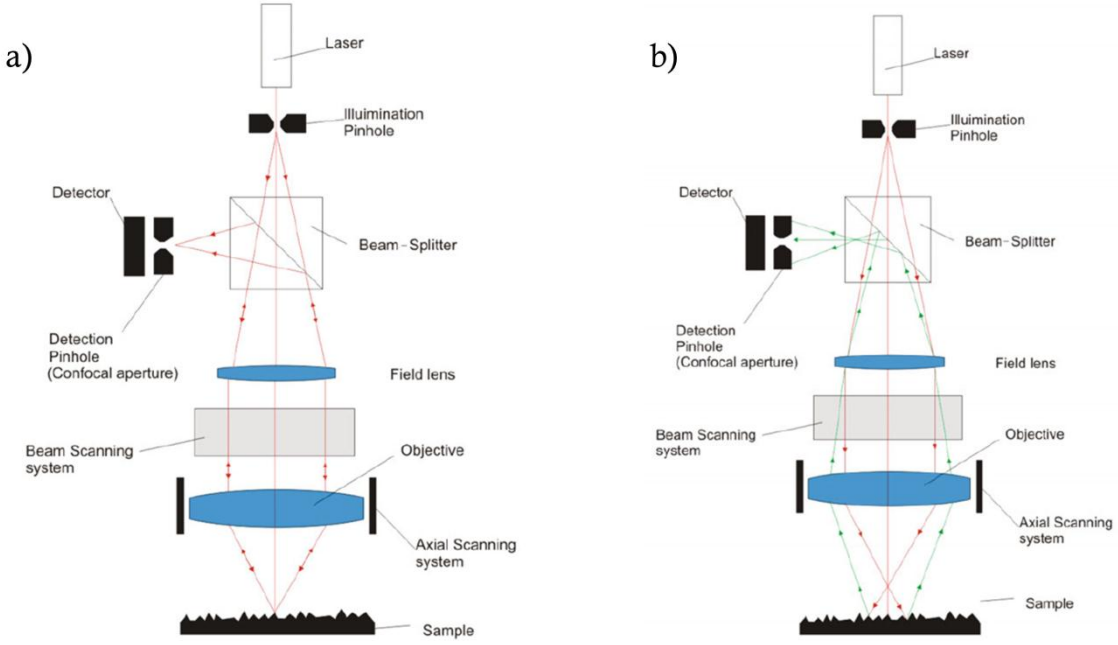

Figure 2.3. Optical setup of confocal instrument. a) surface in focus. b) surface out of focus. From [22].

Areal measurements can be obtained by scanning the surface point by points, for example by deflecting the beam or by repositioning the illumination pinholes. In beam deflection method, the light beam is deflected by altering the optical components in order to laterally scan the sample. In figure 2.3, a beam scanning component is used to deflect the beam. In the pinhole aperture repositioning, three different configurations can be distinguished:

1. Laser Scanning Confocal Microscope (LSCM);
2. Disc Scanning Confocal Microscope (DSCM);

3. Programmable Array Confocal Microscope (PACM);

These methodologies differ in the way the illuminating pinhole is moved or changed. In LSCM, the illumination pinhole filters the light entering the microscope. The detector pinhole, in a conjugate focal plane of the illumination pinhole, filters light incident on the detector [22]. In DSCM, the light beam is collimated and directed onto a perforated disk [23], [24]. The light that is transmitted through the perforations is incident on the sample. When the sample is in focus, the light is reflected back through the same perforation and directed onto a 2D array detector (see figure 2.4a). An advantage of DSCM over LSCM is the ability to sample an area of the sample surface instead of a single point, thereby increasing measurement speed. A disadvantage of DSCM, however, is that the illumination from a single light source must be distributed among several illumination pin-holes, thereby reducing the contrast.

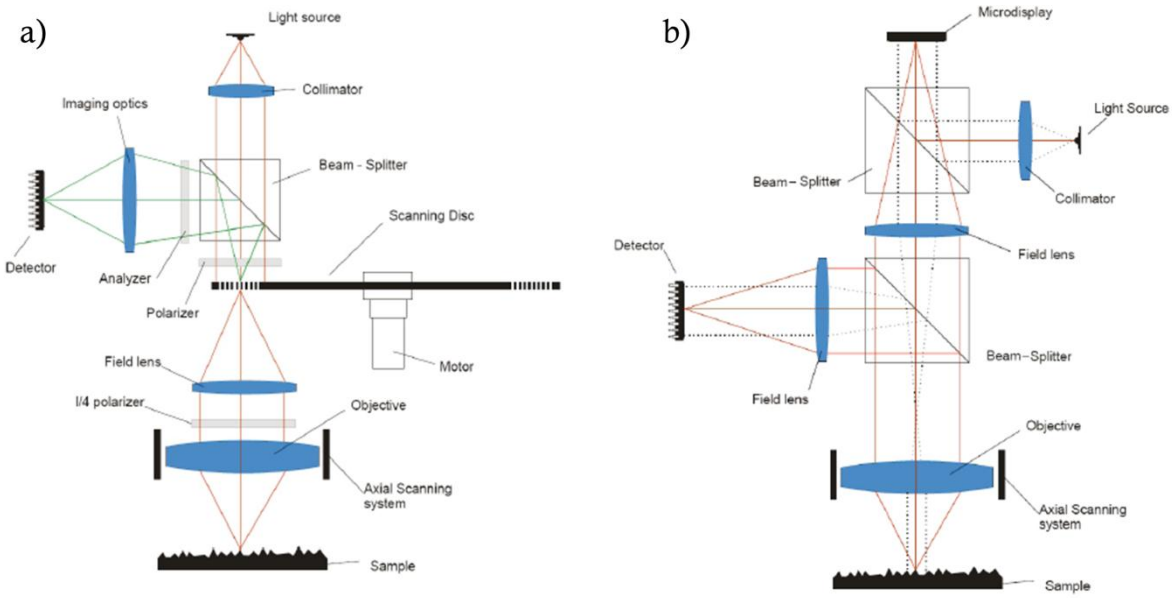

Figure 2.4. a) DSCM optical configuration. b) PACM optical configuration.

PACM employs digital micro-mirror devices or ferroelectric liquid-crystals to modify the position of the illuminating pinhole [25] (see figure 2.4b). Ferroelectric liquid-crystals are devices whose reflectivity can be modified by applying an electric voltage. An array of these devices is employed to programmatically change the illumination to scan the surface point by point. The PACM configuration does not rely on mechanical movement to scan the surface and can therefore achieve increased measurement speed.

The theoretical vertical resolution of a confocal instrument depends on the pinhole size, objective numerical aperture and wavelength of the light [22]. Other factors affecting the vertical resolution include the scanning configuration and the technique with which data is processed. The fastest and least accurate technique is to select the position at which the intensity peak occurs without any data fitting and interpolation. In this case, the resolution

depends on the reliability and step size of the axial scanning system; vertical height resolutions of the order of 50 nm are achievable. However, sub-step height resolution is possible through numerical fitting of the recorded intensity values. The measurement throughput is influenced by the instrument configuration; DSCM or PACM are typically faster than LSCM. Similarly to focus variation an instrument, the maximum achievable throughput is limited by the need of mechanically scanning the surface vertically. Faster measurement configurations are possible by increasing the axial step size and increasing the stage speed, however at the expense of the vertical resolution.

2.3.1.3 Chromatic confocal

In a chromatic confocal instrument, sample height information is spectrally encoded; that is, a dispersive optical element is added to focus different light wavelengths at different vertical positions (see figure 2.5a). This differs from the confocal principle described in section 2.3.1.2, where vertical mechanical scan of the surface is needed to find the best focus position. The surface position in chromatic confocal measurements is inferred by measuring the light intensity for each wavelength: maximum intensity is recorded only at the wavelength for which the surface is in focus (see figure 2.5b). An advantage over previously described techniques is the elimination of axial mechanical scanning. Increased measurement speed results in decreased sensitivity to environmental effects, such as vibrations [26]. Areal surface measurements are possible by lateral scanning of the optical probe.

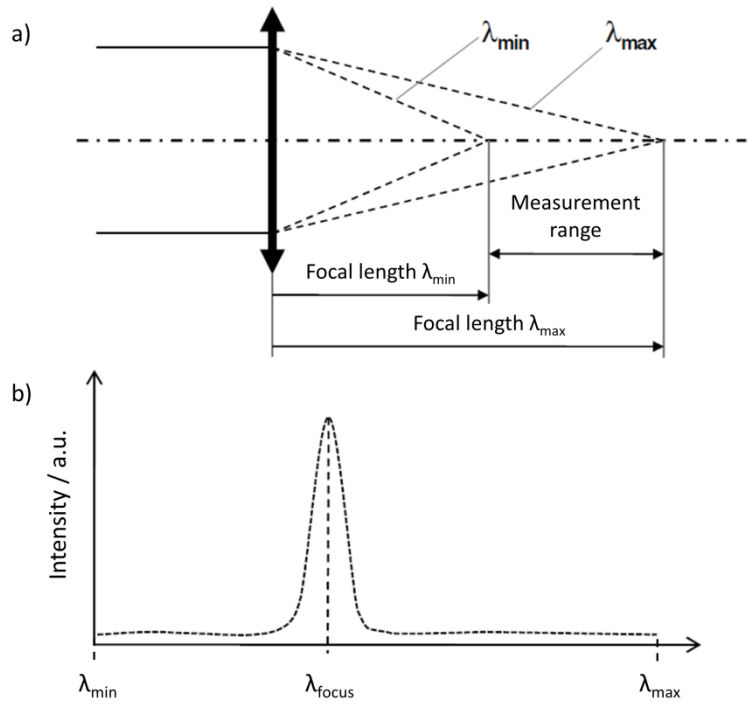

Figure 2.5. a) chromatic confocal optical probe showing chromatic dispersion. b) Example of recorded signal; maximum intensity is recorded at the wavelength corresponding to the position of the surface.

Vertical measurement range depends on the focal lengths associated with the minimum and maximum wavelengths employed, and therefore on the amount of optical dispersion. A spectrometer is employed to record intensities for each/all wavelength/s. As a result, the vertical resolution is limited by the performance of the spectrometer, such as resolution, *i.e.* pixel size and sub-pixel interpolation by peak-fitting, and spectral efficiency, *i.e.* ability to discern various wavelengths and signal intensities. In general, increasing the measurement range decreases the vertical resolution. Typical vertical resolutions range from a few micrometres to several nanometres, depending on measurement mode and optics [27–31]. Measurement speed of several kilohertz is commonly specified by instrument manufacturers. Measurement speed is influenced by sample reflectivity, roughness and the intensity of the generated signal [26]. Chromatic confocal measurement is a well-established technique, as indicated by the number of available commercial instruments [27–31]; the technique is also included in ISO 25178-602 [32]. Further development combine chromatic confocal technique with interferometry [33].

2.3.2 Interferometric techniques

This section described interferometric techniques for areal surface topography measurements. For a description of the physical phenomenon of interference and explanation of waves coherence (temporal and spatial) see Appendix A.

2.3.2.1 Digital Holography Microscopy

Digital holography microscopy (DHM) is an interferometric imaging technique based on holography, a technique first reported in Nature [34]. To record a hologram, light for a laser source is scattered from a 3D object and its interference with a reference wave is used to record the hologram. Consequently illuminating the hologram with the reference wave allows reconstruction of the scattered wave-front of the 3D object [35]. Originally the holograms were imprinted on photosensitive material, and an important step towards practical holographic microscope was the use of digital camera as the recording medium [36]. Recording the digital hologram on a camera allowed the possibility of numerical algorithms to calculate the surface topography from a single digital hologram. In figure 2.6 two optical setups (in reflection and in transmission mode) for a digital holographic microscope are shown.

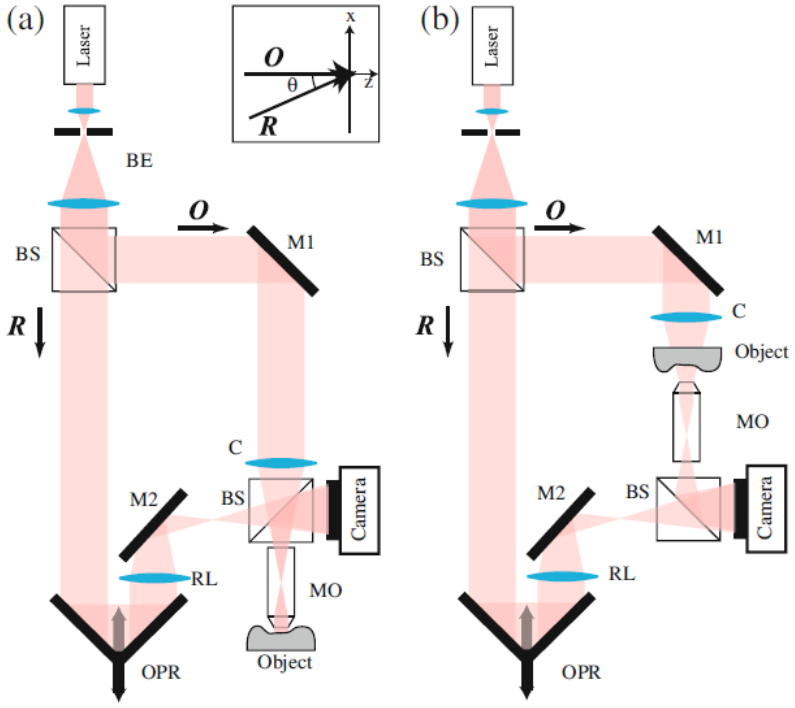

Figure 2.6. Digital Holography Microscope setup. a) Reflection mode optical setup. b) transmission mode optical setup. BE: beam expander; BS: beam splitter; M1, M2: mirrors; OPR: optical path retarder; C: condenser; RL: lens in the reference arm; MO: microscope objective; R: the reference wave and O the object wave (from [37]**).**

The laser beam is split by a beam splitter into the reference and the measurement wave. The measurement wave is shined on an object and the scattered field collected by the magnification objective. The measurement beam is recombined with the reference beam to create the hologram on the camera. An off-axis configuration can be used to introduce a carrier to simplify the signal filtering steps [38].

Reconstruction algorithm is composed of three steps: signal filtering, reconstruction of the complex wave in the hologram plane and its numerical propagation to the plane where the object is focused [37]. First the real or virtual image has to be extracted from equation (7.2.25), *i.e.* only one of the interfering terms is kept and the twin-image and the zero order images filtered out. The complex field so-obtained is multiplied by a digital wave whose parameters correspond to the reference illumination beam [39]. Finally the field is propagated to the object focus position. The propagation can be calculated according to different formulations: single Fourier Transform, convolution or angular spectrum [40]. In figure 2.7 examples of the phase-contrast of a hologram at different processing stages are shown.

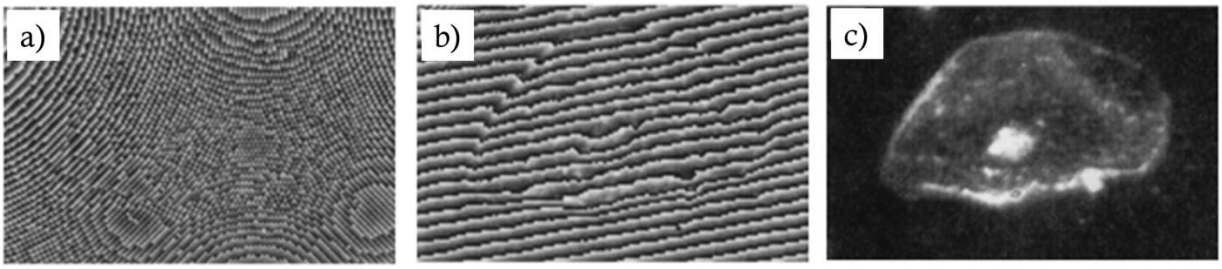

Figure 2.7. a) recorded phase-contrast hologram. b) phase-contrast of the hologram propagated to the object focus without illuminating reference wave. c) Object phase-contrast with reference wave and propagation to object focus. Adapted from [39]**.**

Illumination sources usually employed in DHM are laser sourced. Laser sources consent use of stroboscopic illumination to observe dynamic phenomena such as cells and biological tissues. A High-power fast light source in conjugation with high-speed CMOS camera allow for measurements up to a frequency of 25 MHz [41].

Another advantage of DHM is that it does not require mechanical movement. An image of an object out of focus can be reconstructed numerically by changing the parameters of the algorithm, *i.e.* the focus plane can be dynamically selected [37]. Further advances include structured or oblique illumination to improve spatial resolution or contrast [36].

An example of available commercial product is by the Swiss company Lyncee Tec. The company claims sub-nanometre measurement repeatability and vertical resolution of 2 nm [42]. Other work also reports sub-nm axial measurement repeatability [43].

The main disadvantage of DHMs is the phase ambiguity. In fact, the phase is known modulo 2π and therefore surface discontinuity larger than half of the wavelength in reflection, and an entire wavelength in transmission, cannot be correctly measured. To extend the measurement range ambiguity, hologram for several wavelengths can be recorded and processed [44].

The optical configuration described here and shown in figure 2.6 is referred to as off-axis, due to the reference and measurement beam not having the same optical axis. Another optical configuration is the on-axis: in this configuration the interfering optical beam are co-planar. In order to separate the interfering term from the mean and the twin-image the phase of the hologram needs to be shifted. The phase shifting mode and the algorithm employed to estimate the phase are the same for phase shifting interferometry which is explained in the next section.

2.3.2.2 Phase shifting interferometry

Phase shifting interferometry (PSI) is a measurement technique where surface topography is calculated by estimating the phase difference between the interfering beams. In figure 2.8a a Michaelson interferometer for displacement measurement is shown. Areal surface topography measurements are possible by employing extended illumination and recording the interference

intensity with a camera rather than a single pixel detector (configuration known as Twyman-Green interferometer, see figure 2.8b).

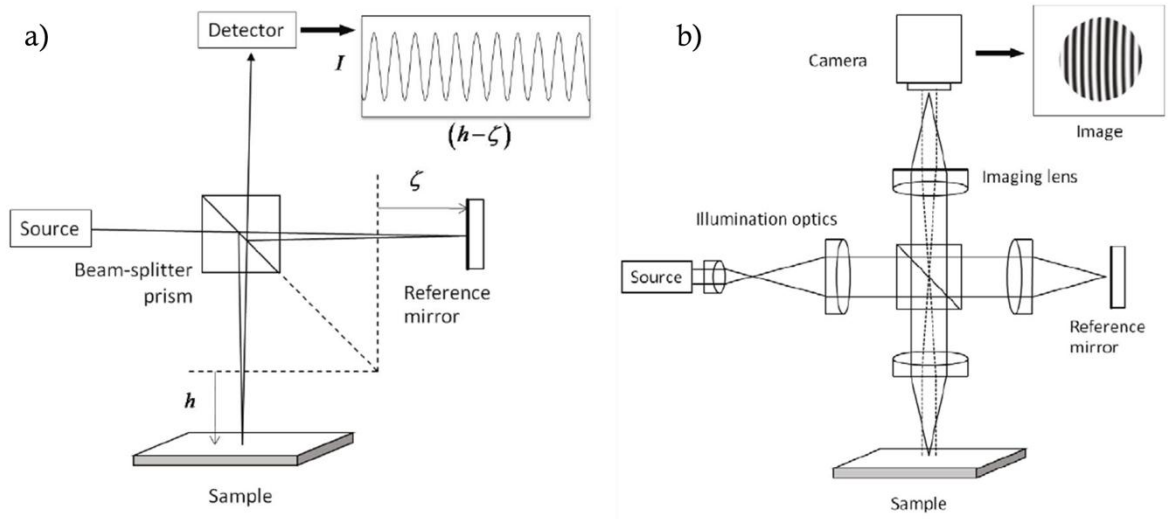

Figure 2.8. a) Michelson phase shifting interferometer to measure surface displacements. b) Linnik interferometer for areal surface topography measurement. Adapted from [45].

The interference signal recorded by each camera pixel in the PSI is a sinusoid whose phase is modulated by the optical path difference between the measurement and the reference arm:

$$I(K,\zeta) = I_{DC} + I_{AC}\cos((h-\zeta)K) \tag{2.3.1}$$

where I_{DC} and I_{AC} are fixed coefficient, the mean and the fringe visibility respectively. The interference signal oscillates as h (the surface height) and ζ (the reference mirror position) changes. K is the fringe frequency and it is equal to:

$$K = {}^{4\pi}/_{\lambda} \tag{2.3.2}$$

where λ is the wavelength of the interfering light.

If the reference mirror position is taken as the zero, the surface height z can be calculated from the phase of the interference signal according to:

$$z = \theta/K \tag{2.3.3}$$

where θ is the phase of the fringe pattern for $\zeta = 0$. In the measurement process the reference mirror is shifted and various intensities are recorded. Therefore the acquired intensity signal would have the form of:

$$I_i(K) = I_{DC} + I_{AC}\cos(zK + \alpha_i) \tag{2.3.4}$$

where α_i is the i-th phase shift. Usually the phase is changed linearly and therefore the phase step is constant:

$$\alpha_i - \alpha_{i-1} = \Delta\alpha \tag{2.3.5}$$

Two modes of recording the intensity value are possible: phase stepping and bucket mode (see figure 2.9a). In phase stepping mode the phase is changed by a constant value and the intensity value recorded: the intensity recorded corresponds to a sample of the sinusoid (see figure 2.9b). In bucket mode the phase is changed linearly and the camera integrates the intensity value over a certain amount of phase shifts. The bucket mode allow for faster measurement at the expense of reduced visibility (see figure 2.9b). The signal processing techniques to estimate the phase are the same for both modes.

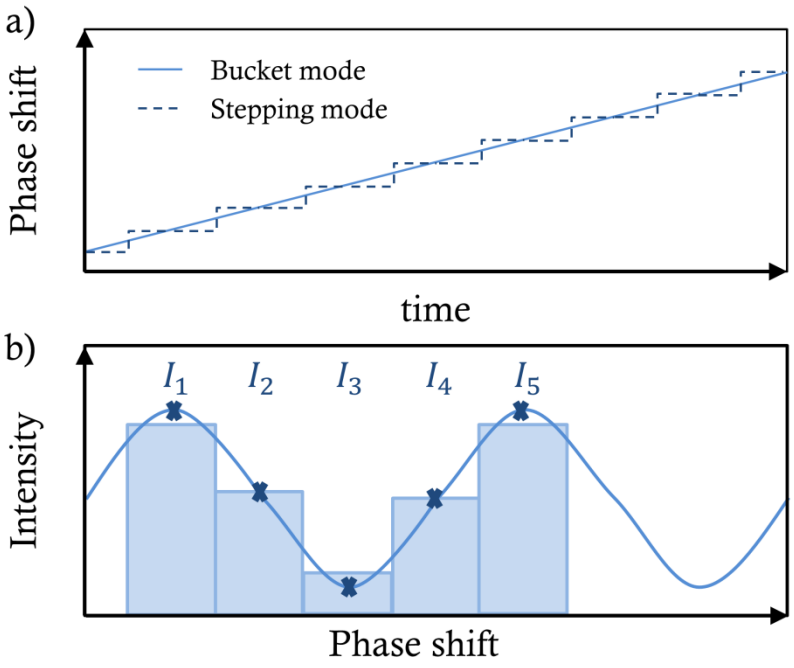

Figure 2.9.a) Phase shift as a function of time. b) Sampled intensity value (cross) in phase stepping mode and averaged intensity (bins) in bucket mode.

2.3.2.2.1 PSI geometrical interpretation

Phase demodulation algorithms focus on estimating the phase from recorded intensity values. The unknowns in equation (2.3.4) are three: mean value (I_{DC}), amplitude (I_{AC}) and initial phase (zK) from which the surface height can be calculated. Therefore to estimate all three unknown at least three intensities needs to be recorded. By applying sum on angle trigonometric identity, and making the substitutions $x_1 = I_{DC}$, $x_2 = I_{AC}cos(zK)$, $x_3 = I_{AC}sin(zK)$, equation (2.3.4) can be rewritten in matrix form:

$$\bar{x} \cdot \bar{c_i} = I_i \qquad for\ i = 1,2,3 \tag{2.3.6}$$

where $\bar{x} = [\,x_1,\, x_2,\, x_3]$ is the unknown vector, $\bar{c_i} = [1, \cos(\alpha_i), -\sin(\alpha_i)]$ is the coefficient vector, I_i is the i-th measured intensity corresponding to the phase shifts α_i., and $\cdot$ denotes the

vector dot product. Equation (2.3.6) is a linear system of three equations in three unknowns. By solving the linear system it is possible to calculate the phase as

$$\theta = \text{atan}\left(\frac{x_2}{x_3}\right)$$

and therefore the surface height z, according to equation (2.3.3). An interesting discussion of a linear system and its solution is the so called geometrical interpretation of PSI algorithm [46]. The solution space $\bar{x} = [\, x_1, x_2, x_3]$ is a three dimensional space where each of the three conditions in equation (2.3.6) define a plane and the system solution is the intersection of the three planes. The solutions space of the system of equation (2.3.6) is the solution space of the homogenous system translated by a particular solution of the non-homogenous system. The homogeneous system is:

$$\bar{x} \cdot \bar{c_i} = 0 \qquad for\ i = 1,2,3. \tag{2.3.7}$$

Solution of equation (2.3.7) is the intersection of three planes perpendicular to the vectors c_i. The vector c_i is a vector of constant modulus rotated around the x_1 axis by $-\alpha_i$ and with an angle of 45 ° with respect to x_1 (see Figure 2.10a). Vectors perpendicular to c_i have also an angle of 45 ° with respect to x_1. If the number of phase shifts is infinite, the solution is the vertex of a conic shape and in the case of a finite number of phase shifts is the intersection of three planes tangent to the cone (see Figure 2.10b).

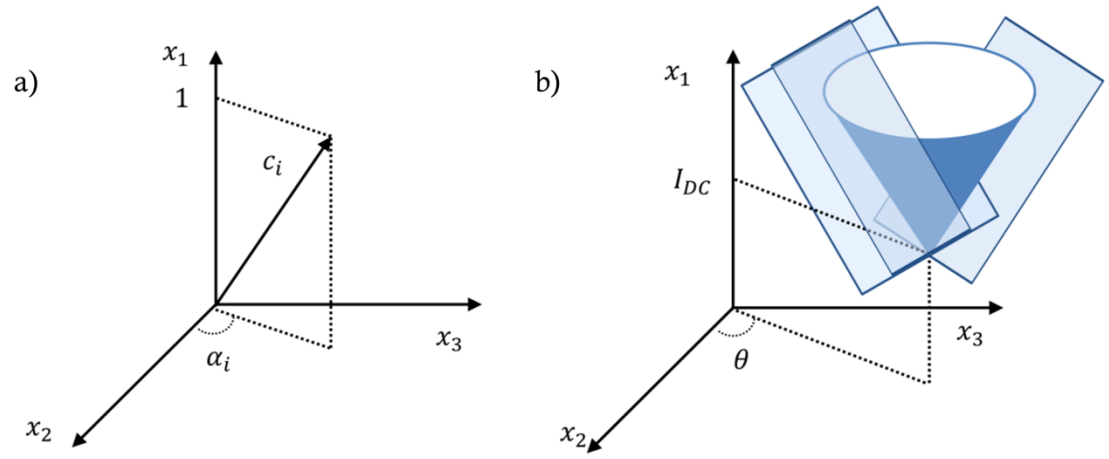

Figure 2.10. a) vector c_i . b) PSI linear system solution from geometrical interpretation.

In general the recorded intensities deviate from the ideal values due to additive noise, and the phase shift α_i is different from the ideal value due to mis-calibration or environmental vibration (*i.e.* phase noise). Noise and phase shift errors are non-ideality that cause the three planes to intersect away from the cone vertex, therefore leading to measurement errors. By employing this model it has been shown how it is possible to implement recursive algorithm which decrease the sensitivity of the algorithm to vibrations [46]. By increasing the number of

intensity measurements to 4, it is also possible to consider α_i as unknown and avoid first-order phase shift calibration errors [47]. Increasing further the number of intensity measurements has multiple effects: higher order calibration error can be corrected and the phase noise is averaged. In fact, when more than 3 phase shifts are done, and the solution for each triplet of system equation is considered, all the solutions will not converge but a cloud of points is obtained, and from averaging these solutions a better estimation in the presence of error can be obtained.

2.3.2.2.2 PSI linear filtering interpretation

Further analysis of a 4 phase shifts algorithm is useful to explain the phase shift algorithm as a linear filtering operation [48]. A common PSI algorithm is the 4-step linear Carré algorithm where the phase is estimated from four phase shifts according to

$$\theta = \text{atan}\left(\frac{I_2 - I_4}{I_3 - I_1}\right). \tag{2.3.8}$$

The algorithm is therefore a multiplication of the recorded intensity by two different set of coefficients, and from their ratio the phase can be estimated. It is possible to write a general phase shifting algorithm as

$$\theta = \text{atan}\left(\frac{\sum_{i=1}^{p} s_i I_i]}{\sum_{i=1}^{p} c_i I_i]}\right). \tag{2.3.9}$$

The variety of PSI algorithms is enormous, for example an analysis of 84 different PSI algorithms is reported in [49]. However, their performances can be explained by considering the algorithm as a linear filter. For instance, consider the sampled interference signal in figure 2.11a. The coefficients s_i and c_i for i=1, 2, 3, 4 for the Carre' algorithm are shown for comparison. In Figure 2.11b the magnitude of the Fourier transform (FT) of the interference signal is compared with the FT of the complex Carre' filter defined as:

$$f_{Carre} = c_i + j\, s_i \qquad i = 1, 2, 3, 4 \tag{2.3.10}$$

The effect of the filter is to separate the conjugate peaks of the signal FT by selecting only one of the two spikes of the signal to extract the signal phase. The Carre' filter shows a magnitude different from zero only at frequencies which are not an integer number. As a consequence, any spurious frequency arising from interference signal distortions is not filtered out, and they introduce error in the phase estimation.

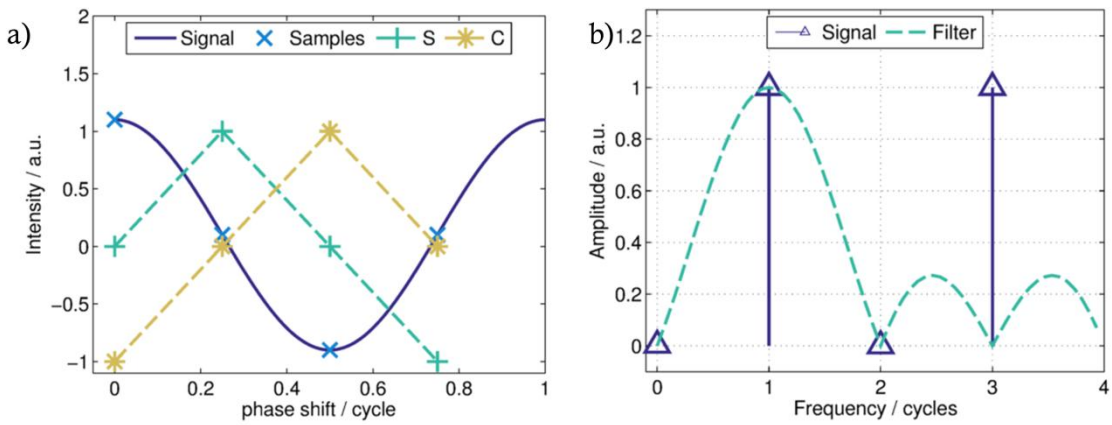

Figure 2.11. a) Interference signal and corresponding sampled intensities. For comparison the Carre' filter coefficients are displayed. b) Interference and Carre' filter FT magnitude.

The spectral response of the PSI filter can be modified by modifying the filter coefficients. For example it has been shown how multiplying the filter coefficients by a known window improves the performances of a PSI algorithm [50], [51]. For instance, let's consider a PSI algorithm obtained by acquiring eight value of intensities with the same phase shift as in the Carre' algorithm, and the same coefficients multiplied by a window function, in this example an Hamming window [52]. In figure 2.12a the obtained coefficients are shown and the filters FT magnitude is compared in figure 2.12b. The effect of windowing the filter coefficient is to reduce the filter sensitivity to higher frequency at the expense of increasing the main lobe width.

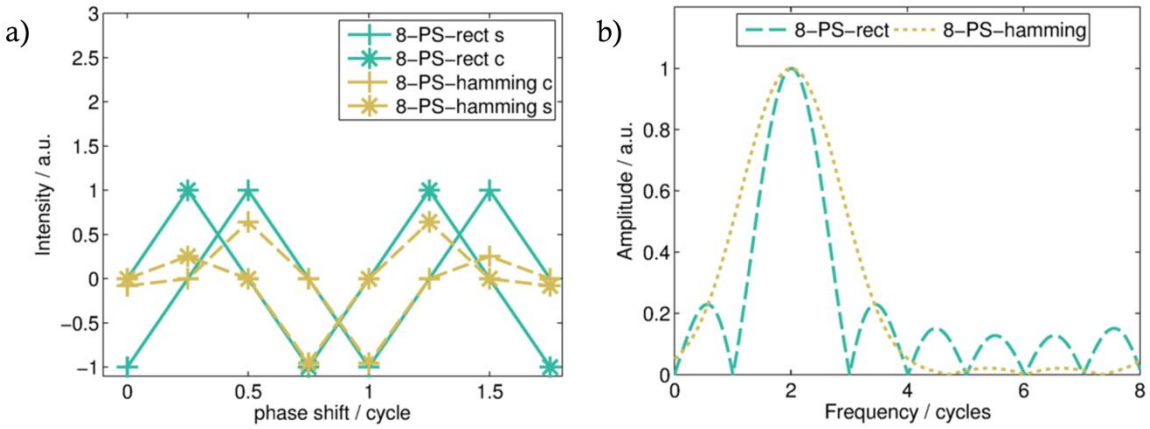

Figure 2.12. a) PSI filter coefficients for a eight phase shift algorithm obtained as the repetition of the Carre' coefficients. In the Hamming window case the coefficient are multiplied by a hamming window therefore reducing their amplitude towards the edges.

Interpreting the PSI algorithms as linear filters allow identifying procedure to design phase demodulation algorithm with the desired properties [53]–[55] and to optimise the parameters of existing algorithms for best performance [56], [57].

The effect of phase shift interferometry non-ideality has been largely studied. For example the effect of vibration [58]–[60] and design of algorithms to suppress known vibration

frequency [61], non-uniform but known phase shift [62], laser-diode output power variation [63] (also called multiplicative noise), random noise [64] and phase change upon reflection influence for high numerical aperture (NA) objective [65]. Error modelling and knowledge of the signal distortion allow designing the phase shifting algorithm for specific need, like in Fizeau cavity [66], [67]. Further development is towards non uniformly spaced phase shifts algorithms [68], and sinusoidal rather than linear phase shifts [69]. Non-linear iterative algorithms allow reducing the effect of vibrations at the expenses of processing complexity and time [70].

PSI instruments are capable of measuring surfaces with sub-nanometre repeatability [17] and they have been employed to measure super-flat surface with sub-Angstrom RMS roughness and waviness [71]. The measurement speed depends on the algorithm employed (more phase steps require more time) and the speed of the CMOS or CCD camera. Moreover, averaging the intensity on the camera can reduce the measurement noise at the expense of speed. In fact, the measurement noise for a given instrument is sometime expressed in $nm/\sqrt{Hz}$ [17], *i.e.* faster measurements are associated with larger noise. The main drawback of the PSI techniques is 2π phase ambiguity. Discontinuous surfaces with step heights larger than $\lambda/2$ cause a phase change larger than 2π. The estimated phase is known modulo 2π and therefore the measured height is known modulo $\lambda/2$. In case of smooth surfaces with heights larger than $\frac{\lambda}{2}$, it is possible to unwrap the phase to obtain ambiguity-free measurement. Another possibility is by estimating the phase for two different wavelength which extends the ambiguity range but do not remove it [72].

An ultimate 101 frames PSI algorithm is discussed in [73] with an estimation of the performance. Indeed, a similar algorithm is employed in coherence scanning interferometry.

2.3.2.3 Coherence scanning interferometry

Coherence Scanning Interferometry (CSI) also known as white light interferometry (WLI) and many other acronyms, is a interferometry metrology technique developed in the 1980s [74]–[76]. Its measurement principle is to scan the sample as in the Focus variation (section 2.3.1.1) or the Confocal (section 2.3.1.2) instruments but to detect the position of zero optical path difference of the measurement arm with respecting to referencing arm [74]–[76]. As the name suggests, a broadband light source is employed in an interferometer setup (see figure 2.13a) and due to the broadband illumination the light coherence length is very short and visible only when the optical path difference (OPD) between measurement and reference arm is a few interference fringes. In figure 2.13b an example of the recorded signal for a single pixel on the camera detector as a function of the scan position is shown.

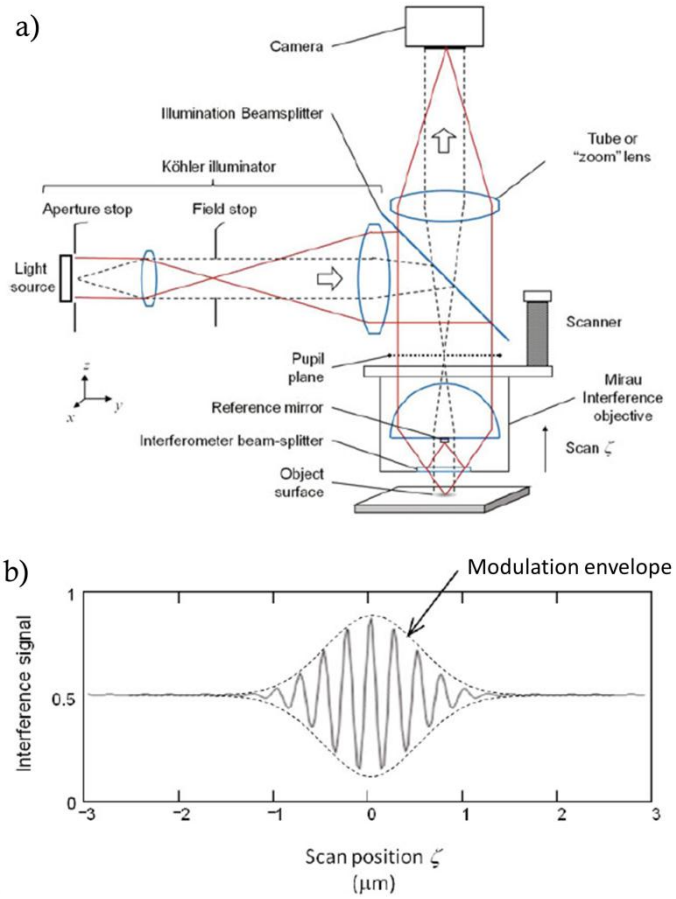

Figure 2.13. a) CSI microscope optical setup. b) example of interference intensity signal for a single pixel of the camera.

In the measurement process the surface is scanned through focus and for each position the interference signal is acquired. At the end of the scan the surface heights can be estimated by analysing the interference pattern for each camera pixel.

The interference signal can be written as:

$$I(\zeta) = I_{DC}(\zeta) + I_{AC}(\zeta - h)\cos(K_0(\zeta - h)) \tag{2.3.11}$$

where I_{DC} is the mean value, I_{AC} is the coherence envelope of the fringes which modulates the amplitude of the interference fringes with a spatial frequency equal to the mean wavenumber of the light source ($K_0 = {}^{4\pi}/_{\lambda_0}$). An example is shown in figure 2.13b.

Initially the envelope was used to estimate the surface height: the coherence envelope peaks $I_{AC}(\zeta - h)$ provides an estimation of the surface height h. Several envelope detection algorithms have been proposed with different performance in term of accuracy, complexity and speed. For example signal processing technique for demodulation of the envelope and peak fitting [77], Fourier domain estimation of the group velocity [78], centroid approach [79] or envelope demodulation by linear [80] or non-linear-filtering [81].

The surface height information is also encoded in the interference fringes phase ($\cos(K_0(\zeta - h))$) which provides measurement repeatability with performance comparable to the PSI technique [82]. Coherence envelope and phase estimation can be combined to obtained measurement with the repeatability of the PSI technique but without fringe order ambiguity [83], [84]. The repeatability improvement from estimation of the coherence envelope and phase have been quantified and modelled theoretically [85]. The envelope peak estimation repeatability is inversely proportional to the coherence length, (long coherence causes higher uncertainty) and proportional to its signal to noise ratio (SNR). On the other hand, the phase detection repeatability is reduced by longer coherence length, or finer vertical stepping, and proportional to the SNR. In some cases the uncertainty caused by the surface roughness can be higher than that due to the SNR, leading to larger uncertainty on rough surfaces [86].

Possible sources of measurement error in white light interferometry could occur at discontinuities with a height smaller than the coherence length of the light [87] or surfaces which slopes approaching the limit of the objective NA [88] sometimes due to wavelength-dependent angle of reflection [89]. Fringe order determination error could be also be due to dispersion [90]. In some cases this error can be resolved by exploiting previous knowledge of the optics systematic effects [83] or by combining phase information for two different wavelengths [91]. A reduction of the errors and consequent reduced measurement uncertainty is possible by characterisation of the slope-dependent optical response of the instruments [92].

Additional interference signal distortion is caused by the signal summation over the objective NA for each wavelength, which causes the spectrum of the interferograms to be consistently distorted for high NA [93].

Harnessing of the spectral properties of the white-light source has been shown to improve the height estimation [94]. Research into methods to correct white-light interferograms in environments with large vibrations have been reported by employing a multiplexed single wavelength PSI [95]. CSI has also been commercialised to be employed for roughness measurement and defect quantification of roll-to-roll processes [96].

With white light interferometry it is possible to measure film thickness by detecting the two reflections from the top and bottom surfaces [97]. The effect of multiple reflection on the recorded interferograms have been studied and are well understood [98].

The coherence scanning interferometry technique is a well-established technique with an associated ISO standard part 604 [99]. Several instrument's manufacturer are available such as Zygo [100] and Taylor Hobson [101]. Both instrument's manufacturers claim sub-nanometre surface topography repeatability (STR) and Angstrom resolution for the heights measurements.

The measurement speed is limited by the needs for mechanical scan of the sample through focus, and therefore the speed is proportional to the surface height to measure. For larger

surface heights the sample needs to be scanned through a larger range thus increasing the measurement time. Further speed improvement is possible by sub-Nyquist signal sampling and *ad-hoc* post-processing [102]. Typical measurement and processing times range from tens of seconds for a few micrometre heights, to tens of minutes for hundreds of micrometre heights.

2.3.2.4 Wavelength scanning interferometry

Wavelength scanning interferometry (WSI) is a metrological technique introduced in the late 1980s [103], [104]. The technique is also known as wavenumber or frequency-scanning, or wavelength/wavenumber/frequency-swept interferometry. Combining information from multiple-wavelengths, like in the CSI technique, avoid the 2π ambiguity error. In WSI the phase shift is introduced by changing the illumination in the interferometer rather than mechanically moving the sample. In figure 2.14 the schematic of a WSI instrument is shown. The light source provides a tuneable illumination, usually with a narrowband spectrum and therefore with a longer coherence length than in CSI. The light is used in an interferometer setup and the interference between the reference and measurement arm recorded. In the measurement process, the illumination is changed sequentially and for each wavenumber (k) an intensity value is recorded by the detector.

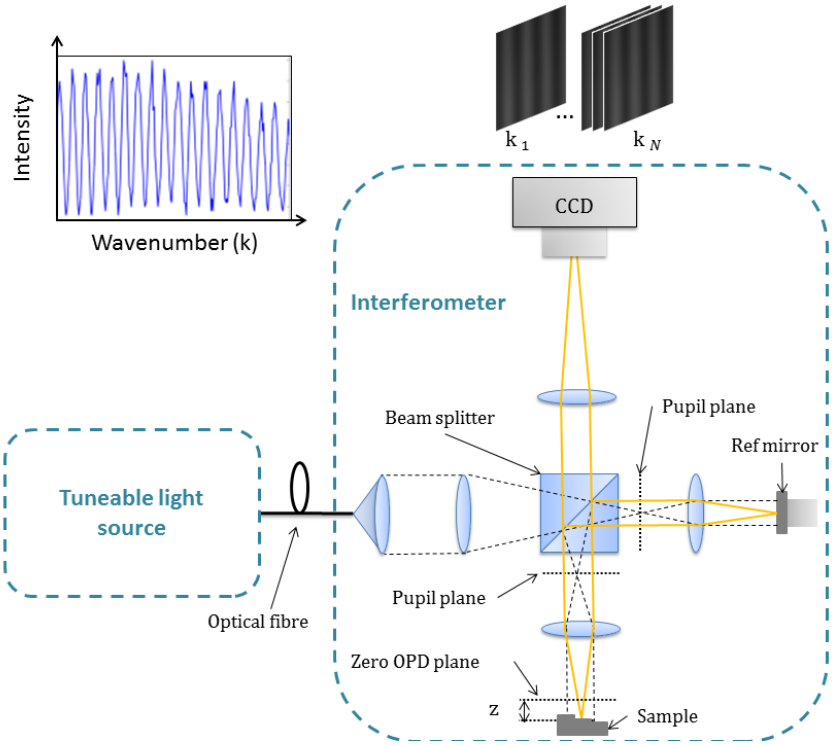

Figure 2.14. WSI instrument schematic. Top left an example of an interference signal recorded with WSI.

The interference signal can be described as:

$$I_{xy}(k) = I_{DC} + I_{AC}\cos(2\, z_{xy}\, k) \tag{2.3.12}$$

where k is the light wavenumber ($k = \frac{2\pi}{\lambda}$), and z is the OPD between the reference and the measurement arm. In the measurement process the wavenumber k is changed linearly and for each selected wavenumber an interference pattern of the surface is acquired. For a value of z equal to zero, all the wavelengths interfere constructively and therefore the interference is a constant value. For value of z not equal to zero, the interference signal has wavenumbers for which the interference is constructive and wavenumbers for which it is destructive. In the case where the wavenumber are scanned linearly, the number of constructive and destructive periods is proportional to the OPD and the value of z can be estimated according to [105]:

$$z = \frac{1}{2}\frac{\Delta\varphi}{\Delta k} \tag{2.3.13}$$

where $\Delta\varphi$ is the phase change corresponding to the wavenumber change of Δk. The algorithm estimates the phase slope (also called the instantaneous frequency) of the interference patterns. A possible frequency estimation can be obtained also from peak fitting of the interference pattern FT [106]. A comparison of known instantaneous frequency estimation algorithms is reported in [107]. The best performance is obtained with the Fourier method for phase demodulation originally published by Takeda et al. [108] followed by a linear fit of the demodulated phase. Non-linear algorithms are used, which increases measurement performance at the expense of signal processing complexity [109].

Typical tuneable light sources employed in WSI instruments are laser diodes where the wavelength is changed by modulating the injection current [110]–[112]. Limiting factor for the laser diode are the narrow available wavelength bandwidth and laser mode hops that cause discontinuities in the wavenumber scan [113]. Wavenumber scan non-linearity affects the accuracy of the measurement [114]. The laser wavelength is sensitive to thermal drift and dual-wavelength sweep in opposite direction has been proposed to compensate for these effects [115]. Thermal warm up of a He-Ne laser has also been used to provide a tuneable wavelength source for absolute displacement measurement [116].

Further improvement is possible by employing external cavity laser diodes which allow for wider tuning ranges without mode hopping [117]–[119]. Further developments, such as acousto-optical-tuneable-filter (AOTF) allow designing wide-band, fast scanning tuneable sources.

WSI has been shown to be able to measure film thicknesses [120], or in general multiple reflection cavities [121], [122].

An example of commercially available WSI is the Verifire MST [123], capable of measuring multiple surfaces samples. Thickness measurements with a peak-to-valley error value of 34 nm are reported by processing the data with a FT based phase-shifting algorithm when compared with a non-linear fitting model of the interference signal [124]. The main advantage of WSI

technique is the speed. No mechanical scanning is needed, and therefore the speed is limited by the detector frame rate and/or the wavelength scan rate.

2.3.2.5 Optical coherence tomography

Optical coherence tomography (OCT) is an imaging technique that allow to capture three-dimensional image of an optical scattering medium[125]. OCT techniques exploit the phenomenon of interference: the OCT image is obtained by detecting the intensity of the interference signal as a function of depth in the scanned sample. The recorded intensity of the interference patter plotted versus the scanned depth provides an estimation of the reflectivity of the layer in the sample. OCT techniques are employed to obtain a three-dimensional image of biological tissue for diagnostic purpose or inorganic material for industrial defect detections (see examples in figure 2.15). OCT employs light sources usually in the IR region since long wavelengths allow deeper penetration into materials than visible light, and they employ a broadband source to limit the observation of the interference within a short coherence length.

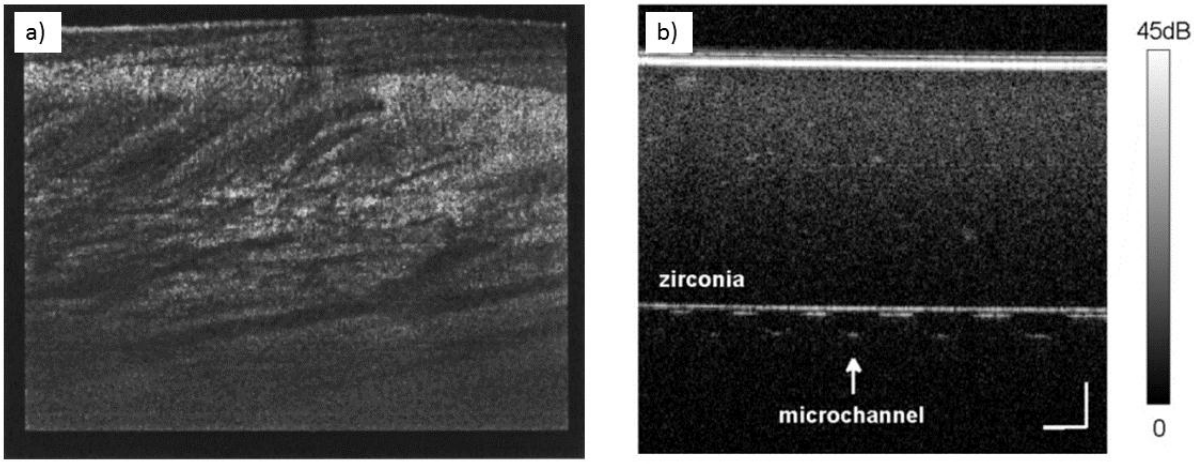

Figure 2.15. OCT images of human skin (a) and microchannel under zirconia ceramic layer (b) (adapted from [125] **and** [126]**).**

Different kind of OCT techniques are: time-domain OCT, spectral OCT and swept-source OCT [127]. In time-domain OCT the interferometer reference arm is scanned to recorded the interference signal intensity for different depth, like in CSI. In spectral OCT a spectrometer decomposes the interference signal into its spectral components. The interference signal is then further processed via a FFT transform and from the frequency of the Fourier peaks it is possible to estimate the depths whilst from their amplitude it is possible to estimate the interference intensities and therefore the surface reflectivity. In swept-source OCT a tuneable laser source allows obtaining the same information as in spectral OCT, by sweeping the illumination wavelength. The main advantage of spectral and swept-source over time-domain OCT is the scanning speed, since in spectral and swept-source no mechanical scan is needed.

The axial resolution depends on the coherence length and therefore on the illumination bandwidth, typical values ranges between 1µm to 10 µm [127]. Improved measurement repeatability has been shown can be achieved by using also the phase of the interference signal [128], and further improvement is possible, for high speed measurement, by solving trigger jitter issue[129].

2.4 Experimental realisation of WSI

In this section the details of the WSI instrument on which this research is based are described. The first section describes the instrument tuneable light source, the second section describes the interferometer head, and the last section describes the algorithm employed to process the interference signal.

2.4.1 Tuneable light source

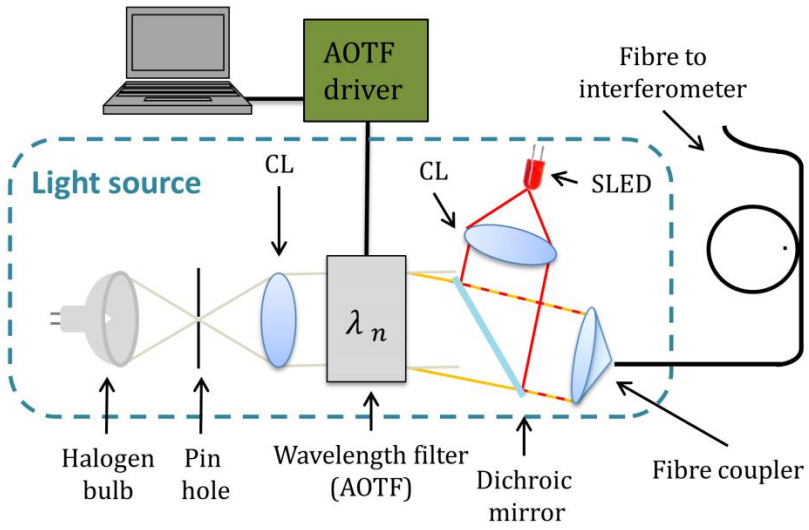

Figure 2.16. Schematic of tuneable light source. CL: Collimating lens. AOTF: Acousto-optic tuneable filter. SLED: super luminescence light emitting diode.

The light used to measure the surface is obtained by filtering the light coming from an halogen lamp. The light from the halogen lamp is focused and spatial coherence is imposed by a pin hole; The beam is then collimated by a collimation lens. The collimated white light passes through an Acousto-Optic-Tuneable-Filter (AOTF) which provides the light filtering capability. AOTFs rely on a specialized birefringent crystal whose optical properties vary upon interaction with an acoustic wave [130]. Changes in the acoustic frequency alter the diffraction properties of the crystal, deflecting only a narrow wavelengths band which is coupled into a fibre. The AOTF enables very rapid wavelength tuning, limited only by the acoustic transit time across the crystal, stated by the instrument manufactured to be 25 µs [131]. On the same fibre is coupled infra-red (IR) light coming from a super-luminescence light-emitting-diode (SLED). The IR light is collimated and aligned with the visible light through a dichroic mirror. Finally, the so-formed

light bundle is coupled into an optical fibre and delivered to the interferometer. The IR light is used for environmental noise compensation [2], whilst the other wavelength is used in the interferometer to generate the signal for surface measurement.

The central wavelength (λ) of the light that is diffracted from the AOTF and the full width half maximum (FWHM) of the filtered wavelength (λ_{FWHM}) can be determined from the equations [130], [132]:

$$\lambda = \frac{\Delta n\, v_a}{f_a}\sqrt{\sin^4\Theta_i + \sin^2 2\Theta_i} \quad , \qquad \lambda_{FWHM} = \frac{0.9\,\lambda^2}{\Delta n\, L\, \sin^2\Theta_i}$$

where Δn is the birefringence crystal refractive index, the v_a and f_a are the velocity and frequency of the propagated acoustic wave respectively, Θ_i is the incident angle of the entrance light beam which is a constant and L is the interaction length between the acoustic wave and optical radiation. Therefore scanning linearly the frequency of the propagated acoustic wave allows for linear scan of the wavenumber ($1/\lambda$). However, non-ideality causes the AOTF response to be non-perfectly linear. A characterisation of the tuneable light source and its non-ideality effects on the measurements are reported and discussed in section 4.2.1. Figure 2.17a shows the measured centroid wavelength and the linewidth for the tuneable light source used. The linewidth is calculated by fitting a Gaussian curve to the measured spectrum and evaluating the drop to half the maximum value (see figure 2.17b for an example of a typical spectrum).

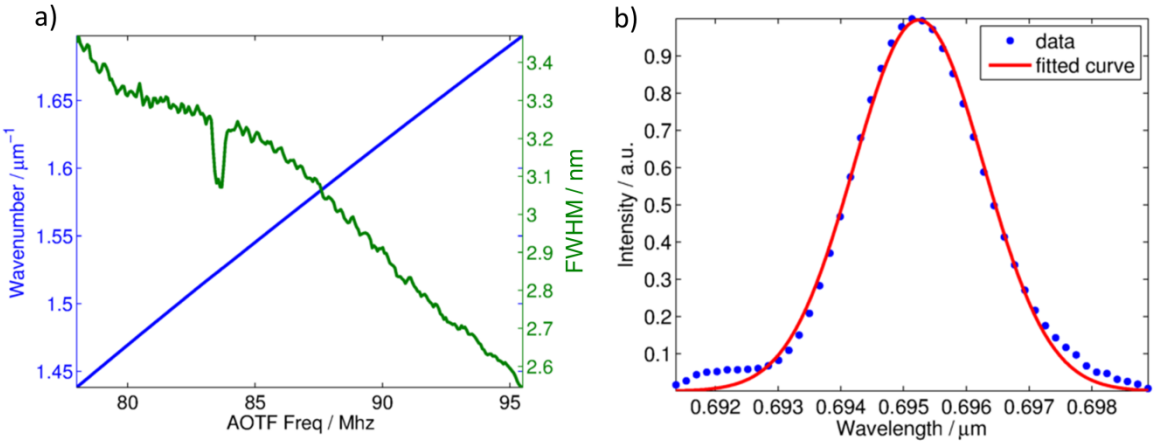

Figure 2.17: a) Centroid wavenumber and FWHM as a function of the AOTF vibration frequency. b) Typical spectrum for a filtered wavelength of ≈695.2 nm.

For a Gaussian spectrum the coherence length can be calculated as $0.32\,\lambda^2/\lambda_{FWHM}$. For the initial and the final wavelength, respectively 695.2 nm and 589.1 nm, the coherence length drop to $1/e^2$ is respectively 44.8 µm and 43.5 µm.

The measured power for the visible light is in the range 10-20 microwatts, whilst the power delivered by the SLED can be tuned and is in the range of a few milliwatts.

2.4.2 Optics setup

Different interferometer setups are possible, and four popular configurations are shown in figure 2.18. In Fizeau configuration reference beam is obtained by the light reflected by a glass plate. In the Fizeau configuration the OPD between reference and measurement arm is usually long and, therefore, this solution is popular for quasi-monochromatic light. To observe high-contrast fringes with non-monochromatic illumination the OPD has to be approximately zero. In Mirau and Michelson interferometer the beam splitter is placed after the objective lens, therefore limiting the working distance. In Linnik configuration beam splitter is placed before the objective lenses, which are duplicated on both reference and measurement arm. For the WSI instrument a Linnik setup has been chosen for its advantages in terms of working distance.

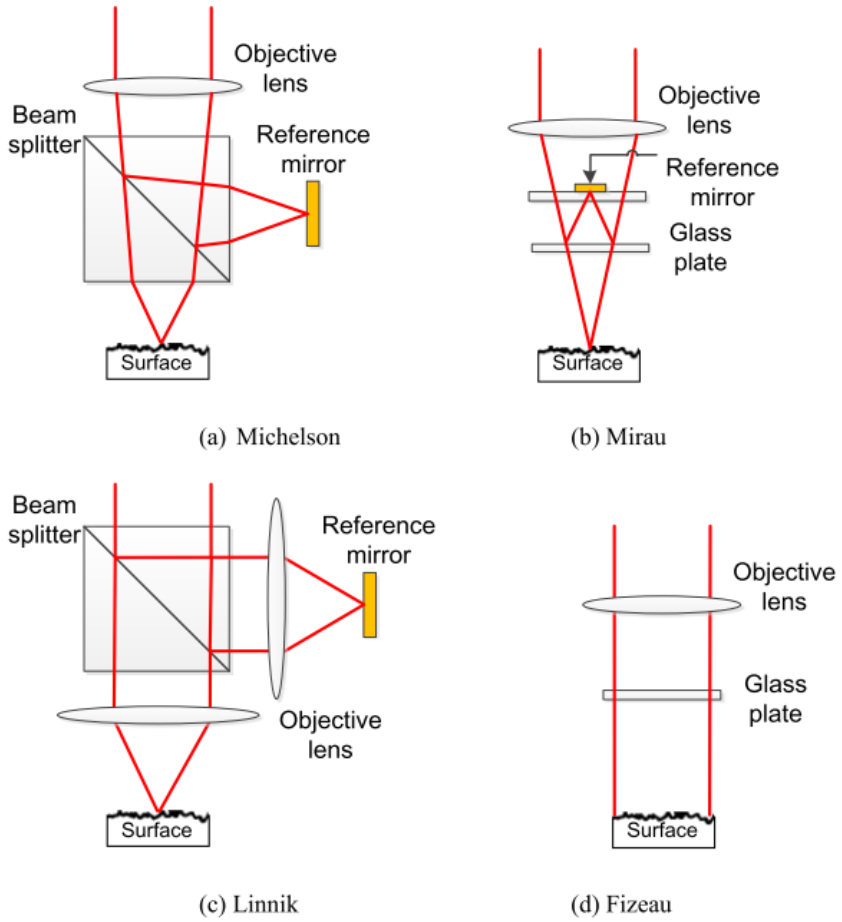

Figure 2.18. Four different interferometer configrations(from [133]**).**

The WSI instrument schematic is shown in figure 2.19. The light delivered by the optical fibre is collimated, and then employed in a Linnik interferometer setup. The recombined beams are then focused by the imaging lens. Two wavelengths are multiplexed on the interferometer at each moment: visible light and IR. Visible light is detected by the CCD camera and employed to estimate the surface topography, whilst IR light is separated with and dichroic mirror and the interference signal detected by a photodetector (PD). The IR interference is employed by a

proportional-integrative controller to move the reference mirror to reduce the OPD change due to environmental noise. The controller has been shown to reduce disturbance by 12.2 dB at a vibration frequency of 40 Hz (for more details see Jiang and al. [2]).

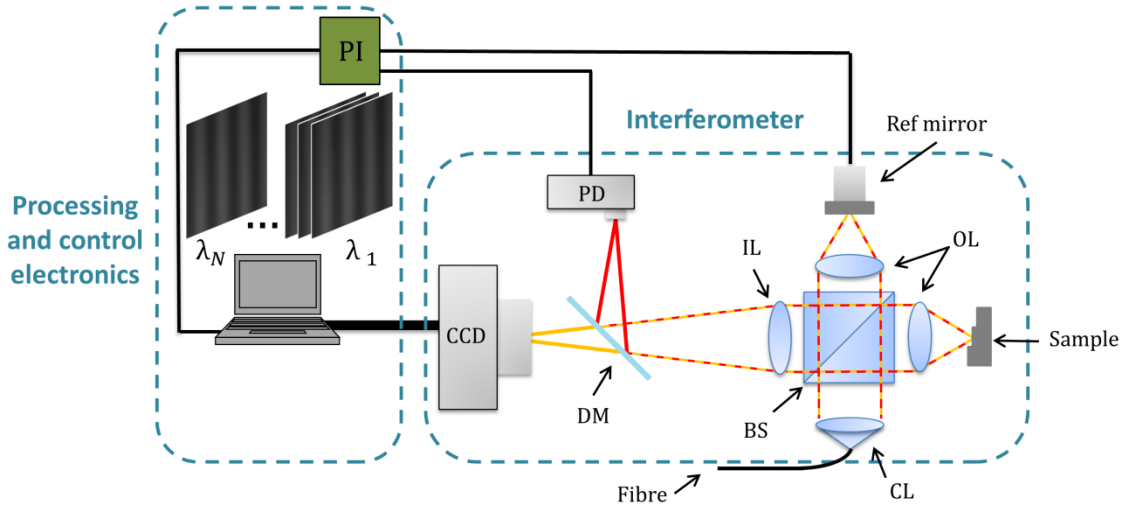

Figure 2.19. WSI setup schematic. CL: Collimating lens. BS: beam splitter. OL: Objective lens. IL: Imaging lens. DM: Dichroic mirror. CCD: Charge-Coupled Device. PD: Photo detector. PI: Proportional-Integrative controller. The fibre core is an extended source and therefore an area of the sample is illuminated allowing areal surface measurements.

In the measurement process the illumination centred on wavelength λ_1 is selected and an interference 2D image of the surface is acquired by the CCD camera. The same process (selection of the wavelength and acquisition of the interference image) is repeated N times until an image for the final wavelength λ_N is recorded. The measurement process speed is limited by the slowest between the CCD camera frame rate and the illumination switching time. In the current instrument the measurement speed is limited by the CCD camera (200 frames per second) whilst the AOTF accessing time stated by the manufacturer (25 µs) allow speed up to 40k frames per second.

2.4.3 WSI processing algorithm

The acquired 3D data cube is then processed to estimate the surface height for each pixel of the CCD camera. Figure 2.20 shows an example of interference signal extracted from the 3D data cube. The calculation is executed in parallel on a GPU leading to a processing time of a few seconds.

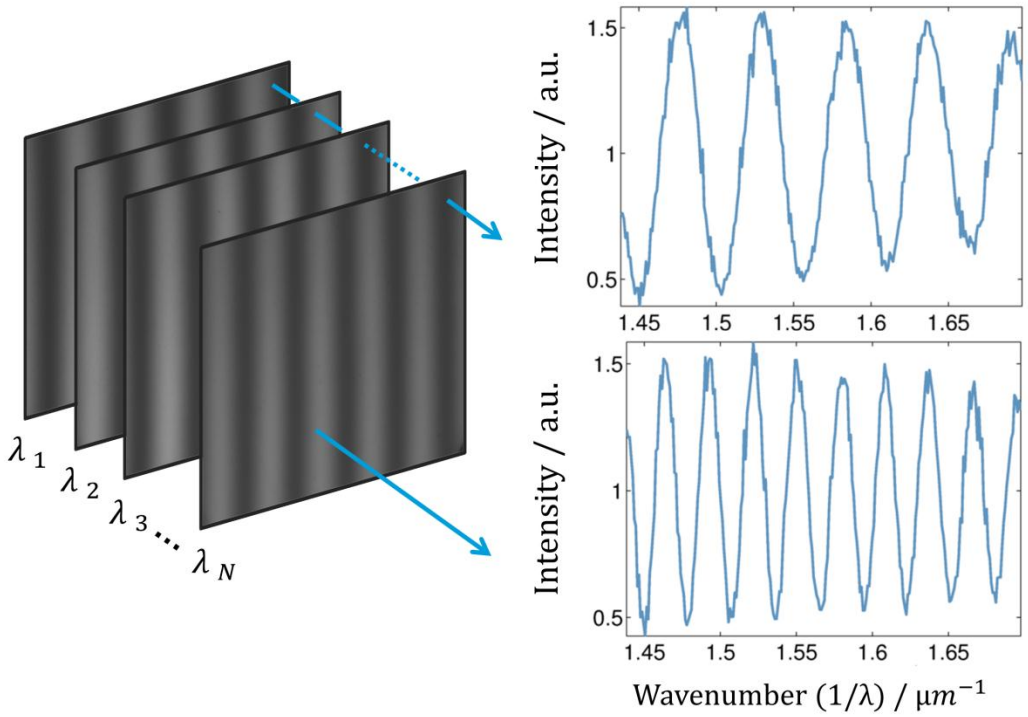

Figure 2.20. Left. 3D data cube resulting from a WSI scan. Right: two examples of the interference signal for two different values of heights.

The algorithm to estimate the height focuses on estimating the frequency of the interference pattern. Comparison of possible frequency estimation algorithms is reported in Muhamedsalih et al. [107]. The best-performing algorithm is the phase demodulation firstly reported by Takeda et al. [108] and is hereby reported for completeness. The interference signal recorded by a wavelength scanning interferometer can be written as:

$$I(k_i) = a + b\cos(4\pi z k_i) \qquad i = 0, \dots, N \tag{2.4.1}$$

where a is the signal offset, b is the signal amplitude, k_i the i-th centroid wavenumber and z is the value of height to estimate. Equation (2.4.1) can be rewritten in terms of complex phasors using Euler's formula:

$$I(k_i) = a + \frac{b}{2}(e^{j\varphi(k_i)} + e^{-j\varphi(k_i)}) \tag{2.4.2}$$

where $j = \sqrt{-1}$ and $\varphi(k_i) = 4\pi z k_i$. An FFT is applied to equation (2.4.2) to obtain the spectrum of the interference pattern (see figure 2.21b). The spectrum contains three terms, as stated in equation (2.4.3):

$$FT\big(I(k_i)\big) = A + B(f - f_0) + B(f + f_0). \tag{2.4.3}$$

The term A corresponds to the signal intensity offset, and the two peaks B correspond to the cosine, the frequency f_0 is the frequency of the fringe pattern and it is proportional to the height z.

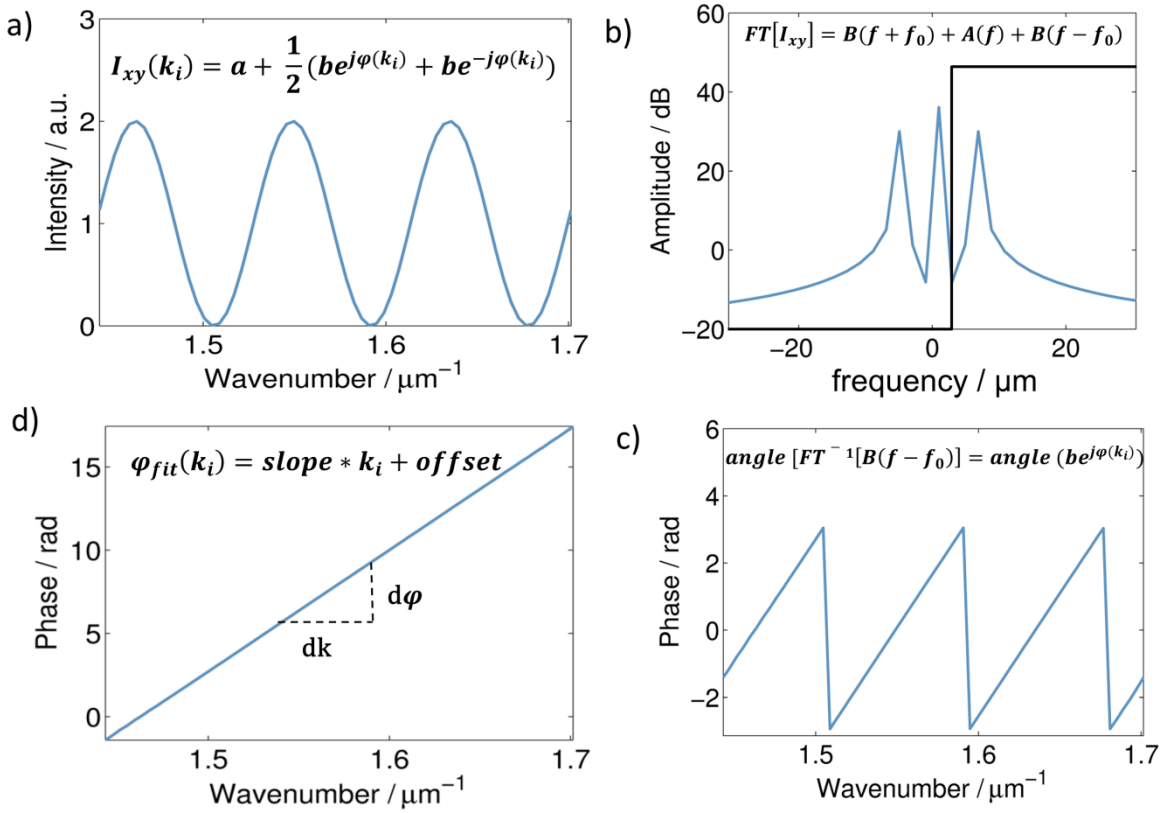

Figure 2.21. Phase demodulation algorithm steps. a) interference signal. b) Fourier transform of the interference signal. c) wrapped phase. d) unwrapped phase whose slope is proportional to the value of surface height.

The purpose of the FFT is to distinguish between the useful information that is represented by the phase change (*i.e.* $B(f - f_0)$ or $B(f + f_0)$) and the unwanted information of constant amplitude (i.e. A). To demodulate the phase only one of the two peaks corresponding to the phase change is selected, the unwanted spectrum A and $B(f + f_0)$ are filtered out and an inverse FFT is applied. From the angle of the inverse FFT it is possible to reconstruct the wrapped phase values (see figure 2.21c):

$$\varphi_{wrapped}(k_i) = angle(FT^{-1}[B(f - f_0)]). \tag{2.4.4}$$

The phase is unwrapped by adding phase jump of 2π when the difference between adjacent samples is larger than π. The unwrapped phase is then linearly fitted to estimate its slope from which the height can be estimated as:

$$z = \frac{1}{4\pi}\frac{\Delta\varphi}{\Delta k} \tag{2.4.5}$$

where $\frac{\Delta\varphi}{\Delta k}$ is the estimate phase slope.

An important assumption needs to be made when employing the described algorithm on the sign of the frequency and therefore of the z value. In fact, the algorithm estimates the same identical value of z, but with a negative sign, if the other peak corresponding to the cosine is filtered (see figure 2.21b). In this case the demodulated phase would have negative slope but same magnitude. Further details and a proposed solution to resolve this ambiguity is described in section 6.1.

2.5 Areal surface topography measuring instruments comparison

The aim of this section is to introduce metrological characteristics (MCs) for optical surface measuring instruments. The MCs are instrument characteristics that affect the measurement uncertainty and they are indicators of instrument's measurement performance. Examples of instruments performance claimed by instrument manufacturers of surface topography measuring instruments are reported and discussed. Secondly, the MCs are defined according to the drafted ISO standard and the concept of calibration and traceability introduced. Lastly, examples of MCs for commercially available instruments are compared with the performance specifications reported by the manufacturer.

2.5.1 Instrument's performance specifications

Manufacturers of surface topography instruments specify their instrument performance with a variety of 'performance indicators'. In table 2.1, table 2.2 and table 2.3, examples of these 'performance indicators' are reported for a focus variation, a confocal, and a CSI instrument, respectively.

The focus variation instrument is an Alicona IF G4, equipped with a 50x objective lens. The manufacturer of this instrument specifies the performance in terms of resolution and accuracy of step height measurements. The confocal instrument is an Olympus Lext OLS4100. The performance specifications are given as repeatability and 'accuracy' for a reference flat surface and step height measurements; the specifications are provided for two magnification objectives. Note that according to the *International Vocabulary of Metrology* or VIM [134] the term accuracy is a qualitative term and therefore its use as a quantitative term is discouraged. The CSI instrument is a Taylor Hobson CCI HD and its performance is specified by the manufacturer as repeatability in step height measurement, repeatability of surface RMS, and resolution.

Table 2.1. Manufacturer specifications for focus variation instrument.

Alicona IF G4 (50×) [20]		
Specification		**Value**
Resolution and application limits	Min. measurable height	0.02 µm
	Height step accuracy (1 mm height step)	0.05 %
	Min. repeatability	0.003 µm
Accuracy	Flatness	U = 0.1 µm
	Height Measurement z = 1 mm	Maximum permissible error (MPE) = 0.5 µm, stdev = 0.1 µm

Table 2.2. Manufacturer specifications for confocal instrument.

Olympus Lext OLS4100 [135]		
Specification		**Value**
Planar measurement	Repeatability (100×)	0.02 µm
	Accuracy	Measurement value ±2%
Height measurement	Repeatability (50×)	0.012 µm
	Accuracy	<0.2 +L/100 µm (L=measuring length)

Table 2.3. Manufacturer specifications for CSI instrument.

Taylor Hobson CCI HD [136]	Value
Resolution	0.01 nm
RMS repeatability	<0.02 nm
Step height repeatability	< 0.1 %

Repeatability and RMS repeatability typically refer to the same instrument property: the intrinsic instrument noise that limits how much the surface topography varies between repeated measurements. The reported value of the instrument noise is not associated with measurement conditions, sample details, or a description of the data post-processing steps—all parameters that can affect the measurement result. For example, averaging multiple measurements or applying a smoothing filter on 'raw' surface topography data can result in a lower value for instrument noise; the reduction in the value of noise would depend on the number of averaged measurements and on the size of the smoothing filter. Absence of clearly-defined criteria means that instrument manufacturers are flexible in the manner with which they calculate and report specifications, sometimes leading to large variance in specified

performance between instruments. A more informative and rigorous description is required to describe and compare the measuring capabilities of these instruments. Some valuable references for this purpose are the *Guide to the expression of uncertainty in measurement* (GUM) [137] and the *International Vocabulary of Metrology* (VIM) [134], both of which are documents developed by the International Organization for Standardization (ISO). The ISO 25178 series of draft standards are dedicated to areal surface topography measurements and are also relevant.

2.5.2 Metrological characteristics

Part 4.14 of the VIM defines resolution as "*the smallest change in a quantity being measured that causes a perceptible change in the corresponding indication*". The value of resolution has to be linked to what is measured, *i.e.* the measurand. For example, common practice when evaluating instrument noise is to smooth the measured surface by applying a spatial filter. Smoothing the surface has the effect of filtering out some noise and therefore to reduce the noise level. However, the obtained value of noise after filtering corresponds to the filtered surface rather than the 'raw' surface sampled at the individual camera pixels. To specify a resolution value, the measurand must be clearly specified.

The term 'RMS repeatability' is open to interpretation and can be misunderstood if not clearly defined. For example, if the specification corresponds to the repeatability of the areal surface parameter RMS (also called *Sq*), then it would be more appropriate to specify the value as *repeatability of the Sq parameter* and to also report the measurement conditions and any processing steps.

Measurement accuracy is defined in the VIM as "*closeness of agreement between a measured quantity value and a true quantity value of a measurand*". It should be noted that in part 2.13, note 1 of the VIM the use of the concept "measurement accuracy" is discouraged, arguing that measurement accuracy is a qualitative concept and therefore cannot be assigned a numerical quantity. In many instances, a more appropriate term to describe a result's closeness to the "true" or reference value is measurement error. The term "maximum permissible error" (MPE) has been widely adopted for specifying an instrument's performance interval and is sometimes stated for step height measurements on surface measuring instruments.

Instrument performance is affected by many influence factors, some of which are common to all surface measuring techniques while others are specific to a particular technique. The ISO standard 25178-600 provides a list of factors that affect the performance of some surface topography measuring techniques. Such lists cannot take into account all measurement scenarios. As a result, quantifying the individual contributions to measurement uncertainty from each influence factor is an unreasonably arduous task. The concept of MCs was introduced

to simplify this problem. MCs are formally defined in ISO 25178 part 600 as *"characteristics of a measuring equipment, which may influence the results of a measurement"*. The MCs of a surface topography measuring instruments are listed in table 2.4 with the axes that are affected (the z-axis corresponds to the height of the surface, while the x and y axes correspond to the lateral directions).

Table 2.4. List of metrological characteristics for a surface topography measurement.

Metrological characteristic	Symbol	Axes	Definition (from [99])
Measurement noise	$N_{m,}$,Sq_{noise}	z	Noise added to the output signal of an instrument during its normal use.
Residual flatness	z_{FLT}, $Sz_{flatness}$	z	Maximum error when measuring a reference calibrated flat surface.
Amplification factor	α_x ,α_y ,α_z	x, y, z	Slope of the linear regression curve obtained from the response curve
Linearity deviation	l_x , l_y , l_z	x, y, z	Maximum deviation from the linear regression curve of the instrument response.
Perpendicularity	Δ_{PERxy}	$x, y,$	Deviation from 90° of the angle between the x- and y-axes
Lateral period limit	D_{LIM}	x, y	Spatial period of a sinusoidal profile at which the height response of an instrument falls to 50 %

Other metrological characteristics that are currently in discussion are topography fidelity and maximum measurable slope [138], [139].

Each metrological characteristic contributes to the final measurement uncertainty and is an attempt at consolidating most, if not all, influence factors of a measurement technique. The calibration process consists of a series of tasks that can be used to quantify the contribution from each MC to measurement uncertainty. Calibration consists of transferring traceability from a reference standard to the indications of the three coordinate axes of a surface measuring instrument.

Traceability is defined in the VIM as *"property of a measurement result whereby the result can be related to a reference through a documented unbroken chain of calibrations, each contributing to the measurement uncertainty".* A traceable measurement result can be related or 'traced' to the definition of the corresponding SI unit through a series of calibrations, which

constitute the traceability chain (see figure 2.22). For dimensional measurements, traceability of a result is established to the definition of the SI unit of length, the metre [140].

Calibration of a surface topography instrument's MCs can be achieved by comparison to standard reference specimens, often called calibration or material standards. For this purpose and to ensure traceability of surface topography measurements, the National Physical Laboratory (NPL) has developed a set of reference surfaces [141], instruments [142]–[144], and test procedures [136–138].

In figure 2.22, a typical traceability chain for surface topography measurements is shown. At the top of the chain is the definition of the metre, which can be realised by the narrowband wavelength of light emitted by a frequency-stabilised laser [148]. The wavelength of non-stabilised lasers can then be calibrated by comparison to the stabilised wavelength, albeit, with a larger uncertainty due to the broader bandwidth. An areal contact stylus instruments at NPL is constructed with these lasers, which can then be used to calibrate primary standards [143]. These primary standards then can be employed to calibrate the MCs of a secondary surface topography instrument therefore specifying the instrument measurement uncertainty. Sometimes, a laboratory may have a working instrument and a reference instrument. In this case, the reference instrument is used to calibrate a secondary standard, which can then be used to calibrate the MCs of the working instrument. Each step of the traceability chain corresponds to a calibration step between a reference and a test gauge or test instrument. Since calibration is a measurement, uncertainty in the reference will be augmented by uncertainty in the measurement procedure. As a result, uncertainty increases with each calibration step.

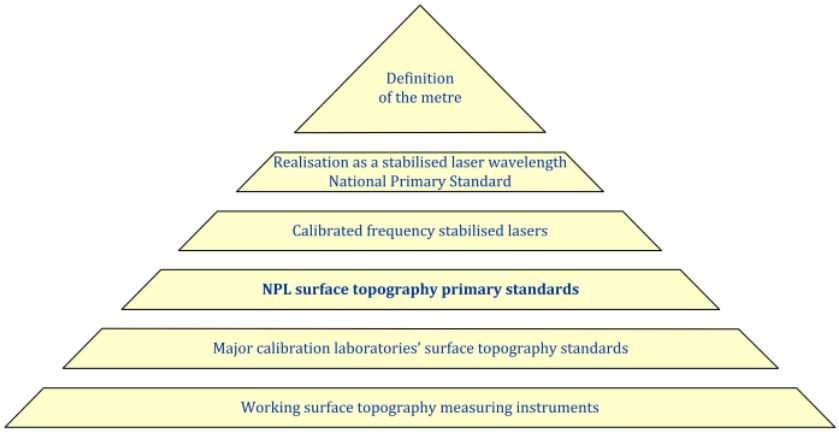

Figure 2.22. Typical traceability chain for surface topography measurement (diagram adapted from [149]).

2.5.3 NPL instruments

Calibration results of the MCs for commercially available surface topography instruments has already been reported [149]. The primary standards used are calibrated by areal surface texture measuring instruments developed at NPL with uncertainties on the order of several nanometres

along the three axes [143], [144]. Calibration results for commercially available instruments are also available in the literature [145]–[147] and have been published as NPL Good Practice Guides (GPGs) [150]. These calibration results are summarised in table 2.5 and correspond to calibration of the instrument vertical range and field of view (FOV) for three instruments: focus variation, confocal and CSI. Calibrated results of an instrument's MCs can be used to provide an indication for expected measurement errors. The maximum value is considered if the error is systematic (*e.g.*, linearity deviation or residual flatness) and the standard deviation is considered if the error is random (*e.g.* measurement noise). More information on measurement conditions and calibration procedures can be found in references [145]–[147], [151]. Methods to calibrate the MCs of focus variation instruments are still in development.

Table 2.5: Comparison of calibrated metrological characteristics of various surface metrology instruments.

Relative Axis	**MCs**	**Focus variation**		**Confocal**		**CSI**	
		20×	50×	20×	50×	20×	50×
z	Measurement Noise /nm	14	6	4.1	1.4	0.17	0.34
	Residual Flatness /nm	26.8	11.9	162	27	1.6	2.2
	Amplification coefficient	--	--	1.000	1.000	1.000	1.000
	Linearity deviation /nm	--	--	19	18	7	7
x , y	Amplification coefficient		--	1.002	0.994	0.999	1.000
	Linearity deviation /nm	--	--	240	77	168	102
	Optical Resolution /μm	--	--	1.3	0.5	1.5	0.8

The aim of reporting these results is to compare the magnitudes of MCs for commercially available instruments. The error value associated with each MC can be propagated to evaluate the uncertainty according to the guidelines specified in the GUM. For example, the combined standard uncertainty u_z in the measurement of a single value of the surface height for a single camera pixel can be calculated as [145], [146]:

$$u_z = \sqrt{{N_m}^2 + \frac{{z_{FLT}}^2}{12} + \frac{{l_z}^2}{3}} \tag{2.5.1}$$

where N_m is the measurement noise, z_{FLT} the maximum amplitude due to the residual flatness, and l_z is the linearity deviation. The values in table 2.5 are substituted into equation (2.5.1) to evaluate the standard uncertainty in vertical measurement for confocal and CSI instruments. The results are compared with manufacturer-specified vertical resolution in table 2.6.

Table 2.6. Comparison of stated vertical resolution with respect to the standard uncertainty in the measurement of a surface height value.

Instrument type	Stated vertical resolution	Standard uncertainty	
		20×	50×
Confocal	12 nm (50×)	48 nm	13 nm
CSI	0.01 nm	4.1 nm	4.1 nm

According to the results in table 2.6, the manufacturer-specified resolution could be inconsistent when compared with the standard uncertainty evaluated from the calibrated MCs.

2.6 Summary

In this chapter a brief introduction is provided for various methods of measuring surface topography. Surface topography instruments can be classified according to their measuring principle since the measured surface is dependent on the measurement procedure. Different measuring principles measures different “surfaces”, and they are able to measure different surface amplitude and lateral features depending on the development of the technique. Optical measuring techniques based on focus detection are discussed. A complete description of the most common interferometer techniques is also described. The advantages of interferometric technique over non-interferometric is the ability to detect changes in surface height of a thousandth of the light wavelength employed to illuminate the surface, therefore in the sub-nm range for visible light [17]. Additionally, measurement taken with interferometric techniques employ the light wavelength to relate the observed phase difference to the surface height dimension, therefore providing a shorter traceability route to the definition of the metre. Performance specifications claimed by the instrument manufacturers are compared to standard uncertainties, which are determined from the calibration of metrological characteristics. Discrepancies in the specified and the observed performance highlight the need for an exhaustive and metrological rigorous characterisation of instrument’s performance. The topic of this thesis is to apply the methods for calibrating the metrological characteristics of a prototype

of a WSI instrument (**Thesis Objective 2**) and to optimize its observed measurement performance (**Thesis Objective 3**).

3 Range, noise and flatness deviation

3.1 Range, noise and flatness deviation

In the following sections the methodologies used to determine the measurement noise and flatness deviation are described and the results are presented. Unless otherwise specified, measurements are made on a WSI placed on an optical table, which has active vibration stabilization, in temperature (20 ˚C ± 0.1 ˚C) and humidity-controlled environment (40 % ± 5 %); additionally, the instrument vibration compensation feedback loop was active [2]. The scanned wavelength range is from 695.1 nm to 589.1 nm, corresponding to a wavenumber range from 1.4386 μm^{-1} to 1.6975 μm^{-1}. The wavenumber range length of 0.2589 $\mu m^{-1.}$ is sampled in 256 points and, therefore, with a sampling rate of ≈1 nm^{-1}/sample. The calibration process is performed with 2× and 5× objectives lenses.

3.2 WSI range

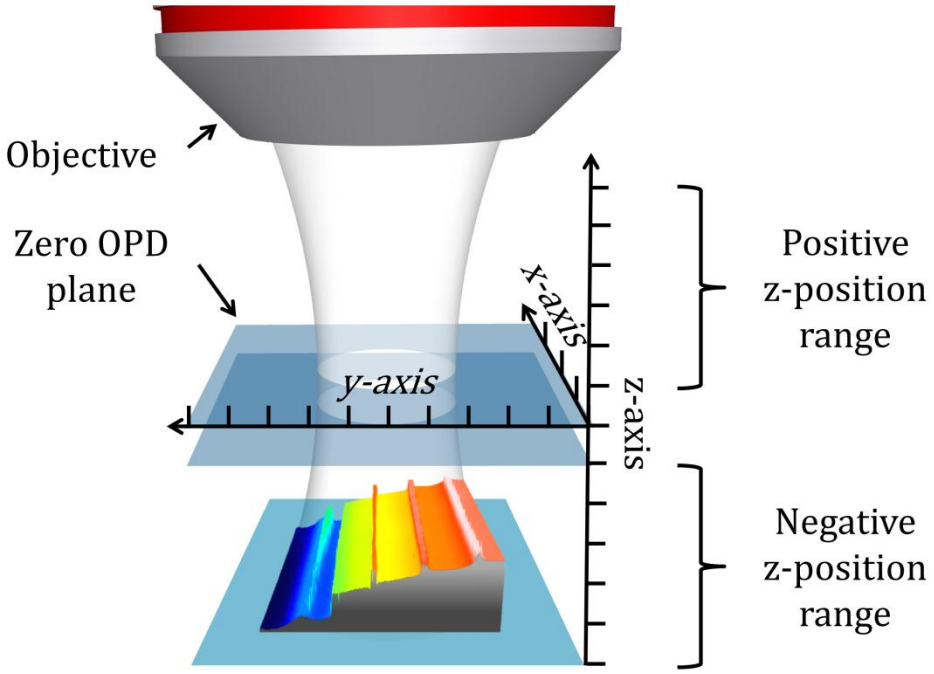

Figure 3.1: Measurement range for WSI. The calibration process aim is to estimate the uncertainty corresponding to each axis measurement.

The algorithm employed to calculate the surface *z*-positions from the interference pattern cannot distinguish between positive and negative *z*-positions, but it can estimate only the absolute distance. Therefore, an additional assumption needs to be made in order to associate higher frequency interference patterns with positive or negative displacement of the surface, *i.e.* to correctly resolve peaks and valleys (see section 2.4.3 for algorithm details and section 6.1 for a solution to solve the ambiguity). The current calibration is performed in the instrument range

corresponding to negative *z*-positions; therefore, higher frequency interference patterns correspond to valleys in the measured surface topography.

To determine the vertical (*z*) range of the instrument, several measurements are conducted on an optical flat at various positions along the *z*-axis. A schematic of the instrument measurement volume is shown in figure 3.1; in this figure, the surface to be measured occupies the instrument negative *z*-range. The instrument provides a point cloud, corresponding to the *x*, *y* and *z* coordinates of the measured surface. The smallest magnitude of *z*-value that can be measured is dependent on the processing algorithm (as explained in section 4.1); the error in measuring z is relatively large for *z*-values between +5 µm and -5 µm. To quantify the largest *z*-value, an optical flat is measured for increasing *z*-positions, until the measured surface shows outliers larger than the noise amplitude. When the interference visibility is low, *i.e.* the interference signal has a low signal to noise ratio (SNR), the measured surface exhibits spike artefacts as shown in figure 3.2. The presence of those artefacts in the measured surface is due to a 2π unwrapping error in the phase, which causes an erroneous evaluation of the phase slope.

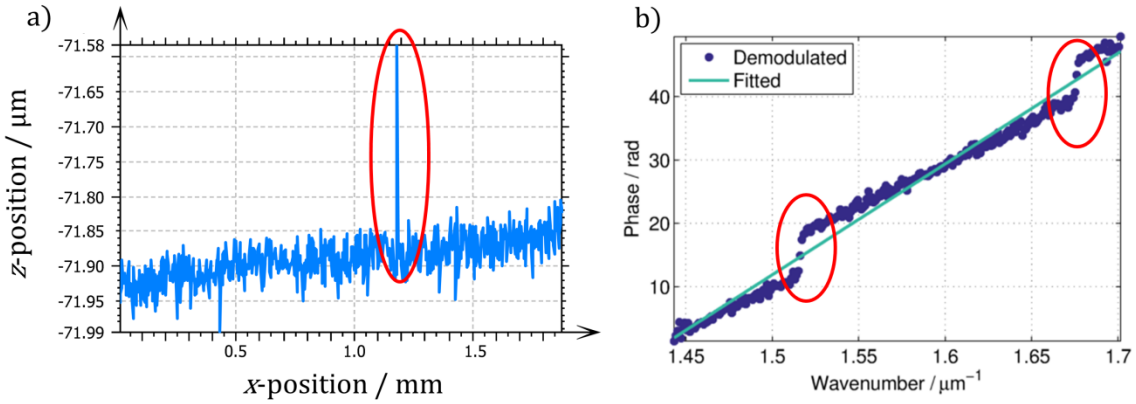

Figure 3.2: a) Spikes appear on the measured optical flat as a result of the 2π phase jumps unwrapping error. b) 2π phase jump unwrapping error in case of low visibility, *i.e.* low SNR interference signal.

When the instrument is equipped with the 2× objective, no spikes appear in the measured flat until a *z*-position of -70 µm, and therefore its measuring range is from -5 µm to -70 µm. The 2× objective lens theoretical DOF is calculated to be ±97 µm (at the shortest wavelength) and therefore only a portion of the possible measurement range is employed. Limitation to use the entire depth of focus are set by the sign ambiguity which limits to negative or positive *z*-height, and the reduced fringe visibility in position further away from the focus position (corresponding to the zero OPD).

For the 5× objective, the measured surface is spikes-free for a maximum *z*-position of -35 µm, compared to a depth of focus of ±15 µm (at the shortest wavelength). Therefore, the *z*-axis working ranges for 5× objective lens is from -5 µm to -35 µm and part of the measurement range lies outside the instrument DOF.

3.3 Measurement noise

Measurement noise is defined as a metrological characteristic that describes the noise added to the output signal of an instrument during its normal use[99]. Measurement noise is a result of multiple sources:

- Instability in the instrument electronics (electronic noise) or variance in the optical power (optical noise). Also called instrument noise, it is the noise in the instrument's output signal when placed in a noise-free environment.
- Environmental noise generated by ground vibrations, sound, ventilation, temperature fluctuations and external electromagnetic disturbance.

The WSI is equipped with an environmental noise compensation feature, capable of attenuating low-frequency environmental disturbances relative to the *z*-axis [3].

To quantify the uncertainty contribution from measurement noise, two techniques are employed. Neither of these techniques requires a dedicated reference flat and each is capable of isolating the measurement noise from the intrinsic roughness of the sample and from the flatness deviation. In these techniques, the surface parameter used to quantify the noise is the root mean square (RMS) value of the scale limited surface, *Sq*. One technique isolates the noise by subtracting two surface measurements, while the other technique isolates the noise by averaging several measurements.

3.3.1 Noise estimation techniques

In the subtraction technique, two measurements are taken in succession at the same position. When one measurement is subtracted from the other, the surface roughness components are cancelled out while the noise contribution is cumulative. Measurement noise can be estimated by dividing the *Sq* value of the subtracted surface by the square root of two [145]:

$$Sq_{noise} = \frac{Sq}{\sqrt{2}} \tag{3.3.1}$$

The averaging technique consists of averaging several measurements to separate the measurement noise from the surface roughness[152]. By averaging multiple measurements, Sq_{noise} should decrease by the square root of the number of measurements whilst the surface roughness and form is constant. The *Sq* value from the unaveraged measurement and the *Sq* of the averaged measurement (Sq_{mean}) can be used to estimate the Sq_{noise} by the following equation[145]:

$$Sq_{noise} = \sqrt{\frac{Sq^2 - Sq_{mean}^2}{1 - \frac{1}{n}}} \tag{3.3.2}$$

where n is the number of averaged measurements.

3.3.2 Measurement noise results

The visibility in the recorded raw fringe pattern varies with the z-position, indicating a varying SNR. To characterise the noise level variation in the instrument range, the noise measurements are repeated in 3 different vertical positions: at the top, the centre and the bottom of the instrument range (see figure 3.3)(≈-5 µm, -37.5 µm, -70 µm, respectively for the 2× objective lens ,and ≈-5 µm, -20 µm, -35 µm, respectively, for the 5× objective lens).

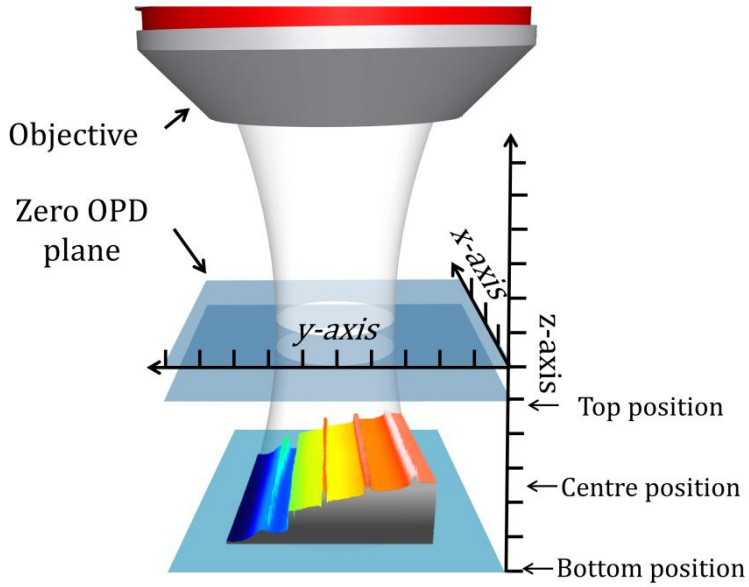

Figure 3.3. Schematics of the instrument range where the top, centre and bottom measurement positions are defined.

Repeated measurements are made in succession at each of the mentioned vertical position and the noise is evaluated. For the subtraction technique, the first measurement is subtracted from the second measurement, the second measurement from the third measurement and so on until all the subtractions are performed. The results from the subtraction technique are shown in table 3.1. The relatively small standard deviation from the subtraction values suggests that a single subtraction of the surface measurements is enough to estimate measurement noise.

Table 3.1. Noise measurements for WSI estimated with the subtraction method. Noise is measured at different vertical positions in the instrument range for 2× and 5× objective lenses.

Sq_{noise} / nm						
Objective lens	2×			5×		
Approx. *z*-position /µm	-5 (Top)	-37.5 (Centre)	-70 (Bottom)	-5 (Top)	-20 (Centre)	-35 (Bottom)
Subtraction run						
1	4.6	10.3	16.2	6.9	8.1	12.3
2	4.5	10.4	16.1	6.9	8.0	12.9
3	4.9	10.3	16.1	6.8	7.8	12.4
4	4.5	10.3	16.3	6.9	7.8	12.4
5	4.5	10.4	16.7	7.1	7.9	12.7
6	4.9	10.3	16.3	6.9	7.9	12.6
7	4.9	10.3	15.6	6.8	7.9	12.4
8	4.5	10.3	16.1	6.7	8.0	12.5
9	4.7	10.2	16.2	6.9	8.0	12.3
Mean	4.7	10.3	16.1	6.9	7.9	12.6
St. dev.	0.2	0.1	0.3	0.1	0.1	0.4

Table 3.2. Noise measurement results with averaging method.

Sq_{noise} / nm						
Objective lens	2×			5×		
Approx. *z* /µm	-5 (Top)	-37.5 (Centre)	-70 (Bottom)	-5 (Top)	-20 (Centre)	-35 (Bottom)
Number of averaged measurements						
2	4.6	10.3	17.2	8.2	8.0	11.8
4	4.9	10.0	17.6	7.4	8.4	13.1
8	5.0	10.0	17.8	6.2	8.2	13.3
16	5.0	9.9	17.4	6.6	8.2	13.2

In figure 3.4a the subtraction of two repeated surface topography measurements is shown, with its Fourier transform (figure 3.4b). The Fourier transformed areal subtraction measurement is considered to verify noise level variation in the instrument's field of view (FOV): the noise appears to be random across the CCD sensor, *i.e.* there are no peaks in the Fourier Transform. In figure 3.4c data along a single profile line on the noise map is presented, with a histogram of the

profile data figure 3.4d. The data in figure 3.4d has a Gaussian distribution, since the noise is a sum of multiple independent noise sources[153]. However, in a well-designed camera the photon shot noise is the dominant contributor; a Gaussian distribution is expected if the largest noise source is the photon shot with a large mean value[86].

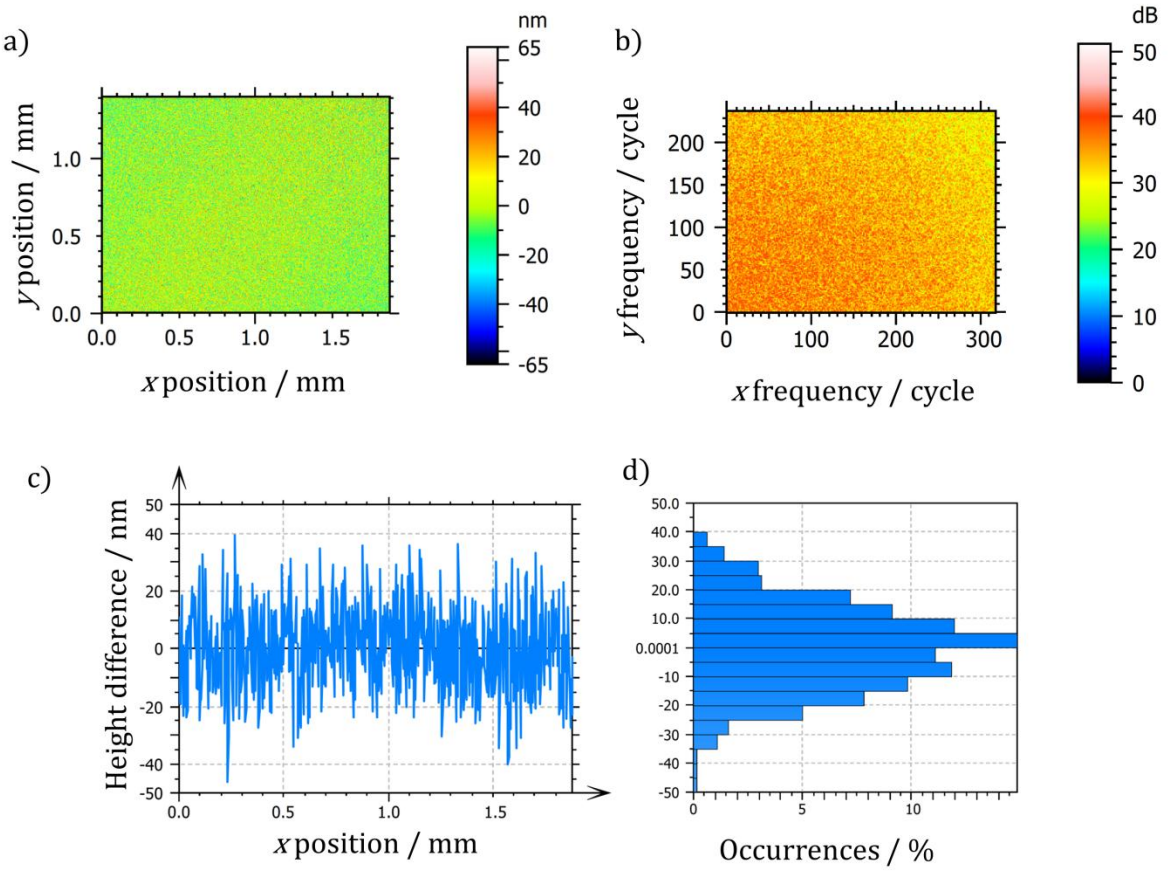

Figure 3.4: 2× magnification lens – subtraction measurements: a) Areal noise map. b) Fourier Transform of the noise map. c) noise map profile. d) profile heights statistical distribution.

Sixteen measurements are used to estimate the noise with the average method. The *Sq* value is calculated for each surface topography measurement and compared with the Sq_{mean} of the averaged surface. The results are shown in table 3.2. The difference in values from averaging various numbers of measurements is small, thus averaging two measurements could be enough to estimate the measurement noise using the averaging method.

Both subtraction and averaging methods are successful in estimating the measurement noise for the WSI. The difference in the result from the two methods is less than 10 %. Measurement noise increases as the surface position along the *z*-axis moves further from the zero *z*-position. This behaviour is a result of the decreasing interference visibility due to limited coherence length, *i.e.* a decreased SNR (see figure 3.5). The noise maximum value is associated with measurements further away from the zero OPD, and these values are 17.4 nm and 13.2 nm, respectively, for 2× and 5× magnification lenses.

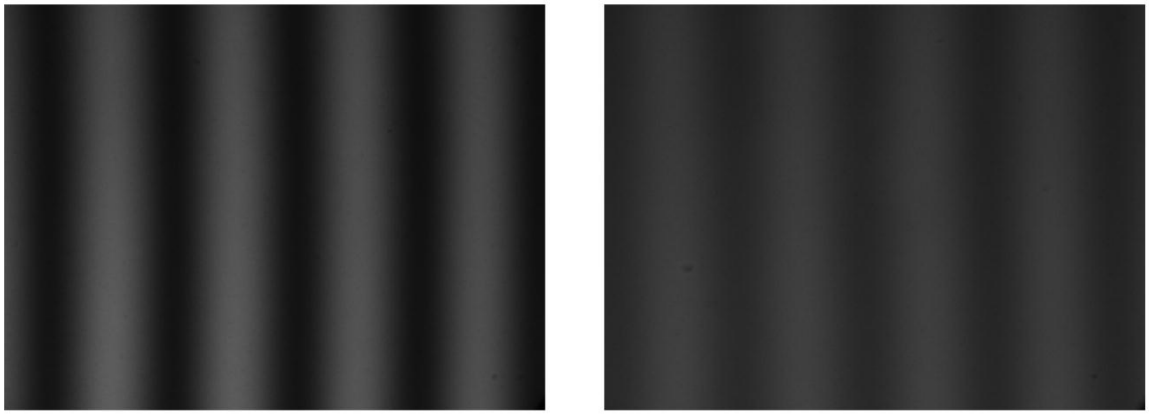

Figure 3.5. Left: Fringe pattern closer to the zero OPD (top of the negative z-position range). Right: Fringe pattern further away from the zero OPD (bottom of the negative z-position range). Both images were obtained with the 5× objective lens. Note the higher contrast in the left image, corresponding to higher SNR.

3.3.3 Noise vs adjustment of number of frames

In the measurement process, the number of frames to acquire a measurement can be dynamically selected. The number of frames influences the maximum *z*-position that the instrument can measure. According to Nyquist-Shannon's sampling theorem: the maximum frequency that can be reconstructed without aliasing for a sampling frequency f_s, is $f_s/2$ [154]. Translating this theorem for the maximum position value, it is obtained that the maximum *z*-position that can be reconstructed for a given sampling frequency is:

$$z_{max} = \frac{f_{max}}{2} = \frac{1}{2}\frac{f_s}{2} = \frac{N}{4\,\Delta k} \tag{3.3.3}$$

where N is the number of recorded frames along the wavenumber range Δk, and the additional factor of two arises because the OPD is twice the z value measured. For a wavenumber range of 0.2589 μm^{-1} (corresponding to wavelengths from 695.1 nm to 589.1 nm), the maximum *z*-value that can be obtained without aliasing for 32, 64,128 and 256 frames is, respectively, 30.9 µm, 61.8 µm, 123.6 µm and 247.2 µm. However, it is good practice to sample a signal with a sampling frequency at least double the frequency stated by the Nyquist-Shannon's theorem [155]. As a result, the maximum experimentally measurable *z*-value range is half the theoretical one, that is, 15.45 µm, 30.9 µm, 61.8 µm, 126.3 µm, respectively, for 32, 64, 128 and 256 frames. The noise is evaluated with the subtraction method and using several sampling frequencies at the position associated with the largest noise, *i.e.* the surface measured at the largest negative *z*-position in accordance to that can be resolved. The results are summarised in table 3.3.

Table 3.3. Measurement noise and range as a function of the recorded number of frames (N) for 2× and 5× objective lenses.

Objective lens	2×		5×	
	z range / μm	Max noise /nm	*z* range / μm	Max noise /nm
Number of Frames (*N*)				
32	-5 to -15.45	16.7	-5 to -15.45	35.4
64	-5 to -30.9	12.7	-5 to -30.9	31.3
128	-5 to -61.8	15.6	-5 to -35	18.4
256	-5 to -70	16.6	-5 to -35	12.5

Reducing the number of frames acquired allows for faster measurement at the expense of higher measurement noise, and shorter measurement range. The maximum noise reaches a value of 16.7 nm and 35.4 nm for 32 frames acquired, respectively for 2× and 5× objective lens, limiting the measurement range from –5 μm to -15.45 μm.

3.4 Flatness deviation

Flatness deviation is a metrological characteristic that describes an instrument's systematic deviation when measuring a flat surface and is determined by measuring a reference optical flat. Possible causes of this deviation are the quality of the interferometer reference mirror or lens aberration. The maximum height surface parameter (*Sz)* can be used to quantify the instrument flatness deviation. Each surface measurement has a *Sz* value that is a combination of the measured optical flat, the instrument reference mirror and other systematic effects of the instrument. To decrease the influence of the optical flat to the *Sz* value, an averaging technique is used. Surface measurements are taken at different horizontal positions on the calibrated optical flat. The averaged resulting surface should preserve the influence of the instrument flatness deviation and minimise the influence of the measured flat. The surface measured is a flat surface from the NPL areal calibration set with a traceable *Sz* value of 7.2 nm $\pm$ 10.3 nm with a 95 % confidence (coverage factor *k* equal 2).

3.4.1 Flatness estimation technique

Flatness measurements can be affected by unwanted features on an optical flat. To eliminate the effect of these features, a high order polynomial fit is applied to the measured surface. A twelfth order polynomial fit is enough to capture the optical flat form and separate it from the roughness and measurement noise [145]. The residual surface is thresholded to remove outliers larger than three times its *Sq* value, which removes the effect of dust or optical flat imperfection but preserves the measurement noise. Finally, the threshold residual surface and the form are

summed, and the *Sz* parameter evaluated. The process flowchart for this procedure is shown in figure 3.6.

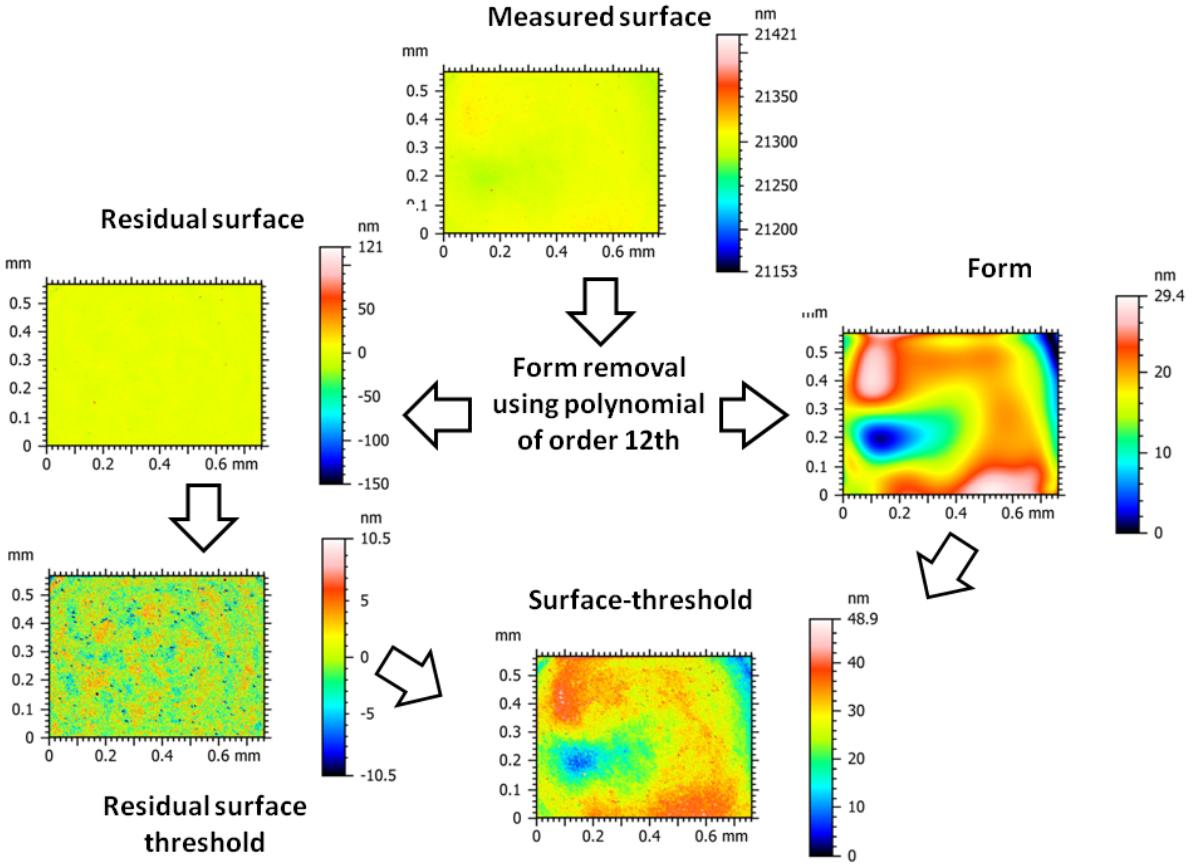

Figure 3.6. Flow chart for the flatness deviation threshold method.

Another approach for estimating the flatness deviation consists of filtering the surface to separate noise and spurious features from the form. The drawback of filtering the surface is that it is difficult to estimate the size of the outliers on the measured surface due to optical flat imperfections; therefore, the surface-fitting-and-threshold approach is employed. The effect of the number of averaged horizontal reference flat measurement on the estimated *Sz* values is shown in figure 3.7 for two cases: fitting-and-threshold on a single measurement and on the reduced noise measurement (obtained by averaging more measurement at the same position on the optical flat). In both cases, the estimated *Sz* value reaches a steady value (variation smaller than 10 %) after averaging at least eight different horizontal measurements on the optical flat. However, the estimated *Sz* value is lower in the case where the measurements have reduced noise level. It was shown in section 3.3 that the peak to valley amplitude ($\pm 3\ Sq$) measurement noise value is between 30 nm and 90 nm approximately for both objective lenses depending on the vertical position of the measurement, a value comparable with the flatness deviation to estimate. Thus, the noise can have an influence on the estimated *Sz* value, and reducing the

noise to peak-to-valley amplitude below the flatness value (*Sz*) improves the flatness deviation estimation.

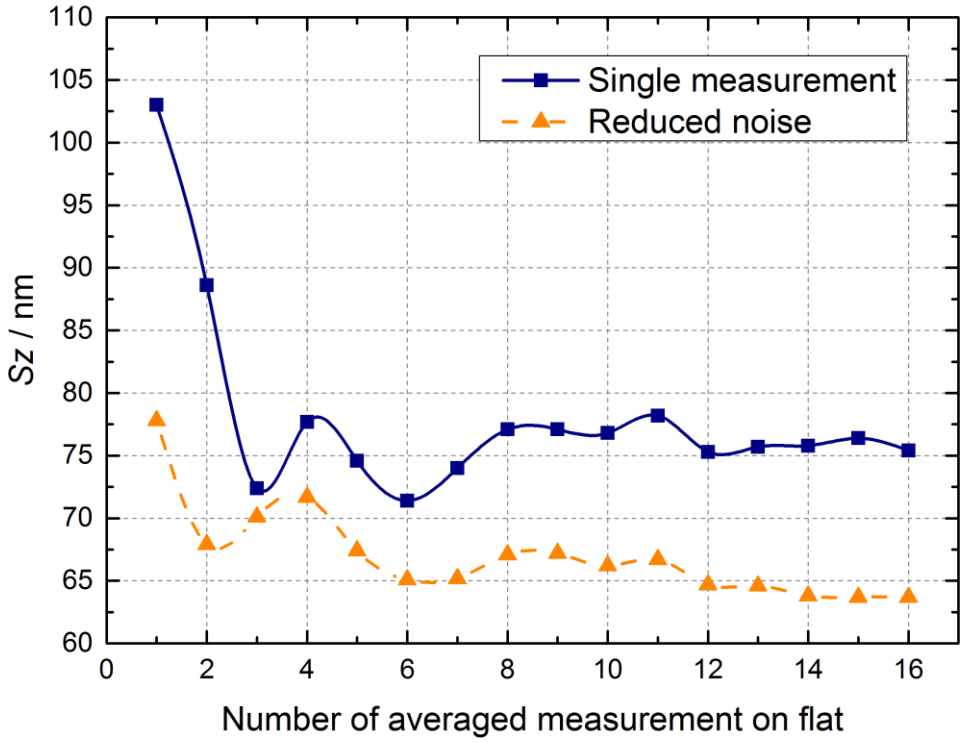

Figure 3.7. ***Sz*** **trend for single measurement and measurement with noise level reduction. The data are relative to the 5× objective lens.**

3.4.2 Flatness estimation results

The results for the flatness deviation measurements are presented in table 3.4 for the 2× and 5× objective lenses. Flatness deviation varies with the measurement *z*-position. After averaging sixteen planar measurements, the maximum flatness deviation along the entire measurement range is 69 nm for the 2× lens and 64 nm for the 5× lens.

Table 3.4. Estimated flatness deviation (*Sz*) along the instrument vertical range for 2× and 5× magnification lens.

$Sz_{flatness}$ /nm						
Objective lens	2×			5×		
Approx. *z*-position /µm	-5 (Top)	-37.5 (Centre)	-70 (Bottom)	-5 (Top)	-20 (Centre)	-35 (Bottom)
Number of averaged measurement						
2	44	59	75	68	64	62
4	42	57	73	72	60	59
8	35	55	72	68	57	56
16	36	54	69	64	53	55

In figure 3.8, the flatness map is shown for both objective lenses at the top, centre and bottom of the instrument range. The flatness deviation form changes with the measurement *z*-position.

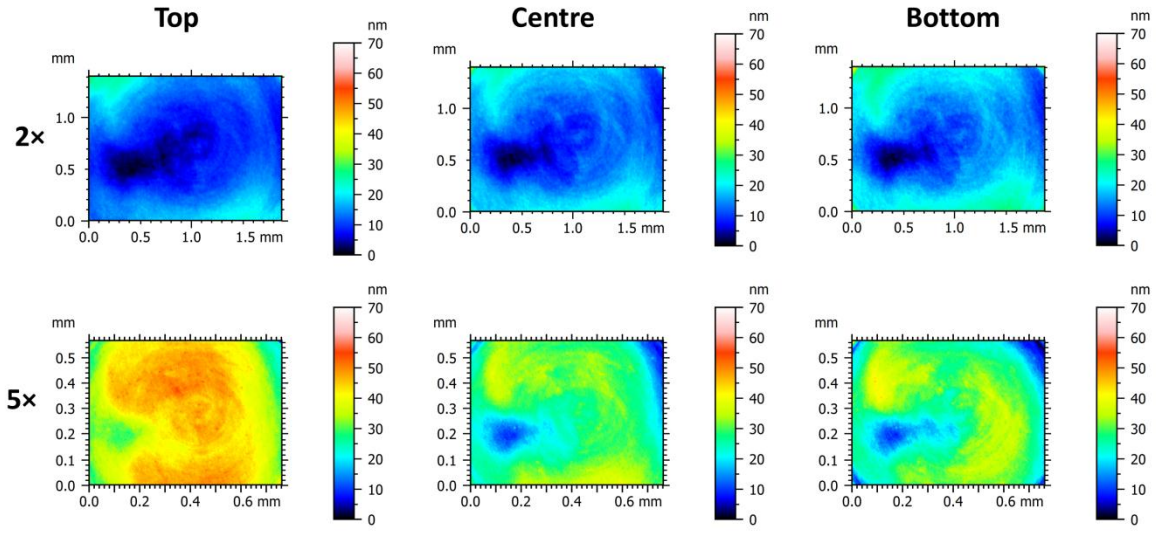

Figure 3.8: Flatness deviation map for 2× and 5× objective lens in different position in the instrument vertical range.

For both objective lenses, the overall shape of the flatness deviation is consistent along the measurement range. However, the surface maximum height parameter, *Sz,* changes. For the 2× objective lens, only one third of the whole depth of focus (DOF) is employed for measurement (70 µm over a theoretical maximum value of 97 µm). Therefore, the flatness map shows a weak dependence on the *z*-position, which corresponds to the distance from the lens focal plane. For the 5× objective lens a range larger than the DOF is employed (15 µm) and the flatness map changes the peak and valley height and depth values whilst retaining the same overall shape. The concentric rings visible in the flatness map deviation for the 2× objective are an artefact

introduced by the fibre that delivers the light to the interferometer. In fact, the instrument's sample illumination does not use a Köhler technique [156] to illuminate the sample, but the optical setup is such that the light source plane (the fibre aperture) is a conjugate plane of the surface and the CCD camera (the image plane). Possible causes for the changing of the *Sz* value are the vertical axis non-linearity (see section 4.1.3) and the defocus aberrations (see section 5.2.3). The vertical axis non-linearity affects the measured residual flatness depending on the position in the vertical range. Furthermore, larger negative *z*-positions are associated with larger distances from the lens focal plane and thus larger defocus aberrations.

3.4.3 Flatness reduction

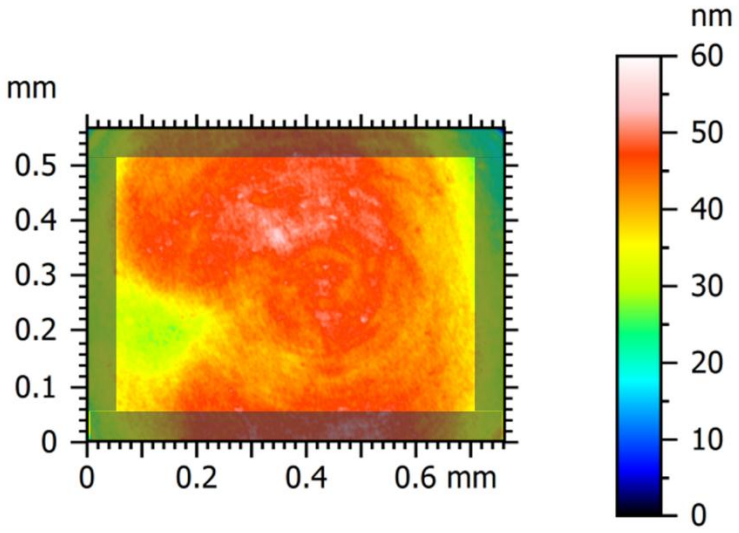

Figure 3.9: Example of FOV reduction to avoid the spike in the flatness map at the FOV corners.

Given that the measured surface exhibited the largest non-flatness at the edges of the FOV, the same flatness deviation evaluation is repeated considering a smaller portion of the FOV; more specifically 30 pixels were removed from each side of the original FOV (see figure 3.9) corresponding to an area reduction of approximately 10 %. Again, the noise was reduced by averaging sixteen measurements. The results are reported in table 3.5, and compared with the original value without restricting the FOV.

Table 3.5. *Sz* value for reduced FOV.

$Sz_{flatness}$ / nm						
Approx. position in range	Top		Centre		Bottom	
Objective lens	Entire FOV	Reduced FOV	Entire FOV	Reduced FOV	Entire FOV	Reduced FOV
2×	36	28	54	31	69	39
5×	64	44	53	50	55	56

For the 2× objective lens, the *Sz* value is reduced from 36 nm to 28 nm at the top of the measurement volume, from 54 nm to 31 nm in the centre and from 69 to 39 nm at the bottom. The results show that a reduction of the maximum flatness deviation error of 43 % is possible by reducing the measurement area by ≈10 %. For the 5× objective, some values are also reduced but to a less extent. At the top of the measurement range, *Sz* drops from 64 nm to 44 nm, whilst in the centre and at the bottom, the value is almost unchanged due to the valley in the centre of the flatness map.

3.4.4 Flatness correction map

It is possible for surface topography measurement to correct for the flatness deviation by subtracting it from the obtained measurements [157]. However, even though the overall shape of the flatness map is consistent for both objectives, there are minor changes both in shape and amplitude depending on the measurement *z*-position in the range.

In order to test the possible improvement due to a flatness map correction, the obtained flatness maps are tested to correct measurement of a flat surface measurement at a different *z*-position and the *Sz* parameter is compared between the original measurement and the corrected measurement. The measured surface outliers are removed with the fitting-and-threshold method and the flatness map is obtained by filtering the average of the sixteen planar measurements with a S-filter selected according to the sampling distance in accordance with ISO 25178 part 3 [158]. The nesting index value (*i.e.* the cut-off frequency) is 10 µm and 5 µm, respectively for the 2× and 5× objective lens. Examples of the correction are shown in figure 3.10. The flatness map used is the map obtained in the centre of the measurement range.

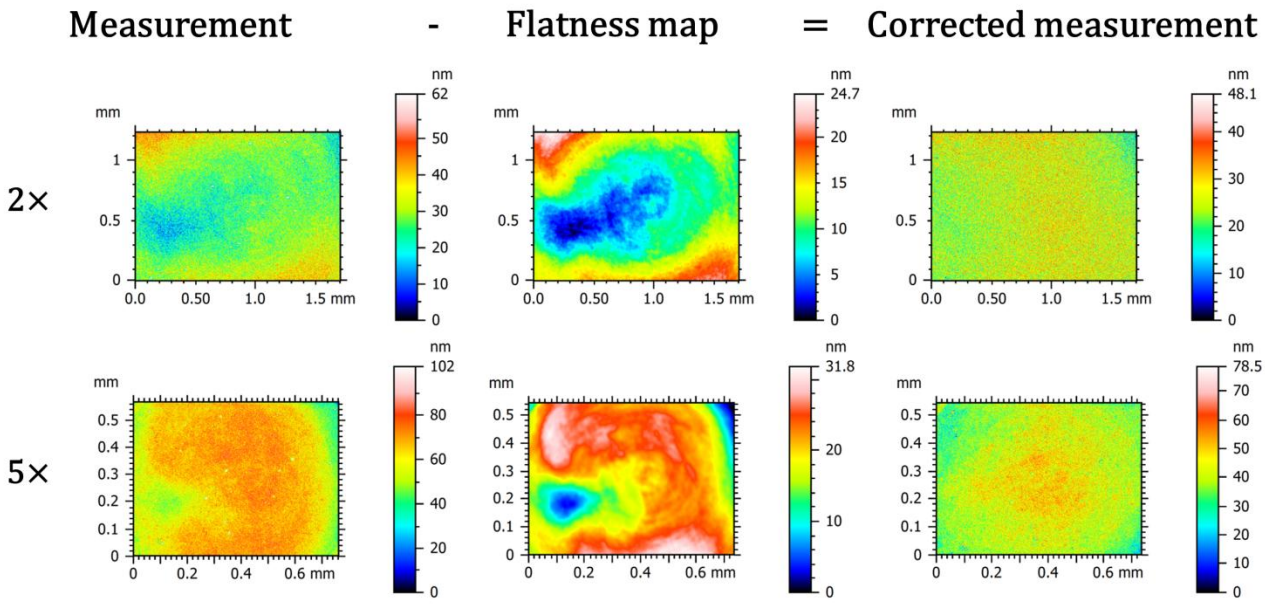

Figure 3.10. Optical flat measurement correction examples.

In the example, the measured surface *Sz* parameter for both objective lenses is reduced from 62 nm to 48 nm for the 2× objective, and from 102 nm to 79 nm for the 5× objective. The corrected measurements show a reduced surface height at the edge of the FOV, but some form is still left due to the different amplitude of the flatness map at the different *z*-position within the instrument range. In general, the surface *Sz* value reduction due to the flatness correction is equal to or less than 25 %.

3.5 Summary

In this chapter methods to calibrate two of the metrological characteristics for WSI are proposed. Subtraction and averaging methods are both successful in estimating the measurement noise. The flatness deviation is estimated via the fit-and-threshold method. It is shown that the measurement noise can affect the flatness deviation estimation and therefore noise reduction by averaging improves the flatness deviation calibration. The flatness map has similar form across the instrument axial range; however, its peaks and valleys amplitudes change. The flatness map is affected by the axis non-linearity (see section 4.1), *i.e.* a tilt of the flat form causes the flatness map to vary also at the same location, depending on the surface orientation and form. The flatness map variation is therefore the main limitation in applying a successful flatness map correction.

4 *z*-axis calibration

The instrument's three orthogonal axes each have the following metrological characteristics:

1. amplification factor, defined as the slope of the least-squares line fit to the response data (see figure 4.1);
2. linearity deviation, defined as the maximum local difference between the line from which the amplification coefficient is derived and the response curve (see figure 4.1);
3. squareness, defined as the perpendicularity deviation between any two of the *x*, *y* and *z* axes

In this section, the linearity of the *z*-axis is described in detail. In section 4.1 the effect of the phase demodulation algorithm on the *z*-axis linearity deviation is described and the algorithm is optimised to reduce the deviation from the ideal linear response curve. Methods to calibrate the amplification coefficient are described in section 4.2. The squareness error between the *z*- and lateral axes is included in the amplification coefficient estimation.

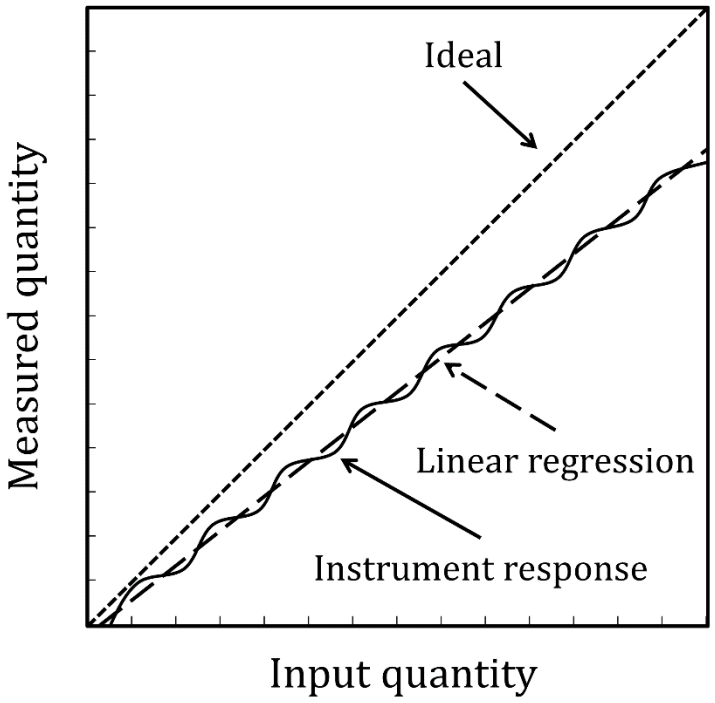

Figure 4.1: Example of instrument response curve. The ideal response is a line with a slope of 1. The instrument response might have ripples around a line with a slope different from 1. The slope of the linear fit curve of the instrument response is the axis amplification coefficient. The maximum deviation of the instrument response from the linear fit curve is the linearity deviation [159].

4.1 Spectral leakage and its effect on *z*-axis non-linearity

The algorithm used to estimate the surface *z*-position from an interference signal is described in detail in section 2.4.3. The algorithm's aim is to demodulate the phase from the sinusoidal

interference signal. To demodulate the phase, the signal is filtered in the Fourier domain to separate the positive (negative) frequency peak corresponding to the sinusoidal pattern from the negative (positive) frequency and from the constant component. The *z*-position estimation process is shown in figure 4.2 for two simulated fringe patterns. If the analysed fringe pattern does not have an integer number of periods, the spectral intensity is not concentrated in a single bin of the Fourier transform. Instead, the spectral intensity is spread such that it occupies multiple bins [52]. As a result, filtering is not as efficient as in the case when no spectral leakage occurs, since sinusoidal peaks leak energy over the whole spectrum. The resulting demodulated phase shows distortions, particularly at the edges of the analysed window. An error in the phase slope estimation is, therefore, introduced. A known way to reduce spectral leakage is by applying a window before performing the Fourier transform [52].

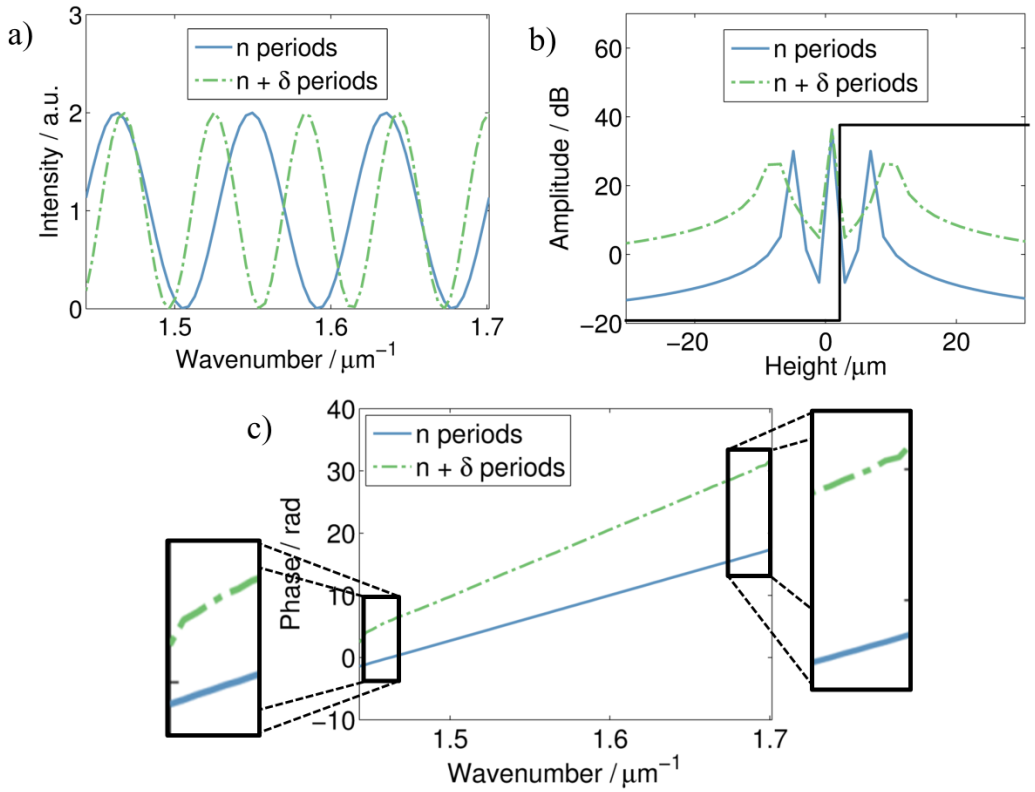

Figure 4.2: An example of spectral leakage introducing an algorithm error in the measurement. a) An example of two noise-free fringe patterns with an integer and non-integer number of periods. b) Magnitude of the Fourier transform of the fringe patterns. The black line is the filter applied to isolate one peak from the other two. c) The extracted phase for the integer and non-integer cases. Insets highlight the distortion from linearity at the phase edges, which introduces error in the estimated heights.

Detailed properties of commonly used windows are well-understood and can be found in Harris et al. [52]. A similar problem exists in PSI techniques where the phase estimation is improved by including a window in the calculation of phase shifting algorithm coefficients [50], [51]. However, the effect of spectral leakage in WSI is different from the PSI technique. In PSI, the frequency of the interference pattern is known and it is proportional to the illumination

wavelength. The PSI algorithm is designed to reduce or eliminate the effects of spectral leakage. Spectral leakage in PSI occurs when there are errors in the assumed laser wavelength or in the phase shifts. In WSI, the frequency of the interference pattern is not known in advance, and needs to be estimated to determine the surface absolute z-position. Therefore, spectral leakage in WSI is not a result of calibration errors. Instead, spectral leakage is intrinsic in the technique: some value of surface z-position corresponds to an interference signal associated with the worst case of spectral leakage.

In figure 4.3a, an example of a fringe pattern obtained from a WSI measurement is given. The demodulated phase and linear fitting from the same signal are shown in figure 4.3b. The demodulated phase distribution deviates from its predominantly linear behaviour at the edges of the analysed window. As a result, an error is introduced in the phase slope estimation. Dropping the phase edge points can improve the phase slope estimation. The next sections report results from simulation and experimental validation to identify the optimal window and the number of dropped phase points to reduce the measurement error.

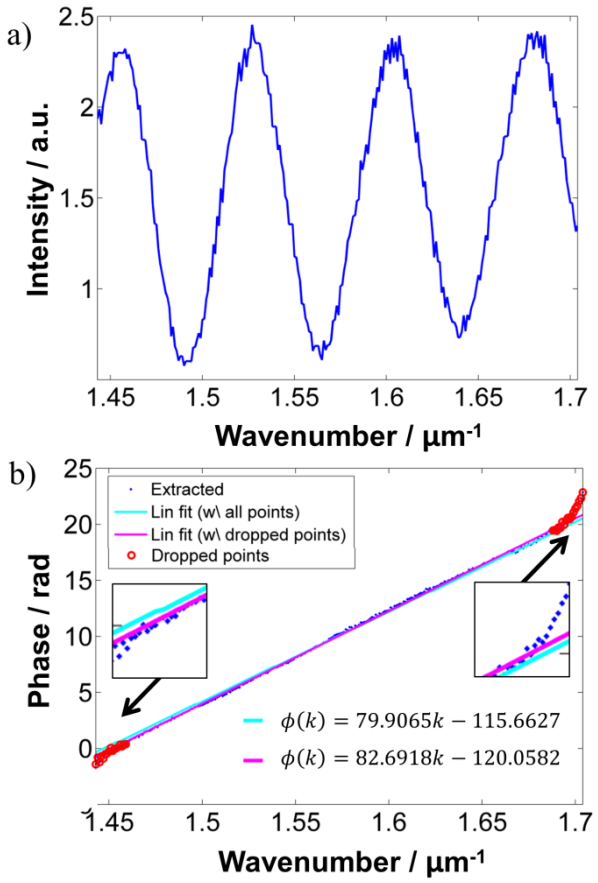

Figure 4.3: Fringe pattern (a) and relative demodulated and fitted phase (b). Insets show the phase deviation from linearity at the edges of the analysed windows. Equations are relative to the phase linear fitted using the entire data set of points or excluding the phase edges.

4.1.1 Phase demodulation algorithm's simulation

The fringe pattern can be described using the following equation:

$$I(k) = q(1 + V\cos(4\pi kz)) \tag{4.1.1}$$

where q is a scale factor related to the light intensity, V is the fringe visibility, k is the wavenumber of the light and z is the z-position to estimate. A set of simulated fringe patterns was generated according to the interference equation (4.1.1) for various z-positions in the range 5 µm to 35 µm. The results hereby discussed are also valid for z-positions from -5 µm to -35 µm, due to the symmetry of the Fourier Transform of the cosine function. This simulation range has been chosen to match the WSI instrument working range for the 5× objective lens, which is restricted to the lens-specific depth of focus. Each simulated fringe pattern is processed by the Fourier transform algorithm and the estimated z value is compared to the true z. The difference between the two values is considered the error. This method was used to obtain the z-position error as a function of the true z-position for different windows: rectangular, Gaussian, Hann and Hamming. A rectangular window is equivalent to a truncation of a theoretically infinitely long signal, whilst the other windows truncate and modify the signal at its edges (see figure 4.4). The fringe pattern is multiplied by the respective window functions before applying the Fourier transform. Figure 4.5 shows the simulated z-position error as a function of the nominal z-position.

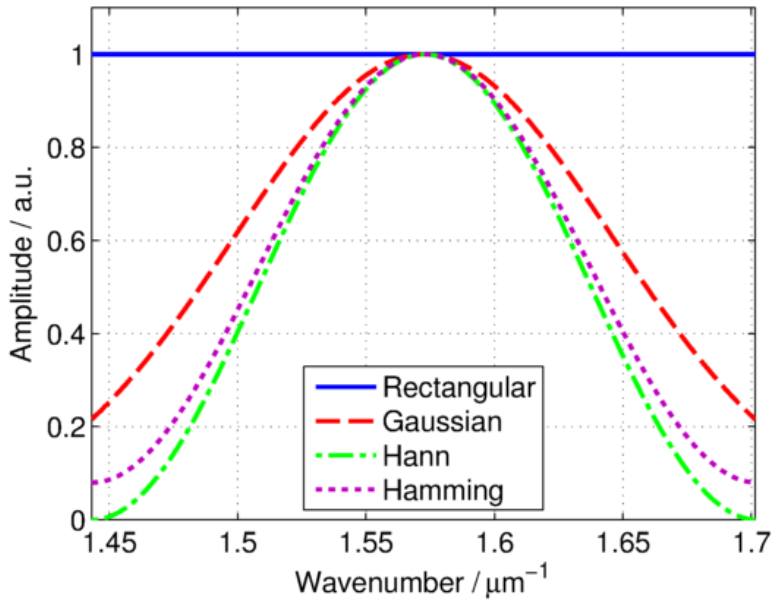

Figure 4.4. Windows used in the algorithm optimisation.

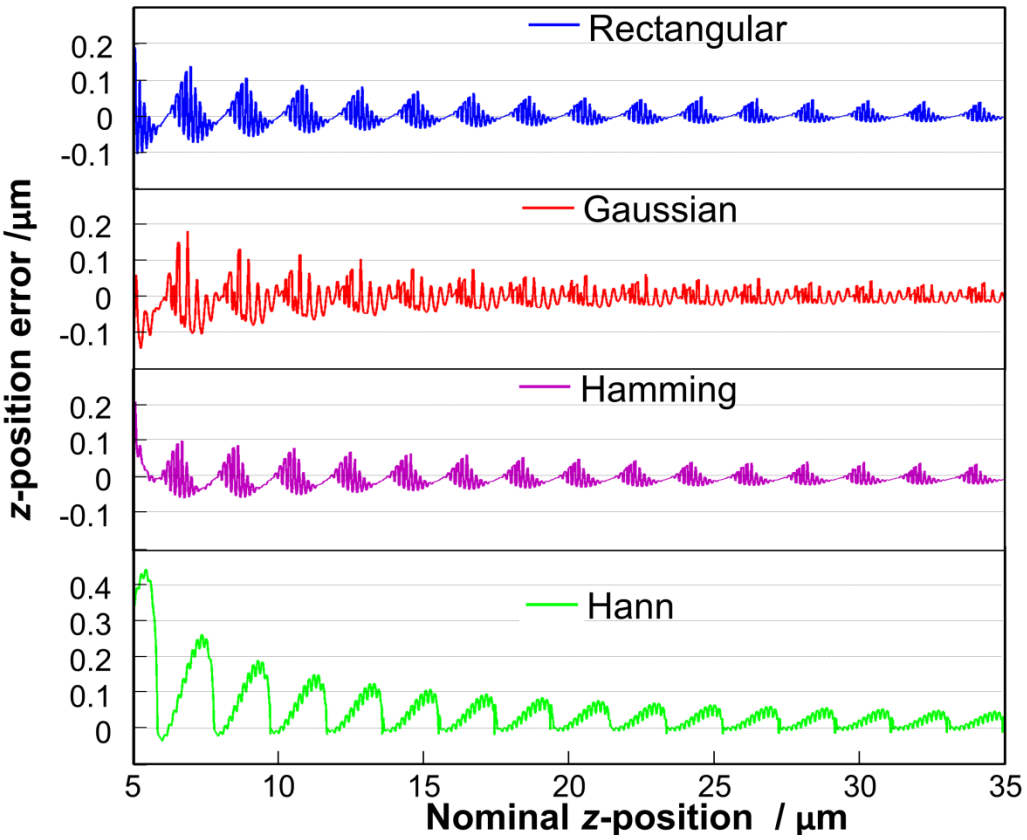

Figure 4.5: *z*-position error simulation results as a function of nominal *z*-position in the range 5 µm to 35 µm.

For the Gaussian window, the standard deviation has been optimised to a value that gives the lowest error by trial and error ($\sigma = 73$ samples for a fringe pattern sampled with 256 points). The number of sampling points per fringe pattern (256), and therefore the sampling frequency (f_s), was chosen to go well beyond the Nyquist-Shannon theorem ($2f_s$), and it is set to $5f_s$, which should ensure no aliasing for the expected frequencies. Note that for all cases, the DC offset is removed from the fringe pattern by subtracting the calculated mean value. In each case, the error exhibits an oscillatory behaviour with decreasing amplitude for larger nominal heights. Therefore, to ensure measurement accuracy, only a short portion of the instrument range should be used. The periodic zeroes in the *z*-position errors correspond to points where a fringe pattern has an integer number of periods and thus no spectral leakage occurs. The decreasing amplitude in error as the z value increases can also be explained in terms of the spectral leakage. Larger z values result in interference patterns with a higher frequency; therefore, the used frequency spectrum peak is well isolated from spectral leakage into the negative Fourier domain. As a result, less information is lost when these negative frequencies are filtered. It was found that the best performing window when no phase edges are dropped is the rectangular function, with a maximum error of 140 nm and an RMS error of 24 nm.

Non-linearity in the extracted phase appears to be isolated mainly in the edges of the analysed window. Therefore, the algorithm's performance may be improved by omitting edge data in the estimation of the phase slope. This concept is shown in figure 4.3b.

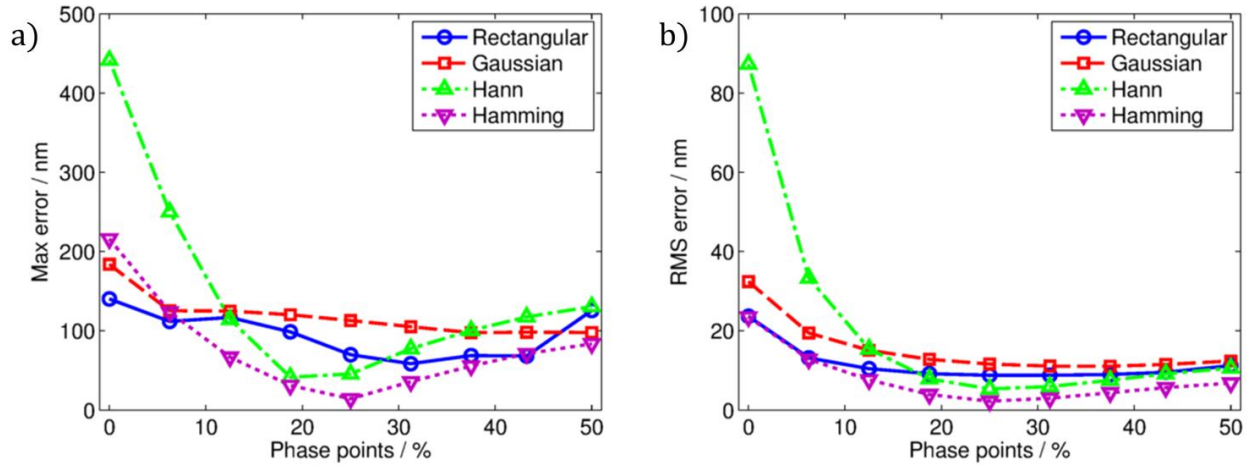

Figure 4.6: Maximum (a) and RMS (b) height error in the range 5 µm to 35 µm against percentage of dropped extremity phase points.

In figure 4.6, the maximum and RMS estimation errors are plotted as a function of the percentage of dropped phase points for the various windows. Phase points are dropped symmetrically from both edges of the data set. When more than 6.25 % of phase data were dropped, the Hamming window exhibits the lowest errors of all the windows. The Hamming window provides maximum and RMS errors of 14 nm and 2 nm, respectively, when 25 % of the phase points are dropped. These errors are an order of magnitude smaller than the errors observed using the rectangular window with no dropped phase points. It is worth noting that the error when using the Hann window decreases substantially when the phase point percentage increases. In figure 4.7, the extracted phase derivative is presented for each window. The dotted line corresponds to the derivative of the phase fit line; the derivative is a constant value, corresponding to the phase slope. The solid line represents the derivative of the original data after the window is applied. In all cases, the derivative of the original data deviates from the fitted slope, particularly at the wavenumber extremities. The insets indicate the extracted derivatives in the central portion of the data, when edge points are excluded. When the Hamming window is applied, the derivative of the original data exhibits the smallest deviation from the fit derivative.

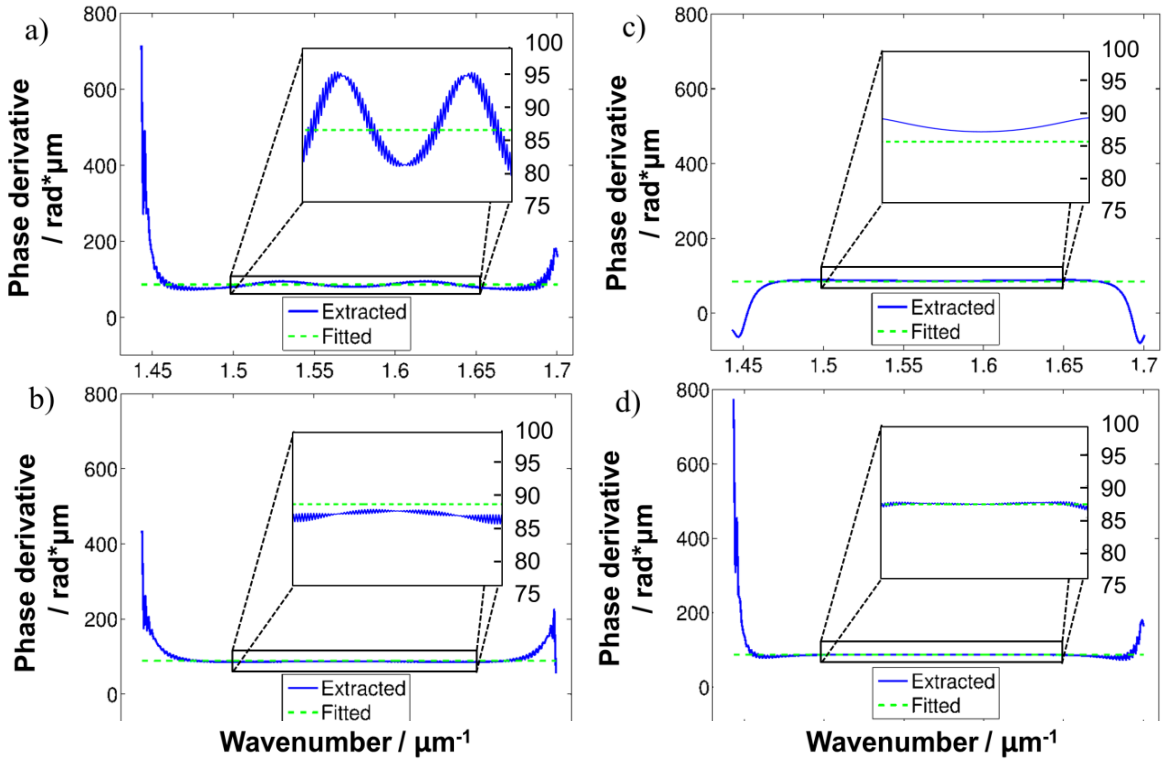

Figure 4.7: Comparison of the extracted phase derivative for different window corresponding to a height of 6.9064 µm for rectangular (a), Gaussian (b), Hann (c) and Hamming (d) windows. Inset shows the central phase derivative portion zoomed. The phase derivative that shows the closest linear behaviour is the one processed with the Hamming window (note the almost perfect overlap between the extracted and fitted phase derivative).

The performance of the Hamming window can be explained from the different window properties [52]. The Hamming window is optimised for reducing the short range spectral leakage. As a result, a different amount of information is filtered out, leading to a different shape and distribution of non-linearity in the extracted phase slope. The Hamming window, in particular, leads to a perfect linear behaviour of the demodulated phase at the centre of the data and large non-linearity limited at the data edges

4.1.2 Algorithm's optimisation measurement

An optical flat surface from the NPL areal calibration set [160] was measured with the WSI to evaluate the algorithm's performance on real data. The flat was intentionally tilted to provide a continuum of different *z*-values in the range of -5 µm to -7 µm, with the assumption that the response of the instrument across the field of view lead to a measurement error smaller in magnitude than the error due to the algorithm. The tilted optical flat was placed at the extremity of the working range since this is where the Fourier transform algorithm exhibits the highest *z*-position errors (see section 4.1.1). The simulated and experimental profiles for different windows are in agreement and the results are shown in figure 4.8a and figure 4.8b. The main difference between the simulated and measurement data occurs for the Hann window. The

simulated results do not exhibit the spikes that are visible in the experimental data. The spikes could be a result of noise in the real data. In figure 4.8c, the measured profiles are shown for a Hamming window with an increasing number of dropped phase points, and the in figure 4.8d for Hann window. As the number of dropped phase points increases, the surface determined by the algorithm becomes smoother, approaching the expected values for the optical flat.

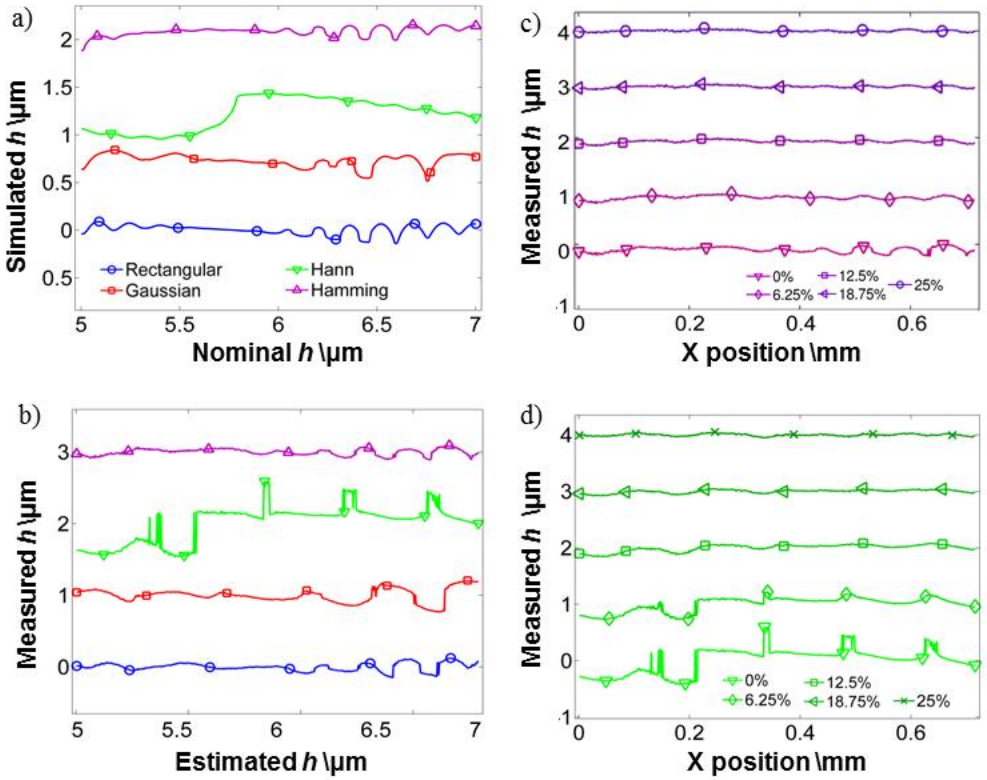

Figure 4.8: Simulated (a) and measured (b) flat profiles in the 5 µm to 7 µm range. Plots (a) and (b) share the same legend. The measured profiles after applying the Hamming window is plotted in (c) and for Hann window in (d) for varying number of dropped phase points. Note how the measured surface becomes smoother as more phase points are dropped. Note that the profiles are offset and the tilt is removed for clarity reason.

To determine the optimal number of dropped phase points, the RMS of the height value, *Sq*, of the measured surface was evaluated after surface levelling by a least-squares plane. The results are shown in figure 4.9. The RMS surface value generally decreases when the number of discarded phase points increases. For the rectangular and the Gaussian windows, a minimum value of, respectively, 26 nm and 38 nm is achieved when 12.5 % of the phase points are discarded. The *Sq* values without any dropped points for the rectangular and Gaussian windows are, respectively, 56 nm and 98 nm. The Hann window provides the largest *Sq* value among the tested windows (183 nm with no points dropped), which is reduced to the minimum value of 21 nm when 25 % of the points are discarded. The Hamming window estimates the lowest *Sq* value among those analysed and the estimated value reaches a minimum value of 17 nm when 25 % of the points are dropped from an initial value of 47 nm.

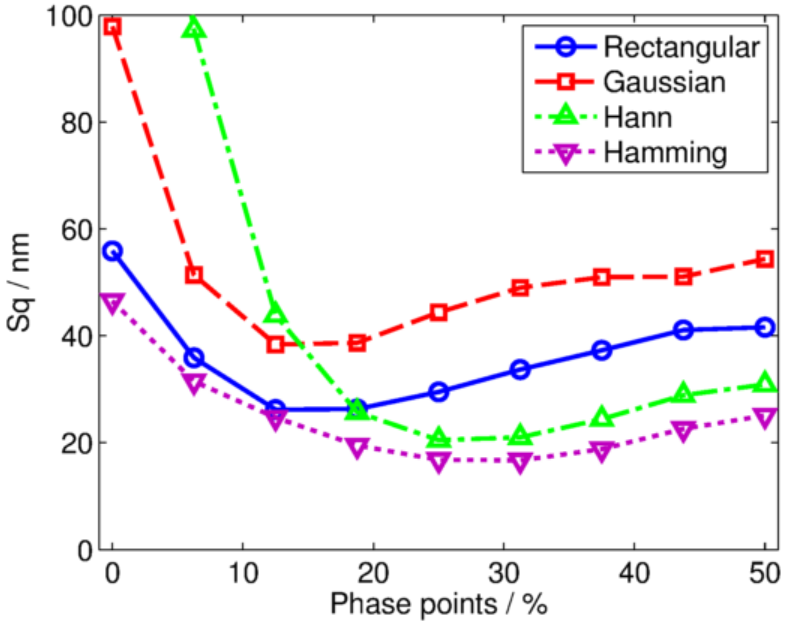

Figure 4.9: Measured *Sq* value plotted as a function of discarded phase points for the optical flat surface from the NPL areal calibration set.

4.1.3 Residual non-linearity

It has been shown in the previous section that the non-linearity in the *z*-axis instrument response is mostly due to the phase demodulation algorithm. An algorithm optimisation is described to reduce the linearity deviation (l_z), that is, the deviation from the ideal linear response. To estimate the algorithm non linearity, a tilted flat is measured several times by shifting the surface towards negative *z*-position until the entire *z*-position range is covered. The non-linear profile is obtained by averaging surface measurements along the non-tilted lateral direction. This is done to reduce the effects of noise and non-flatness deviation (figure 4.10).

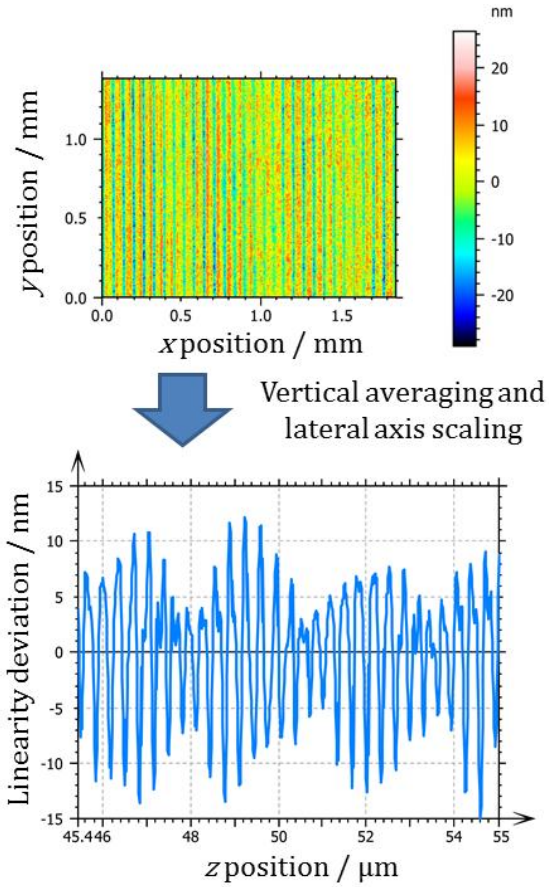

Figure 4.10. Example of linearity deviation estimation by measurement of a tilted optical flat. Top: The tilted flat measurement is levelled to show ripples in the direction of the tilt (horizontal axis). Bottom: The horizontal profiles are averaged in order to reduce the effect of noise, non-flatness and spurious data. The resulting profile provides an estimation of the linearity deviation in the z-position range where the tilted flat is measured (in this example from 46 µm to 55 µm).

The profile x coordinates are scaled between the minimum and maximum z-positions of the surface measurement to allow for aligning and stitching together all the profiles; in this way, the z-axis deviation from linearity can be obtained (see figure 4.11).

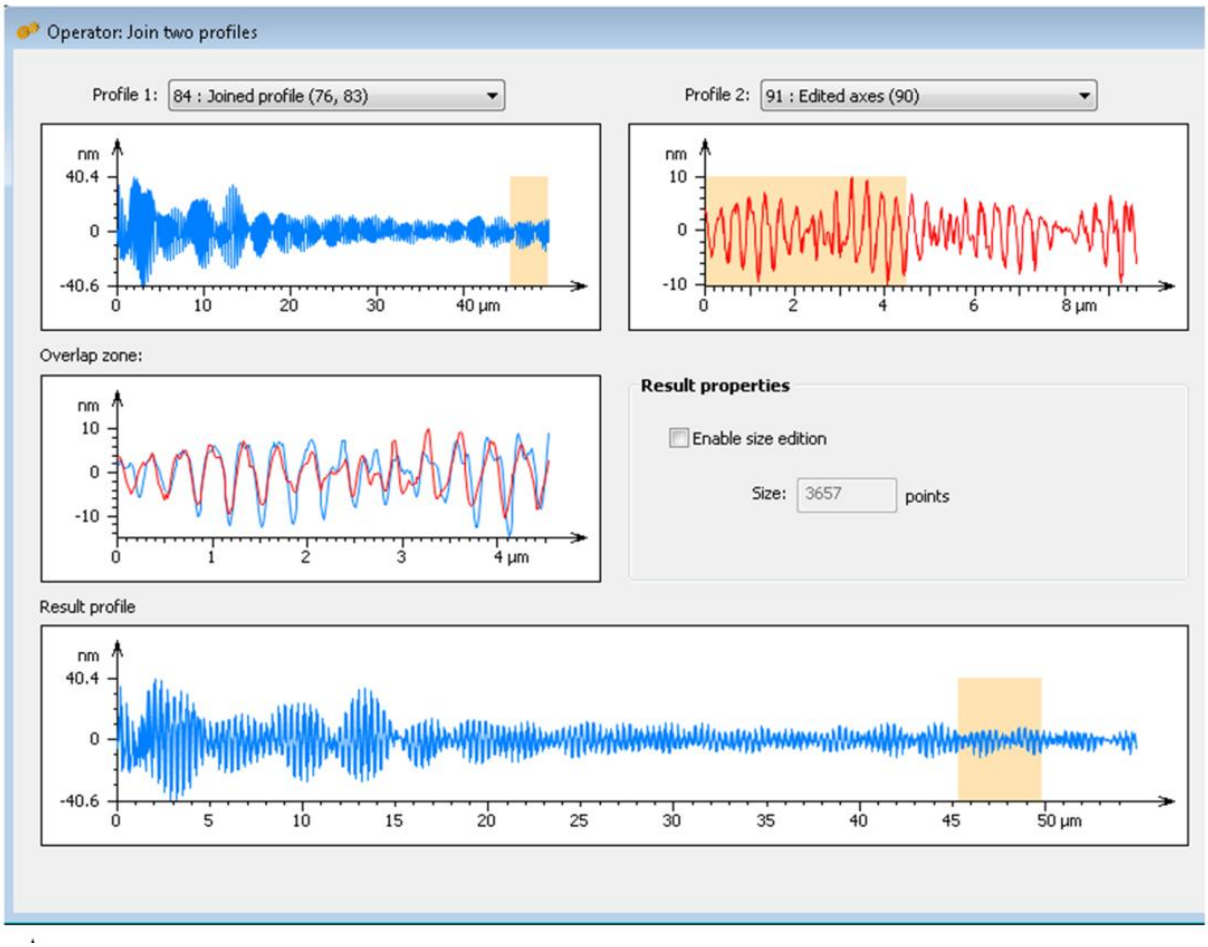

Figure 4.11. Example of profile stitching to obtain the *z*-axis linearity deviation.

There are several limitations in the tilted flat method to estimate the linearity deviation. Firstly, the vertical axis estimation is coupled with lateral axes non-linearity through surface averaging step. However, the estimation error of the linearity deviation due to the lateral distortion is estimated via simulation to be smaller than 5 nm. Another possible source of error in this method is the NA of objective lens. The interference signal formation is an integration over the objective lens acceptance cone angle which leads to interference signal spectrum broadening [93]. Measuring a tilted flat fills the objective exit pupil by a different amount depending on the tilt angle. In order to minimise the effect of the tilt angle on the estimated linearity deviation, the angle of the tilted flat is considerably lower than the objective lens limit. For the 2× objective lens, the angle of the measured tilted flat is 0.32˚, whereas the maximum acceptance angle is 3.15˚ (NA equal to 0.055). For the 5× objective lens, the angle of the tilted measured flat is 0.41˚, while the maximum acceptance angle is 7.97˚ (NA equal to 0.14). The estimated non-linearity as a function of the *z*-position for the 2× and 5× objective lens are presented in figure 4.12.

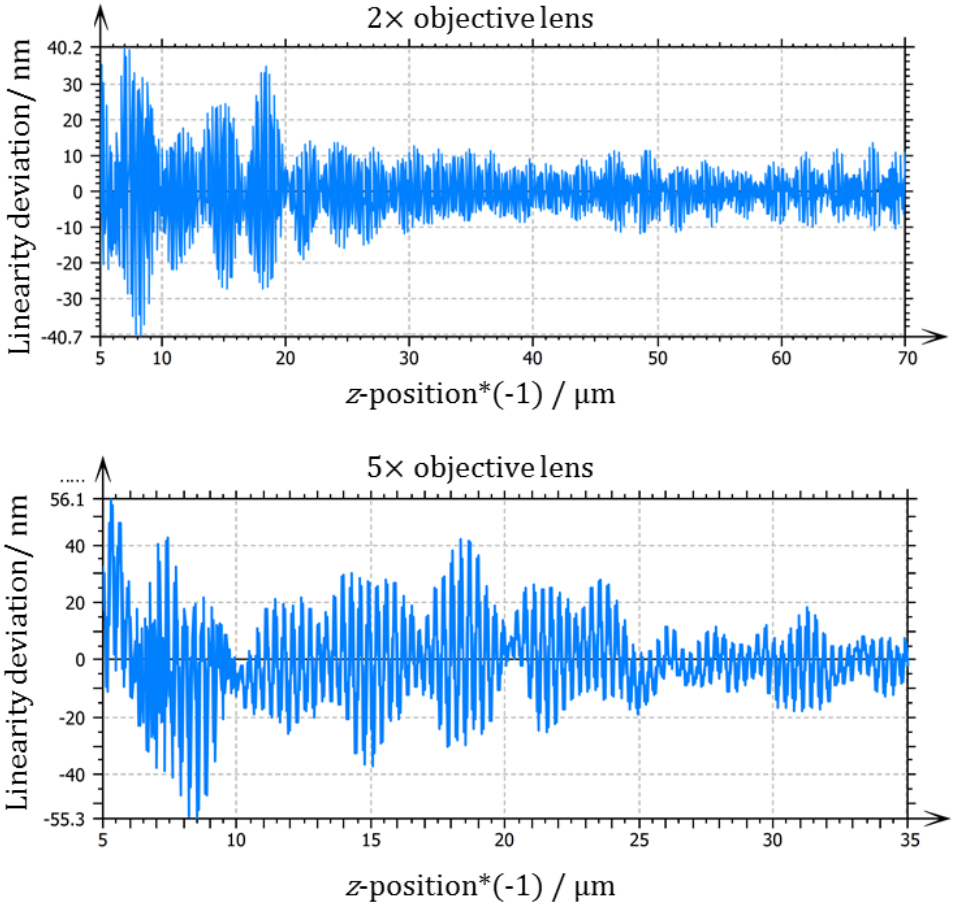

Figure 4.12. Linearity deviation distribution estimated through tilted flat measurement.

The differences of the linearity deviation distribution between simulated (see section 4.1.1) and experimental data can be explained in terms of signal non-ideality. In simulation, the fringe pattern is perfectly sinusoidal, with constant amplitude and with a constant mean value. In the experimental cases, the fringe pattern may not be perfectly sinusoidal (variable wavenumber linewidth and wavenumber scan non-linearity may affect it, see section 4.2.1), its amplitude and its mean are non-constant. Signal non-ideality causes the spectral peaks of the interference signal to have a spectrum broader than the ideal single sinusoid and, therefore, the spectrum leaks differently from the simulation, leading to a different linearity deviation distribution. However, the overall trends in the simulated and experimental data are similar: the linearity deviation exhibits an oscillatory behaviour with a periodic envelope. Furthermore, the linearity deviation decreases in amplitude for larger z-positions, which is in agreement with the simulated results.

The linearity deviation as a function of the z-position can be used to calculate the instrument response to a step height. The error in the measurement of a step height is the difference between the linearity deviation at the two positions where the step height surfaces are placed. For example, for a step height of 500 nm, the non-linearity value at a z-position of 5 µm is

subtracted from the linearity value at a *z*-position value of 5.5 µm. The same calculation is repeated for every sample along the *z*-position and for several values of step height. The maximum errors in the entire *z*-position range as a function of the step height values are shown is figure 4.13 for the 2× and 5× objective lenses.

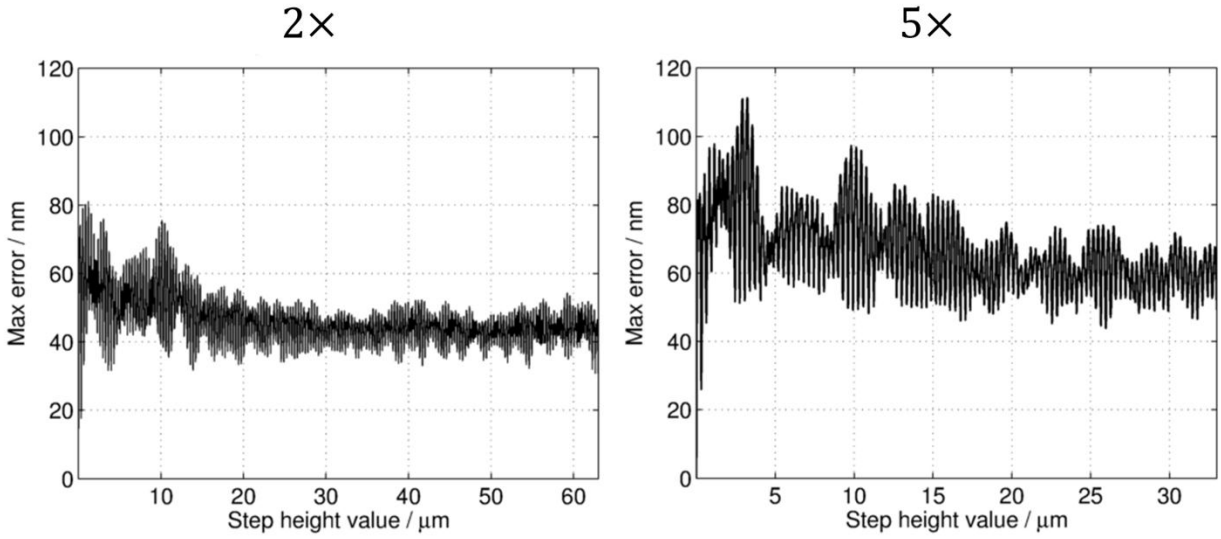

Figure 4.13. Maximum error as a function of the measured step height value for 2× (left) and 5× (right) objective lenses.

The maximum error is found to be for a step height of 1.2 µm for the 2× objective lens and is equal to 81 nm. For the 5× objective lens, the maximum error is 111 nm for a step height value of 3.2 µm. The statistical distribution of the step height error in the instrument range for the cases where the maximum error occurs is shown in figure 4.14. In both cases the statistical distribution is plotted with the best Gaussian fit curve; the respective coefficient of determination values are 0.98 and 0.96 for the 2× and the 5× objective lens, respectively. The statistical distribution of the error is useful when propagating the error contribution into the measurement uncertainty, and it is discussed more in detail in section 4.3.

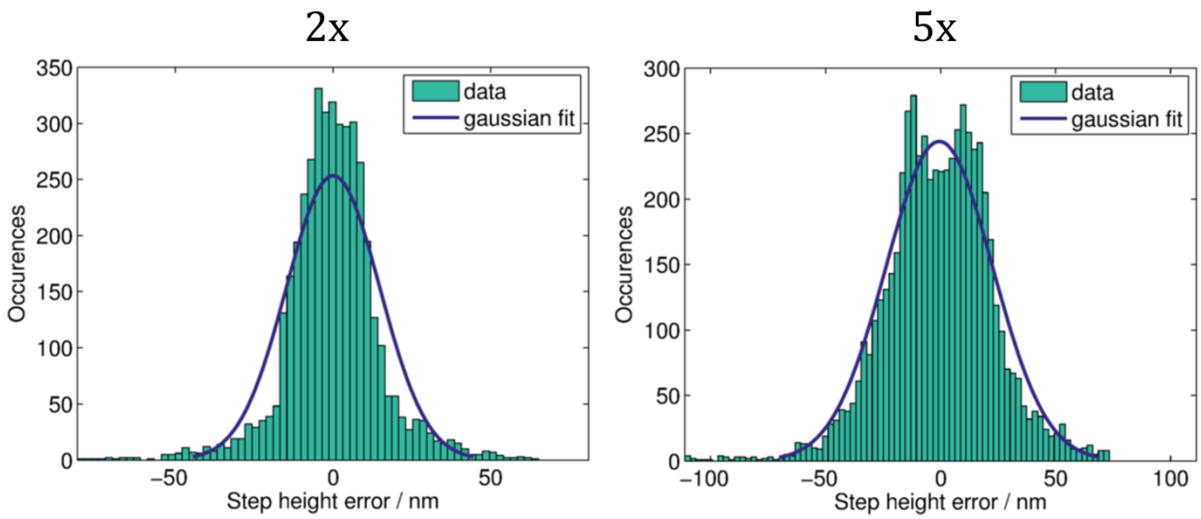

Figure 4.14. Statistical distribution and Gaussian fit of the step height error. The step height value considered is the value for which the maximum error occurs, *i.e.* 1.2 µm for the 2× objective lens and 3.2 µm for the 5× objective lens.

4.2 Amplification coefficient of *z*–axis

In this section, determination of the *z*-axis amplification coefficient and possible causes of its deviation from ideal value are described and supported by experimental data. Possible reasons for the observed differences in the amplification coefficient are:

1. error in the wavenumber range;
2. systematic non-linearity in the wavenumber scanning.

Both of these errors are a consequence of light source calibration errors. The light source calibration results are reported in section 4.2.1. A model to estimate the effect of these errors in the measurements is derived in section 4.2.2 and verified by experimental data in section 4.2.3. Lastly, a comparison of two methods to estimate the amplification coefficient is reported in section 4.2.4.

4.2.1 Light source calibration

A key component in WSI is the AOTF which can filter light of a specific wavelength depending on the radio-frequency (RF), in the range of Megahertz, at which the crystal is vibrated [131].

The spectrum of the selected illumination is acquired for each of the 256 AOTF driving frequencies, normally sampled during a wavenumber scan, and the centroid wavenumber is calculated. The AOTF driving frequencies are uniformly spaced between 78 MHz and 95.5 MHz. The result of the wavenumber measurements are shown in figure 4.15a. The measurements are taken with a spectrometer (CCS175 Thorlabs) with a resolution of 0.16 nm/pixel. The wavenumber is calculated as the centroid of the spectrum, therefore, the effective resolution achieved is in the sub-pixel range [161]. The scanned wavenumbers deviate from ideal linearity,

showing a quadratic distribution as a function of increasing AOTF frequency. The maximum error from the ideal linearity of the wavenumbers is 3.3×10^{-3} μm^{-1}, which corresponds to a wavelength error of 1.3 nm (see figure 4.15b).

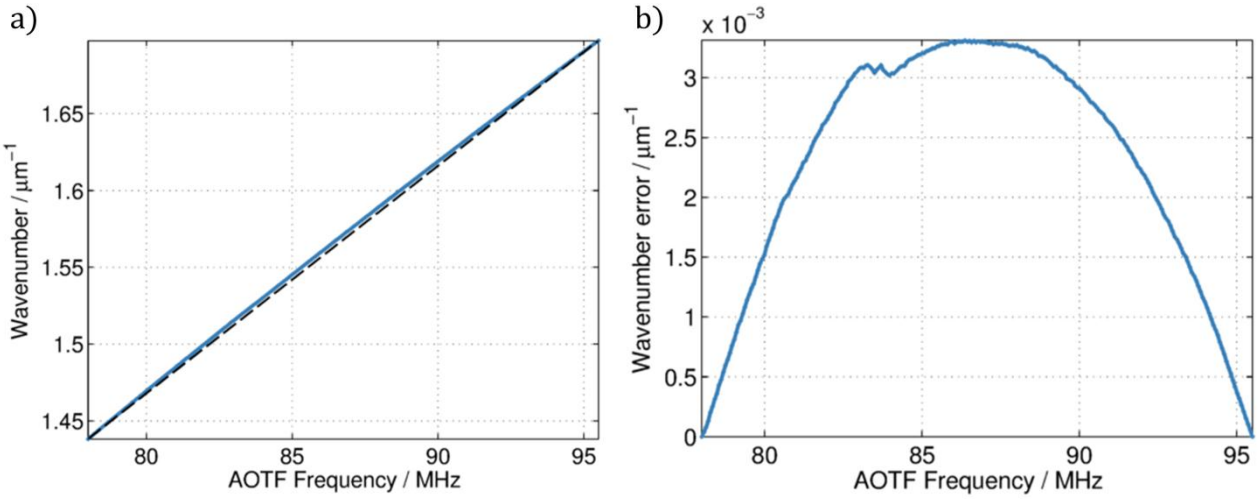

Figure 4.15: a) Measured wavenumber as a function of AOTF frequency. In the ideal case (dashed) and experimentally observed for the WSI (solid blue). Right: difference between measured and ideal wavenumber scan.

The experimentally observed relationship between the AOTF frequency and the measured wavenumber is not linear. If the AOTF frequencies are uniformly spaced, the wavenumber is scanned quadratically rather than linearly and, therefore, the fringe pattern phase will have a quadratic, rather than linear, behaviour. This quadratic behaviour in the wavenumber scan has been simulated for noise-free fringe patterns and the effects on measurement results are evaluated.

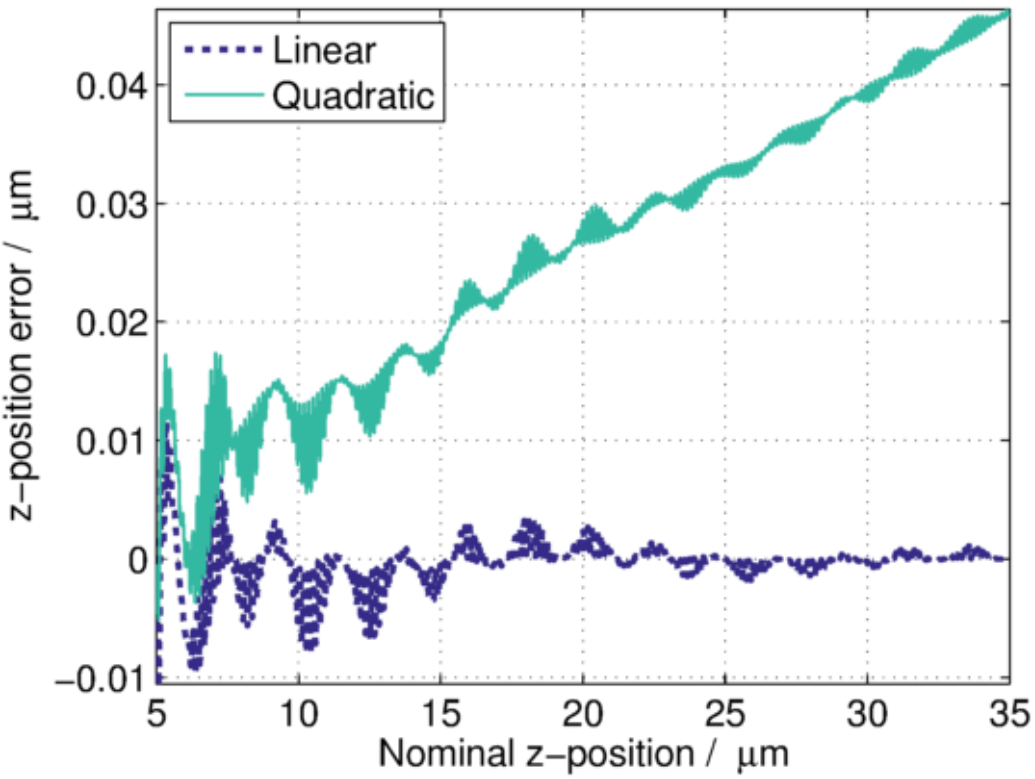

Figure 4.16: Simulated *z*-axis response for a perfectly linear wavenumber scan and with the measured quadratic wavenumbers scanned.

It is shown in figure 4.16 that a non-linear wavenumber scan affects the vertical axis amplification coefficient by introducing a slope in the instrument's *z*-axis response. The estimated amplification coefficient due to the quadratic scan is 1.001 376 compared to an ideal value of 1.000 000. For a step with a nominal height of 2.1 µm, the erroneous amplification coefficient results in a height measurement error of 2.9 nm. This error contribution is smaller than the effects due to instrument noise, flatness deviation and residual non-linearity of the *z*-axis. However, for larger step heights and low noise measurements, this contribution to measurement error may be significant.

The light source driving relationship is adjusted by fitting a least-squares quadratic curve to the measured wavenumber data. The equation for the fit is given below:

$$k = a_2x^2 + a_1x + a_0 \tag{4.2.1}$$

where k is the selected wavenumber, x is the AOTF frequency, and a_2, a_1 and a_0 the fitted polynomial coefficients. To improve the linearity of the wavenumber scan, equation (4.2.1) can be inverted to calculate the AOTF frequencies corresponding to a desired set of wavenumbers. The inverted equation is shown below:

$$x = \frac{-a_1 + \sqrt{{a_1}^2 - 4a_2(a_0 - k)}}{2a_2} \tag{4.2.2}$$

which is the formula to calculate the roots of a quadratic equation where only one solution has been selected to obtain values of x corresponding to a frequency at which the AOTF can vibrate. This correction is implemented in the WSI software and it allows the user to specify a calibration file with the three polynomial coefficients in order to invert the relationship and calculate the AOTF frequencies corresponding to a linear wavenumber scan.

Figure 4.17a shows the residual of the second order polynomial fit for spectral measurements. The maximum wavenumber residual is 2.4×10^{-4} μm^{-1}, which corresponds to a wavelength residual of 0.13 nm. The residual is an order of magnitude smaller than the maximum error prior to correction. The residuals could be relative to spikes or irregularities in the spectrum of the halogen lamp or spectrometer calibration error. Uncertainty in the corrected wavelength is propagated to an uncertainty in the final surface measurement. Following the calculation of the uncertainty in the selected wavelength are reported.

To estimate the repeatability on the selected centroid wavenumber error, the difference between two repeated scans is evaluated. To allow the lamp thermal drift to reach a steady state, the two measurements are repeated 20 minutes after the halogen lamp has been switched on. Figure 4.17b shows the results of the difference between the two measurements. The largest error due to repeatability in the wavenumber measurement is -3.1×10^{-5} μm^{-1}, corresponding to a wavelength error of 0.01nm. The standard deviation of the spectrometer wavelength noise is 0.002 nm corresponding to a wavenumber repeatability error of 5.6×10^{-6} μm^{-1}.

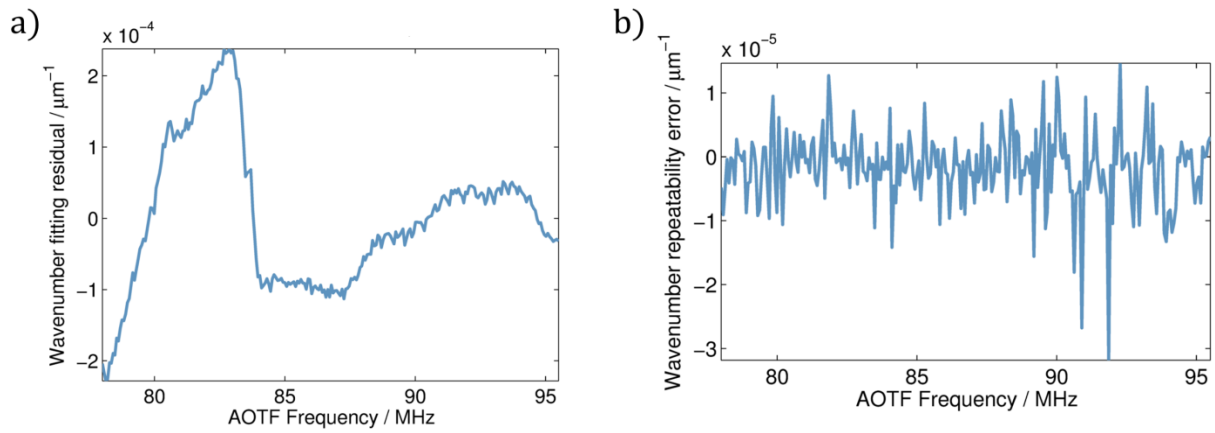

Figure 4.17: a) Residual of the second order polynomial fit. b) Repeatability error on sequential measurements of the light source centroid wavenumbers.

Another source of uncertainty in the wavelength selection is the uncertainty due to the spectrometer calibration. According to its manufacturer, the spectrometer uncertainty in the measured wavelength is maximum 0.2 nm.

According to the *Guide to the expression of uncertainty in measurement (GUM)* [137], the standard uncertainty associated with a measurement can be written as a quadratic sum of two components, named Type A and Type B measurement uncertainty:

$$u_C = \sqrt{u_A^2 + u_B^2} \tag{4.2.3}$$

According to the GUM, the Type A standard uncertainty is obtained from a probability density function derived from an observed frequency distribution, *i.e.* it is determined statistically. The Type B standard uncertainty components are taken from: "previous measurement data; experience with or general knowledge of the behaviour and properties of relevant materials and instruments; manufacturer's specification; data provided in calibration and other certificates; uncertainties assigned to reference data taken from handbook". If the Type B uncertainty components are uncorrelated, the uncertainty can be calculated according to the following equation:

$$u_B^2 = \sum_{i=1}^{n} C_i^2 u^2(x_i) \tag{4.2.4}$$

where C_i^2 is the *i-th* sensitivity coefficient, and $u(x_i)$ is the uncertainty in the *i-th* component. Therefore, for the wavelength measurement, the standard uncertainty is calculated as a quadrature sum of the repeatability random errors (Type A uncertainty), and a priori (Type B uncertainty): spectrometer calibration and residual of the quadratic fit.

Both calibration and residual errors are propagated as a rectangular distribution and therefore with a standard deviation of , $u = \frac{\delta}{\sqrt{3}}$, where δ is the maximum amplitude of the error, according to the GUM [137]. The uncertainty budget is presented in table 4.1.

Table 4.1. Uncertainty calculation summary for wavelength selection.

Type A	Type B		Standard uncertainty
u_A /nm	$u_{B\text{-calibration}}$ /nm	$u_{B\text{-residual}}$ /nm	$u_{c\text{-}\lambda}$ /nm
0.002	0.115	0.075	0.14

The main uncertainty source is the calibration of the spectrometer, followed by the residual of the fit. To reduce further the uncertainty in the wavelength selection, a high resolution spectrometer can be employed. If the residual errors are larger than the spectrometer calibration contribution, a look-up table rather than inversion of a quadratic fit can also be considered.

4.2.2 Measurement principle and error model

Once the phase is demodulated from the fringe pattern, a linear fitting step provides an estimation of the *z*-position according to:

$$z = \frac{1}{4\pi}\frac{\Delta\varphi}{\Delta k} \tag{4.2.5}$$

where $\Delta\varphi$ is the phase change corresponding to a wavenumber change of Δk. Equation (4.2.5) defines the measurement principle for WSI, *i.e.* the relationship between the estimated phase change and the measured z -position. The parameter Δk is selected by the user and is the dimensional factor that links the phase change to the *z*-position; any error in the wavenumber range measurement results in an error of the *z*-position measurement. Considering a linear approximation, the error in the *z*-position, due to errors in $\Delta\varphi$ and Δk is given by:

$$\begin{aligned} \delta z \approx \frac{1}{4\pi}\left(\frac{\partial z}{\partial \Delta k}\delta\Delta k + \frac{\partial z}{\partial \Delta\varphi}\delta\Delta\varphi\right) = \frac{1}{4\pi}\left(-\frac{\Delta\varphi}{\Delta k^2}\delta\Delta k + \frac{\delta\Delta\varphi}{\Delta k}\right) \\ = z\left(-\frac{\delta\Delta k}{\Delta k} + \frac{\delta\Delta\varphi}{\Delta\varphi}\right) = z(\alpha + \beta) \end{aligned} \tag{4.2.6}$$

where $\delta\Delta k$ is the error in the wavenumber range measurement and $\delta\Delta\varphi$ is the error in the phase change estimation, $\alpha = -\frac{\delta\Delta k}{\Delta k}$ and $\beta = \frac{\delta\Delta\varphi}{\Delta\varphi}$. Equation (4.2.6) indicates that δz is proportional to the value of *z*-position measured through the two coefficients α and β. In the ideal case the wavenumber range and the phase change are known with infinite precision and, therefore, α=β=0. Therefore, the measurement error δz is equal to zero, and the amplification coefficient value is equal to 1, *i.e.* the measured *z*-position has no scaling error. In reality, experimental errors in the measurement of the wavenumber range ($\alpha \neq 0$) and/or in the estimation of the phase change ($\beta \neq 0$) propagates to an error in the measured *z*-position δz. As a result, the amplification coefficient differs from the ideal value of 1. The wavenumber range error coefficient α takes into account error in the wavenumber range measurement, whilst the phase change estimation coefficient β takes into account errors in the phase change estimation. For example, one of the sources of error in the phase change estimation is due to the phase demodulation algorithm. The phase change estimation error due to the algorithm has been minimised and it has been described in section 4.1. The effects of α are described in more detail in section 4.2.3.

4.2.3 Experimental verification of the error model

The efficacy of the linear approximation for determining δz given by equation (4.2.6) can be tested by measuring a step height for different values of $\delta\Delta k$. The step height value is calculated from the surface areal measurement according to the following procedure (see figure 4.18):

- level the surface using least-squares plane;

- the mean profile is extracted by averaging all the profiles in the areal measurement excluding the top and bottom one sixth to avoid non-uniformity at the edge ;
- evaluate step height on the mean profile according to ISO 5436 [162].

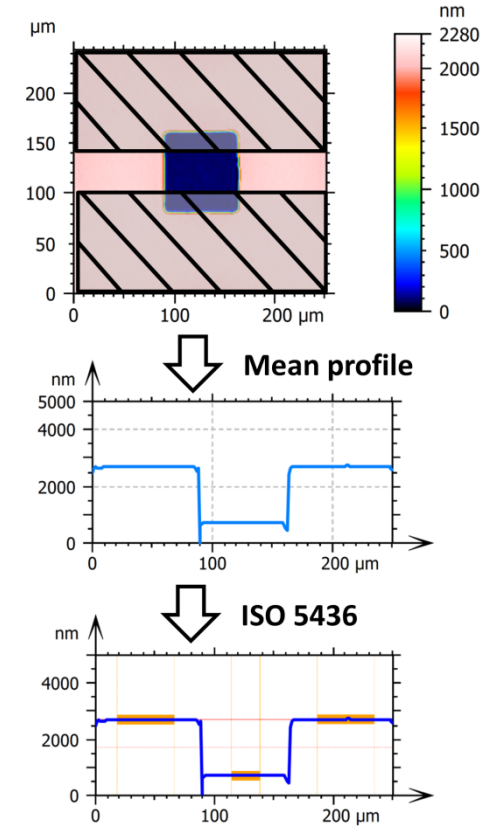

Parameters	Step 1	Unit
Width	24.1	µm
Mean depth	2010	nm

Figure 4.18: Step height evaluation procedure. Top: Areal measurement of the height protrusion. Only the central profiles across the step height are averaged to obtain a single profile. Middle: Result of the averaged profile. Bottom: Details of the application of the ISO 5436 standard procedure to evaluate the step height. Highlighted are the points used to evaluate the step height.

4.2.3.1 Wavenumber range error (α)

The wavenumber range Δk is the measurement parameter that links the phase change to the z-position according to equation (4.2.5). To first approximation, error in the wavenumber range causes an error in the measured z-position proportional to z-position to measure, *i.e.* the z-axis has an amplification coefficient different from the ideal value of 1. The amplification coefficient differs from the unity by $\alpha = -\frac{\delta\Delta k}{\Delta k}$, where $\delta\Delta k$ is the error in the wavenumber range measurement. According to equation(4.2.6), overestimation of the wavenumber range would cause an underestimation of the phase slope, while underestimation of the wavenumber range would cause an overestimation of the phase slope. For example for a wavenumber range of

0.2589 μm^{-1} (106 nm) a systematic error of 3.1×10^{-4} μm^{-1} (0.16 nm), gives α= 0.001 198 and, therefore, an amplification coefficient of 1.001 198.

To show the effect of the wavenumber range error on the vertical axis amplification coefficient, step height measurements are made in the presence of known errors in the wavenumber range; the corresponding errors in the measured step heights are observed. Measurements are taken with the 2× objective lens and are repeated five times to evaluate the repeatability. The results are shown in figure 4.19. The relative error in percentage of the measured step height is plotted as a function of relative error in percentage of the wavenumber range.

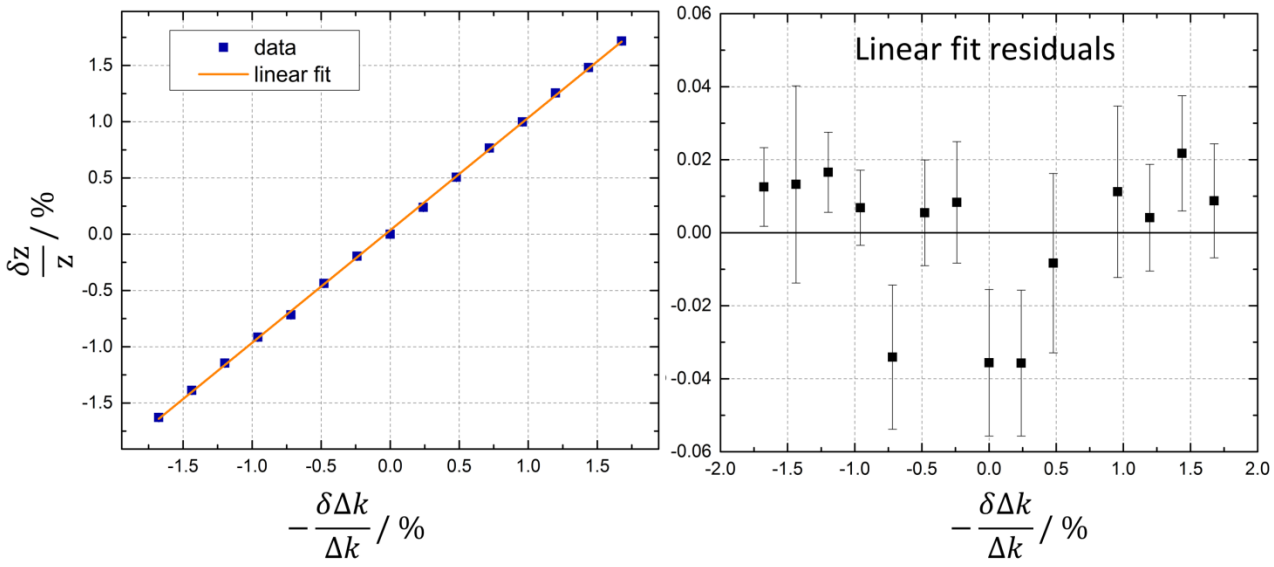

Figure 4.19. Measured step height relative error as a function of relative error of the wavenumber range, 2× objective lens. The error bars represents the standard uncertainty due to the repeatability contribution. The data are linearly distributed, as expected from the error model.

The results indicate that the measured step height variation is linearly dependent on the wavenumber range error. Therefore, errors in the *z*-axis amplification coefficient are proportional to errors in the wavenumber range measurement.

4.2.3.2 Phase change estimation error verification (β)

An amplification coefficient different from the ideal value of 1 can also be the result of a non-perfectly linear wavenumber scanning (see figure 4.16 for the case of linear wavenumber scan with an added quadratic component). The demodulated phase of the fringe pattern can be written as:

$$\varphi(k) = 4\pi z\big(k + \varepsilon(k)\big) \tag{4.2.7}$$

where $\varepsilon(k)$ takes into account the non-linear wavenumber scan contribution. The phase slope is estimated by a least-squares linear fitting of the demodulated phase and, therefore, non-

linearity of the wavenumber scan may influence the estimated phase change. The phase change, including the non-linear contribution is:

$$\Delta\varphi = 4\pi z\Delta k(1 + \tau) = 4\pi z\Delta k + \delta\Delta\varphi \tag{4.2.8}$$

where τ is the fitted phase slope due to the light-source non-linearity $\varepsilon(k)$ and $\delta\Delta\varphi = 4\pi z\Delta k\,\tau$ is the estimated phase change error due to the influence of the non-linear wavenumber scan on the linear fit. The additional non-linearity in the wavenumber scan introduces an error in the phase change estimation ($\delta\Delta\varphi$) and therefore in the measured z-position. According to the error model in equation (4.2.6) the coefficient β is:

$$\beta = \frac{\delta\Delta\varphi}{\Delta\varphi_{ideal}} = \frac{4\pi z\Delta k\,\tau}{4\pi z\Delta k} = \tau \tag{4.2.9}$$

The β coefficient value is proportional to the additional phase change bias resulting from the wavenumber non-linearity. To estimate the influence of the wavenumber non-linearity on the amplification coefficient, the residual of the light source calibration, reported in section 4.2.1, are linearly fitted. The data and the relative linear fit result are shown in figure 4.20. The shape of the residual leads to a linear fit with a slope of the order of 10^{-6} and, therefore, a coefficient β of the same order of magnitude, a contribution three order of magnitude smaller than the 10^{-3} due to the wavenumber range error and therefore it has been neglected.

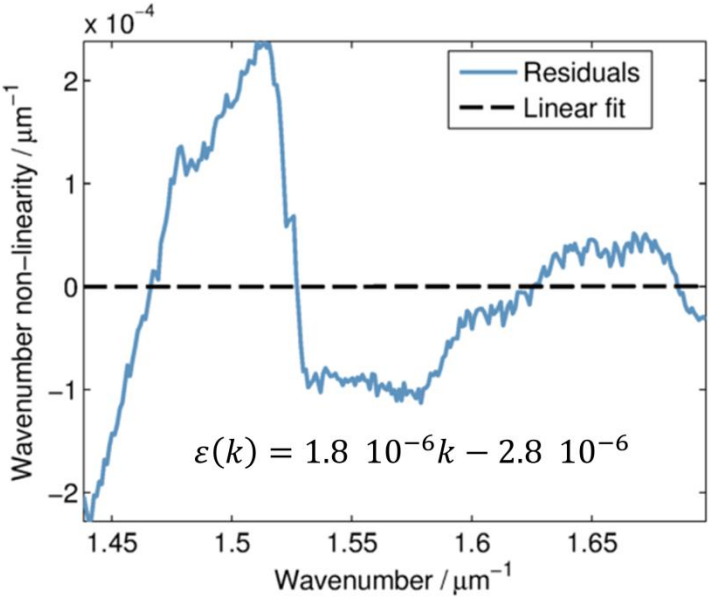

Figure 4.20. Wavenumber scan non-linearity and relative least-squares linear fit. The linear fit slope is small and, therefore, the effect of the wavenumber non-linearity of the amplification coefficient can be neglected.

4.2.4 Amplification coefficient determination

The amplification coefficient is typically calibrated by measuring several calibrated step height standards (SHS) and comparing the measured values with the reference values. The

amplification coefficient is subsequently estimated as the slope of the linear regression curve of the instrument response. The estimated amplification coefficient uncertainty is affected by the linearity deviation of the instrument and by the SHS calibration uncertainty. For commercially available SHS, the expanded uncertainty is typically on the order of 0.6 % [163], a value that increases for SHS of tens of micrometre, the main limitation being issues in manufacturing a deep and uniform step height profile. As a result, the uncertainty of the SHS can be larger than the interferometer resolution and, therefore, the amplification coefficient uncertainty is mainly affected by the dimensional quality of the SHS. It has been shown by de Groot et al. [163] that a lower uncertainty in the amplification coefficient can be achieved for a CSI by calibrating the scanning rate through a wavelength standard.

In this section, two methods for calibrating the amplification coefficient are compared. The first method is the standard calibration by measuring SHSs. The second method employs the error model in equation (4.2.6), and therefore calibration of the amplification coefficient by measuring the scanned wavenumber range, *i.e.* by means of the wavelengths. The last method will be referred to as the wavelength standard (WS) method.

4.2.4.1 SHS method

Unless otherwise specified, the measurement of the step height is the mean of 125 measurements: five repeated measurements are averaged to reduce the effect of noise, and this is repeated 5 times to evaluate the repeatability contribution. The measurements are repeated at five different position in the instrument vertical range (at 0 %, 25 %, 50 %, 75 %, 100 % of the *z*-position range) to evaluate the reproducibility of the measurement. The repeatability contribution is the maximum of the SHS standard deviation in the five vertical positions, *i.e.* it is the largest variation in the instrument range when repeating measurements. The reproducibility contribution is the standard deviation of the mean heights at each vertical position, *i.e.* the reproducibility is the variation of the measurement due to its different position in the instrument range. The standard uncertainty for the step height measurements are the quadrature sum of the repeatability, reproducibility and the traceable contribution. The results are shown and reported in figure 4.21 and table 4.2 for the 2× objective lens, and figure 4.22 and table 4.3 for the 5× objective lens. Four SHSs have been measured for the 2× objective lens, and five for the 5× objective lens. The SHS standard with nominal height of 200 nm has a width below the lateral resolution for the 2× objective lens and it was not possible to measure it.

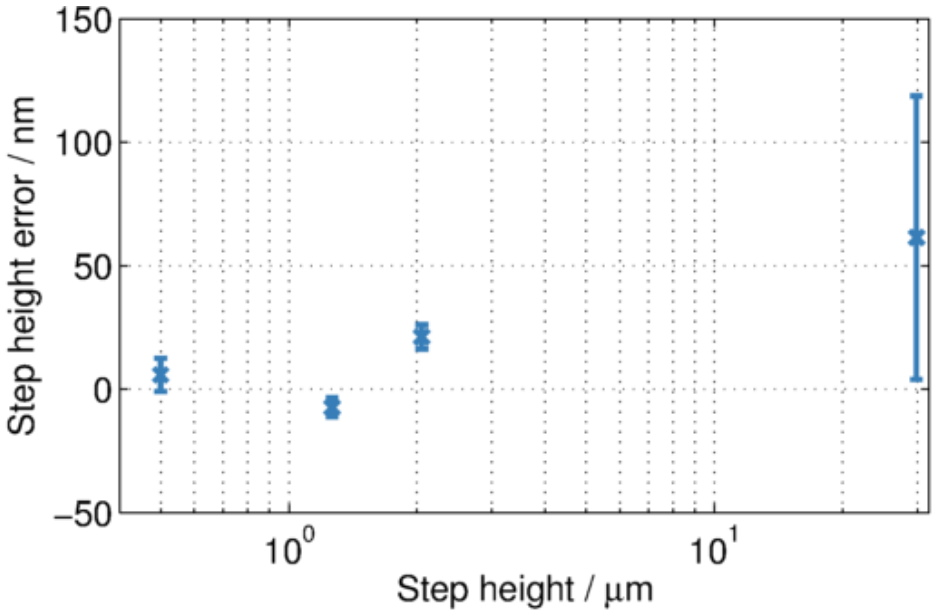

Figure 4.21: *z*-axis SHS error for 2× objective lens.

Table 4.2: Summary of *z*-axis calibration results for 2× objective lens.

Nominal height	δ_{err} /nm	δ_{repet} /nm	δ_{reprod} /nm	$\delta_{traceability}$ /nm	δ_{tot} /nm
500 nm	5.8	5.0	4.1	2.1	6.7
1.2 µm	-7.4	2.2	2.4	2.2	3.9
2.1 µm	21.2	2.6	3.5	2.1	4.9
30 µm	61.4	9.3	5.9	56.3	57.4

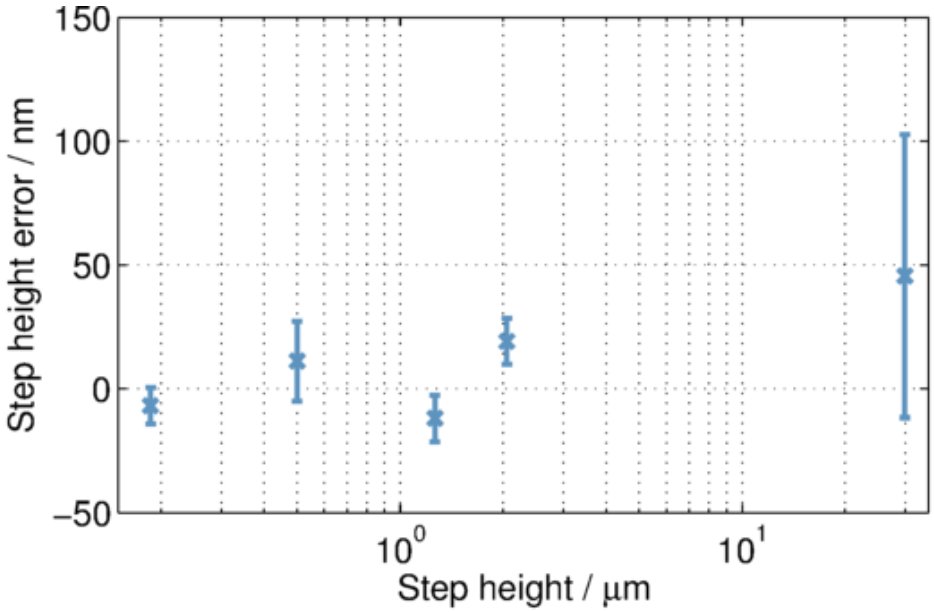

Figure 4.22: *z*-axis SHS error for the 5× objective lens.

Table 4.3: Summary of *z*-axis calibration results for 5× objective lens.

Nominal height	δ_{err} /nm	δ_{repet} /nm	δ_{reprod} /nm	$\delta_{traceability}$ /nm	δ_{tot} /nm
200 nm	-6.9	4.9	5.0	2.3	7.4
500 nm	11.1	3.6	15.6	2.1	16.1
1.2 µm	-12.0	5.2	7.4	2.2	9.4
2.1 µm	19.1	6.6	6.2	2.1	9.3
30 µm	45.5	7.2	2.6	56.7	57.2

The amplification coefficient is calculated as the slope of the linear regression curve of the instrument *z*-axis response curve sampled at the step height value points. The uncertainty in the slope is affected by two contributions:

1. the uncertainty in the measured step height values;
2. the non-linear distribution of the data, *i.e.* the residuals of the linear fit.

The SHS standard errors contribute to the uncertainty in the slope coefficient through the fitting matrix and are assumed to have a Gaussian distribution.

The residuals of the linear fit contribute to the slope uncertainty through the fitting matrix but the assumption of Gaussian distribution is not valid. The standard errors of the linear fit have a Student's t distribution with n-2 degrees of freedom, where n is the number of observation data points employed for the linear fit [137]. In this case, n=4 for the 2× objective lens and n=5 for the 5× objective lens. Therefore, the standard error due to the residuals is scaled by the tabulated coefficient of the t-distribution to encompass 68 % of the probability distribution. The

standard uncertainty in the amplification coefficient estimation is the quadrature sum of the standard uncertainty due to the repeatability, reproducibility and traceability (u_{rrt}) and the standard uncertainty due to the residuals of the linear fit ($u_{residual}$). A summary of the results is shown in table 4.4.

Table 4.4. Value and uncertainty contributions for the amplification coefficient estimation.

Objective lens	α_z	$u_{\text{residuals}}$	u_{rrt}	u_{tot} (k=1)
2×	1.001 935	0.010 817	0.001 821	0.010 969
5×	1.001 499	0.008 808	0.001 608	0.007 514

The difference in the calibrated amplification coefficient between the two objective lenses is less than 0.05 %. The standard uncertainty due to uncertainty in the step height is similar for both objective lenses. The standard uncertainty due to the residuals is larger for the 2× objective due to the lower number of data points. The final uncertainty in the amplification coefficient estimation is approximately 1.1 % for the 2× objective lens and 0.8 % for the 5× objective lens.

4.2.4.2 WS method

The amplification coefficient can be calibrated also according to equation (4.2.6), *i.e.* by measuring the scanned wavenumber range. The start and the end wavelengths are measured and the amplification coefficient uncertainty is determined by propagating the uncertainty in the wavelength measurements. The main disadvantage of the WS method is that it does not consider the effects of the interferometer optics. However, it is known that objective lenses can alter the effective spacing of the fringes depending on the NA of the lens used through the so-called obliquity factor [164]. This influence is taken into account in the uncertainty calculations. Therefore, the error contributions to the measurement of the amplification coefficient with the WS method are:

1. uncertainty in the wavenumber selection, (described in section 4.2.1), and
2. obliquity factor due to objective NA.

However, the obliquity factor can be calculated and the amplification coefficient corrected. Assuming the objective lens pupil is entirely and uniformly filled, the obliquity factor (Ω) is approximated by the Sheppard formula [163]:

$$\Omega = \frac{3}{2}\frac{(1-cos^2(\theta))}{(1-cos^3(\theta))} \tag{4.2.10}$$

where $\theta = sin^{-1}(NA)$, and NA is the numerical aperture of the objective lens.

The wavenumber range, including the obliquity factor contribution, can be calculated according to the following equation:

$$\Delta k = \frac{1}{\Omega}(k_{end} - k_{start}) = \left(\frac{1}{\Omega}\right)\left(\frac{1}{\lambda_{end}} - \frac{1}{\lambda_{start}}\right) \tag{4.2.11}$$

where $k_{start}(\lambda_{start})$ is the first wavenumber (wavelength) selected in the scan, $k_{end}(\lambda_{end})$ is the last wavenumber (wavelength) selected, and Ω is the obliquity factor. For the 2× objective lens (NA = 0.055), the obliquity factor is 1.000 757, while for the 5× objective lens (NA = 0.14) is 1.004 940. The obliquity factor takes into account that the interference signal is a sum over the objective pupil, *i.e.* a sum of plane waves within the maximum acceptance angle of the objective lens. A plane wave with an angle θ results in fringe spacing slightly longer along the optical axis (see figure 4.23 and also [93]).

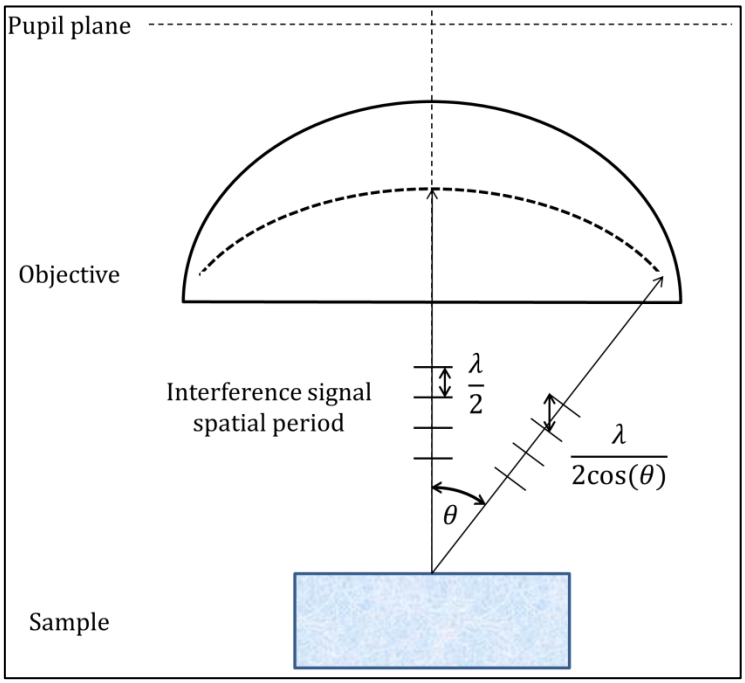

Figure 4.23. Schematic of the interference signal formation. Only the ray passing through the objective optical axis contributes to the interference signal with a spatial frequency of λ/2. Ray with an angle with respect to the optical axis contributes with an effective spatial frequency proportional to the cosine of the angle. The interference signal is a sum over the entire objective cone angle.

The wavenumber range uncertainty is calculated according to the guidelines in the GUM [137]:

$$u^2(\Delta k) = c^2_{\lambda_{start}} u^2(\lambda) + c^2_{\lambda_{end}} u^2(\lambda) \tag{4.2.12}$$

where $u^2(\lambda)$, is the variance of the wavelength uncertainty. The sensitivity coefficients $(c^2_{\lambda_{start}}, c^2_{\lambda_{end}})$ corresponding to each uncertainty contribution are given below:

$$c^2_{\lambda_{start}} = \left(\left|\frac{\partial \Delta k}{\partial \lambda_{start}}\right|\right)^2 = \left(-\frac{1}{\Omega}\frac{1}{\lambda^2_{start}}\right)^2 \tag{4.2.13}$$

$$c_{\lambda_{end}}^2 = \left(\frac{\partial \Delta k}{\partial \lambda_{end}}\right)^2 = \left(-\frac{1}{\Omega}\frac{1}{\lambda_{end}^2}\right)^2 \tag{4.2.14}$$

Finally, the standard uncertainty in the amplification coefficient propagates according to:

$$\alpha = \frac{\delta \Delta k}{\Delta k} = \frac{u(\Delta k)}{\Delta k} \tag{4.2.15}$$

The results for each uncertainty contribution are summarised in table 4.5, where λ_{start} and λ_{end} are equal to 695.2 nm and 589.1 nm, respectively, and the obliquity factor is 1.000 757 and 1.004 940, for the 2× and 5×, respectively.

Table 4.5. Wavenumber range uncertainty contribution terms.

Objective lens	$c_{\lambda_{start}}$ μm^{-2}	$c_{\lambda_{end}}$ μm^{-2}	$u(\lambda)$ μm		$\boldsymbol{u(\Delta k)}$ μm^{-1}	$\boldsymbol{\alpha = \frac{u(\Delta k)}{\Delta k}}$
2×	2.067 530	2.879 342	0.000 14		0.000 497	**0.001 917**
5×	2.058 924	2.867 357			0.000 494	**0.001 917**

The data indicates that, for both objective lenses, the largest source of uncertainty in the wavenumber determination is the wavelength measurement uncertainty at the final (shortest) wavelength due to the higher sensitivity coefficient. The second largest contribution is the wavelength uncertainty at the start wavelength due to lower sensitivity coefficient.

Comparison of the amplification coefficient values and respective uncertainties for the SHS and the WS methods are presented in table 4.6 and figure 4.24. The amplification coefficients calibrated with the SHS and WS method agree to within their uncertainty values; however the WS method provides a lower measurement uncertainty. The lower uncertainty is due to the fact that it is easier to obtain lower uncertainties by measuring light wavelength than through traceable SHSs, whose uncertainty is affected by the factors discussed at the beginning of section 4.2.4. For the 2× objective lens, the standard uncertainties are 1.1 % and 0.2 % for the SHS and WS method, respectively. For the 5× objective lens, the uncertainties are 0.8 %, and 0.2 % for the SHS method and the WS method, respectively.

Table 4.6: Estimated amplification coefficient values and uncertainties for the SHS and WS method.

Objective lens	Method	Amplification coefficient	Standard Uncertainty (k=1)
2×	SHS	1.001 935	0.010 969
	WS	1.000 000	0.001 917
5×	SHS	1.001 499	0.007514
	WS	1.000 000	0.001 917

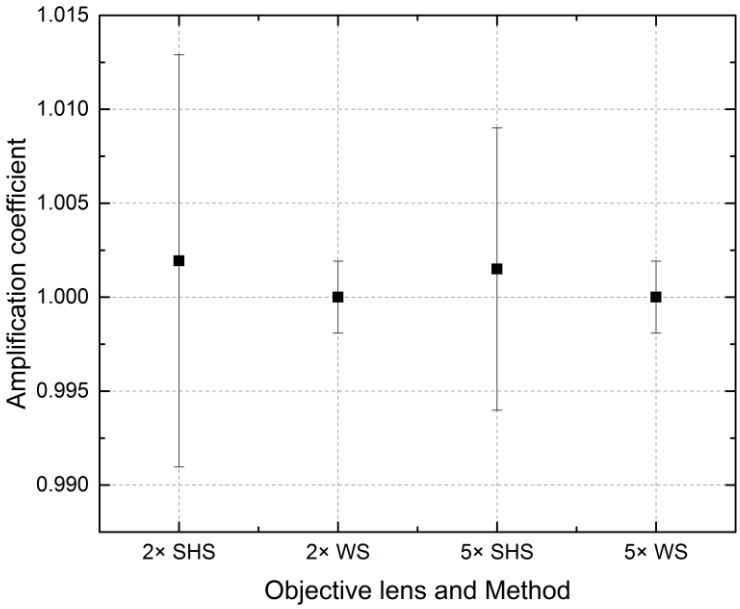

Figure 4.24. Amplification coefficient values and standard uncertainty estimated with SHS and WS method for both objective lenses.

4.3 *z*-axis measurement uncertainty

Each metrological characteristic contributes to the uncertainty in the surface measurement made by the WSI. The uncertainty is calculated according to the guidelines given in *GUM* [137]. The calibration of the metrological characteristics is part of calculation for determining the Type B uncertainty. Therefore, each metrological characteristic corresponds to a separate component of the Type B standard uncertainty and the final Type B uncertainty can be calculated according to equation (4.2.4).

4.3.1 Noise and flatness deviation

Measurement noise and flatness should be filtered before being included in the uncertainty calculation. The largest measured values of noise and flatness deviation are used in the

uncertainty calculation for the entire WSI vertical range. These values are typically observed in measurement made at the largest negative *z*-position. Table 4.7 reports the value of S and L filters used according to the ISO-25178 [158].

Table 4.7. S- and L-filters for 2× and 5× objective lens. S-filter value is selected according to the sampling distance.

ISO 25178 part3 filters	2×	5×
S-filter / µm	10	5
L-filter / mm	0.7	0.5

The noise is propagated as a normal distribution with zero mean and variance equal to the square of the value of the measurement noise. The residual flatness deviation is propagated in the form of a rectangular distribution that has a variance equal to $Sz^2{}_{flatness}/12$ [137]. The combined effect of the measurement noise and flatness deviation on the *z*-axis measurement standard uncertainty is given by the following equation:

$$u_{NF} = \sqrt{Sq_{noise}^2 + \frac{Sz_{flatness}^2}{12}} \tag{4.3.1}$$

The combined effect of the measurement noise and flatness deviation, on the z-axis measurement standard uncertainty is presented in table 4.8.

Table 4.8. Measurement noise and flatness deviation contribution to the *z*-axis measurement uncertainty for 2× and 5× objective lenses.

Uncertainty contribution	2×	5×
Sq_{noise} /nm	7.0	6.0
$Sz_{flatness}$ /nm	26.1	34.4
u_{NF} / nm	10.3	11.6

4.3.2 Amplification, linearity and perpendicularity

The measurement uncertainty due to the amplification coefficient (α_z) and the linearity deviation (l_z) is usually estimated with SHS method. However, it has been shown how the amplification coefficient and the linearity deviation can be estimated separately with the WS method and measurement of a tilted flat, respectively. In this section the uncertainty due to the amplification coefficient and linearity deviation is compared for the two methods.

The SHS method is conceptually shown in figure 4.25. The amplification coefficient and the linearity deviation are estimated from the sampled instrument response curve.

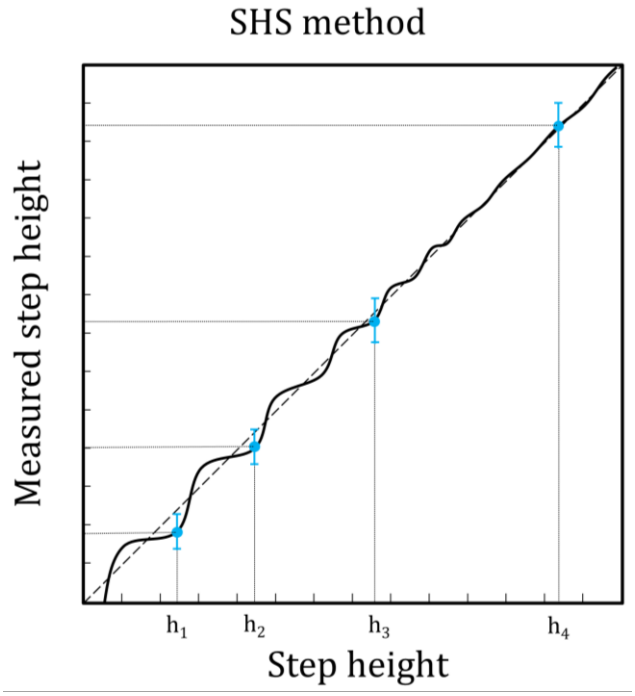

Figure 4.25. Conceptual schematic of the SHS method. The amplification coefficient and the linearity deviation are estimated from the sampled instrument response curve (blue dots).

The contribution of the linearity errors to the measurement uncertainty is propagated in the form of a rectangular distribution that has a variance equal to the square of the step height error value divided by three ($u_{error}^2 = \delta_{error}^2/3$). The repeatability and reproducibility contribution are propagated in the form of a normal distribution with zero mean and variance equal to the square value of the repeatability or reproducibility ($u_{repeat}^2 = \delta_{repeat}^2$ and $u_{reprod}^2 = \delta_{reprod}^2$). The combined effect of the measurement repeatability, reproducibility and traceable contrribution (u_{T-z}) is given by:

$$u_{T-z} = \sqrt{u_{error}^2 + u_{repeat}^2 + u_{reprod}^2 + u_{traceab}^2} \tag{4.3.2}$$

The perpendicularity between the *z*-axis and the areal reference is included into the measurement error along the *z*-axis. The uncertainty values are shown in table 4.9.

Table 4.9. Amplification and linearity contribution to the z-measurement uncertainty.

Objective lens	**2×**					**5×**				
Nominal height /nm	u_{error} /nm	u_{repeat} /nm	u_{reprod} /nm	u_{traceab} /nm	$u_{\text{T-z}}$ /nm	u_{error} /nm	u_{repeat} /nm	u_{reprod} /nm	u_{traceab} /nm	$u_{\text{T-z}}$ /nm
200	--	--	--	--	**--**	4.0	4.9	5.0	2.3	**8.4**
500	3.3	11.1	9.1	2.1	**14.9**	6.4	3.6	15.6	2.1	**17.3**
1200	4.2	4.8	5.4	2.2	**8.7**	7.0	5.2	7.4	2.2	**11.7**
2100	12.3	5.8	7.9	2.1	**15.9**	11.0	6.6	6.2	2.1	**14.4**
30000	35.4	20.9	13.3	56.3	**71.0**	26.3	7.2	2.6	56.3	**63.0**

For the 200 nm, 500 nm, 1200 nm and 2100 nm the u_{error}, u_{repeat} and u_{reprod} are always larger than the traceability contribution. The resulting measurement uncertainty $u_{T\text{-}z}$ is approximately between 10 nm to 20 nm for both the 2× and 5× objective lens. For the 30 µm step height, the largest uncertainty is due to its non-uniform profile. The disadvantages of the SHS method are several. Traceable measurements are ensured only for surfaces with heights shorter than the largest SHS measured, in this specific case 30 µm. For SHS of tens of micrometres, the traceable contribution is likely to be the main uncertainty contribution due to the non-uniformity of the step height profile limiting the measurement uncertainty of the instrument. Furthermore, the sampling of the instrument response curve with SHSs might not provide an exhaustive characterisation of the non-linearity. To overcome the limitations of the SHS method, the estimation of the amplification coefficient and linearity deviation are estimated separately with the WS method and the tilted flat, respectively. Figure 4.26 shows schematically this separation.

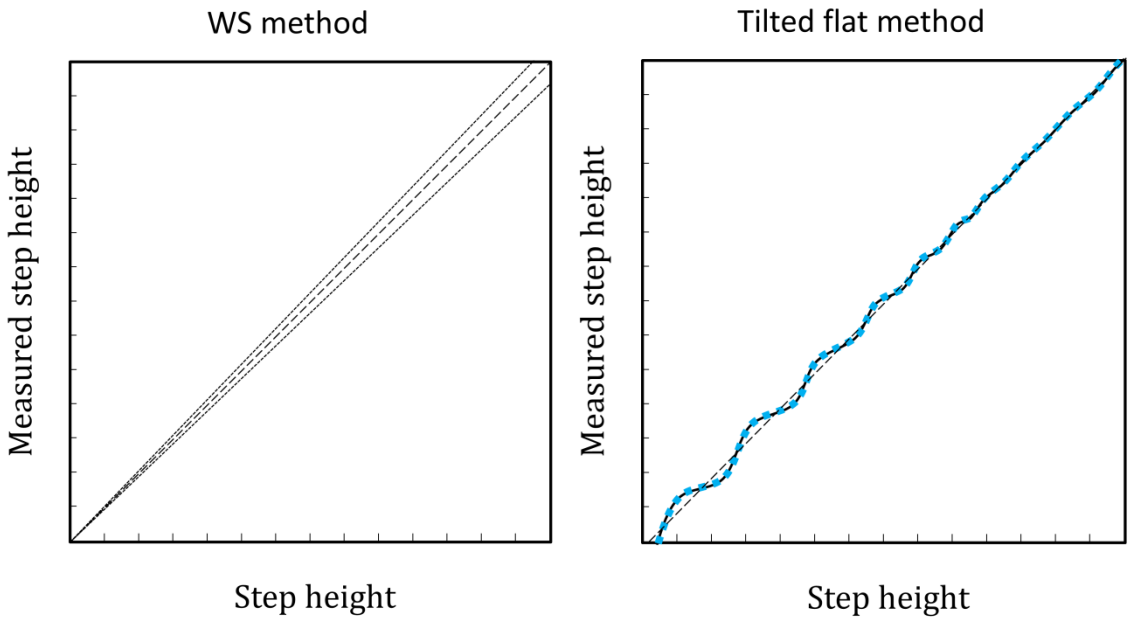

Figure 4.26. With the WS method and the tilted flat estimation of the amplification coefficient and the linearity deviation are separated. With the WS method the estimation of the amplification coefficient has lower uncertainty than with the SHS method. The tilted flat method allows a more detailed characterisation of the instrument response curve by sampling the curve more finely than with the SHS method.

There are several advantages of using the WS method. By calibrating the wavelength, traceability of the amplification coefficient measurement can be achieved over the entire instrument range. This is not the case for the SHS method, as the extent along the instrument range to which traceability can be achieved is limited by the largest step height available. Furthermore, it has been shown in section 4.2.4 how the achieved amplification coefficient estimation is lower with the WS method. The estimated amplification coefficient with the WS method is the ideal value of one with a standard uncertainty of ± 0.2 % for both the 2× and 5× objectives. The amplification coefficient contribution to the uncertainty is propagated as a percentage of the measured height range.

The linearity deviation estimation with the tilted flat provides a finer sampling of the *z*-axis response curve, therefore, providing a more detailed characterisation (see section 4.1.3 and figure 4.13) of the instrument response curve than the SHS method. The linearity deviation is the maximum amplitude of the non-linearity response profile (see figure 4.13) and it was shown to have a normal distribution. Therefore, the standard uncertainty is the maximum amplitude (corresponding roughly to five times the standard deviation) divided by five ($u_{lz} = \frac{\delta_{error}}{5}$). The linearity deviation estimated with the tilted flat method, considering the entire instrument range, are 81 nm and 111 nm for the 2× and 5× objective lens, respectively. The standard uncertainty due to the linearity deviation is, therefore, 16.2 nm and 22.2 nm. The uncertainty component estimated with the WS and the tilted flat methods are summarised in table 4.10.

Table 4.10. Amplification coefficient and linearity deviation contribution to the z-axis measurement uncertainty.

WS method		Tilted Flat method	
$u_{\alpha z}$ / %		$u_{lz} = \frac{\delta_{error}}{5}$ /nm	
2×	5×	2×	5×
0.2%	0.2%	16.2	22.4

The uncertainty due to the amplification coefficient and the linearity deviation estimated with the WS method and the tilted flat method is calculated as:

$$u_{T-z} = \sqrt{\left(\frac{\delta_{error}}{5}\right)^2 + (u_{\alpha z}\, h)^2} \tag{4.3.3}$$

where h is the maximum value of the surface height being measured.

Knowledge of the linearity deviation distribution within the instrument range allows placing the surface to measure in a position in the vertical range with the lowest linearity deviation to reduce its uncertainty contribution.

For example, by employing the lowest 30 µm for the 2× objective lens, *i.e. z*-positions ranging from −40 µm to −70 µm, the linearity deviation contribution to the measurement uncertainty is reduced from 16.2 nm to 5.1 nm when compared to *z*-position range from -5 µm to -70 µm. For the 5× objective lens, employing the bottom 10 µm, *i.e. z*-position ranging from -25 µm to -35 µm, the uncertainty due to the linearity deviation reduces from 22.2 nm to 7.2 nm when compared to the *z*-position range from -5 µm to -35 µm. Figure 4.27 compares the estimated uncertainty due to the amplification coefficient and the linearity deviation with the two methods, and for the WS and tilted flat method also on a reduced portion of the instrument range.

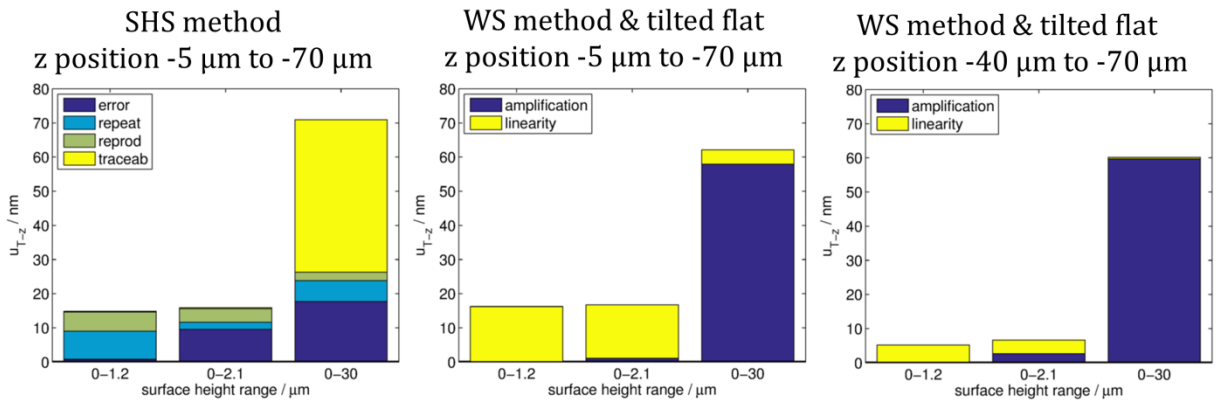

Figure 4.27. Uncertainty due to amplification coefficient and linearity deviation estimated with the SHS method (left), WS and tilted flat method (centre) and WS and tilted flat method on a reduced instrument range (right). The results are relative to the 2× objective lens.

The uncertainty estimated with the SHS and the WS and tilted flat method are equivalent when the entire instrument vertical range is employed. For the SHS method the main contribution to the uncertainty are the error, repeatability and reproducibility for surface with heights smaller than 2.1 µm. For heights up to 30 µm, the main uncertainty contribution is the traceability of the step height. For the WS and tilted flat method, the main uncertainty is due to linearity deviation for heights smaller than 2.1 µm, and the amplification coefficient for heights up to 30 µm. Knowledge of the distribution of the linearity deviation allows selecting the *z*-position range with the lowest linearity deviation, therefore reducing the uncertainty.

A comparison of the estimated uncertainty with the two methods for the 5× objective lens is shown in figure 4.28.

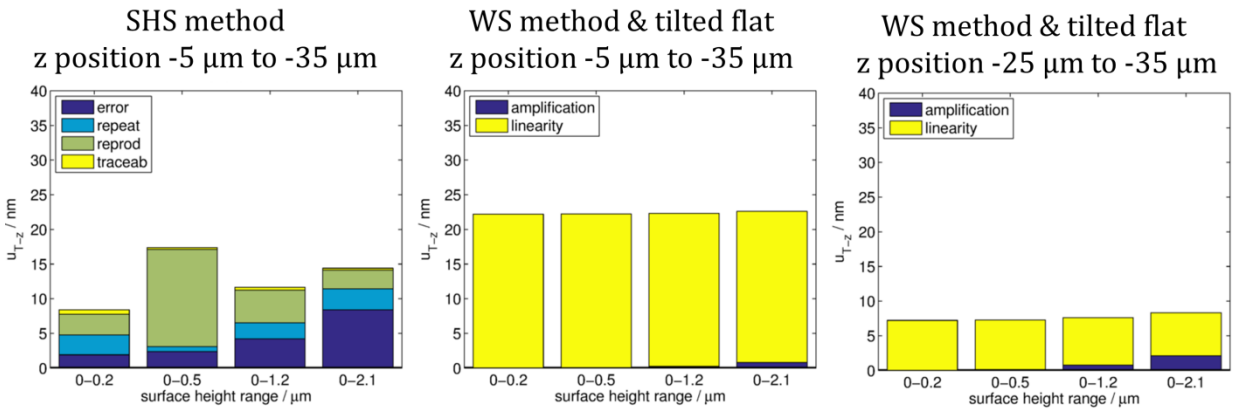

Figure 4.28. Uncertainty due to amplification coefficient and linearity deviation estimated with the SHS method (left), WS and tilted flat method (centre) and WS and tilted flat method on a reduced instrument range (right). The results are relative to the 5× objective lens.

The WS and tilted flat method estimate larger uncertainty than the SHS method. The main uncertainty contribution is due to the linearity deviation up to heights of 2.1 µm. Also, for

measurement on a reduced portion of the range the main uncertainty contribution is due to the linearity deviation.

4.3.3 Combined uncertainty

The combined contribution of the MCs can be calculated using equation (4.2.4), where the sensitivity coefficient (C_i) are all equal to one, and $u(x_i)$ is the contribution of each of the metrological characteristics. The equation for the combined standard uncertainty of the *z*-axis coordinate measurement is:

$$u_z = \sqrt{{u_{NF}}^2 + {u_{T-z}}^2} \tag{4.3.4}$$

In figure 4.29, the combined uncertainty for the 2× and 5× objective lens is shown, in the case when the entire instrument measurement range is employed for measuring, with the individual uncertainty contributions, namely noise, flatness deviation, linearity and amplification coefficient.

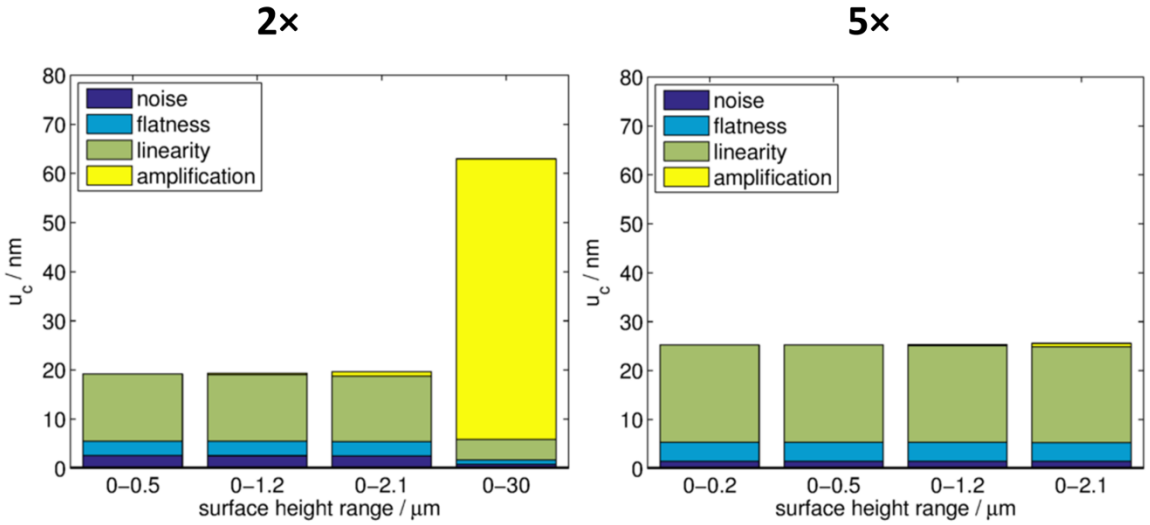

Figure 4.29. Combined measurement uncertainty in the z-axis for the 2× (left) and 5× (right) for several height ranges.

For heights lower than 2.1 µm the uncertainty main contribution are the linearity deviation followed by the measurement noise and flatness deviation for the 2× objective lens, and by the flatness deviation for the 5× objective lens. The amplification coefficient contribution increases proportionally with the measured height and becomes the most important only for large height measurements.

4.3.4 Step height uncertainty example

In the previous section the combined uncertainty for a single value of height measured with the WSI is calculated. When the measurand is a function of many of the individual points of the measured surface, like for example any surface parameters, the measurement uncertainty can

be propagated according to the measurand function. For example the noise and flatness deviation uncertainty contribution when measuring a step height are reduced due to the averaging of all the measured step height profiles in the instrument FOV. In this section an example of uncertainty calculation for a step height measurement is reported.

A step height with a nominal value of 12.5 µm is measured and details of the analysis are shown in figure 4.30. The step height is estimated by averaging the surface measurement's profile and applying the ISO 5436 standard procedure to measure the step height. The ISO 5436 standard procedure consists in fitting two lines between the upper and bottom data of the profiles and measuring the distance between the fitted lines.

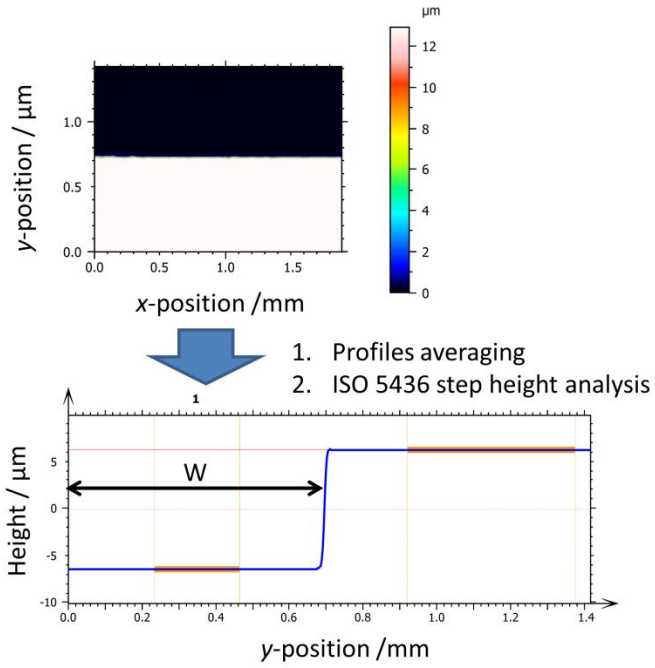

Figure 4.30: Step height measurement. Top: Surface measurement. The surface measurement's profiles are averaged to reduce the noise and the influence of the flatness deviation. Bottom: Resulting averaged profile with details of the application of the ISO 5436 standard procedure to evaluate the step height. Highlighted are the points used to evaluate the step height.

Since the step height analysis calculates the mean profile along the *y*-axis of the instrument some of the effects of the *y* axis flatness deviation on the measurement uncertainty associated with the step height calculation are reduced (see figure 4.31). The u_{NF} for a step height can be estimated by measuring *Pt,* the total height of the profile (note that *Pt* was used instead *Sz* as the analysis is performed on a profile).

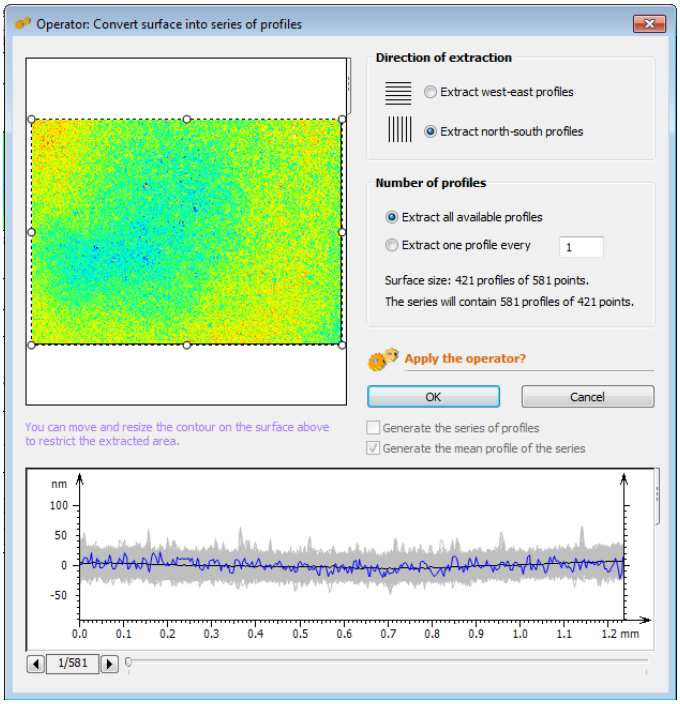

Figure 4.31: Extraction of the mean profile along the *y* axis.

The measurement noise and the flatness deviation are superimposed such that the combined contribution is propagated in the form of a rectangular distribution with inexactly prescribed limits that has a variance equal to $Pt_{flatness}^2/12 + \sigma_{Pt}^2/9$, where σ_{Pt} is the standard deviation. It follows that the u_{NF} for the 12.5 µm step height using the 2× objective lens is 4 nm (see table 4.11).

Table 4.11.Example of u_{NF}values for the 2× objective lens.

Measurement no.	Pt/nm
1	13.5
2	15.9
3	13.7
4	11.2
5	13.6
Average	13.6
$Pt_{flatness}^2/12$	3.9
Repeatability (σ_{Pt})	0.7
u_{NF}	4.0

The step height analysis algorithm calculates the distance between two parallel lines that are fitted through a restricted number of the topography data points (see figure 4.30). The

sensitivity coefficients that are used to propagate the measurement noise and flatness deviation components are given by:

$$C_{NF}^2 = \frac{3d}{W} + \frac{3d}{2W} = 4.5\frac{d}{W} \tag{4.3.5}$$

where C_{NF} is the sensitivity coefficient, d is the sampling interval and W is the width of the groove. For the measurement here considered the width (W) is approximately 700 µm and the sampling distance 3 µm and therefore the sensitivity coefficient (C_{NF}) is equal to $0.019^{1/2}$.

The contribution of amplification and linearity deviation remains unchanged such that the amplification coefficient is 0.2 % of the step height and the linearity deviation is 16 nm (see table 4.10), and the sensitivity coefficient is equal to one.

4.3.4.1 Type A evaluation of standard uncertainty

The Type A standard uncertainty is calculated as the standard deviation of the mean of five repeated measurements.

Table 4.12.Measurement of a 12.5 µm step height physical measurement standard.

Measurement no.	Height /nm
1	12673
2	12695
3	12673
4	12667
5	12687
Average	12679
u_A	5

According to equation (4.2.4) the combined standard uncertainty associated with the step height artefact measurement is:

$$u_c^2 = u_A^2 + u_B^2 = (5^2 + 0.019{\times}4^2 + (0.002 * 12679)^2 + 16^2)\, nm^2 \cong 924\, nm^2. \tag{4.3.6}$$

4.3.4.2 Expanded uncertainty

The calculation of the expanded uncertainty requires the value of the coverage factor (k) for a 95% confidence level. The value of the coverage factor is based on the number of effective degrees of freedom (ν) that can be calculated with

$$\upsilon = (n-1){\times}\frac{u_c^4}{u_A^4} = 4{\times}\frac{924^2}{5^4} \cong 5464. \tag{4.3.7}$$

Value for k can be obtained from table G2 page 78 of the *GUM* [137]. For this example the coverage factor is equal to two because the effective degree of freedom is larger than 100. It follows that the measurement result can be expressed as:

$$h = 12679\ nm \pm 30\ nm\ (k = 2) \tag{4.3.8}$$

4.4 Summary

In this chapter the results of the calibration of the linearity deviation and the amplification coefficient are reported. It is shown how the linearity deviation is due to the algorithm response when estimating the frequency of a fringe pattern. A possible algorithm optimisation is proposed to minimise the linearity deviation and therefore reduce the measurement uncertainty.

Alternative methods to estimate the amplification coefficient and the linearity deviation are reported and the results discussed and compared with the SHS method. The WS method achieves lower uncertainty in measuring the amplification coefficient of the instrument when compared with the SHS method, and therefore is preferable. The WS method ensures traceability of the measurements through a wavelength standard comparison (*i.e.* calibration of the spectrometer). Additionally, the WS method is cheaper since a spectrometer only is needed rather than a set of SHSs and it is quicker to perform. It has been shown that the amplification coefficient uncertainty is not the main contribution to the combined uncertainty for height smaller than 2 μm.

The tilted flat method provides a reliable estimate of the linearity deviation when compared to the SHS method. Furthermore, knowledge of the non-linearity distribution with the tilted flat method allows a reduction of the measurement uncertainty when the *z*-position of the measured surface can be chosen.

Lastly, the *z*-axis type B measurement uncertainty budget is calculated, which includes the contribution of noise, flatness deviation, amplification and linearity deviation. The main source of type B uncertainty is the linearity deviation for both objective lenses, followed by the measurement noise for the 2× objective lens, and by the flatness deviation for the 5× objective lens. The amplification coefficient uncertainty contribution becomes the most important only for height measurements of tens of micrometres.

At the end of the chapter an example of calculation of uncertainty of a step height physical artefact is also reported.

5 Lateral axes uncertainty

In this chapter the results of the calibration of the WSI lateral axes are presented. In section 5.1, the methodology and the results from the calibration of the amplification coefficients (α_x, α_y) and linearity deviations (l_x, l_y) of the lateral WSI instrument axes are reported. Two methods are described in sections 5.1.1 and 5.1.2, and the results are compared in section 5.1.3. In section 5.2, a method to evaluate the instrument lateral resolution is presented and the results are discussed.

5.1 Lateral distortion

5.1.1 Reference grid method

To calibrate the *x*- and *y*-axis of the measuring instrument, a cross grating standard artefact (type Areal Cross Grating (ACG)) is measured. The ACG artefact consists of a rectangular array of protrusions on a flat surface (see figure 5.1). In order to assess the lateral axes distortion, the surface measurement made with the WSI instrument is compared to the traceable measurement made on a CSI.

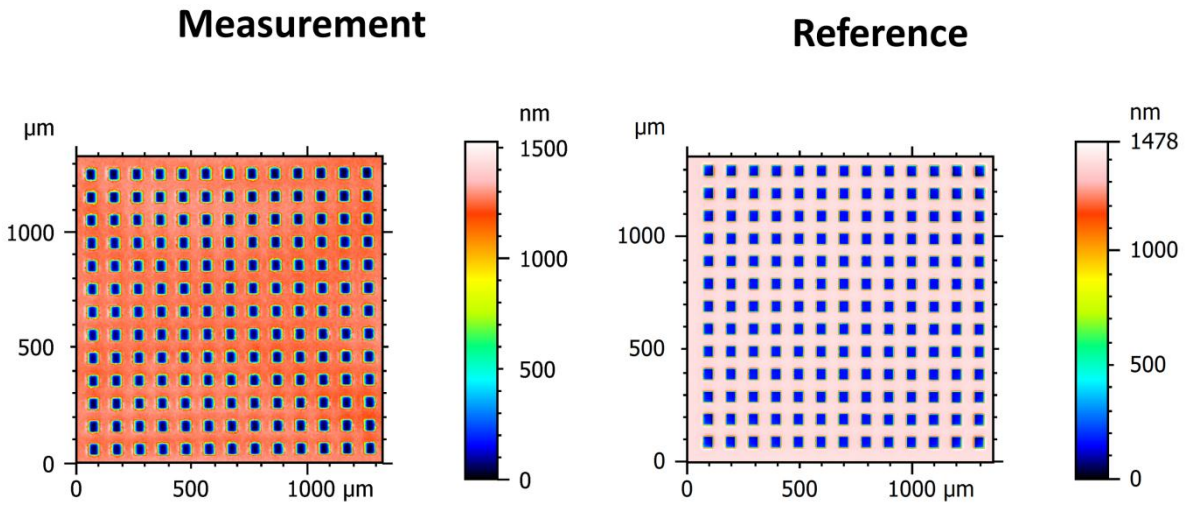

Figure 5.1. In order to calibrate the lateral axes coordinates of a WSI, the measurement of an ACG type surface (left) is compared to traceable reference measurement made on a CSI.

The surface measurements are processed in order to estimate the centres of gravity of the protrusion. It is possible to infer the instrument lateral axis errors and the lateral distortion by comparing the centre of gravity of the two measurements. Before calculating the centres of gravity, the surface data are levelled by subtracting a least-squares plane, and the surface is filtered with a Gaussian S-filter with cut-off frequency equal to one tenth of the nominal cross grid pitch. This pre-processing step minimises the effects of noise and spurious data. The protrusion features are detected by applying a *z*-threshold to the surface measurement.

Subsequently, the *x* and *y* coordinates of the centre of gravity are calculated using the following equation:

$$x_c(i,j) = \frac{\iint x\, z(x,y)dx\, dy}{\iint z(x,y)dx\, dy} \quad i \in [1,2 \dots, n_x] \text{ and } j \in [1,2 \dots, n_y] \qquad (5.1.1)$$

where the integral is evaluated using the value of the surface *z(x,y)* corresponding to the identified protrusion peak with indexes (*i,j*) and n_x and n_y are the number of protrusions in the *x* and *y*-direction, respectively. The same equation is valid for calculating the *y*-coordinate $y_c(i,j)$ of the centres of gravity by substituting *x* with *y* in the numerator. In order to minimise errors due to misalignment of the two ACG surfaces, the centre of gravity coordinates corresponding to the WSI measurement are translated and rotated through a non-linear least squares fitting routine to be aligned with the reference centres of gravity. Finally, the reference coordinates are subtracted from the rotated and translated coordinates to obtain the lateral distortion map [146], [165].

In the next section, the results from the calibration of the WSI lateral axes are reported for both 2× and 5× objective lenses. The procedure consists of measuring two ACG surfaces with nominal pitch of 100 μm and 40 μm. The ACG surface measurements are repeated five times at five different instrument vertical positions. At each vertical position, five measurements are made, each time shifting the surface by half the pixel size towards positive and negative directions for both the *x* and *y* axes. The lateral shift takes into account sub-pixel effects in determining the centre of gravity. The contribution to uncertainty from the measurement repeatability is taken as the largest standard deviation observed from the measurements at different *z*-positions. The uncertainty contribution from reproducibility is given by the standard deviation of the mean errors between measurements at different *z*-positions. Uncertainty in the reference measurements also contributes to uncertainty in the estimated metrological characteristics. This contribution is given by the lateral (*x,y*) uncertainty of the reference measurements, and it is referred to as the traceable uncertainty contribution. The traceability contribution is the lateral uncertainty of the instrument used to provide the reference measurement of the ACG surface. The total uncertainty is given by the quadrature sum of the repeatability, reproducibility and traceability contributions.

5.1.1.1 Results

The lateral distortion maps obtained for the 2× and the 5× objective lenses are shown in figure 5.2. Arrows are plotted in bright (turquoise) when their error values are smaller than the standard uncertainty, whilst the arrows are plotted in dark (blue) when their error value is larger than the standard uncertainty. The uncertainty is calculated as the quadrature sum of the repeatability, reproducibility and traceability contributions. There is systematic behaviour in

the lateral distortion for both objective lenses. In both cases, the magnitude of the arrows has been normalised with respect to the ACG nominal pitch.

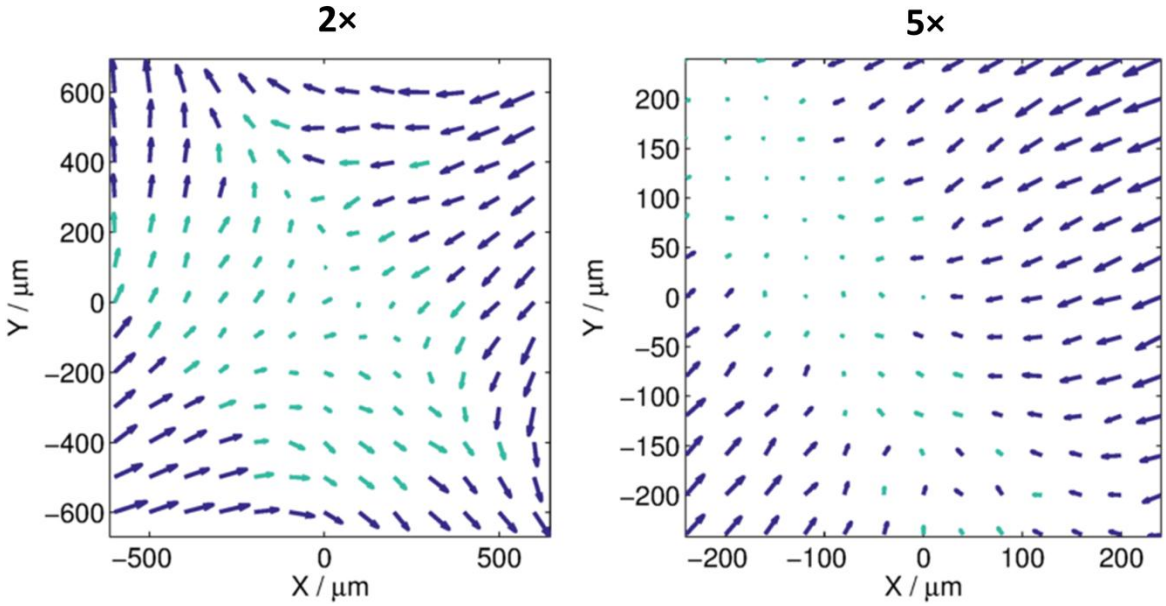

Figure 5.2. Lateral distortion map for 2× (left) and 5× (right) objective lenses. The arrow are coloured in bright or dark, depending whether the magnitude is below or above the standard uncertainty. The arrow magnitude is normalised to the cross grid pitch. The largest distortion for the 2× and 5× objective lens occurs at the top right corner and has a magnitude of 3.7 µm.

For the 2× objective lens, most distortions are smaller than the uncertainty. This behaviour is due to large uncertainty contribution of the reference measurement (1.4 µm). For the 5× objective lens, uncertainty from the reference measurement is relatively small (0.45 µm) when compared to the maximum distortion of 3.7 µm. As a result, a smaller portion of data is smaller than the standard uncertainty. Additionally, for the 5× objective lens, the lateral distortion errors are not centred in the FOV. In table 5.1 and table 5.2, detailed values of the x and y errors for the central row and column are reported with uncertainty contributions from repeatability, reproducibility and reference measurement.

Table 5.1. 2x objective lens lateral distortion errors and uncertainty contributions relative to the central row (*x*-axis) and central column (*y*-axis).

Nominal length	δ_{error}		δ_{repeat}		δ_{reprod}		$\delta_{traceab}$		Combined standard uncertainty	
	x	*y*	*x*	*y*	*x*	*y*	*x*	*y*	*x*	*y*
/ µm										
-600	0.167	0.399	0.250	0.149	0.105	0.098	1.400	1.400	1.426	1.411
-500	0.081	-0.431	0.153	0.232	0.066	0.106	1.400	1.400	1.410	1.423
-400	-0.178	0.267	0.171	0.096	0.059	0.074	1.400	1.400	1.412	1.405
-300	0.066	-0.584	0.195	0.102	0.060	0.072	1.400	1.400	1.415	1.406
-200	0.186	0.298	0.126	0.145	0.031	0.131	1.400	1.400	1.406	1.413
-100	-0.253	-0.344	0.175	0.132	0.012	0.013	1.400	1.400	1.411	1.406
0	0.000	0.000	0.000	0.000	0.000	0.000	1.400	1.400	1.400	1.400
+100	-0.751	-0.036	0.080	0.101	0.029	0.015	1.400	1.400	1.403	1.404
+200	-1.009	-0.671	0.100	0.067	0.019	0.025	1.400	1.400	1.404	1.402
+300	-1.689	-0.777	0.178	0.078	0.028	0.022	1.400	1.400	1.412	1.402
+400	-1.927	-1.357	0.120	0.105	0.023	0.007	1.400	1.400	1.405	1.404
+500	-2.473	-1.135	0.149	0.098	0.032	0.031	1.400	1.400	1.408	1.404
+600	-2.258	-1.462	0.174	0.046	0.029	0.069	1.400	1.400	1.411	1.402

Table 5.2. 5x objective lens lateral distortion errors and uncertainty contributions relative to the central row (*x*-axis) and central column (*y*-axis).

Nominal length	δ_{error}		δ_{repeat}		δ_{reprod}		$\delta_{traceab}$		Combined standard uncertainty	
	x	*y*	*x*	*y*	*x*	*y*	*x*	*y*	*x*	*y*
/ µm										
-240	0.729	-0.749	0.305	0.430	0.248	0.189	0.450	0.450	0.598	0.650
-200	0.616	-1.145	0.340	0.338	0.128	0.177	0.450	0.450	0.578	0.590
-160	-0.021	-0.465	0.271	0.331	0.233	0.089	0.450	0.450	0.575	0.566
-120	0.102	-0.447	0.382	0.367	0.084	0.067	0.450	0.450	0.596	0.585
-80	-0.088	-0.136	0.317	0.294	0.151	0.041	0.450	0.450	0.571	0.539
-40	-0.298	-0.086	0.254	0.236	0.158	0.084	0.450	0.450	0.540	0.515
0	0.000	0.000	0.000	0.000	0.000	0.000	0.450	0.450	0.450	0.450
+40	-0.975	0.284	0.302	0.214	0.179	0.010	0.450	0.450	0.571	0.498
+80	-1.398	0.309	0.341	0.407	0.190	0.073	0.450	0.450	0.595	0.611
+120	-1.748	0.268	0.316	0.241	0.130	0.057	0.450	0.450	0.565	0.514
+160	-2.090	0.457	0.281	0.182	0.113	0.074	0.450	0.450	0.542	0.491
+200	-2.471	0.732	0.304	0.178	0.132	0.045	0.450	0.450	0.559	0.486
+240	-2.544	0.730	0.370	0.201	0.155	0.063	0.450	0.450	0.603	0.497

The central protrusion is taken as the zero point in both the measurements and, therefore, its value is always zero, with no uncertainty from repeatability and reproducibility. For 2× objective lens, the uncertainty from reproducibility is smaller than the uncertainty from repeatability. The repeatability value is always larger for measurements at large *z*-positions; therefore, the increased noise may have a role in the smaller repeatability of the lateral position. For the 5× objective lens, the contribution from reproducibility is larger than the 2× objective lens; this behaviour could be due to the fact that the entire DOF is employed, resulting in larger defocus aberration. However, in both cases, the largest contribution to the uncertainty is the traceability. For the 2× objective lens, the traceability contribution is at least one order of magnitude larger than the contribution from the repeatability and the reproducibility. For the 5× objective lens, all three contributions are of the same order of magnitude.

Both objective lenses exhibit a linear scaling error with differing magnitude along the *x* and the *y* directions. A possible reason for this observation is the variation in the magnification, which causes the sampling distance to be different from the nominal value. The nominal sampling distance is determined by dividing the CCD camera pixel size by the magnification; the nominal sampling distance is 2.960 μm and 1.184 μm for the 2× and 5× objective lenses, respectively. A correction is applied to the nominal sampling distance to account for scaling error. For the 2× objective, the scaling corrections are +0.28 % and -0.10 % for the *x* and *y* directions, respectively. For the 5× objective, the scaling corrections are +0.76 % and +0.4 % for the *x* and *y* directions, respectively. The magnification is defined as the ratio between the focal length of the imaging lens and the objective lens. The pixel corrections are within the focal length tolerance of the imaging lens (Thorlabs AC256-250-B-ML), stated to be 1 %. After correcting for the offset and the scaling along the *x* and *y* directions the resulting lateral distortion map is shown in figure 5.3.

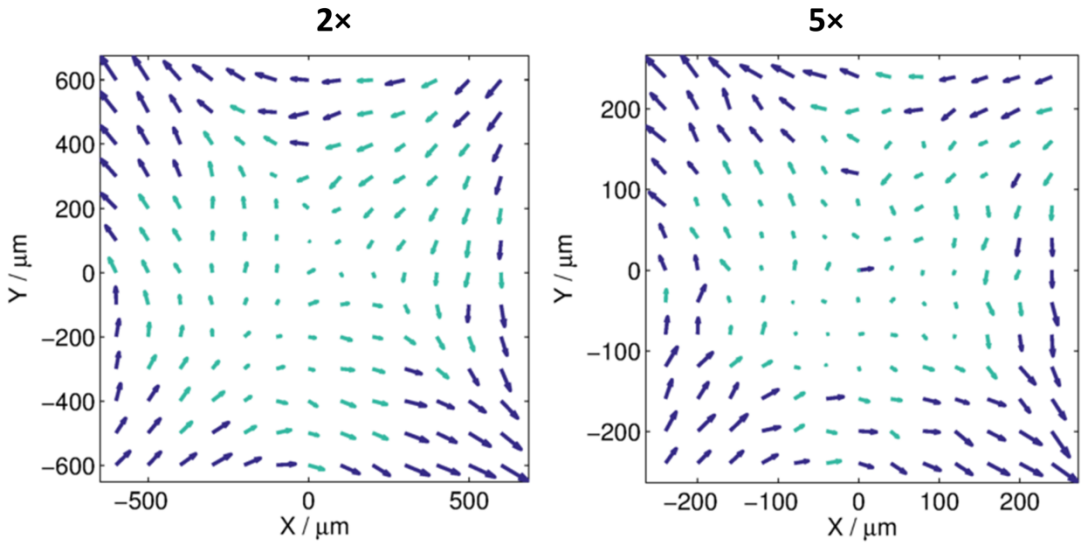

Figure 5.3. Lateral distortion map after correcting for offset and scaling for 2× (left) and 5× (right) objective lenses. Dark arrows have magnitude above the measurement uncertainty, whilst bright arrows have magnitude below the measurement uncertainty.

5.1.1.2 Lateral correction

A general approach for lateral distortion correction is employing a 'dewarping' algorithm, which can correct for distortion of higher order than a scaling coefficient[166]. The dewarping algorithm provides a transformation from the measured coordinates (x, y) to the true coordinates (x', y'). For the ACG surface, the measured centres of gravity can be compared with the reference values to determine the coefficients of the transformation C:

$$\begin{bmatrix} x' \\ y' \end{bmatrix} = \begin{bmatrix} c_{1,1} & c_{2,2} & c_{3,3} & \cdots & c_{1,7} & c_{1,8} & c_{1,9} & c_{1,10} \\ c_{2,10} & c_{2,2} & c_{2,3} & \cdots & c_{2,7} & c_{2,8} & c_{2,9} & c_{2,10} \end{bmatrix} \begin{bmatrix} 1 & x & y & \cdots & x^3 & x^2y & xy^2 & y^3 \\ 1 & x & y & \cdots & x^3 & x^2y & xy^2 & y^3 \end{bmatrix}^T = \begin{bmatrix} \overline{c_x} \\ \overline{c_y} \end{bmatrix} [\bar{x}\ \bar{y}] = C\ [\bar{x}\ \bar{y}] \quad (5.1.2)$$

where the first row of the c coefficients dewarps along the x-direction and will be referred to as c_x, while the second row dewarps along the y-direction and will be referred to as c_y. A least-squares method can be applied to equation (5.1.2) to calculate the vector c_x and c_y. The dewarping coefficients evaluated from the error map are reported in table 5.3.

Table 5.3. Dewarping algorithm calculated coefficients for 2× and 5× objective lenses.

Objective lens		1	x	y	x^2	x y	y^2	x^3	$x^2 y$	xy^2	y^3
2×	c_x	7.64*e*-01	1.01*e*+00	2.83*e*-03	4.86*e*-07	8.54*e*-07	-8.68*e*-07	-6.41*e*-09	1.32*e*-08	-8.05*e*-09	1.48*e*-08
	c_y	9.76*e*-02	3.50*e*-03	1.00*e*+00	9.57*e*-08	-1.78*e*-06	-2.33*e*-06	1.18*e*-09	-4.60*e*-09	5.04*e*-09	-1.40*e*-08
5×	c_x	7.64*e*-01	1.01*e*+00	2.83*e*-03	4.86*e*-07	8.54*e*-07	-8.68*e*-07	-6.41*e*-09	1.32*e*-08	-8.05*e*-09	1.48*e*-08
	c_y	9.76*e*-02	3.50*e*-03	1.00*e*+00	9.57*e*-08	-1.78*e*-06	-2.33*e*-06	1.18*e*-09	-4.60*e*-09	5.04*e*-09	-1.40*e*-08

Residual lateral distortion maps are shown in figure 5.4 after applying linear (left) and third order dewarping (right) for the 2× objective lens. All the errors are smaller than the standard uncertainty; however, the errors are of similar magnitude when correcting with the linear coefficients or with the third orders. The maximum error is reduced from 3.7 μm to 1.28 μm and the mean error is reduced from 2.01 μm to 0.47 μm after linear correction is applied. The maximum and mean errors do not decrease substantially after applying a third order correction: maximum error is reduced from 1.28 μm to 1.26 μm, while mean error is reduced from 0.47 μm to 0.46 μm. Similar results are observed after dewarping the lateral distortion map for the 5× objective lens, as is shown in figure 5.5. The maximum error is reduced from an initial value of 3.7 μm to 1.0 μm and the mean error is reduced from 1.24 μm to 0.44 μm after the linear correction is applied. Also for the 5× objective lens, the maximum and mean errors do not decrease substantially after applying a third order correction: mean error is reduced from 1.0 μm to 0.96 μm, while the average error is reduced from 0.44 μm to 0.34 μm. After applying both linear and third order dewarping, only a few distortion vectors are larger than the standard uncertainty. Therefore, for both objective lenses, the main errors are due to the non-correct scaling of the *x* and *y* axes and their non-perpendicularity.

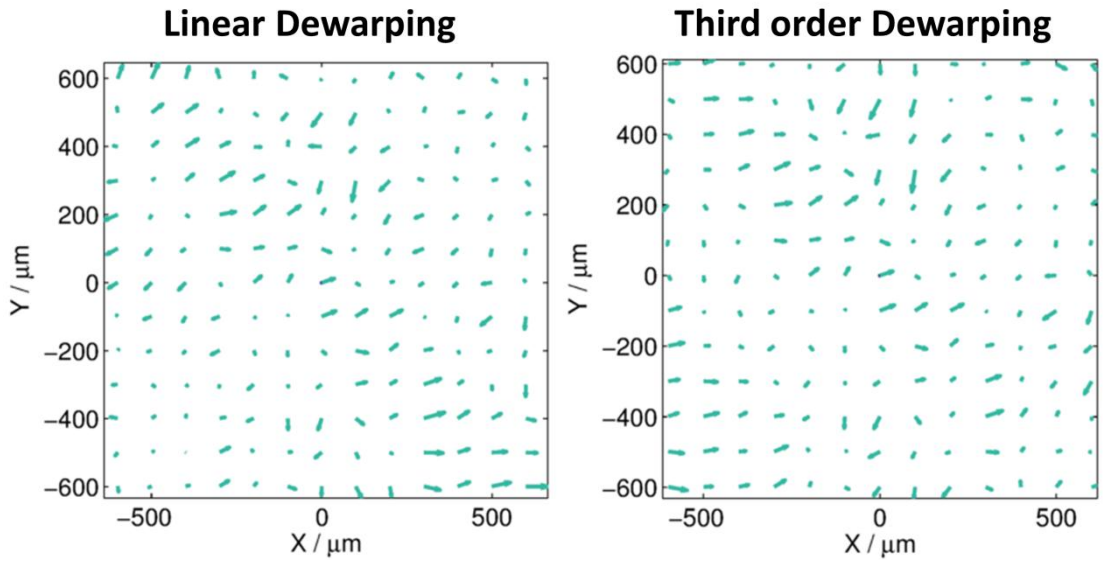

Figure 5.4. Residual lateral errors after first order (left) and third order (right) correction for 2× objective lens.

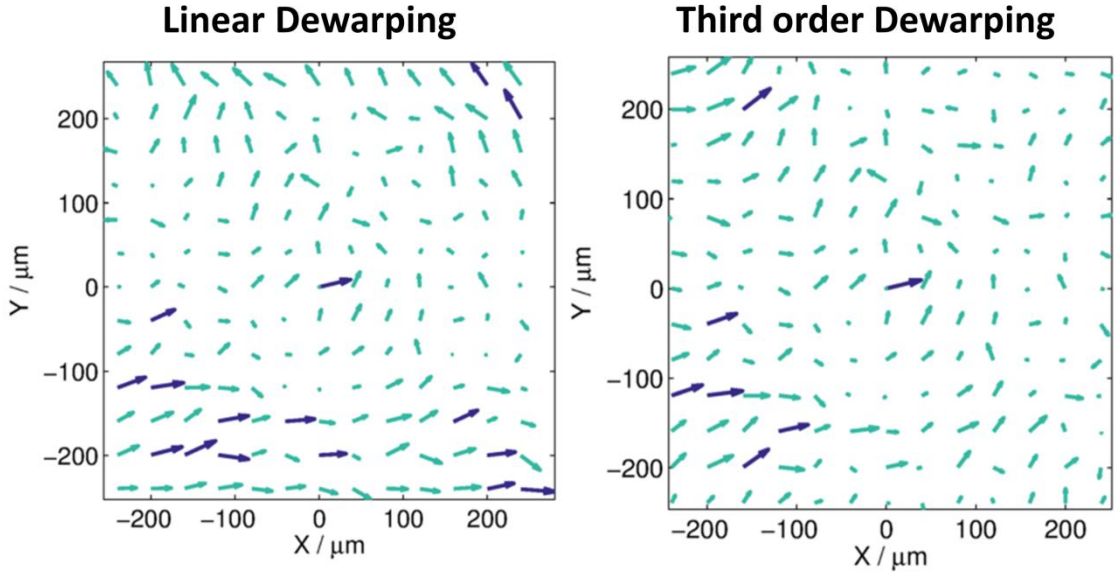

Figure 5.5. Residual lateral errors after first order (left) and third order (right) correction for 5× objective lens.

The method hereby described to estimate the lateral error map may not be the best in the presence of non-perpendicularity. The transformation to align the centres of gravity is a linear transformation, in which only the constant (translation) and the linear coefficient (rotation) are employed. Executing this step before subtracting the error map may affect the calculated dewarping coefficient.

The grid alignment transformation can be expressed by the matrix R:

$$R = \begin{bmatrix} r_{cos} + c_x & -r_{sin} + c_{xy} \\ r_{sin} + c_{yx} & r_{cos} + c_y \end{bmatrix} \tag{5.1.3}$$

where $r_{cos} = \cos(\theta)$ and $r_{sin} = \sin(\theta)$ are the rotation contribution to align the grid with the reference, and the c coefficients take into account the actual grid distortion. The alignment step of the two grids cannot separate the contribution of the rotation and distortion, thereby causing a potential bias of the results. In order to improve the lateral distortion calibration step, a self-calibration method is applied and described in the next section.

5.1.2 Self-calibration method

5.1.2.1 Method

Self-calibration methods consist of measuring the same object in various positions and orientations. Differences in the measurement of the same features are indications of systematic errors in the measurement instruments [167]. In the ACG measurement case, a three-dimensional artefact is measured and the two-dimensional centre of gravity of each protrusion is evaluated. The mathematical foundation of the self-calibration method is explained in Forbes et al. [167] and is briefly reported here for completeness.

Let y_j where $j = 1, \dots, n_Y$, be the location of the centre of gravity for the *j*-th protrusion and let

$$\boldsymbol{y}_{j,k} = T(\boldsymbol{y}_j, \boldsymbol{t}_k) \tag{5.1.4}$$

be the true coordinate of the *j*-th target in the *k*-th measuring position. The roto-translation transformation T is specified by three parameters $\boldsymbol{t}$, defining the translation vector and the angle of rotation. If $x_{j,k}$ is the measurement of the *j*-th target in the *k*-th position, then the observation equation is:

$$\boldsymbol{x}_{j,k} + \boldsymbol{e}(\boldsymbol{x}, \boldsymbol{b}) = \boldsymbol{y}_{j,k} + \boldsymbol{\varepsilon}_i \tag{5.1.5}$$

where $\boldsymbol{b}$ is the vector of error parameters, $\boldsymbol{e}(\boldsymbol{x}, \boldsymbol{b})$ is the error function depending of the position $\boldsymbol{x}$ in the instrument FOV and the error parameters ($\boldsymbol{b}$), and $\boldsymbol{\varepsilon}_i$ is the random error in the target location measurement.

Equation (5.1.5) suggests that the measured position of each target plus the error correction is equal to the "true" position of the target plus a random effect. Estimation of $\boldsymbol{y}_{j,k}$ and $\boldsymbol{e}(\boldsymbol{x}, \boldsymbol{b})$ can be achieved by solving the non-linear least-squares problem:

$$min_{\{\boldsymbol{y_j}\},\{t_k\},\boldsymbol{b}} \sum_{j,k} \boldsymbol{f}_{jk}^T \boldsymbol{f}_{jk} \tag{5.1.6}$$

where $\boldsymbol{f}_{jk}(\boldsymbol{y}_j, \boldsymbol{t}_k, \boldsymbol{b}) = \boldsymbol{x}_{j,k} + \boldsymbol{e}(\boldsymbol{x_{j,k}}, \boldsymbol{b}) - \boldsymbol{y}_{j,k}$. The minimisation problem returns the parameters $\boldsymbol{b}$ of the error map, the transformation $\boldsymbol{t}_k$ and the "real" positions of the targets $\boldsymbol{y}_j$.

The minimisation problem is applied to a set of three measurements of the centres of gravity of the cross grid: the first measurement taken has no transformation applied, the second one

rotated by 90˚, and the third one with same 90˚ rotation and an offset along the positive *x*-direction equal to the nominal cross grid pitch.

5.1.2.2 Results of the self-calibration method

The self-calibration lateral distortion error map for the 2× and the 5× objective lenses are shown in figure 5.6. The error maps differ slightly in magnitude from the error maps obtained with the reference grid method. Additionally, the error map exhibit scaling and perpendicularity errors, also observed in the reference grid method.

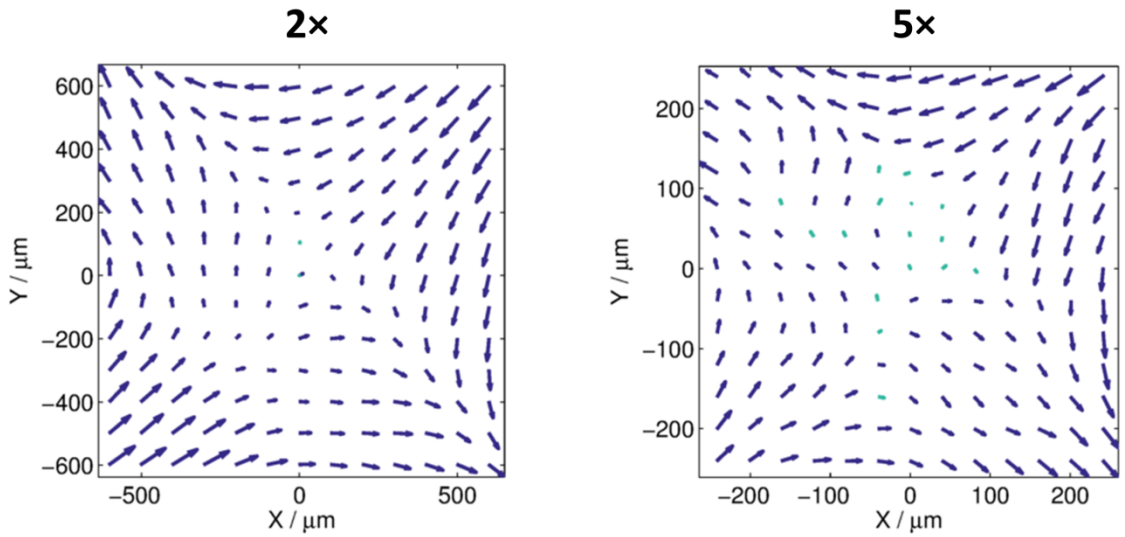

Figure 5.6. Lateral distortion error map for 2x (left) and 5x (right) objective lenses with the self-calibration method

The maximum error for the 2× objective lens is 3.65 µm, which is slightly smaller than the value obtained with the reference grid method. The directional behaviour of the error vectors is also similar to the error vectors from the reference grid method. However, the error directionality is not at an angle of 45˚, potentially a result of removing the alignment step with the reference grid. For the 5× objective lens, the distortion map is similar to the map obtained with the reference grid method, after correcting for the scale error. The maximum error for the 5× objective lens prior to any correction is 1.75 µm. The scaling correction in the *x* and *y* axis are, respectively, +0.15% and -0.27% for the 2× objective lens, and 0.04% and -0.3% for the 5× objective lens. These values are within the magnification error due to the focal length tolerance of the imaging lens, specified to be ±1% according to the instrument manufacturer. When applying the dewarping algorithm, a large improvement is observed when correcting for the scaling and the perpendicularity errors (linear factors). For the 2× objective lens, the maximum error is reduced from an initial value of 3.65 µm to 1.21 µm for the linear factor correction, and increases to 1.56 µm for the third order correction. The average error is reduced from 1.87 µm to 0.53 µm for the linear dewarping, and to 0.55 µm for the third order (see figure 5.7 for the

corresponding error maps). For the 5× objective lens, the initial maximum error of 1.75 µm is reduced to 0.81 µm and 0.72 µm, whilst the average error decreases from 0.79 µm to 0.32 µm and to 0.22 µm for the linear and third order dewarping correction, respectively, (see figure 5.8 for the corresponding error maps). For the 2× objective lens, increasing the degree of the polynomial correction above the first does not reduce the residual errors. Additionally, the residuals are larger than the combined standard uncertainty, suggesting that the distortion map is not well described by a third order polynomial function. For the 5× objective lens, the majority of the error vectors are smaller than the combined standard uncertainty after the linear dewarping, and only a few are larger after the third order dewarping

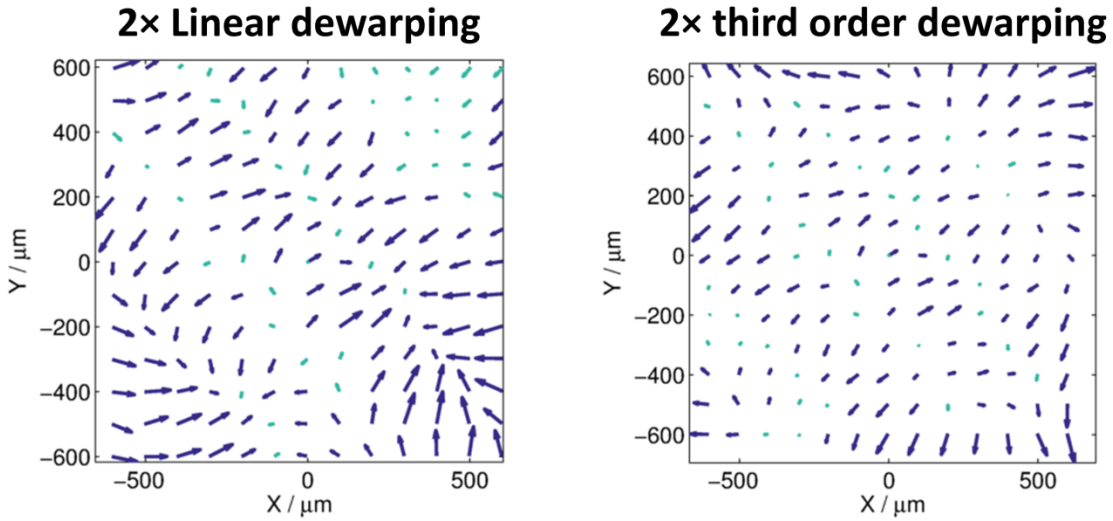

Figure 5.7. 2× objective lens error map after dewarping using a linear coefficient (left) and up to third order coefficients (right).

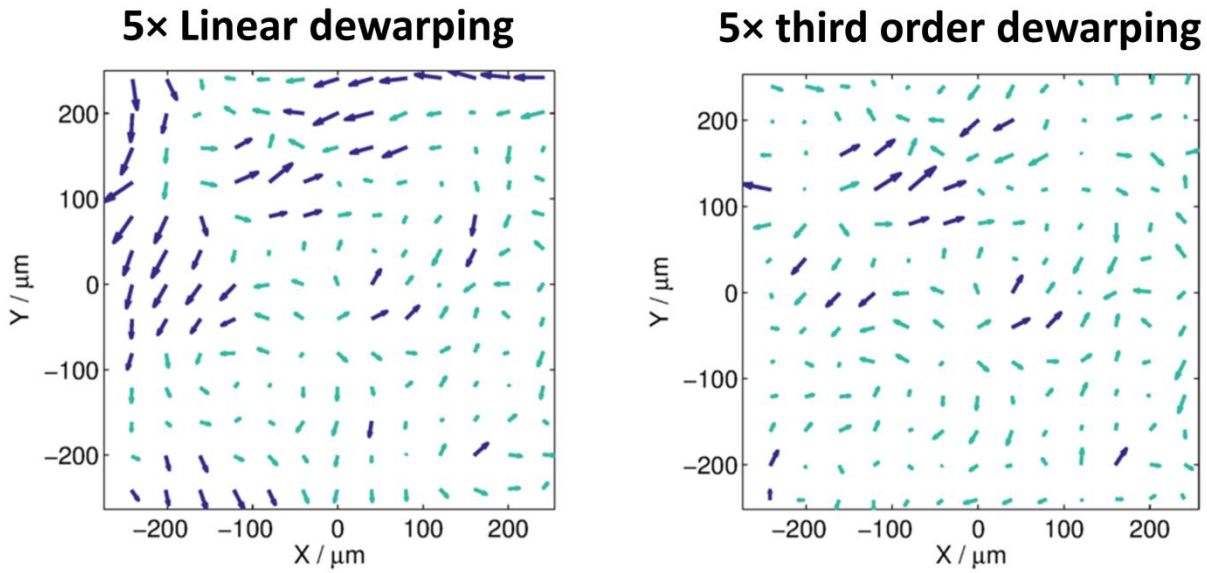

Figure 5.8. 5× objective lens error map after dewarping using a linear coefficient (left) and up to third order coefficients (right).

5.1.3 Method comparison

The linear dewarping coefficients associated with the dewarping algorithm are compared for the two methods (reference grid and self-calibration) in table 5.4.

Table 5.4. Dewarping linear coefficient for 2× and 5× objective lens for two lateral calibration methods: reference grid and self-calibration.

Objective lens	Method	vector	1	*x*	*y*
2×	Reference	c_x	0.65888	1.00282	0.00337
		c_y	0.34866	0.00341	0.99905
	Self-calibration	c_x	0.04955	1.00150	0.00357
		c_y	0.06272	0.00364	0.99731
5×	Reference	c_x	0.76449	1.00761	0.00283
		c_y	0.09762	0.00350	1.00445
	Self-calibration	c_x	-0.05142	1.00044	0.00291
		c_y	-0.11401	0.00437	0.99670

For the 2× objective lens, the offset coefficients are one order of magnitude smaller with the self-calibration method. The linear coefficients in the two cases describe similar errors: the *x*-axis has an amplification coefficient larger than one and the *y*-axis has an amplification coefficient smaller than one, in addition to a perpendicularity error. For the 5× objective lens, the results with the two methods are significantly different. According to the reference grid method, both *x* and *y* axes have an amplification coefficient larger than one in addition to not be perfectly perpendicular. According to the self-calibration the *x*-axis has an amplification coefficient larger than one and the *y*-axis has an amplification coefficient smaller than one. The perpendicularity correction is also different between the two methods: for the 2× objective lens cross-correlation coefficients of 0.00337 and 0.00341 are calculated for the reference grid method, whilst 0.00357 and 0.00364 for the self-calibrating method. Also in for the 5× objective the cross-correlation coefficients are different: 0.00283 and 0.00350 for the reference grid method whilst 0.00291 and 0.00437 for the self-calibrating method.

5.1.3.1 Perpendicularity

In order to evaluate the error due to the non-perpendicularity of the axes, lines are fitted between centre of gravity at the edge of the cross grid. The angle between the lines are calculated at each intersections and its difference from the angle obtained from the same procedure applied to the reference cross grid are calculated.

For 2× objective lens, the maximum perpendicularity error in the instrument FOV is 0.49° with no dewarping correction applied and 0.071° with the linear dewarping correction applied; these values correspond to a cosine error of 0.0037 % and 0.000077 % of the measured length. The longest measurable distance in the calibrated FOV is 1.8 mm, along the diagonal in the calibrated FOV, leading to a maximum perpendicularity error of 70 nm and 1 nm, respectively before and after the correction. For the 5× objective lens, the maximum perpendicularity error is 0.60 ° and 0.10 °, respectively, without and with the linear dewarping algorithm applied; the corresponding length percentage error are 0.0054 % and 0.00017 %. The maximum length measurable is along the diagonal of the calibrated FOV (0.735 mm) and leads to a maximum error of 40 nm and 1 nm.

5.1.4 Summary

In conclusion, when no correction is applied to the 2× objective lens data, the amplification coefficients are 1.00150 and 0.99731, respectively, for the *x* and *y* axis. The linearity deviation is equal to 3.7 μm, roughly 1.25 times larger than the sampling distance. When the amplification coefficient and the perpendicularity are corrected through a dewarping algorithm, the linearity deviation is reduced to 1.21 μm, less than half the sampling distance. For the 5x objective lens, the *x* and *y* axis amplification coefficients are 1.00044 and 0.99670, respectively. The linearity deviation is 1.75 μm, which is 1.5 times larger than the sampling distance. After linear dewarping, the linearity deviation is reduced to 0.81 μm, which is again half the sampling distance.

5.2 Resolution

In this section, the estimation of measurement resolution for the WSI is covered. A brief introduction on optical resolution definition criteria is reported for both 2D and 3D measurements. Furthermore, the instrument resolution is estimated and limitations of the method employed are discussed.

5.2.1 Resolution criteria

The lateral resolution of an optical instrument is conventionally defined as the ability to resolve two adjacent source points. When imaging an infinitesimally small point source, an optical instrument will image a finite size spot due to its finite wavelength and numerical aperture (NA). The spot is defined as point spread function (PSF) of an optical instrument. The Rayleigh criterion states that two point sources are resolvable when the maximum of the PSF produced by the first point source falls on the first minimum of the PSF produced by the second source. In the case of incoherent illumination, the Rayleigh resolution criterion is (see figure 5.9):

$$R = 0.61\,\frac{\lambda}{NA} \tag{5.2.1}$$

where λ is the wavelength of the light and NA is the lens numerical aperture[168]. Other resolution criteria that are commonly used differ by a multiplicative factor from the Rayleigh criterion.

The Sparrow criterion is defined as the distance between the PSFs, relative to the two point sources, for which the intensity distribution has no curvature in the centre [169], [170] and the multiplicative factor is equal to 0.47.

Approaching the resolution definition from a different perspective, the Abbe resolution limit is the largest diffraction grating pitch that cannot be detected by the optical system [171], and the multiplicative factor is equal to 0.5. The Abbe criterion is, therefore, related to objects that have a spatial frequency spectrum with an infinitely small single peak, whilst the Rayleigh and the Sparrow criteria are relative to objects with an infinitely small object in the space domain.

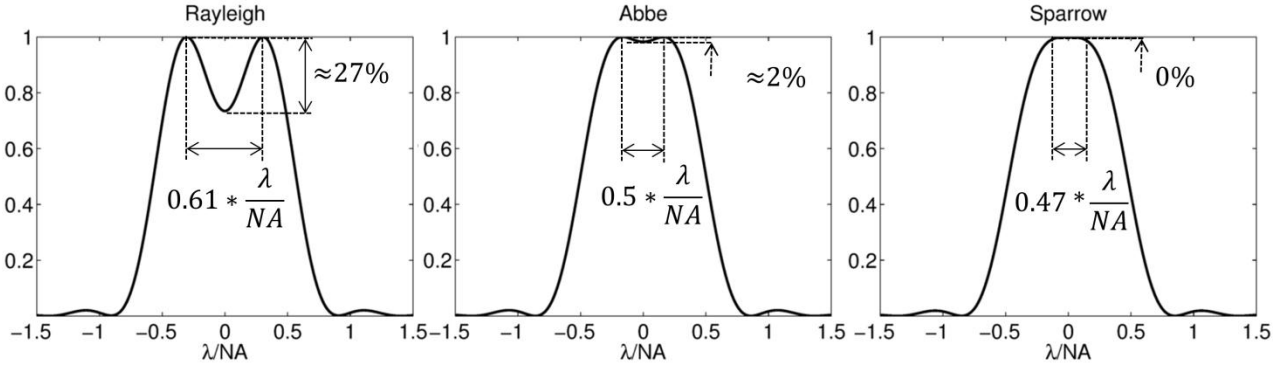

Figure 5.9. Adjacent PSF separated by a distance equal to the Rayleigh (left), Abbe (centre), Sparrow (right), resolution criteria.

Each resolution criterion can also be described in terms of intensity contrast: for incoherent light, an intensity contrast of $\approx$ 27 %, $\approx$ 2 %, $\approx$ 0 %, respectively, for Rayleigh, Abbe and Sparrow criteria is observed when imaging two infinitesimally small object (see figure 5.9).

For coherent illumination, the two adjacent points have equal phase, thereby leading to different results when summing the field from the two point sources. It is not possible to define the Rayleigh criterion in the coherent case because it is not possible to distinguish the two point sources in the intensity map. For the Abbe and Sparrow criteria, the multiplicative factors in the coherent case are, respectively, 1 and 0.73 [172].

A more complete description of the response of an imaging system can be obtained by characterising the instrument response in the Fourier domain, *i.e.* measuring the modulation transfer function (MTF). Figure 5.10 provides an example of an ideal MTF for incoherent illumination and a uniformly illuminated circular pupil. The resolution criteria explained above are samples of this curve. The MTF describes how an optical system modifies the amplitude of a

sinusoid of a given spatial frequency. The overall shape of the MTF depends on several factors, for example, coherence of the light, apodisation of the pupil function and quality of the optics [169], [170].

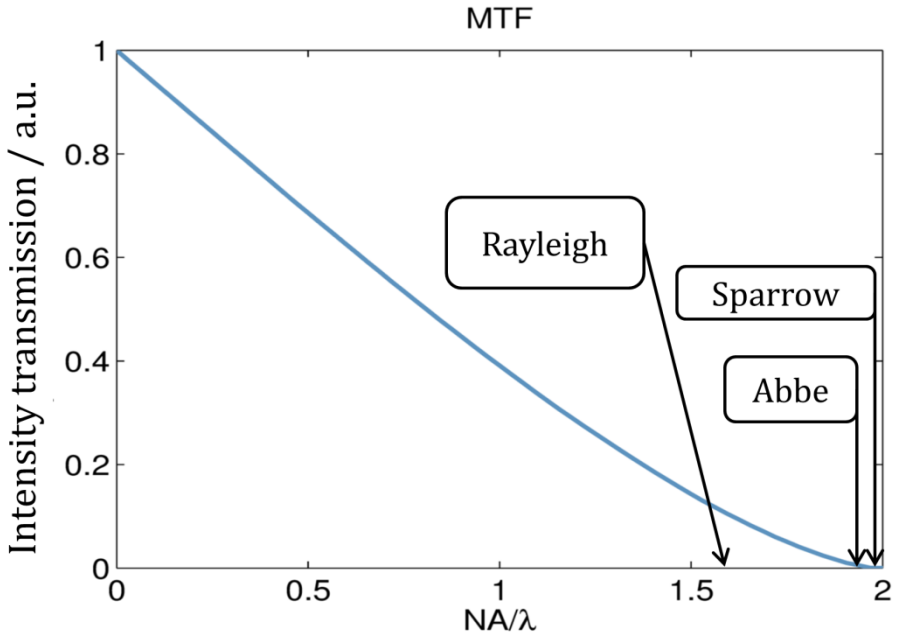

Figure 5.10. Example of optical MTF with highlighted resolution criteria.

The digression above is applicable to an imaging system, where the intensity of the light has to be measured. However, for optical interferometers, the desired information is not in the light intensity or amplitude, but in the phase. Therefore, a more general optical transfer function (OTF) can be defined, the values of which are complex: the modulus of the OTF is also called the MTF, and defines how much the phase variation due to a sinusoidal surface of a given spatial frequency is attenuated by the optical system[172]. The phase of the OTF, called the phase transfer function (PTF), describes the phase modification introduced by the optics when collecting light that is diffracted from a sinusoidal surface of a given spatial frequency.

The OTF describes the correlation between the lateral and vertical resolution of the instrument. The resolution limitation can be formalised in terms of an uncertainty product [173], [174]:

$$\delta x \, \delta z = constant \tag{5.2.2}$$

i.e. the product of the lateral resolvable distance (δx) and the vertical uncertainty (δz) is equal to a constant, the value of which depends on the instrument. Therefore, it is possible to trade-off some lateral resolution to acquire the distance z with less uncertainty. A practical example of the trade-off is a common practice by the instrument manufacturer, in which the instrument's z uncertainty is determined by measuring a step height [139]. The value of the specified

uncertainty when measuring a step height corresponds to the case in which all the lateral resolvable distance is traded in favour of the vertical uncertainty. Therefore the stated vertical uncertainty does not give any useful information when measuring a surface with a different spatial frequency spectrum. In order to describe the relationship between the vertical uncertainty and the lateral resolution the OTF is a more appropriate tool.

The OTF describes the instrument's response to each surface spatial frequency when the measurement can be considered a linear filtering process. Under the assumption of linearity, the surface can be decomposed into the sum of its Fourier components. Each component is attenuated and shifted according to the value of the modulus and phase of the OTF at that specific spatial frequency. The measured surface is finally a sum of the instrument response to all the surface spatial frequencies.

However, in general, the imaging cannot be considered a linear filtering process. For example, discontinuous surfaces, high slopes, and multiple reflections invalidate the linearity assumption and errors are introduced in the measurement[88].

Under restrictive assumptions on the surface, the measurement can be approximated as a linear filtering process [175]–[178]. The assumptions are as follows:

- surface heights are smaller than a quarter of the wavelength;
- surface varies slowly;
- objective lens has a low NA;
- object reflection angle is independent from the wavelength;
- there is no multiple scattering;
- field measured in the far-field;
- system is fully coherent or incoherent.

Under these assumptions, the filtering process can be considered linear and a measurement of the OTF is possible.

Knowledge of the instrument's OTF allows measurement improvements: it is possible to measure the OTF for a CSI with a spherical reference artefact, and the information obtained can be used to correct the fringe pattern before calculating the surface heights in order to reduce the measurement uncertainty [92], [179], [180]. However, it has been argued that a spherical object is not enough for a complete measurement of the OTF, but at least two spherical objects or two measurements of a rotated oblate spheroid are needed [181].

A schematic of the measurement process is shown in figure 5.11. The light scattered from the surface is collected by the optical system to create an image on the camera. As described

previously, the optical performance can be described by the MTF of the instrument when the image is an intensity distribution, or by the instrument's OTF when measuring the phase of the wavefront. The analogue signal is digitised into the pixel space of the CCD camera. This digitisation step might affect the system lateral resolvable distance and the vertical uncertainty. Finally, an algorithm retrieves the surface heights from the recorded interference signal digital value.

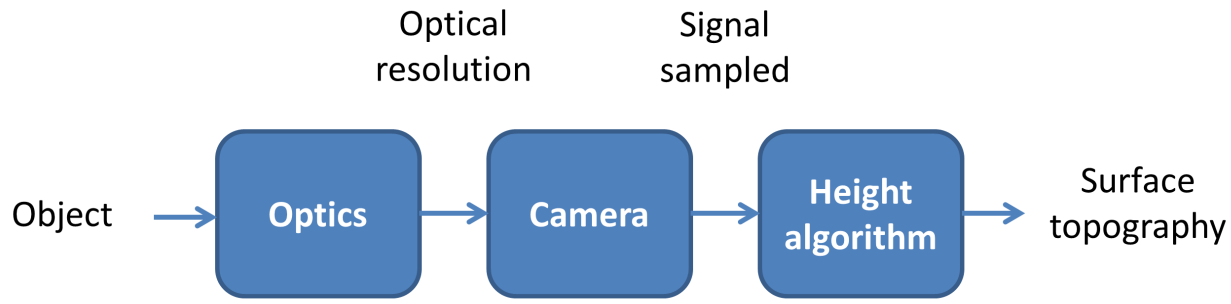

Figure 5.11: Schematics of the measurement steps in an interferometer. The optical and camera setup, affects lateral and vertical resolution, whilst the algorithm employed to retrieve the surface height affects only the vertical resolution.

In the following sections, the theoretical best achievable MTF is calculated by combining the effect of the optics and the CCD camera. The method used to estimate the lateral resolution is described and the results are reported.

5.2.2 2D resolution

The MTF for a diffraction-limited incoherent optical system with a circular pupil function can be determined analytically as the autocorrelation of the pupil function[178]:

$$H(\nu) = \begin{cases} \frac{2}{\pi}\left(\arccos(\nu) - \nu\sqrt{1-(\nu)^2}\right) & for\ \nu < \frac{2\,NA}{\lambda} \\ 0 & otherwise \end{cases} \tag{5.2.3}$$

where λ is the light wavelength, NA is the objective's numerical aperture and ν is the normalised spatial frequency. This function is shown in figure 5.10, with the indicative position of the spatial frequency specified by the different resolution criteria mentioned in section 5.2.1.

The camera digitization affects the signal spatially and introduces noise. The intensity value is electronically recorded and quantised; as a result, noise (quantisation and electronic) is introduced. Spatially, the intensity distribution on the sensor is sampled and averaged. A continuous intensity distribution $I(x,y)$ is averaged in discrete locations (x_i, y_i) according to the following equation:

$$I(x_i, y_i) = \int_{x_i-\frac{\Delta x}{2}}^{x_i+\frac{\Delta x}{2}} \int_{y_i-\frac{\Delta y}{2}}^{y_i+\frac{\Delta y}{2}} I(x,y)dxdy = \tag{5.2.4}$$

$$= \int_{-\infty}^{+\infty} \int_{-\infty}^{+\infty} I(x,y) * g(x - x_i, y - y_i) dxdy = [I \otimes g]((x_i, y_i))$$

where Δx and Δy are the pixel length in two orthogonal directions and g is the averaging pixel function. The intensity function is convolved with the averaging pixel function, corresponding to a multiplication in the Fourier domain. In conclusion, the effect of the lateral averaging of the camera is a multiplication by a transfer function equal to the Fourier transform of the pixel averaging function. Considering $\Delta x = \Delta y = d$ and a uniform averaging pixel function, the detector MTF is a sinc function with the first zero at a spatial frequency of $1/d$ (see figure 5.12).

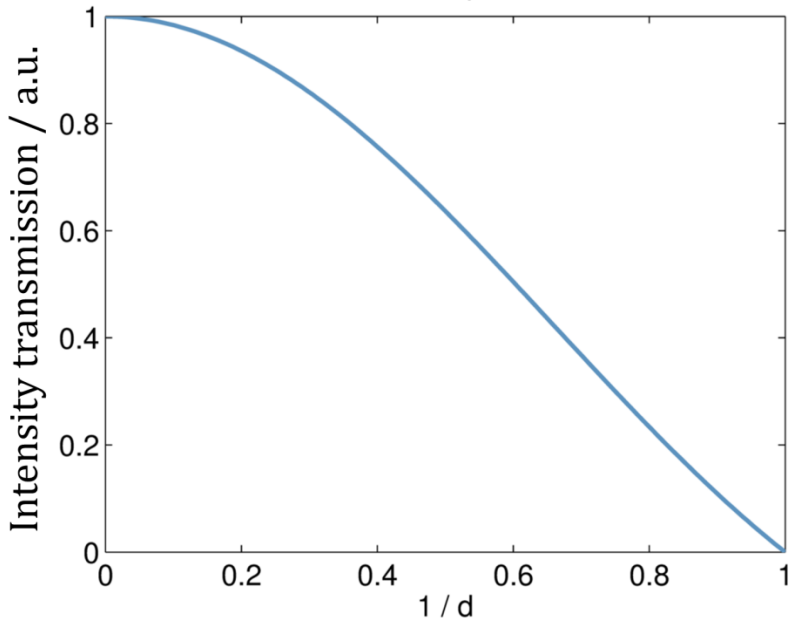

Figure 5.12. Example of detector transfer function.

The combination of the theoretical diffraction-limited MTF and the detector MTF for the 2× and 5× magnification objective lenses are shown in figure 5.13. In these cases the calculation for the optical MTF are relative to the longest wavelength used in the WSI scan, *i.e.* 0.695 µm.

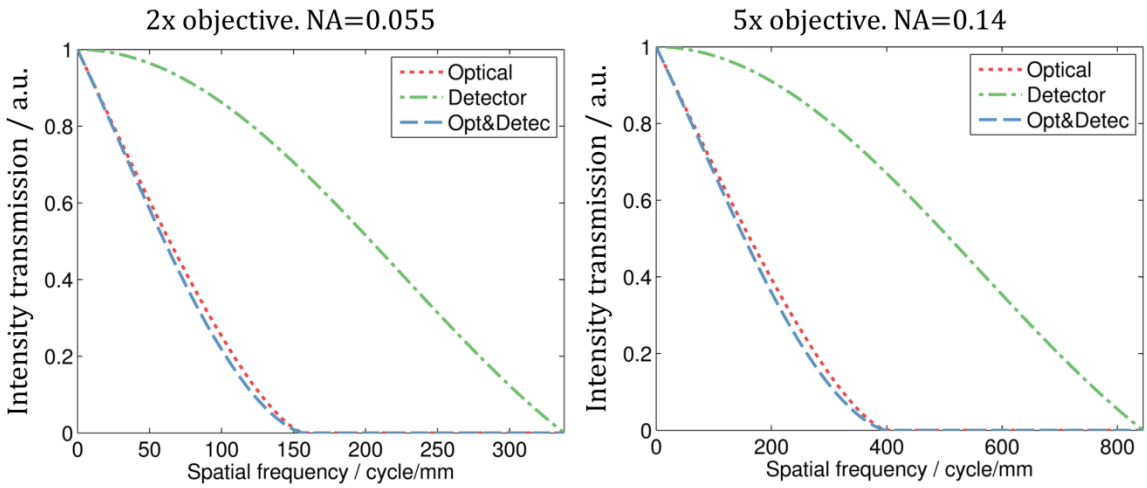

Figure 5.13. Combination of the optics and detector transfer functions. The pixel size does not affect the lateral resolution

The detector pixel size is small enough to not reduce considerably the optical MTF. Potentially an intensity image of a sinusoid with a spatial frequency up to 150 cycle/mm and 400 cycle/mm can be detected, respectively, for the 2× and 5× objective lens. These frequency values are upper bounds on the achievable surface topography resolution, since no phase can be measured if the interference signal has no intensity. The calculated MTF is the best achievable from an objective lens with no aberration. However, the WSI measures surfaces out of focus and, therefore, defocus aberration and other optical non-ideality will results in the actual MTF being different from the theoretical one.

5.2.3 Optical aberrations

The effect of defocus aberration on the OTF is known and has been modelled analytically [178]. When a focusing error is present, the centre of curvature of the spherical wavefront converging towards the image of an object point-source lies either to the left or to the right of the image plane (see figure 5.14).

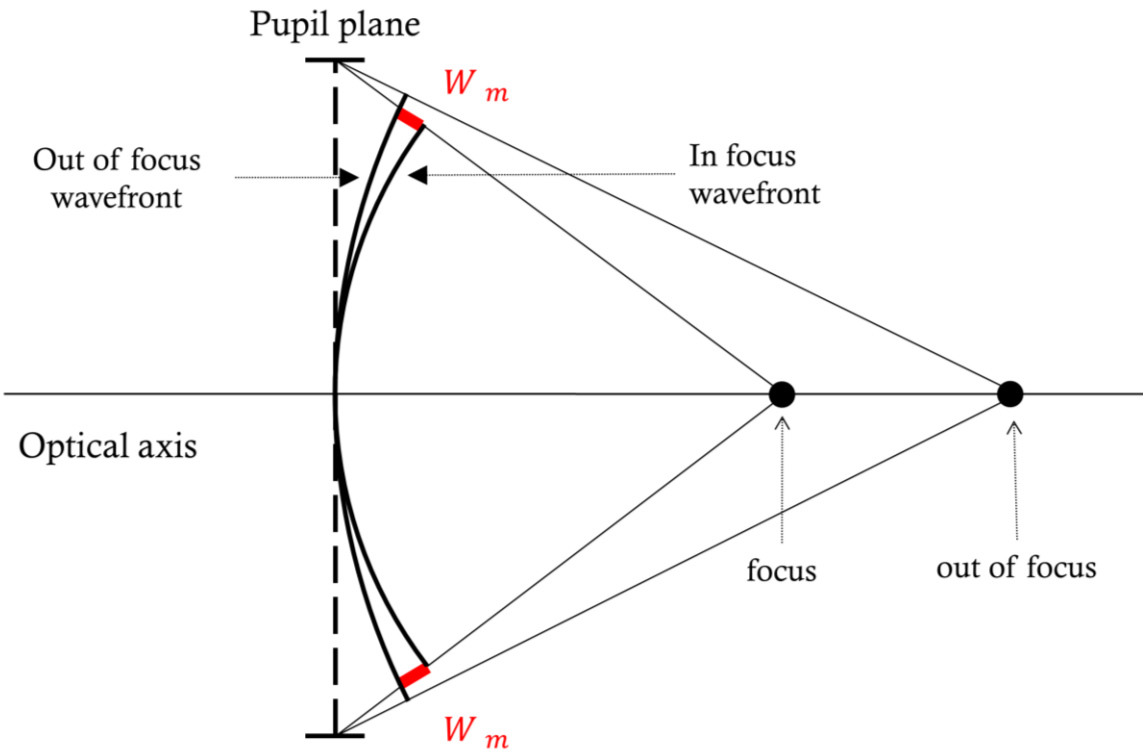

Figure 5.14. Wavefront error due to defocus aberration.

For a point on the optical axis the ideally spherical phase distribution (with the paraxial approximation) is:

$$\phi(x,y) = -\frac{k}{2z}(x^2+y^2) \tag{5.2.5}$$

where k is the wavenumber of the propagating light, z is the distance of the focal spot and x and y the orthogonal coordinates in the pupil plane. When a point-source is not at the focal spot the wavefront difference between the in-focus and out-of-focus wavefront is:

$$kW(x,y) = -\frac{k}{2}\left(\frac{1}{z_{in}}-\frac{1}{z_{out}}\right)(x^2+y^2) \tag{5.2.6}$$

which has a maximum value at the extreme of the pupil, *i.e.* when $r^2 = x^2+y^2$,where r is the pupil radius. The maximum wavefront error therefore can be written as:

$$W_m = -\frac{1}{2}\left(\frac{1}{z_{in}}-\frac{1}{z_{out}}\right)r^2 \tag{5.2.7}$$

Rewriting the wavefront error explicating the maximum value it becomes:

$$kW(x,y) = k\,W_m\frac{(x^2+y^2)}{r^2} \tag{5.2.8}$$

where W_m is the maximum wavefront error and it is used as a measure of the severity of the defocus error.

The pupil function in general can be written as an intensity of the radiating field multiplied by a factor which takes into account the wavefront distribution across the pupil:

$$P_c(x,y) = P(x,y)e^{jkW(x,y)} \tag{5.2.9}$$

For an aberration-free lens the wavefront is equal to zero across the pupil. In all cases the OTF can be calculated as the autocorrelation of the pupil function [178]. Figure 5.15c and figure 5.15d shows the MTF for different amount of defocus aberration, for two cases, uniform and Gaussian pupil intensity distribution, in figure 5.15a and figure 5.15b, respectively.

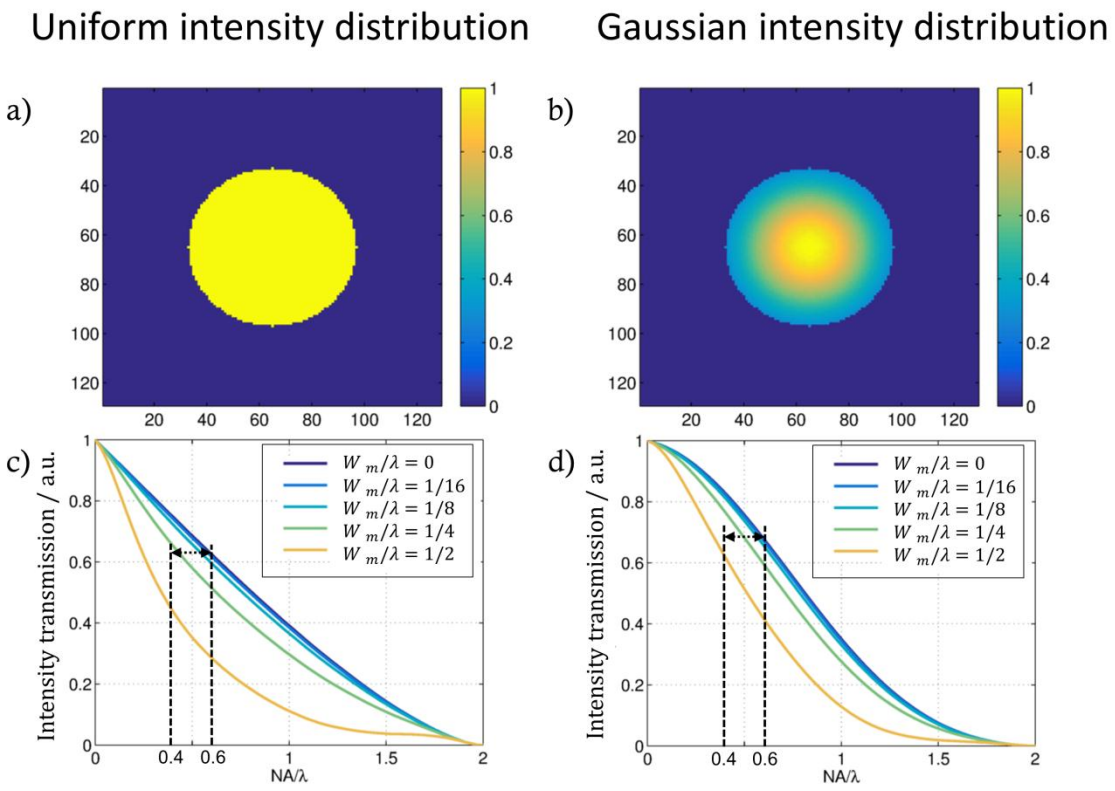

Figure 5.15. a) Uniform pupil intensity distribution and c) MTF for several amount of defocus aberration. b) Gaussian pupil intensity distribution and d) MTF for several amount of defocus aberrations. On the MTF curve the observed full width full transmission spatial frequency range has been highlighted.

The defocus aberration affects the MTF mainly in the mid-spatial frequency range. For an increasing amount of defocus the lateral resolution for a given contrast decreases. The lens depth of focus is defined as the amount of focus for which the wavefront error does not exceed a quarter of the wavelength [182]. The objective lenses used have a NA of 0.055 and 0.14, for the 2× and 5× objective, corresponding to a DOF of ±97 µm and ±15 µm, respectively. The wavefront distortion due to defocus might also introduce errors along the *z*-axis. The interference is obtained by comparing the surface wavefront from the measurement and reference arm. The reference mirror is always in focus whilst the measured surface has a variable amount of defocus depending on its position in the measurement range.

The effects of defocus aberration on height measurement with a PSI have been measured experimentally. Takuma et al [183] observe an increasing surface curvature which depends on the defocus position.

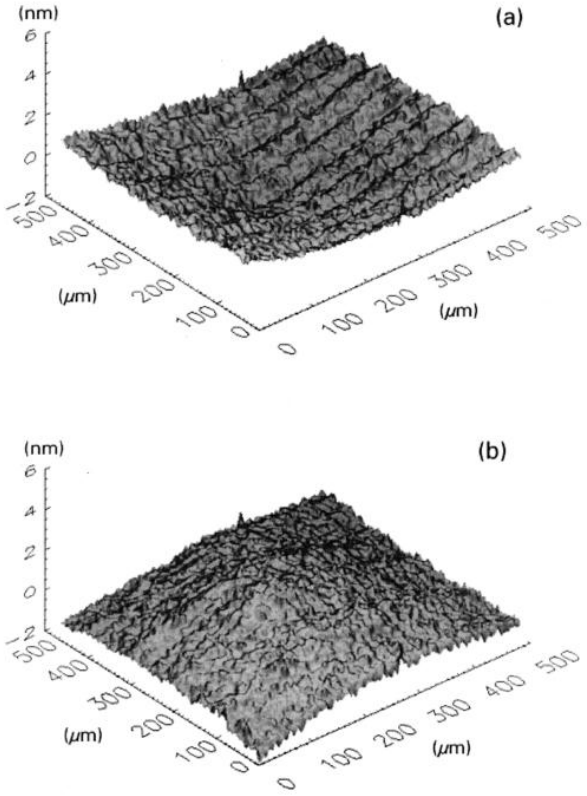

Figure 5.16. Surface shape observed in a PSI instrument at two different defocused positions corresponding to a) +35 % and b) -35% of the DOF(from[183]**).**

The surface curvature causes an error in step height measurement of 0.11 nm per fringe with an objective lens with NA equal to 0.4 and evaluated in an interval of $\pm$35 % of the objective lens depth of focus.

Such an error is two orders of magnitude smaller than the observed z-axis non-linearity as reported in section 4.1.3. The amplitude of the z-axis non-linearity errors makes difficult to observe and quantify the defocus aberration effect of the surface topography. Further work is required to reduce the noise and the z-axis non-linearity to a value smaller than the error introduced by the defocus aberration, in order to characterise and eventually correct it. For a Gaussian intensity distribution across the pupil, the lateral resolution decreases by approximately 40% from its value at the best focus.

5.2.4 3D resolution

It was discussed in section 5.2.1 that the OTF is a complete characterisation of an instrument's lateral and vertical resolution. However, the ISO standards for determining OTF of an optical measuring instrument are not yet published.

Widely accepted criteria to determine the lateral resolution are: the Rayleigh and Sparrow criteria for incoherent illumination and Sparrow for coherent illumination. ISO standard 25178 part 600[99] and Giusca et al. [147] define definitions relative to the lateral resolution such as the lateral period limit or the width full limit for full height transmission.

The instrument period limit is defined as *"the spatial period of a sinusoidal profile at which the height response of an instrument falls to 50%",* while the width full limit for full height transmission is defined as the *"width of the narrowest rectangular groove whose measured height remains unchanged by the measurement".*

In order to measure the instrument period limit, a sinusoidal surface with varying pitch can be used. This artefact is usually in the form of a chirp artefact [184]. Several measurements are required to evaluate the response as a function of the direction. On the other hand, a three-dimensional Siemens star (areal star groove (ASG) type physical measurement standard[185]) can be used to approximate the lateral period limit [147] or the limit for full height transmission. The advantage of a three-dimensional Siemens star is to provide a continuum of spatial periods in all lateral directions potentially providing good lateral resolution estimation.

To measure the modulus of the OTF, ISO standard 25178-604 suggests measuring a step height much smaller than the mean wavelength of the illumination. This suggestion is given to avoid increased sensitivity to spatial frequencies beyond the Sparrow criterion, *i.e.* to avoid spatial frequency nonlinear coupling [175]. A disadvantage of the MTF modulus measurement, as in the sinusoidal artefact, is that it only provides a unidirectional estimation of the lateral resolution.

5.2.5 Type ASG analysis

Estimation of the lateral period limit for optical instruments has been reported through measurement of ASG type artefacts [147]. To obtain the instrument response for a continuous set of spatial frequencies the Siemens star is assessed with the profile along the radial direction. Two profiles are needed for the lateral resolution evaluation: one profile from two diametrically opposed raised petals (see figure 5.17(left)) and one from two opposed lowered petals (see figure 5.17(right)). The difference between two adjacent profiles represents the measured step height for several value of lateral period (see figure 5.18(top)), also called the instrument response profile (IRP) [147]. The lateral resolution can be assessed by observing the measured height trend for increasing spatial frequency value, *i.e.* approaching the star centre. In order to evaluate the instrument period limit, the measured height and the lateral distance are scaled. The height is normalised to evaluate the position where the measured height drops by 50 %; the lateral axis is scaled by $\pi/18$, which is the scaling factor between the diameter and the groove lateral period for a Siemens Star with 36 petals.

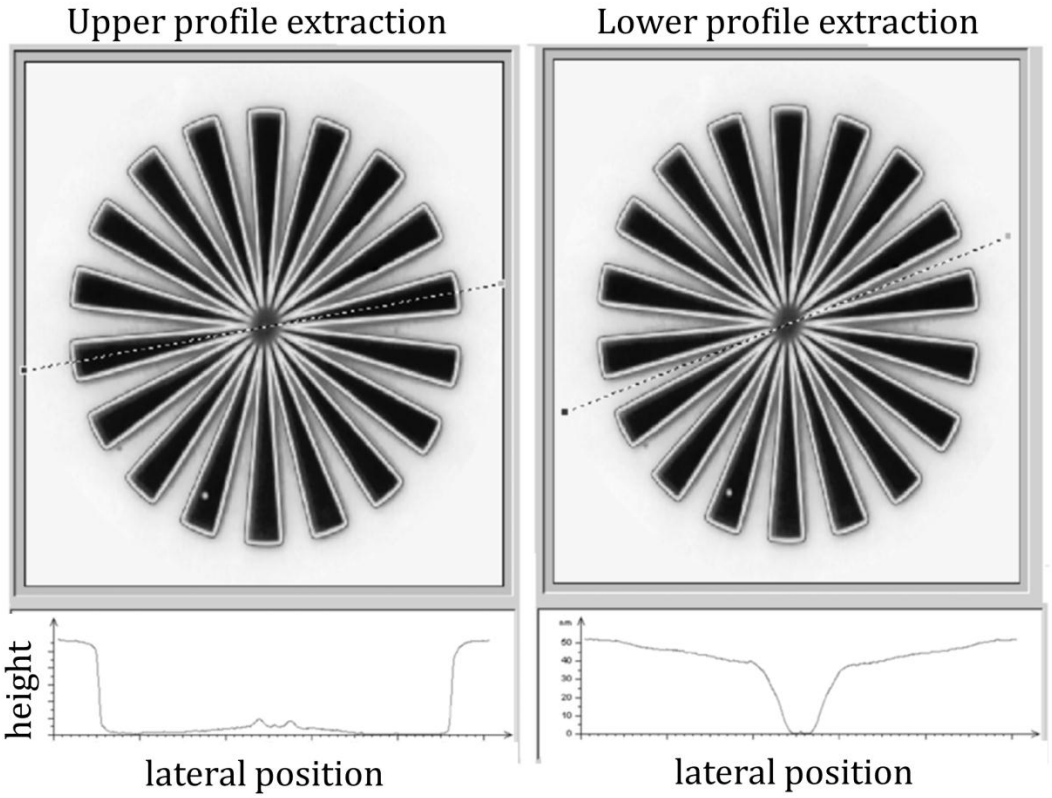

Figure 5.17. Lower petal profile extraction (left) and upper petal profile extraction (right).

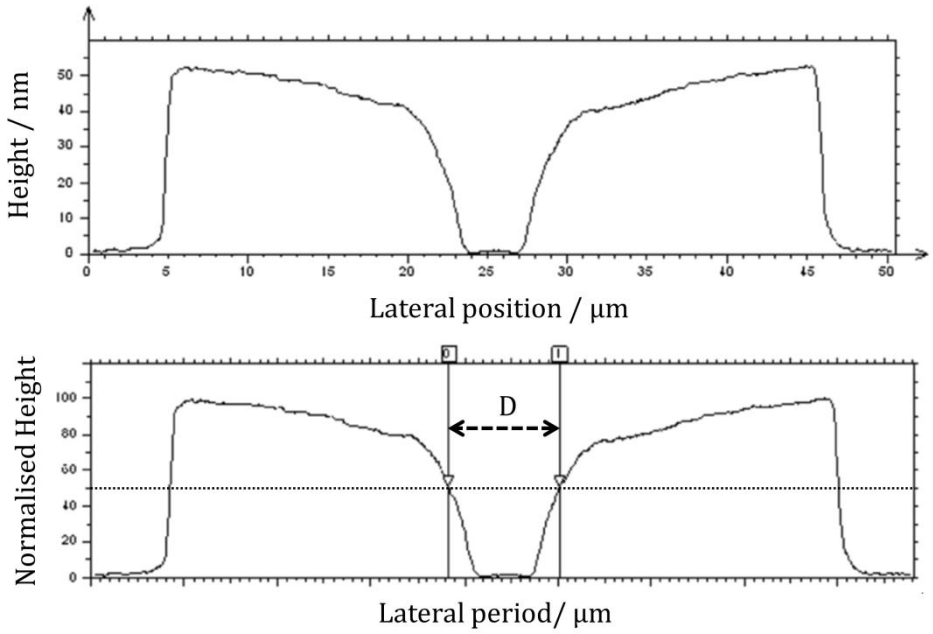

Figure 5.18: Upper and lower petal subtraction result (top). Instrument Response Profile (IRP) normalised to 100 in order to extract the 50% cut-off resolution. The lateral distance between the 50 % cut-off points is proportional to the lateral period limit D.

5.2.6 ASG Analysis for WSI

A procedure to assess the lateral resolution of the WSI instrument is hereby reported. The measured Siemens star has an inner diameter of 12 µm and an outer diameter of 230 µm, and a

nominal height of 200 nm. Therefore, the range of lateral period available in the star goes from 2.1 µm to 40 µm, or alternatively, from 476 cycle/mm to 25 cycle/mm. A height of 200 nm does not satisfy the condition for considering the measurement a linear filtering process, ($h<<\lambda$) since the illumination wavelengths are in between 589 nm and 695 nm. Optical instrument are sensitive to spurious signals coming from the top and the bottom star surface[88] and, therefore, large measurement errors are introduced at the edge of the step heights (see figure 5.19(bottom)).

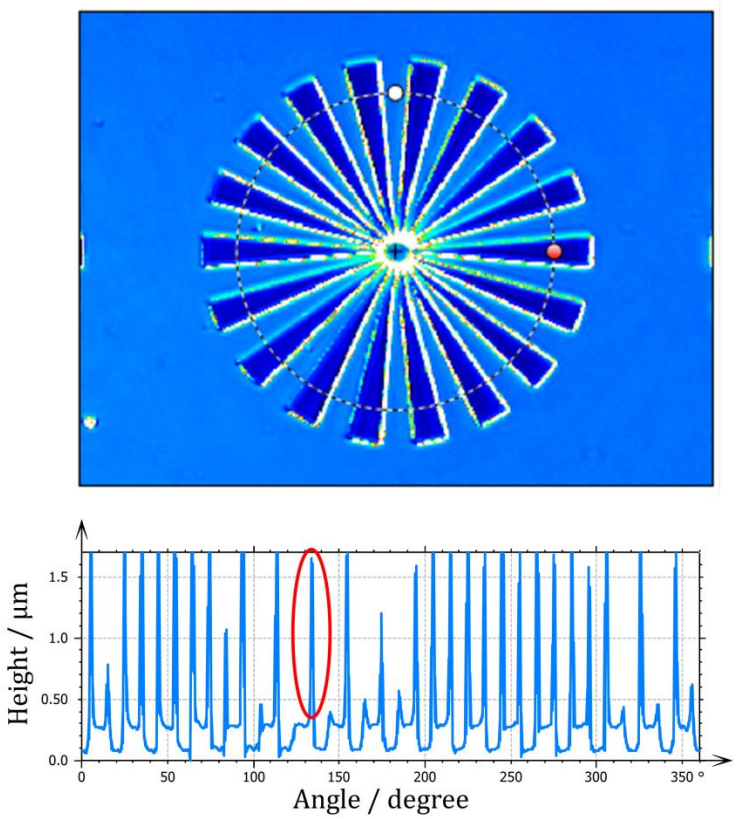

Figure 5.19: Example of ASG type artefact measurement of WSI. Top: Areal measurement. Bottom: extracted circular profile dashed in the areal measurement; note the artefacts at the step height edges (only one is marked for clarity).

The edge error becomes an important contribution when the analysis reported in section 5.2.5 is applied to the measurement. The IRP exhibits large spikes close to the apex of the star (see figure 5.20). The presence of such spikes affects the 50 % cut-off frequency estimation. Therefore, the width limit for full transmission criterion is employed. To estimate the full transmission resolution, the distance between points corresponding to a change in height greater than 10 % is measured (see figure 5.20). The 10 % condition is chosen to agree with the worst case of measurement noise for 2× and 5× objective lenses (see section 3.3) which is in between 15 to 20 nm and, therefore, approximately 10 % of the ASG height.

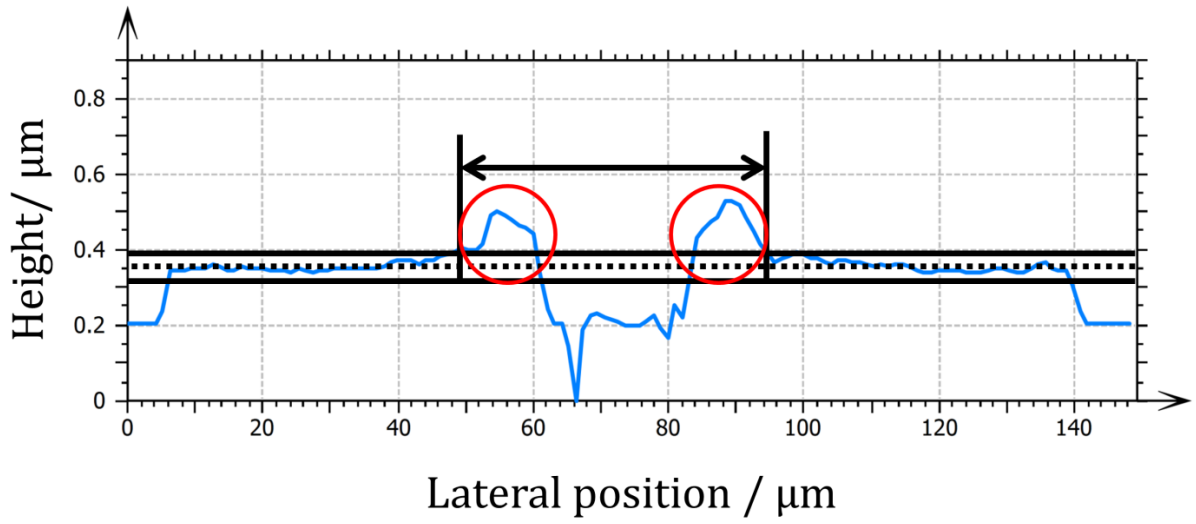

Figure 5.20. Example of ASG extracted profile on WSI. Note the spike when approaching the centre of the siemens star.

The analysis is repeated for two orthogonal directions in the lateral plane, and at five negative *z*-positions in the instrument range. The IRPs for the 5× objective lens are shown in figure 5.21 and their analysis is summarised in figure 5.22.

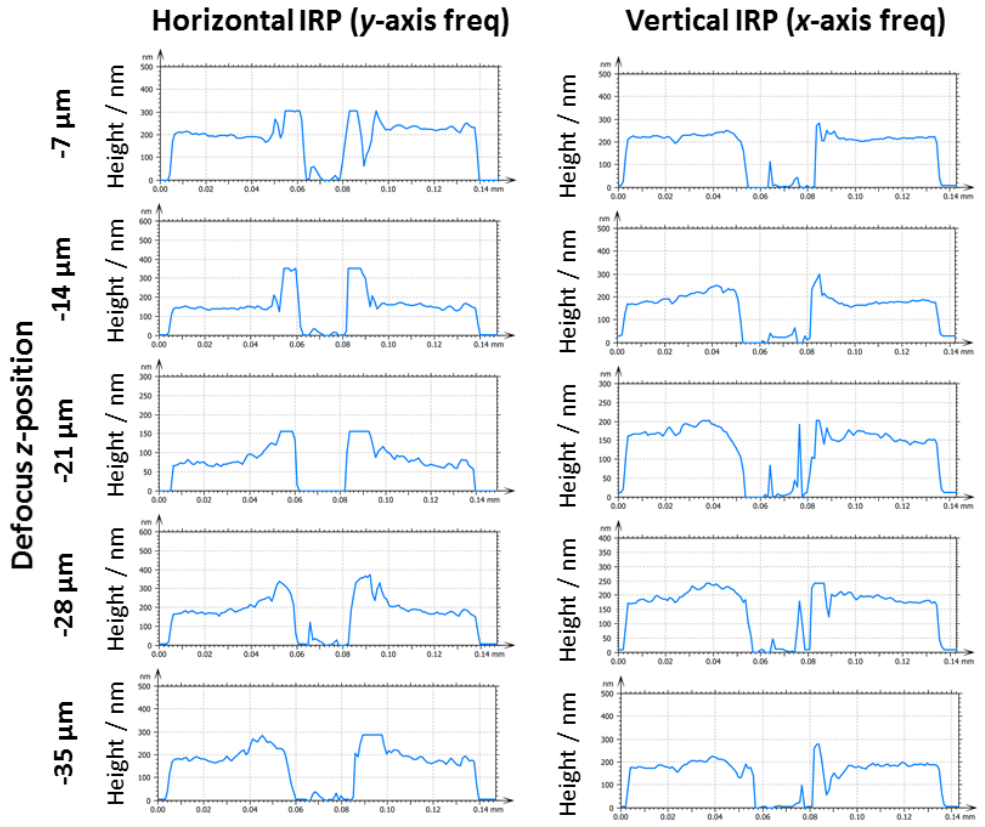

Figure 5.21. IRPs for two orthogonal directions as a function of the defocus position. Horizontal profiles are relative to the frequency along the *y*-axis and vertical profile are relative to frequency along the *x*-axis.

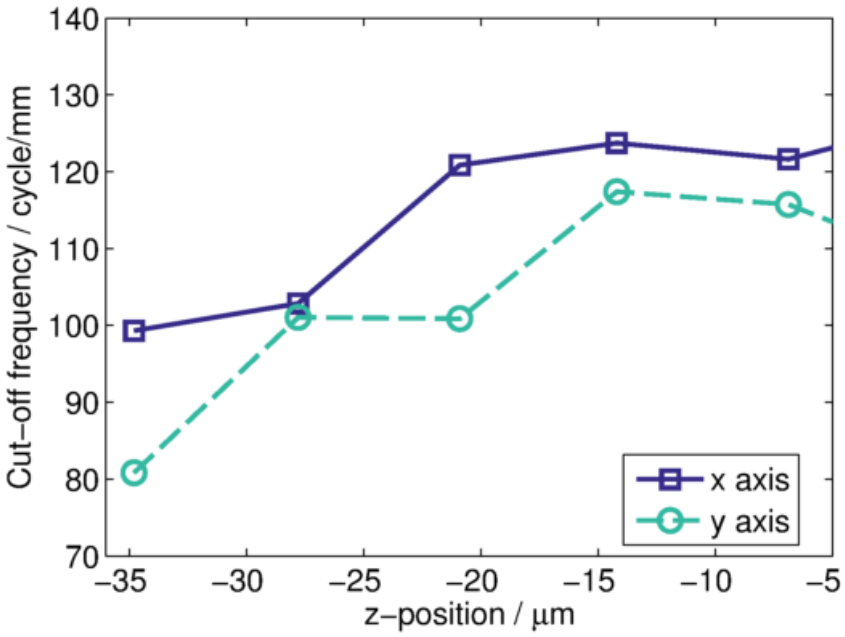

Figure 5.22: Width full limit for full transmission cut-off frequency results.

The frequency response along the two perpendicular axes is different. In particular along the *y*-axis the cut-off frequency is lower than along the *x*-axis. This effect could be due to optical aberrations which affect differently the two orthogonal directions such as astigmatism. For increasing negative *z*-position the cut-off frequency decreases due to increasing defocus aberrations. The maximum cut-off frequency is 124 cycles/mm when the measurement is taken close to the focal plane and along the *x*-axis. The minimum cut-off frequency is approximately 80 cycle/mm measured at a position farther from the focal plane along the *y*-axis.

The uncertainty in the lateral resolution estimation depends on the pixel size, the measurement noise, and the manufactured accuracy of the Siemens star. In a simple model, the length measurement uncertainty due to the pixel size is propagated in the form of a triangular distribution with a variance ${S_d}^2/6$ where S_d is the pixel size in the image space [186]. For a pixel size of 1.2 µm, the standard uncertainty in the length measurement is 0.490 µm. Therefore, the maximum resolution standard uncertainty is 0.27 cycle/mm. The estimated full width full transmission resolution estimated for the 5× objective lens has a maximum of 124 cycle/mm and a minimum of 80 cycle/mm, corresponding to a spatial frequency range from $0.6\frac{NA}{\lambda}$ to $0.4\frac{NA}{\lambda}$, respectively, calculated at the longest wavelength. In table 5.5 a comparison of the measured width full transmission period/frequency estimated is compared with the Rayleigh and Sparrow resolution criteria and the detector cut-off period/frequency.

Table 5.5. Summary of theoretical resolution criteria(Rayleigh and Sparrow) the measured width at full transmission and the pixel size for the 2× and 5× objective lenses.

Objective lens	2×		5×	
	Period µm	Frequency Cycle/mm	Period µm	Frequency Cycle/mm
Rayleigh resolution (at λ=695 nm)	7.7	130	3.0	333
Sparrow resolution (at λ=695 nm)	5.9	168	2.3	429
Estimated width full transmission	--	--	12.5 8.0	Min: 80 Max:125
Camera cut-off period/frequency	3.0	333	1.2	833

The Rayleigh criterion for the NA of the discussed objective lens for the longest wavelength employed is 3 µm, which corresponds to 333 cycles/mm which is a value three times larger than the estimated width full transmission measured. However, the Rayleigh criterion refers to an intensity image with a decreased contrast. In interferometry instruments, a phase image (rather than intensity) is evaluated, and therefore in the measurements reported a phase image without any contrast reduction is employed to evaluate the lateral resolution. Furthermore, aberrations, such as defocus and astigmatism, and other optical non-ideality might lower the resolution.

In the case of the 2× objective lens (NA=0.055) the widest Siemens star does not cover the required range of spatial frequency needed. In figure 5.23, data from the areal measurement of a Siemens star is shown at the top, while the subtraction of two horizontal profiles is shown at the bottom. Large errors are evident at the edge of the steps and profile height data is missing at the extremes of the IRP.

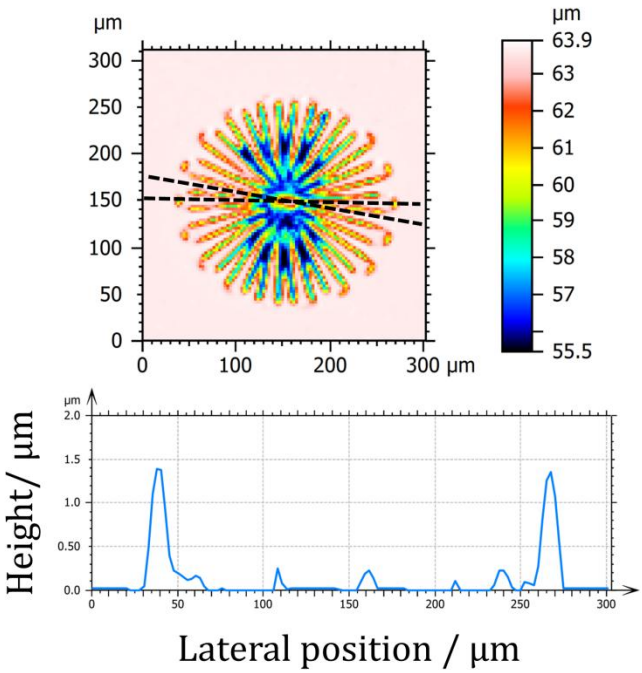

Figure 5.23. ASG type artefact measured with 2× objective lens. Top: areal measurement. Bottom: Profiles subtraction.

To estimate the lateral resolution for the 2× objective lens, a Siemens star with lower spatial frequency range is needed. The lower frequency value can be achieved in two ways: manufacture a larger Siemens star or manufacture a Siemens star with a decreased number of petals. However, such an artefact could not be obtained.

It was discussed at the beginning of section 5.2.4 that a sinusoidal artefact can be used to sample the ITF in discrete steps. However, the low NA imposes a limit of the maximum acceptable slope:

$$P_t \pi f < NA \tag{5.2.10}$$

where P_t is the sinusoidal amplitude (peak to valley), f is the spatial frequency of the sinusoid and NA is the objective numerical aperture. More than a single value of spatial frequency would be needed to extrapolate the lateral response cut-off curve. Another possibility to estimate the lateral resolution is measuring the ITF with a step height. However, to avoid the non-linearity regime, a step height smaller than 80 nm ($h<<\lambda$) with a width large enough to cover several pixels (>30 µm) has to be measured [99]. Figure 5.24 shows the measurement of an ACG surface with nominal height of 20 nm measured with the 5× objective lens, the step edge artefacts are still present. Therefore, the step edge artefacts are likely to be introduced by the algorithm which is sensitive to interference signal which is a combination of interference from the top and the bottom surface. Due to the presence of the measurement edge artefact, the step

edge response has not been explored as a possibility to measure the instrument lateral resolution.

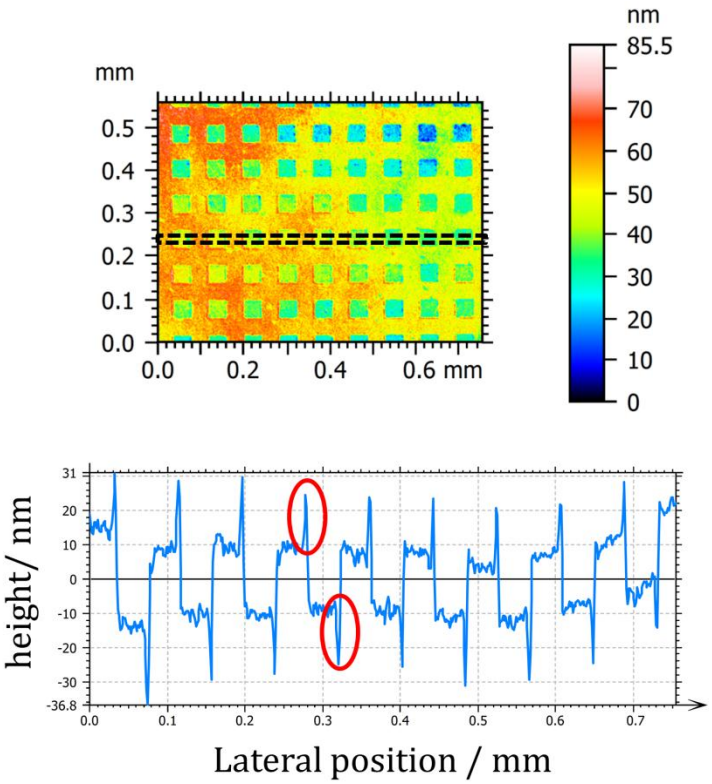

Figure 5.24. Areal measurement of ACG surface with a nominal height of 20 nm measured with 5× objective lens (top). Highlighted is the area whose profiles are vertically averaged. The resulting average profile (bottom) shows edge artefacts.

5.3 Lateral axes combined measurement uncertainty

5.3.1 Amplification and linearity

To estimate the lateral axis uncertainty the amplification and linearity deviation contribution estimated with the self-calibration method are used. The contribution of the linearity errors to the measurement uncertainty is propagated in the form of a rectangular distribution that has a variance equal to the square of the step height error value divided by three ($u_{error}^2 = \delta_{error}^2/3$). The repeatability and reproducibility are propagated in the form of a normal distribution with zero mean and variance equals to the square value of the repeatability ($u_{repeat}^2 = \delta_{repeat}^2$, $u_{reprod}^2 = \delta_{reprod}^2$). The combined effect of the measurement errors, repeatability and reproducibility on the co-ordinate measurement standard uncertainty (u_{T-z}) is given by:

$$u_{T-i} = \sqrt{u_{error}^2 + u_{repeat}^2 + u_{reprod}^2} \tag{5.3.1}$$

The results for $u_{T-\mathrm{x}}$ and u_{T-y} measurement uncertainty are shown in table 5.6 and table 5.7 for the 2× and 5× objective lens, respectively. For both objective lens the maximum $u_{T-\mathrm{i}}$ (0.73 µm

and 0.57 μm, for the 2× and the 5× objective lens, respectively) is below the theoretical optical lateral resolution (7.7 μm and 3.0 μm).

5.3.2 Perpendicularity

The perpendicularity contribution to the measurement uncertainty (u_{PER}) is propagated in the form of a rectangular distribution, with an amplitude equal to the perpendicularity error for the maximum possible length (1 nm after the linear dewarping step for both objective lenses). Therefore, the contribution is equal to 0.6 nm.

5.3.3 Lateral resolution

The lateral resolution contribution to the measurement uncertainty u_{Res} is propagated in the form of a rectangular distribution that has a variance equal to $\frac{Res^2}{3}$, where Res is the width full-limit for full transmission. For the 5× objective lens, the minimum cut-off frequency in the vertical range corresponding to the width full-limit for full transmission is 80 cycle/mm corresponding to a period of 12.5 μm. Therefore, the measurement uncertainty contribution is 7.2 μm. For the 2× objective lens the lateral resolution was not estimated, due to unavailability of artefacts covering the lateral periods of interest.

Table 5.6. Combined uncertainty relative to the top row (x-axis) and left column (y-axis) with the self-calibration method after the linear dewarping step for the 2× objective lens.

Nominal length	$u_{error} = \sqrt{\frac{\delta_{error}^2}{3}}$		u_{repeat}		u_{reprod}		u_{T-x}	u_{T-y}
	x	y	x	y	x	y	x	y
				/ µm				
100	0.11	0.16	0.32	0.32	0.105	0.098	**0.35**	**0.37**
200	0.02	0.12	0.30	0.30	0.066	0.106	**0.31**	**0.34**
300	0.12	0.01	0.28	0.29	0.59	0.074	**0.67**	**0.30**
400	0.16	0.08	0.27	0.28	0.06	0.072	**0.32**	**0.30**
500	0.20	0.20	0.26	0.26	0.031	0.0131	**0.33**	**0.33**
600	0.20	0.14	0.25	0.25	0.012	0.013	**0.32**	**0.29**
700	0.10	0.06	0.24	0.24	0.029	0.015	**0.26**	**0.25**
800	0.31	0.18	0.22	0.23	0.019	0.025	**0.39**	**0.30**
900	0.56	0.06	0.21	0.22	0.028	0.022	**0.60**	**0.23**
1000	0.57	0.50	0.20	0.21	0.023	0.007	**0.60**	**0.54**
1100	0.55	0.64	0.18	0.19	0.032	0.031	**0.58**	**0.67**
1200	0.62	0.71	0.14	0.17	0.029	0.069	**0.63**	**0.73**

Table 5.7. Combined uncertainty relative to the top row (x-axis) and left column (y-axis) with the self-calibration method after the linear dewarping step for the 5× objective lens

Nominal length	$u_{error} = \sqrt{\frac{\delta_{error}^2}{3}}$		u_{repeat}		u_{reprod}		u_{T-x}	u_{T-y}
	x	y	x	y	x	y	x	y
				/ µm				
40	0.09	0.13	0.21	0.21	0.25	0.19	**0.34**	**0.31**
80	0.10	0.04	0.23	0.24	0.13	0.18	**0.28**	**0.30**
120	0.00	0.12	0.24	0.25	0.23	0.09	**0.33**	**0.30**
160	0.01	0.20	0.24	0.27	0.08	0.07	**0.26**	**0.34**
200	0.06	0.21	0.25	0.29	0.15	0.04	**0.30**	**0.36**
240	0.08	0.31	0.26	0.30	0.16	0.08	**0.31**	**0.44**
280	0.11	0.32	0.26	0.31	0.00	0.00	**0.28**	**0.45**
320	0.25	0.36	0.26	0.33	0.18	0.01	**0.41**	**0.48**
360	0.38	0.26	0.27	0.34	0.19	0.07	**0.51**	**0.43**
400	0.15	0.35	0.27	0.35	0.13	0.06	**0.33**	**0.50**
440	0.02	0.37	0.26	0.37	0.11	0.07	**0.29**	**0.53**
480	0.06	0.41	0.24	0.39	0.13	0.05	**0.28**	**0.57**

5.3.3.1 Combined uncertainty

The combined uncertainty can be calculated according to the following equations:

$$u_x = \sqrt{{u_{T-x}}^2 + {u_{Res}}^2 + {u_{PER}}^2} \tag{5.3.2}$$

$$u_y = \sqrt{{u_{T-y}}^2 + {u_{Res}}^2 + {u_{PER}}^2} \tag{5.3.3}$$

For the 5× objective lens, the lateral axes uncertainty is dominated by the lateral resolution. The second contribution is the amplification factor and linearity deviation and, lastly, the perpendicularity contribution. The u_x and u_y standard uncertainty at the full height transmission is approximately 7.22 µm for both axes, *i.e.* the resolution dominates all other uncertainty contributions

5.4 Summary

In this chapter the calibration of the MCs relative to the WSI lateral axes are discussed and the results reported. For the amplification coefficient and linearity deviation, two methods are compared: reference grid method and the self-calibration method. The reference grid method results are potentially affected by the alignment of the two measured grids. Furthermore, the reference grid method adds the traceable contribution to the final uncertainty, which in the 2× objective lens case is one order of magnitude larger than the repeatability and reproducibility uncertainty of the measurement. On the other hand, the self-calibration removes the traceable uncertainty contribution and it is not affected by errors due to the alignment of the two grids. A dewarping algorithm is applied to correct for the lateral axes distortion, and the correction coefficient obtained with the two methods are compared. The full-width full-transmission lateral resolution is estimated by employing an ASG sample for the 5× objective. Finally the combined uncertainty associated with a measurement of lateral distance with no height contrast reduction is calculated.

6 WSI measurement dynamic range improvements

It has been shown in section 4.3 how the main contribution to the *z*-axis measurement uncertainty is given by the non-linearity introduced by the processing algorithm. In this chapter two algorithm improvements are proposed which improve the measurement performances of the WSI by reducing the *z*-axis linearity deviation and extending the range (section 6.1) or by reducing the *z*-axis linearity deviation and the measurement noise (section 6.2).

6.1 Quadrature WSI

To eliminate the *z*-position sign ambiguity, a further wavelength scanning measurement can be taken in order to obtain two interference patterns in quadrature and arrange them respectively on the real and imaginary axis to describe a complex signal. The real part can be expressed as

$$I_{real}(k) = q(k) + V(k)\cos(\pm 4\pi k z_m - 4\pi k z_r). \quad \text{with } z_r = 0 \tag{6.1.1}$$

where the position of the surface in the measurement and reference arm is expressed in distance from the objective lens focus plane (z_m and z_r). In standard WSI technique the surface position in the reference arm is taken as zero position $z_r = 0$. The imaginary part is taken in order to have the same frequency as the real part, but with a constant phase shift of π/2 (the so-called quadrature condition), thus

$$I_{imag}(k) = q(k) + V(k)\cos\left(\pm 4\pi k z_m - {}^{\pi}/_{2}\right). \tag{6.1.2}$$

The imaginary part is obtained by introducing a phase shift in the reference arm as a function of wavelength by simply shifting the reference mirror at each scan step. The condition on the amount of spatial translation of the reference mirror is

$$-4\pi k z_r = -{}^{\pi}/_{2} \tag{6.1.3}$$

Inverting equation (6.1.3) gives the amount of displacement for the reference mirror as a function of wavelength

$$z_r = {}^{1}/_{8k} \tag{6.1.4}$$

Rewriting the interference pattern as a sum of the real and imaginary parts after background subtraction and amplitude normalisation gives

$$I_{complex}(k) = \cos(\pm 4\pi k z_m) + i\cos\left(\pm 4\pi k z_m - {}^{\pi}/_{2}\right) = \cos(\pm 4\pi k z_m) + i\sin(\pm 4\pi k z_m) = e\text{^}(\pm i 4\pi k z_m). \tag{6.1.5}$$

Equation (6.1.5) describes a vector that rotates clockwise or counter-clockwise depending on whether the measured z_m is negative or positive. In the complex signal case, the phase can be

extracted directly from the recorded signal, without the need for direct and inverse Fourier transforms. Sequentially, the phase is unwrapped and a linear fit allows the phase slope to be estimated and the *z*-position to be determined as in the standard WSI algorithm.

6.1.1 Cramer-Rao bound derivation

A model has been developed to compare the performances of the *z*-height estimation through frequency or phase in the presence of additive noise. In real measurements other noise sources are present, such as multiplicative noise and phase noise. After filtering multiplicative noise can be assimilated to additive noise[64], and phase noise, such as vibration, could be filtered out by designing an appropriate phase demodulating algorithm[58]. In a stable environment and with an appropriate phase shifting algorithm, phase noise can be minimised and therefore the minimum achievable variance in the estimation is set by the additive noise.

In the measurement, the surface *z*-height should be estimated from *N* observations (samples) of the interference pattern. The observational model perturbed by an additive random effect is given by:

$$I_n(\boldsymbol{\alpha}) = S_n(\boldsymbol{\alpha}) + W_n \qquad n \in [0, \dots, N-1] \tag{6.1.6}$$

where $I_n(\boldsymbol{\alpha})$ is the n^{th} observation point, *i.e.* the intensity recorded at the n^{th} wavenumber k_n, $S_n(\boldsymbol{\alpha})$ is the modelled ideal system response where $\boldsymbol{\alpha}$ is the vector of unknown parameters and W_n is a random effect. For a given set of wavenumbers $\{k_n\}_{n=0}^{N-1}$, $S_n(\boldsymbol{\alpha})$ describes an *N*-dimensional model surface in $\mathbb{R}^p$, where *p* is the number of parameters in the vector $\boldsymbol{\alpha}$ and *N* is the number of observed points. The observed data vector $I_n(\boldsymbol{\alpha})$ is the perturbed system response from the ideal response $S_n(\boldsymbol{\alpha})$, where $\boldsymbol{\alpha}$ describes the true state of the system (see figure 6.1).

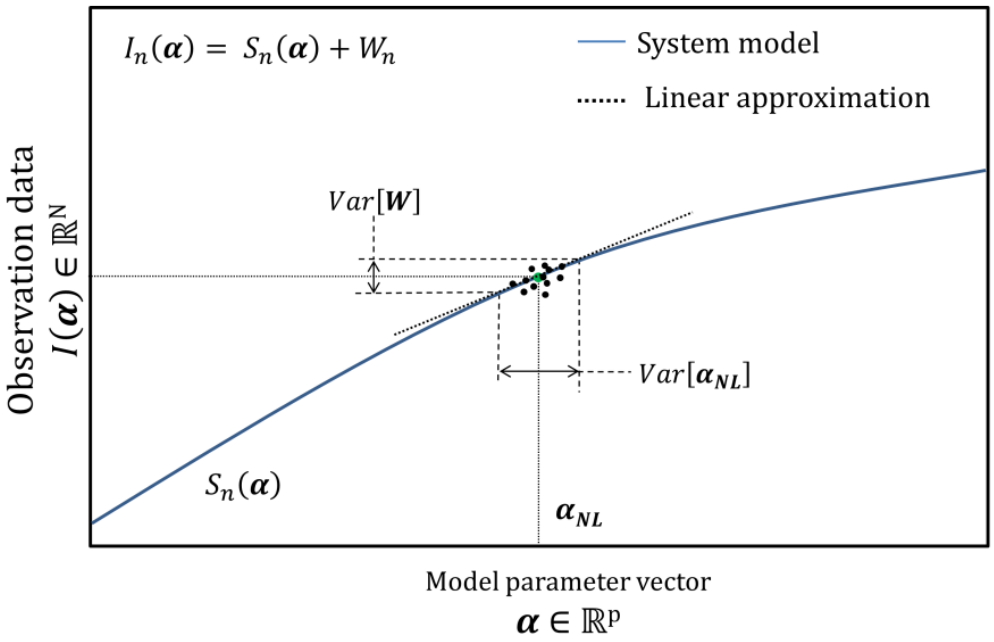

Figure 6.1. System model response and its linear approximation. The ideal fringe pattern intensities observed at N points are a function of the model parameters α to the vector of observed data $S(\alpha)$. Noise causes the observations to not be exactly at the ideal point along the system response curve, but in a point cloud around the ideal. The statistical property of the noise can be propagated to obtain the uncertainty of the model parameters.

In vectorial form, equation (6.1.6) can be written as:

$$I = S(\boldsymbol{\alpha}) + W \,. \tag{6.1.7}$$

The noise vector W is assumed zero-mean, white additive Gaussian noise and therefore its uncertainty matrix (also called covariance or dispersion matrix) is equal to $U_W = COV[W] = \sigma^2 \Im$, where $\Im$ is the identity matrix. The uncertainty matrix is a matrix whose elements in the *i,j* position is the covariance between the *i-th* and the *j-th* elements of a vector of random variables. If the system response is linear, then $S(\boldsymbol{\alpha})$ is a linear function of the parameter $\boldsymbol{\alpha}$, and the maximum-likelihood estimation method is of least-squares form [187]. Furthermore, if the estimation is unbiased, it is possible to propagate the effect of W to obtain the uncertainty matrix U_{LS} associated with the least-squares estimate $\boldsymbol{\alpha}_{LS}$. If the system response $S(\boldsymbol{\alpha})$is not linear, the estimator is not biased and the noise is sufficiently small, the problem can still be linearized around the solution $\boldsymbol{\alpha}_{LN}$ to determine an approximate uncertainty matrix U_{NL} [187]:

$$U_{NL} \approx \sigma^2 [J^T J]^{-1} \tag{6.1.8}$$

where $J$is the Jacobian matrix of the system response at the solution $\boldsymbol{\alpha_{NL}}$ defined as:

$$J_{nj} = \left. \frac{\partial S_n(\boldsymbol{\alpha})}{\partial \alpha_j} \right|_{\alpha = \alpha_{NL}} \qquad n \in [0, \ldots, N-1];\ j \in [0, \ldots, p-1] \tag{6.1.9}$$

The result of equations (6.1.8)and (6.1.9)is also known as the Cramer-Rao bound (CRB) and is a known result in the signal processing field both for real and complex tone estimation [188]. The CRB establishes a lower bound on the variance of the estimation of a deterministic parameter from measured data with additive noise [189]. For clarity, the CRB is adapted for the case in which the frequency, the amplitude and the phase are the unknown, and the *z*-height is the aim of the estimation.

For the real fringe pattern algorithm (standard WSI) the system response is

$$S_n(\boldsymbol{\alpha}) = b\cos\left(4\pi k_0 z_p + 4\pi(k_n - k_0)z_f\right) = b\cos(\varphi_n) \quad n \in [0, \dots, N-1] \qquad (6.1.10)$$

where $\boldsymbol{\alpha} = [b, z_f, z_p]^T$, is the vector of the unknown parameters, and in particular z_p and z_f are the estimated *z*-positions from the phase and frequency respectively.

Applying equation (6.1.8)and (6.1.9) and to the particular case of equation (6.1.10) gives

$$\boldsymbol{W_{WSI}} \approx \sigma^2 \begin{bmatrix} \sum_{n=0}^{N-1}[cos(\varphi_n)]^2 & '' & '' \\ \sum_{n=0}^{N-1} -4\pi(k_n - k_0)b\, cos(\varphi_n)\sin(\varphi_n) & \sum_{n=0}^{N-1}[4\pi(k_n - k_0)b\, sin(\varphi_n)]^2 & '' \\ \sum_{n=0}^{N-1} -4\pi k_0 b\, cos(\varphi_n)\sin(\varphi_n) & \sum_{n=0}^{N-1}[4\pi b\, sin(\varphi_n)]^2\,(k_n - k_0)k_0 & \sum_{n=0}^{N-1}[4\pi k_0 b\, sin(\varphi_n)]^2 \end{bmatrix}^{-1} \qquad (6.1.11)$$

where the second element on the diagonal is the variance in the *z*-position estimation from the frequency due to an additive noise perturbation with variance σ^2. Note that the CRB depends on the *z*-position to estimate from the phase φ_n. Summing the sampled value of a cosine or sine over an integer number of periods would give a lower value than summing over samples of a sinusoid with a non-integer number of periods.

For the case in which an imaginary fringe pattern is recorded (Q-WSI), the system model is

$$S(k_n, \boldsymbol{\alpha}) = b * e^{i[4\pi k_0 z_p + 4\pi(k_n - k_0)z_f]} = b * e^{i[\varphi_n]} \qquad n \in [0, \dots, N-1] \qquad (6.1.12)$$

and, therefore, the propagated variance in the parameters estimation due to a perturbation in the observed data is

$$\boldsymbol{W_{Q-WSI}} \approx \sigma^2 \begin{bmatrix} N & '' & '' \\ \mathbf{0} & \sum_{n=0}^{N-1}[4\pi(k_n - k_0)b]^2 & '' \\ \mathbf{0} & [4\pi b]^2 k_0 \sum_{n=0}^{N-1}(k_n - k_0) & (4\pi k_0 b)^2 N \end{bmatrix}^{-1} \qquad (6.1.13)$$

The variance in the *z*-position estimation from the frequency is the second diagonal element for both cases. An important difference is that, in the complex case (Q-WSI), the bound is independent from the *z*-position being estimated.

6.1.2 Signal processing simulations

In this section, simulations of the algorithm response for both the standard WSI and proposed Q-WSI method are presented. The system response is simulated with equation (6.1.11) and (6.1.13) for a given z-position. White independent Gaussian noise is added to the ideal system response in order to achieve a desired ratio between the sinusoid amplitude and the noise standard deviation ($\frac{b}{\sigma}$). For a real sinusoidal signal, the power is $\frac{b^2}{2}$, whilst for a complex sinusoidal signal, it is b^2. Therefore, the signal to noise ratio is 3dB higher in the Q-WSI case. Ten different noise patterns were generated and the root mean square (RMS) error of the estimated z-position through the frequency is calculated. For consistency in measurement time, the WSI and Q-WSI are simulated with the same total number of measured points: the WSI pattern is sampled in N points, while the Q-WSI has $N/2$ samples for the real part and $N/2$ samples for the complex part, *i.e.* the sampling density is less in the Q-WSI case. The Nyquist-Shannon theorem is satisfied in both cases.

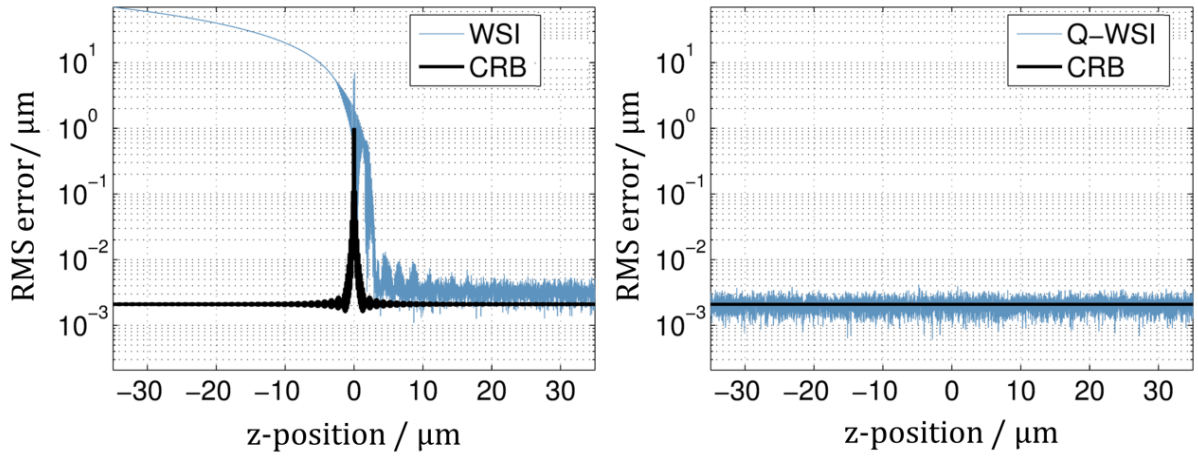

Figure 6.2: Comparison of the algorithms response with 256 total samples. Real interference pattern algorithm response with a SNR of 30dB (left), complex interference pattern algorithm response with a SNR of 33dB (right). The black line is the Cramer-Rao bound.

Figure 6.2 shows the algorithm response for the two cases in terms of the RMS error in the z-position estimation from the frequency. z-position estimation from a real interference pattern allows measurement in only half of the instrument's potential measurement range. There are periodic non-linearity in the system response with increasing amplitude closer to the zero height (zero OPD point), and there is a CRB singularity for a height of zero. This error and its minimisation is discussed in section 4.1 [190]. In contrast, the complex interference pattern algorithm is able to exploit the full vertical range of the instrument and does not show significant non-linearity.

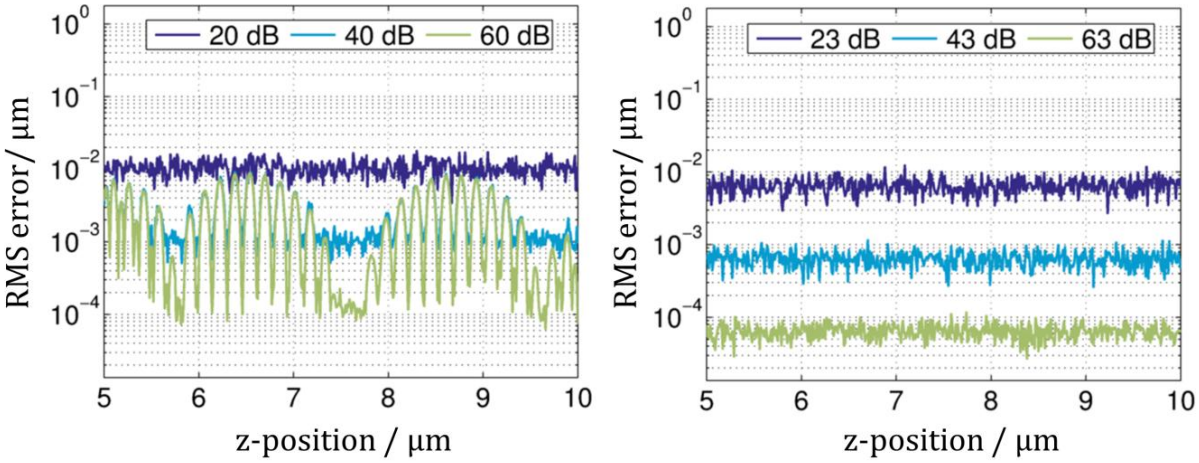

Figure 6.3: Comparison of real WSI (left) and complex Q-WSI (right) methods in terms of RMS error for a positive range of heights at three representative SNRs.

Figure 6.3 is a comparison of the two cases, in the positive *z*-position range, for several SNRs. The RMS error in the real pattern case (WSI) decreases substantially up to a SNR of 60dB. Beyond 60dB, the reduction is marginal and the algorithm non-linearity, which are already visible at 40 dB, dominate the RMS error. For the complex pattern case (Q-WSI), the RMS error reduces with the SNR without showing algorithm non-linearity.

6.1.3 Error sources

The ideal recorded interference signal is distorted due to errors such as mean offset, different real and imaginary components amplitude and lack of quadrature [191]. While in a traditional quadrature system the mean and amplitude are constant, in WSI they are a function of the wavenumber (k). In general, a more realistic interference signal is

$$I_{complex}(k) = q_{real}(k) + V_{real}(k)\cos(\pm 4\pi k z_m) + \mathrm{i}[\mathrm{q}_{imag}(\mathrm{k}) + \mathrm{V}_{imag}(\mathrm{k})\cos(\pm 4\pi k(z_m - z_r))] \quad (6.1.14)$$

where $q_{real}(k)$ and $q_{imag}(k)$ are the mean intensity function of the real and imaginary components respectively, and $V_{real}(k)$ and $\mathrm{V}_{imag}(k)$ the interference envelope functions which are both not constant. The *z*-axis actuator a calibration errors are modelled by substituting $z_r(k) = -\frac{1}{8k} + P(k)$, where $P(k)$ takes into account the lack of quadrature. Substituting in equation (6.1.14) and using trigonometric identities leads to

$$I_{complex}(k) = q_{real}(k) + V_{real}(k)\cos(\pm 4\pi k z_m) + \mathrm{i}(q_{imag}(\mathrm{k}) + V_{imag}(\mathrm{k})[\pm \sin(4\pi k z_m) cos\big(4\pi k P(k)\big) + \cos(4\pi k z_m) sin(4\pi k\, P(k))] = C(k) + i\, S(k) \quad (6.1.15)$$

where the ideal system response is obtained by assuming $q_{real}(k) = q_{imag}(k) = 0$, $V_{real}(k) = V_{imag}(k)$ and $P(k) = 0$. The relative phase is then given by

$$\Theta(k) = \mathrm{atan}\left(\frac{S(k)}{C(k)}\right) \quad (6.1.16)$$

which, in the ideal case, is perfectly linear. The phase deviates from a perfect linear distribution due to signal non-ideality (offset, envelope, and phase shift error). The distortion of the phase due to those effects can be obtained analytically with a linear approximation of the model around the ideal system response

$$\Theta(k) = \Theta_0(k) + \frac{\partial\Theta}{\partial q_{real}} q_{real}(k) + \frac{\partial\Theta}{\partial q_{imag}} q_{imag}(k) + \frac{\partial\Theta}{\partial V_{real}} V_{real}(k) + \frac{\partial\Theta}{\partial V_{imag}} V_{imag}(k) + \frac{\partial\Theta}{\partial P} P(k) \quad (6.1.17)$$

where q, V and P are functions which take into account the shape of the means, amplitude and phase errors. Analytically we can obtain

$$\Theta(k) = \pm 4\pi k h_m \mp q_{real}(k)\sin(4\pi k z_m) + q_{imag}(k)\cos(4\pi k z_m) + (V_{imag}(k) - V_{real}(k)[\pm \sin(4\pi k z_m)\cos(4\pi k z_m)] + 4\pi k P(k)\,[\cos(4\pi k z_m)]^2 \quad (6.1.18)$$

In effect, the ideal linear varying phase is distorted with added ripples. Those ripples have amplitude proportional to the expression of the means, envelopes and actuator calibration errors. The mean offset component leads to a ripple with the same frequency as the interference signal. The envelopes add a ripple with a frequency twice that of the fringe pattern frequency. Finally, the actuator phase shift error adds a ripple with twice the fringe pattern frequency and a constant bias.

Figure 6.4 shows a simulation of those errors, and compares the simulated phase ripples with the approximate model derived above. Figure 6.4a shows the case for a constant background of 30% the fringe visibility with a quadratic drop to zero towards the signal edges, the maximum amplitude of the phase ripple is 0.433 radians (see figure 6.4b). For a signal with a different envelope (20% amplitude difference with quadratic drop towards the edge and a maximum shifted by 0.05 μm^{-1} in figure 6.4c), the maximum phase error is 0.238 radian and reaches zero when the envelope amplitude is the same (see figure 6.4d). For the actuator phase shifting error, a constant offset error of 10 nm and a linear error of 10% are simulated (see figure 6.4e). The phase ripple has maximum amplitude of 0.225 radians (see figure 6.4f). For all the cases,

the simulated and the linear approximated error in equation (6.1.18) have similar shapes. These phase distortions cause a bias in the linear fitting of the phase slope if not taken into account.

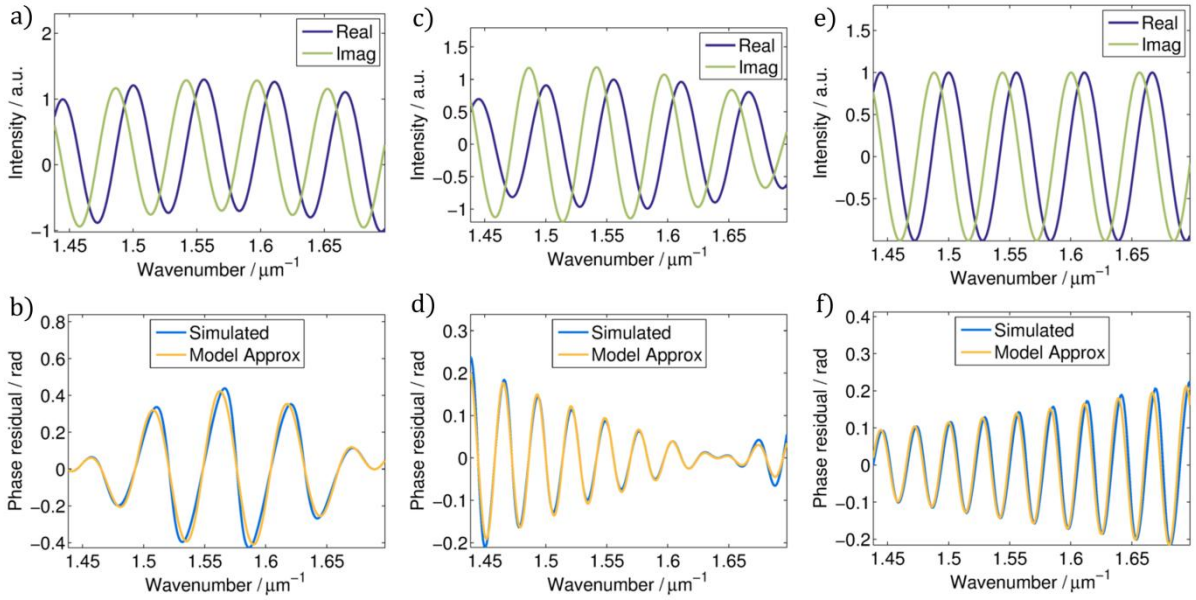

Figure 6.4: Effect of error sources in the Q-WSI method. The real and imaginary components of the interference signal are shown (a,c,e) for three cases: non-zero mean (a), different envelope amplitudes (c), and piezo phase shift error (e). The relative phase distortion from the ideal linear case is plotted (b,d,f) from the simulation and according to the approximated linear model.

6.1.4 Experimental results

Two surfaces have been measured in order to evaluate the measurement performance of the proposed Q-WSI method in a real instrument. Note that for the presented method the environmental stabilisation has been deactivated to allow controlling the reference mirror displacement. As previously discussed the main advantage of Q-WSI over the standard WSI technique is that it is able to distinguish between positive and negative *z*-positions and can estimate *z*-positions around the zero OPD point. Figure 6.5 shows the measurement of a tilted optical flat across the zero *z*-position plane by both the standard WSI and the Q-WSI methods implemented with the same hardware. The standard WSI technique begins to display significant error for heights shorter than 3 µm. In this range, the surface is not correctly measured and shows a very spiky topography where no spikes exist. The Q-WSI method can measure the *z*-positions in this range, with a relatively small residual ripple. This ripple is due to phase distortion caused by the signal non-ideality, as described in section 6.1.3.

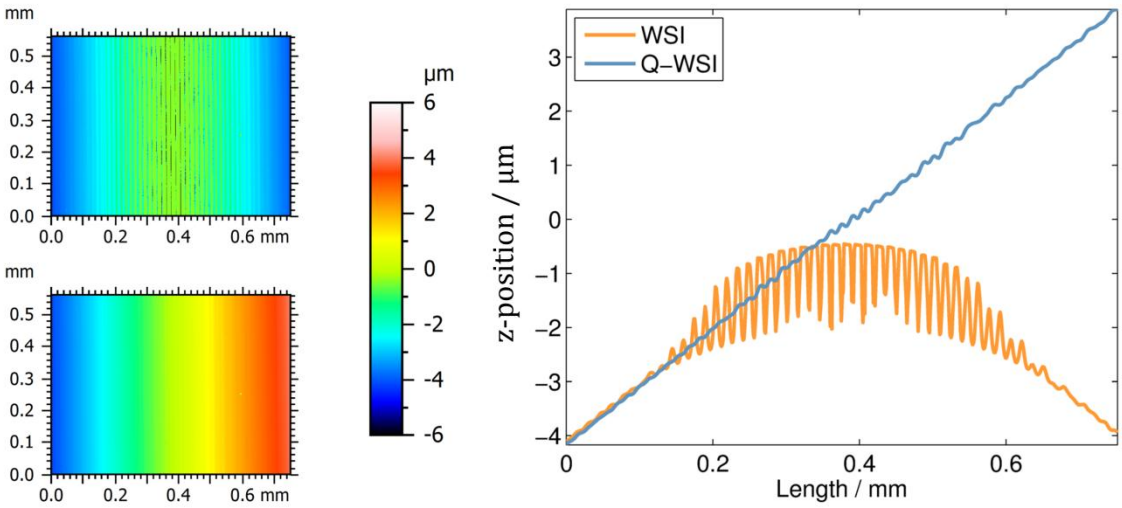

Figure 6.5: Comparison of tilted optical flat across the zero height measured with standard WSI (top left) and Q-WSI (bottom left). On the right the averaged horizontal profiles of the measurement on the left are compared.

To further show the extended range of the instrument, a step height with a nominal value of 30 µm is measured across the zero *z*-position plane. Figure 6.6 shows the surface topography measurement and the corresponding ISO-5436[162] step height calculation for both the standard WSI and Q-WSI methods. The step height is correctly measured only with the Q-WSI method since the positive height is erroneously assumed to be negative in the WSI method, leading to a measured step height of 0.7223 µm. A step height of 30 µm is measured with the Q-WSI method which is within the calibrated value given by a traceable contact stylus instrument (29.864 ± 0.116 at $k = 2$).

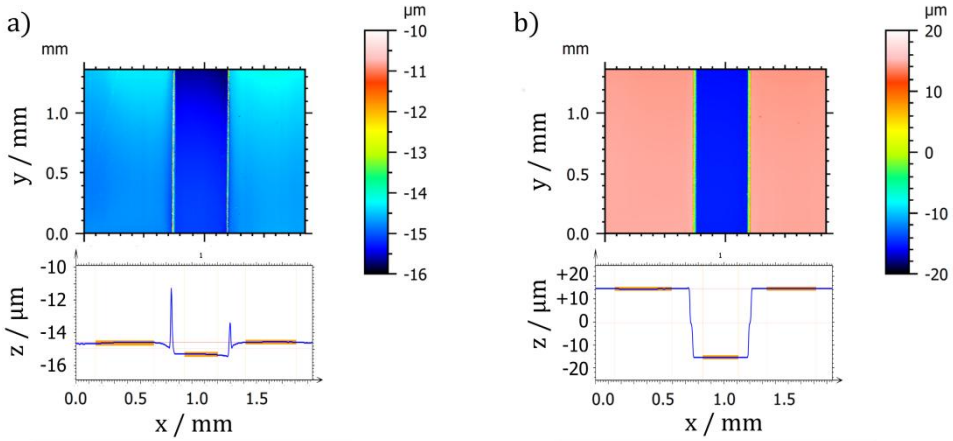

Parameters	Step 1	Unit
Width	0.2603	mm
Mean depth	0.7228	µm

Parameters	Step 1	Unit
Width	0.2778	mm
Mean depth	29.7997	µm

Figure 6.6: a) step height areal measurement (top) and ISO-5436 analysis (bottom) with the standard WSI technique. b) step height areal measurement (top) and ISO-5436 analysis (bottom) with the Q-WSI technique.

Another advantage of the Q-WSI method is to improve the vertical axis linearity. Since the phase is extracted directly from the angle on the complex signal and no Fourier transform is needed, the vertical axis error caused by spectral leakage is eliminated [190]. A tilted optical flat is measured away from the zero height in order to evaluate the algorithm non-linearity, see figure 6.7.

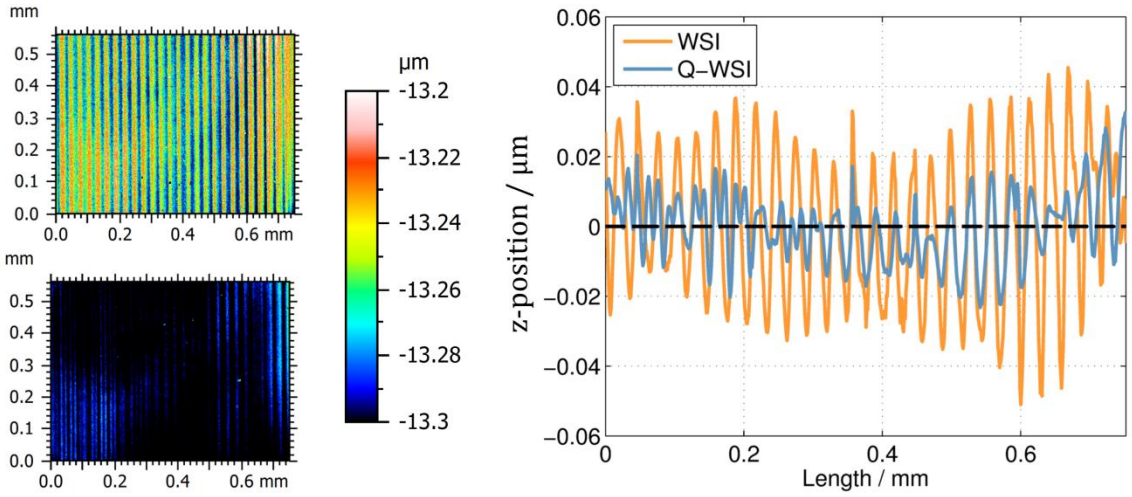

Figure 6.7: Comparison of tilted optical flat measured with standard WSI (top left) and Q-WSI (bottom left) away from the zero height position. The surfaces are levelled and plotted on the same scale to show the vertical axis non-linearity differences. A comparison of the averaged horizontal profiles of the surfaces is shown on the right.

As can be seen from Figure 6.7 the improvement is substantial: the surface root mean square roughness parameter (*Sq*) decreases from 25.9 nm to 13.5 nm compared to a calibrated value smaller than 2.6 nm. The *Sq* value is still higher than the calibrated value on the flat due to the ripple.

6.1.5 Q-WSI Summary

In conclusion, a Q-WSI method has been proposed and demonstrated experimentally. Compared to the standard WSI method, the Q-WSI method is able to exploit the whole fringe visibility range available to the WSI technique. Specifically, the method can distinguish between positive and negative *z*-positions, effectively doubling the instrument's working range. Moreover, the method is capable of measuring *z*-positions from fringe data containing less than a period, *i.e.* the short range spanning across zero OPD is now accessible. Furthermore, the method significantly reduces the non-linearity in the instrument's vertical axis due to the processing algorithm. Algorithm vertical axis non-linearity due to signal non-ideality are still evident as a small ripple and a model is proposed to account for these. However, whilst mean and envelope errors can be estimated and corrected, it has not been possible to remove the effect of the phase shift errors. The Q-WSI method also has a superior performance in the presence of additive Gaussian noise by closely approaching the CRB. The main disadvantage of the Q-WSI technique

is that some mechanical scanning is reintroduced. However, the mechanical scanning reintroduced does not affect the measurement speed. With a 5× objective lens it is possible to measure heights up to 70 μm in approximately 1.28 seconds, mainly limited by the CCD camera speed (200 fps). For comparison, a CSI measurement of surface with heights up to 70 μm, at a scan rate of 80 nm per frame and same speed camera would take 4.375 seconds. Multiple phase shifted intensity can be acquired in a single shot by employing a phase shift mask [192] or multiple cameras [193], avoiding any mechanical scan.

6.2 Phase and fringe order determination in WSI

The demodulated phase, including the effect of dispersion and phase change upon reflection, can be written as:

$$\varphi(k) = 4\pi k_0 z + 4\pi(k - k_0)z + \tau(k - k_0) + \gamma_0 \tag{6.2.1}$$

In equation (6.2.1), the first term on the right hand side is the initial phase of the fringe pattern, the second term relates to its frequency, which is proportional to the difference in the optical path between the measurement and reference arm ($2z$), the third term (τ) takes into account the dispersion difference between the interferometer arms, and γ_0 is the phase bias and/or phase change difference on reflection between the interferometer arms, present for example when the reference mirror and the sample are made of different materials. These terms are summarised schematically in figure 6.8.

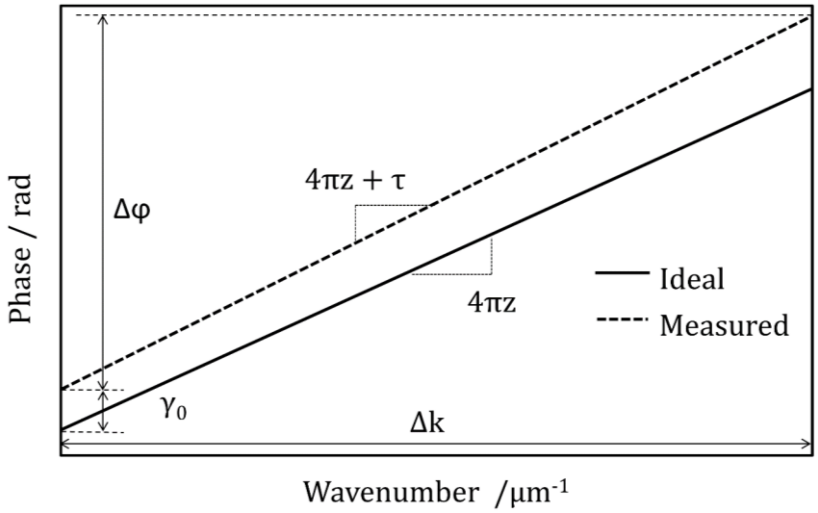

Figure 6.8. Explanatory plot of terms in the demodulated phase, Eq. (4). The measured phase differs from the ideal value due to dispersion (τ) and phase change upon reflection (γ_0).

In WSI, the absolute height measurement is usually performed through estimation of the instantaneous frequency. The instantaneous frequency is calculated by taking the derivative of equation (6.2.1):

$$z_f = \frac{1}{4\pi}\frac{d\varphi}{dk} = z + \frac{\tau}{4\pi} + \frac{\delta(z)}{4\pi} \tag{6.2.2}$$

where the estimated height z_f, is different from the "true" height z. Dispersion causes the absolute height measurement to differ from the "true" value when estimated through the frequency of the interference pattern. An additional error δ in the height estimation through the frequency is included: this error is known as "ripple error" or "fringe-bleed through"[194]. The ripple error is a consequence of the algorithm's varying performance which depends on the frequency of the processed fringe pattern [190]. This error is a function of the *z*-height and, therefore, unknown *a priori*. Assuming τ and δ are known, the estimated value of z with the corrections is:

$$\hat{z}_f = \frac{1}{4\pi}\left(\frac{d\varphi}{dk} - \tau - \delta(z)\right) \tag{6.2.3}$$

The *z*-height can also be estimated using the phase intercept. The fringe pattern phase at the initial wavenumber (k_0) is known with a 2π phase ambiguity and is shifted by the phase change upon reflection:

$$\varphi(k_0) = 4\pi k_0 z_{amb} + \gamma_0 \tag{6.2.4}$$

where z_{amb} is the ambiguous *z*-height estimated through the phase. The unambiguous *z*-height is then:

$$z_p = \frac{1}{4\pi}\frac{\varphi(k_0)}{k_0} + \frac{m}{2k_0} = z_{amb} + \frac{1}{4\pi}\frac{\gamma_0}{k_0} + \frac{m}{2k_0} = z + \frac{1}{4\pi}\frac{\gamma_0}{k_0} \tag{6.2.5}$$

where m is an integer specifying the fringe order. The phase change on reflection has the effect of adding a bias to the phase estimation. By subtracting the offset due to the phase change on reflection from the phase, if it is known, the unambiguous estimated *z*-height through the phase is:

$$\hat{z}_p = \frac{1}{4\pi k_0}\left(\varphi(k_0) + 2\pi m - \gamma_0\right) \tag{6.2.6}$$

Figure 6.9 shows a profile of a measured tilted flat both *via* the frequency and the ambiguous phase.

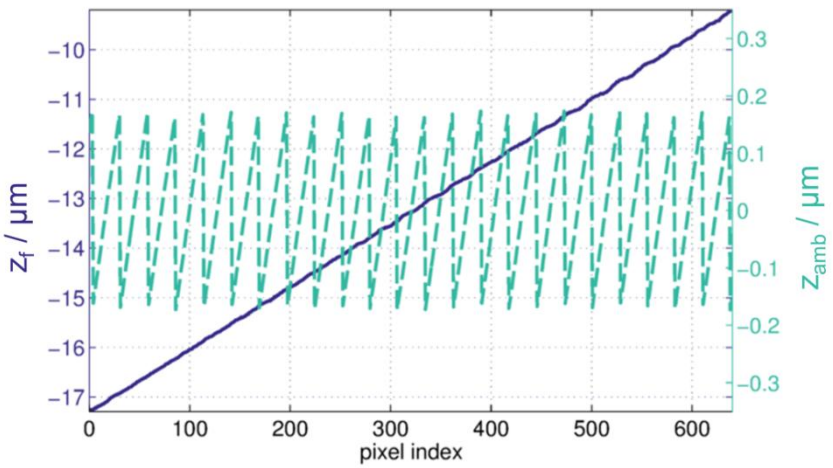

Figure 6.9. Example of tilted flat profile measurement. z_f is the unambiguous measurement via estimation of the frequency of the fringe pattern. z_{amb} is the ambiguous profile measurement via estimation of the phase of the fringe pattern.

The fringe order can be recovered from the unambiguous z_f, thus

$$m = Round[h'] = Round\left[\left(z_f - z_p - \frac{1}{4\pi}\left(\delta(z) + \tau - \frac{\gamma_0}{k_0}\right)\right)2k_0\right] \tag{6.2.7}$$

where h' is the data used to calculate the fringe order and *Round is* a function rounding to the nearest integer. z_f forms a stair-like shape by subtracting the phase and rounding to the closest integer (see figure 6.10).

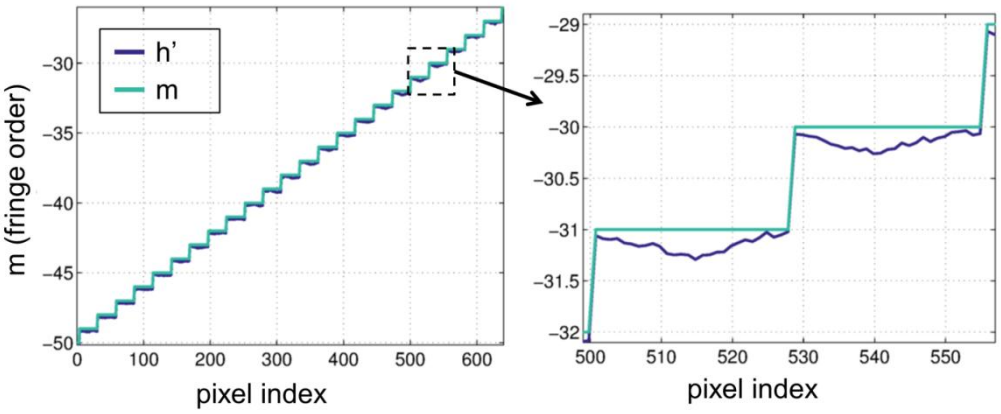

Figure 6.10. Fringe order determination. The profile h' can be employed to determine the fringe order m.

In general, δ, τ and γ_0 are not known *a priori*. $\delta(z)$ is a function of the measured displacement, and both τ and γ_0 may not be constant across the instrument's field-of-view. The fringe order can be estimated *via* equation. (6.2.7) assuming $\delta(z) = \tau = \gamma_0 = 0$. This assumption does not cause errors in the fringe order determination if the following condition is satisfied:

$$\left|\frac{1}{4\pi}\left(\delta+\tau-\frac{\gamma_0}{k_0}\right)\right|<\frac{1}{4k_0} \tag{6.2.8}$$

i.e. if the ripple plus the offsets (dispersion and phase change on reflection) are not larger than each half stair jump (see figure 6.10). This is satisfied in the WSI considered here, since the value of $\delta/4\pi$ is in the range of $\pm$40 nm, whilst the coefficients τ and γ_0 are estimated to cause an offset smaller than one fifth of the fringe order step (≈350 nm). Finally, the z_p profile can be obtained from the determined fringe order and the phase according to equation (6.2.6). The difference between the profile measured *via* estimation of the frequency and the phase can be compared by subtraction, see figure 6.11.

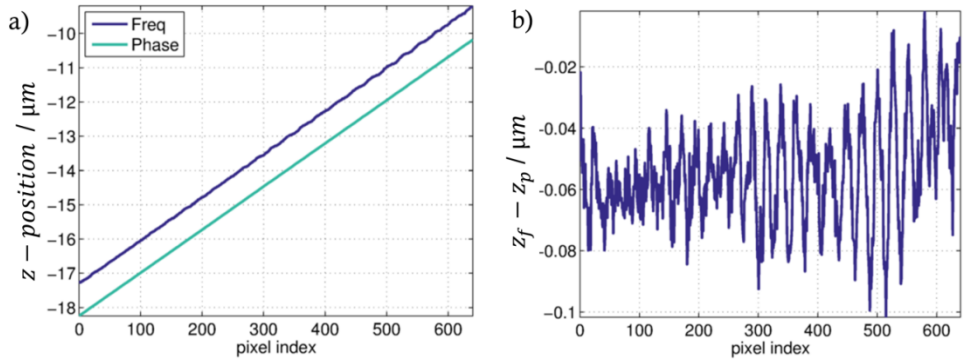

Figure 6.11. a) Tilted flat profile measured via estimation of the frequency and via the phase. An offset of 1 µm has been added for clarity. b) Difference between the two profiles.

The difference between the two profiles is equal to the difference between equation (6.2.3) and (6.2.5) and:

$$\Delta z = z_f - z_p = \frac{1}{4\pi}\left(\tau+\delta(z)-\frac{\gamma_0}{k_0}\right) \tag{6.2.9}$$

The ripple $\delta(z)$ is a major source of error in the measured profile with the standard WSI technique, *i.e.* estimation through only the frequency. The effect of ripple error on the measurement is completely removed by employing the frequency derived *z*-height only to resolve the fringe order for the ambiguous phase derived *z*-height, provided the ripple satisfies the condition specified in equation (6.2.8). Further research is required to estimate the distribution of the coefficients τ and γ_0 relative to the systematic effects of the optics of the interferometer (sometimes referred to as the phase gap analysis [83]).

6.2.1 CRB for frequency and phase

For the case in which a complex fringe pattern is recorded, the system model is:

$$S_n([b, z_f, z_p]) = be^{i[4\pi k_0 z_p + 4\pi(k_n - k_0)z_f]} \qquad n \in [0, \ldots, N-1] \tag{6.2.10}$$

where the parameter model vector $\boldsymbol{\alpha} = [b, z_f, z_p]$, *i.e.* the model unknowns are the amplitude, and two *z*-heights proportional to the frequency and phase. The propagated variance in the parameters estimation due to a perturbation in the observed data is:

$$U_{NL} \approx \sigma^2 \begin{bmatrix} c_b & 0 & 0 \\ 0 & c_f & c_{fp} \\ 0 & c_{fp} & c_p \end{bmatrix}^{-1} \tag{6.2.11}$$

where

$$c_b = N \tag{6.2.12}$$

$$c_f = (4\pi b)^2 \sum_{n=0}^{N-1} (k_n - k_0)^2 = (4\pi b)^2 N(N-1)(2N-1)\frac{\delta k^2}{6} \tag{6.2.13}$$

$$c_p = (4\pi k_0 b)^2 N \tag{6.2.14}$$

$$c_{fp} = (4\pi b)^2 k_0 \sum_{n=0}^{N-1} (k_n - k_0) = (4\pi b)^2 k_0 N(N-1)\frac{\delta k}{2} \tag{6.2.15}$$

where the substitution $k_n - k_0 = n\,\delta k$ and the formulae for the sum of the first $(N-1)$ integers and the sum of their squares have been used ($\sum_{n=0}^{N-1} n = N(N-1)/2$; $\sum_{n=0}^{N-1} n^2 = N(N-1)(2N-1)/6$). The inverse of a symmetric matrix has an analytical solution:

$$U_{NL} \approx \sigma^2 [J^\dagger J]^{-1} = \sigma^2 \frac{adj[J^\dagger J]}{\det[J^\dagger J]} \tag{6.2.16}$$

where † denote the transpose and complex conjugate operator, *adj* is the adjugate matrix of its argument and *det* the matrix determinant[195]. The adjugate matrix is the transpose of the cofactor matrix and, therefore:

$$\begin{aligned} U_{NL} \approx \sigma^2 [J^\dagger J]^{-1} &= \frac{\sigma^2}{c_b(c_p c_f - c_{fp}^2)} \begin{bmatrix} c_p c_f - c_{fp}^2 & 0 & 0 \\ 0 & c_b c_p & -c_b c_{fp} \\ 0 & -c_b c_{fp} & c_b c_f \end{bmatrix} \\ &= \sigma^2 \begin{bmatrix} d_b & 0 & 0 \\ 0 & d_f & d_{fp} \\ 0 & d_{fp} & d_p \end{bmatrix} = \sigma^2 D \end{aligned} \tag{6.2.17}$$

The elements along the diagonal of the matrix U_{NL} are the propagated variance in the estimation of the parameters in the system model vector $\boldsymbol{\alpha}$, *i.e.* the minimum achievable estimation variance in the presence of additive noise for the amplitude, the *z*-height estimated *via* the frequency and *via* the phase of the fringe pattern. Expanding the different contributions leads to:

$$c_f c_p - c_{fp}^2 = (4\pi b)^2 N(N-1)(2N-1)\frac{\delta k^2}{6}(4\pi k_0 b)^2 N - \left[(4\pi b)^2 k_0 N(N-1)\frac{\delta k}{2}\right]^2 = \frac{(4\pi b)^4}{12} N^2(N-1)(N+1)k_0^2\delta k^2. \quad (6.2.18)$$

and, therefore:

$$d_b = \frac{1}{c_b} = \frac{1}{N} \quad (6.2.19)$$

$$d_f = \frac{c_p}{c_f c_p - c_{fp}^2} = \frac{(4\pi k_0 b)^2 N}{\frac{(4\pi b)^4}{12} N^2(N-1)(N+1)k_0^2\delta k^2} = \frac{1}{(4\pi b)^2}\frac{12}{N(N-1)(N+1)\delta k^2} \approx \frac{1}{(4\pi b)^2}\frac{12}{N^3\delta k^2} = \frac{1}{(4\pi b)^2}\frac{12}{N\Delta k^2} \quad (6.2.20)$$

$$d_p = \frac{c_f}{c_f c_p - c_{fp}^2} = \frac{(4\pi b)^2 N(N-1)(2N-1)\frac{\delta k^2}{6}}{\frac{(4\pi b)^4}{12} N^2(N-1)(N+1)k_0^2\delta k^2} = \frac{1}{(4\pi b)^2}\frac{2(2N-1)}{N(N+1)k_0^2} \approx \frac{1}{(4\pi b)^2}\frac{4}{Nk_0^2} \quad (6.2.21)$$

$$d_{fp} = \frac{-c_{fp}}{c_f c_p - c_{fp}^2} = \frac{-(4\pi b)^2 k_0 N(N-1)\frac{\delta k}{2}}{\frac{(4\pi b)^4}{12} N^2(N-1)(N+1)k_0^2\delta k^2} = \frac{-6}{(4\pi b)^2 N(N+1)k_0\delta k} \approx \frac{1}{(4\pi b)^2}\frac{-6}{N^2 k_0\delta k} \quad (6.2.22)$$

where the substitution $N\,\delta k = \Delta k$ has been used, and the approximations are valid for large N. d_f and d_p are the variance in the estimation of the z-height *via* the frequency or the phase. The variance is always proportional to the inverse of the signal to noise ratio (SNR$=10\log_{10}[b^2/\sigma^2]$). The z-height estimation variance via the frequency is inversely proportional to the square of the wavenumber range ($N\delta k = \Delta k$), *i.e.* increasing the wavenumber range decreases the variance of the frequency estimation. Additionally, the phase and frequency variance is inversely proportional to the number of samples. The estimation *via* the phase is inversely proportional to the square of the wavenumber for which the phase is evaluated (k_0). In a wavelength period, the phase varies by 2π and, therefore, shorter wavelengths (larger wavenumbers) reduce the variance in the z-height estimation through the phase, as expected. For example, for a SNR of 20 dB ($b/\sigma = 10$) and 128 samples, the z-estimation CRB through the frequency for a wavenumber range of 1.66 μm^{-1} to

1.43 μm^{-1} (wavelength range from 600 nm to 700 nm) is approximately 10 nm. On the other hand, the *z*-estimation CRB through the phase for a wavenumber of 1.43 μm^{-1} and, with the same parameters as the frequency estimation, is approximately 1 nm. The ratio between the CRB through the frequency and the phase, for large *N*, is equal to:

$$\frac{d_f}{d_p} = \frac{12}{N\Delta k^2}\frac{Nk_0^2}{4} = 3\left(\frac{k_0}{\Delta k}\right)^2 \tag{6.2.23}$$

which, for the wavenumber values reported above corresponds to an improvement of the standard deviation of the *z*-height estimation of approximately ten.

For the case where *N* is equal to 2, the model agrees with the improvement discussed by de Groot [17] for Fourier analysis of CSI interferograms and it is equal to:

$$\frac{d_f}{d_p} = 2\left(\frac{k_0}{\Delta k}\right)^2 \tag{6.2.24}$$

Figure 6.12 shows the results of the simulation of the RMS error of the *z*-height estimation as a function of the number of samples and SNR from the frequency (left) and from the phase (right). The wavenumber range employed for the estimation through the frequency is 1.43 μm^{-1} to 1.70 μm^{-1} (corresponding to a wavelength range of 695.2 nm to 589.1 nm) and the estimation through the phase is for the initial wavenumber 1.43 μm^{-1}.

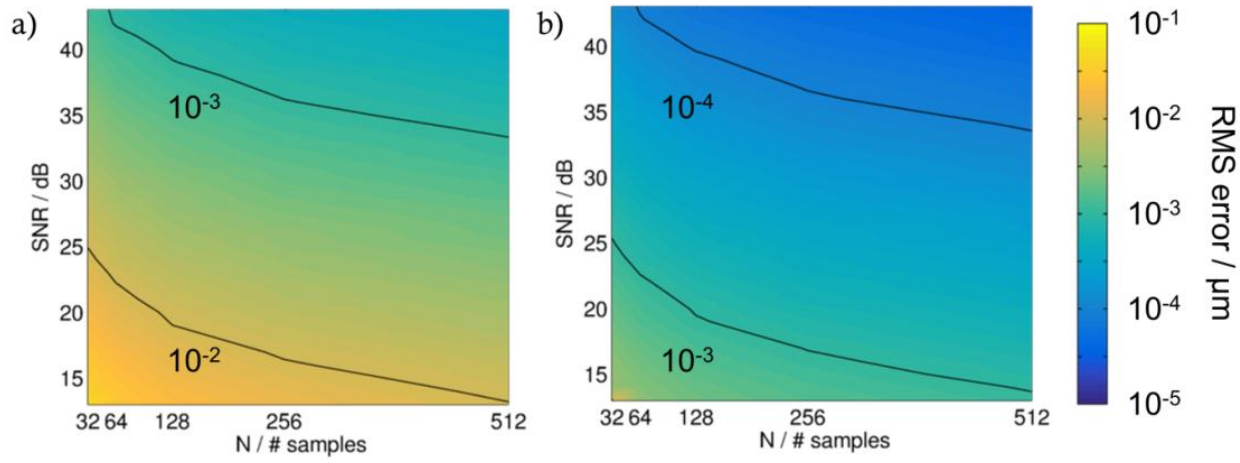

Figure 6.12. Comparison of RMS error of *z*-height estimation through the fringe pattern frequency (a) and through the phase (b) as a function of the SNR and the number of samples (N).

The improvement is approximately an order of magnitude for all cases. The RMS error reaches sub-nanometre values for every number of samples for a SNR above 25 dB, corresponding to a noise amplitude of approximately 6 % of the fringe visibility.

6.2.2 Experimental results

To evaluate the improvements achieved, comparisons using surface measurements are reported. It should be noted that in a real WSI instrument, the fringe visibility decreases when

further away from the zero OPD position and, therefore, the SNR and resulting measurement performance will vary within the instrument's measurement range. In figure 6.13 an example of measurement noise evaluated by subtraction of repeated measurements is shown on two different planes of a step height with a nominal height of 12.5 µm (*N* is equal to 256 in this case). The *Sq* surface parameter of the subtraction divided by the square root of two is an estimation the measurement noise[145]. In both cases the measurement noise is reduced by an order of magnitude. Note that no spatial filtering has been applied in both cases.

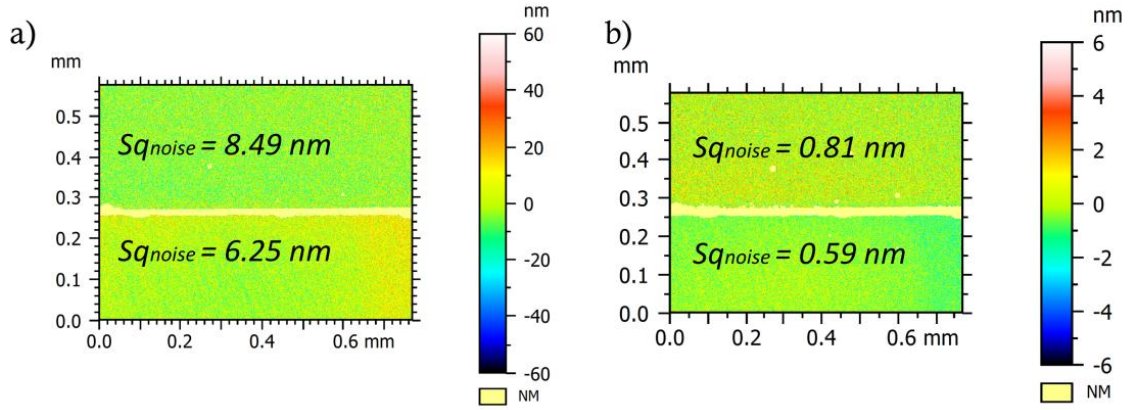

Figure 6.13. Measurement repeatability on the two planes of a 12.5 µm step height. a) Measurement noise via frequency estimation and b) measurement noise via phase estimation.

In figure 6.14 the measurement noise is shown as a function of the number of samples recorded. The noise scales as the square root of the number of samples in agreement with the model. Acquiring fewer samples allows for faster measurements but increases the value of the measurement noise. The minimum number of samples required is given in accordance to the Nyquist-Shannon theorem [154]. The measurement speed is ultimately limited by the camera frame rate. For 2 × 128 acquired samples the measurement time is 1.25 s for a 200 fps camera, allowing measurements of *z*-heights in the range ±120 µm. For comparison, a CSI fringe acquisition of the same vertical range would need to step the piezo-transducer by 71 nm per camera frame [163]; with the same camera the entire acquisition would take at least 16.9 s. For the specific implementation presented here, the measurement noise including the effect of the measurement time is 6.9 nm/$\sqrt{\text{Hz}}$ *via* frequency estimation and 0.65 nm/$\sqrt{\text{Hz}}$ *via* phase estimation, mainly limited by the power of the light source.

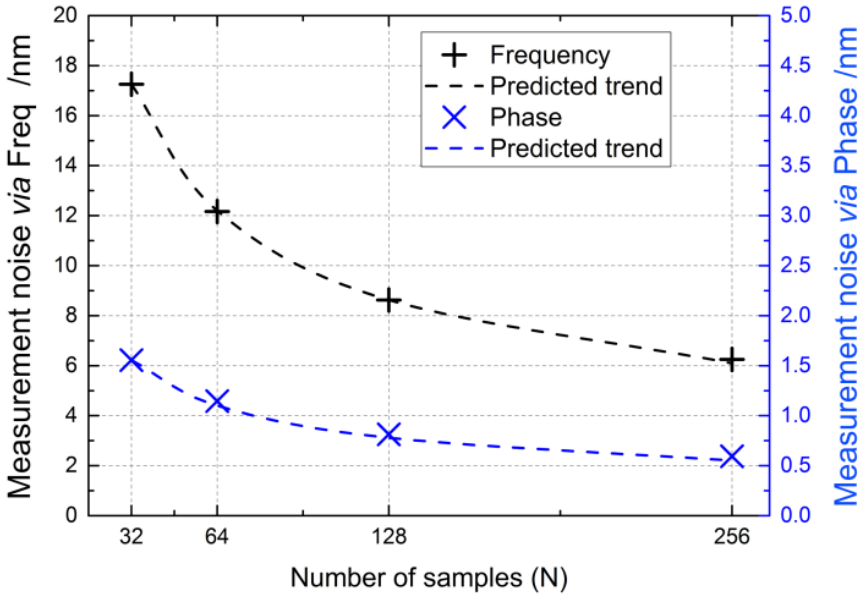

Figure 6.14. Noise as a function of samples acquired for measurement via frequency estimation, and phase estimation. In both cases the noise is compared with the square root of the number of samples acquired curve. Note the different scales for the two curves.

In figure 6.15, two measurements of an areal cross grating (type ACG) surface with a nominal height of 15 nm are compared. The improvement is clearly noticeable when comparing two profiles. The profile estimated *via* the frequency shows a higher level of noise, bias in the step height measurement and edge artefacts. The profile measured *via* the phase shows a lower level of noise, a consistent step height profile measured and minimal edge artefacts.

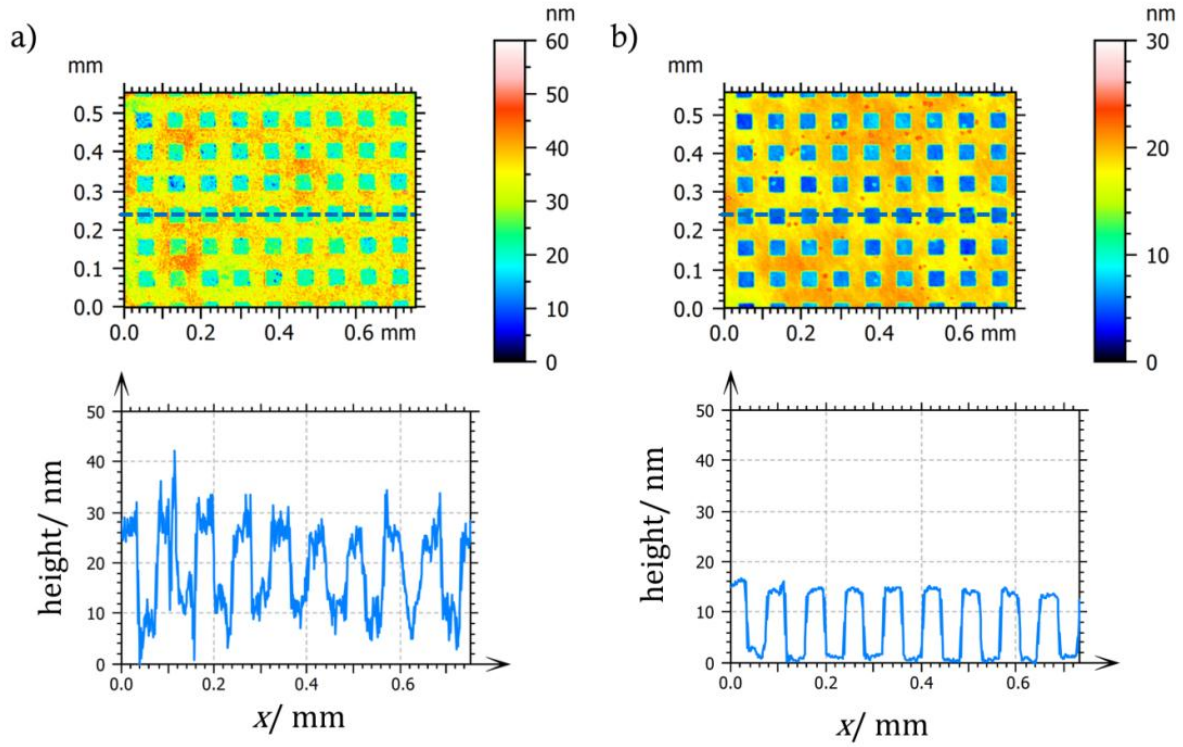

Figure 6.15. Areal surface topography measurements and extracted profiles of a 15 nm nominal type ACG surface using *z*-height estimation *via* the frequency (a) and *via* the phase (b).

The unwanted bleed-through or ripple-error [194], discussed in section 4.1 and section 6.2, is caused by bias in the frequency estimation depending on the value of the frequency to be estimated [190]. The ripple can be observed by measuring a tilted flat. The levelled surface shows ripples perpendicular to the direction of the tilt (see figure 6.16). For the measurement *via* estimation of the frequency, the ripples have an amplitude of the order of tens of nanometres ($\pm$20 nm), whilst for the phase case, the ripples are reduced by an order of magnitude ($\pm$2 nm). These axis non-linearities may be due to non-linearity in the light source wavenumber scan, and/or the phase demodulation algorithm's sensitivity to these non-uniform phase shifts.

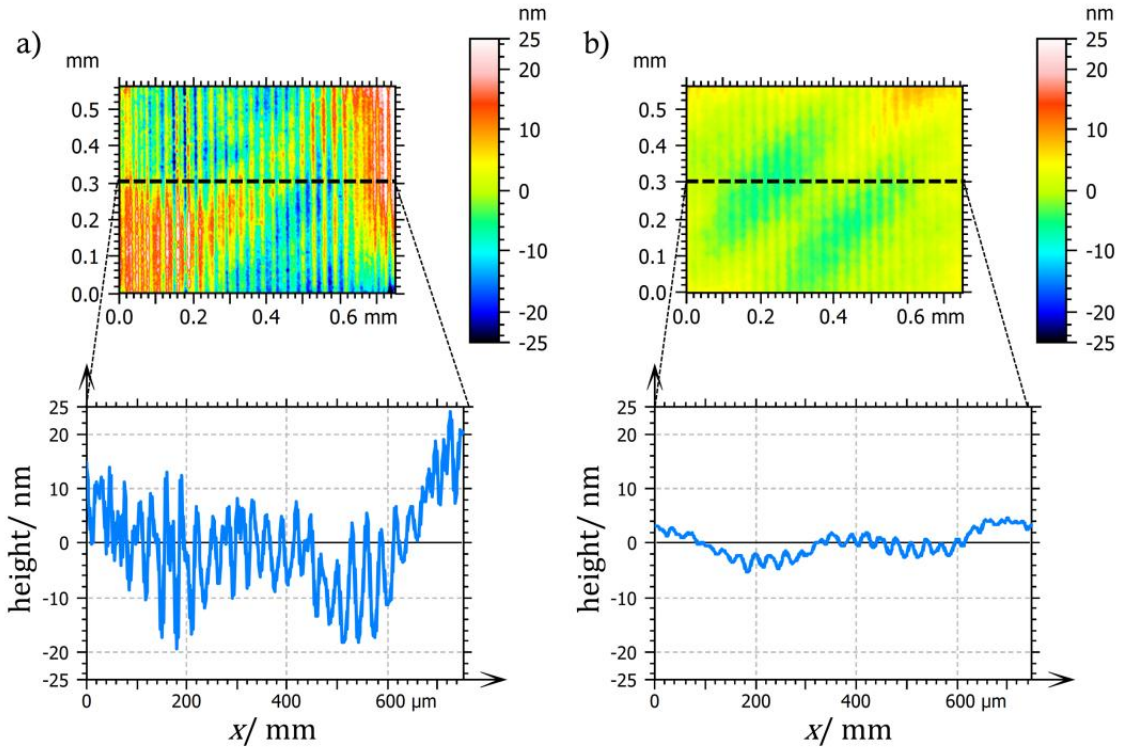

Figure 6.16. Areal surface topography measurements and extracted profiles of a calibrated tilted flat (maximum surface height *Sz* of 17.5 nm at coverage probability of 95 %) using *z*-height estimation *via* the frequency (a) and *via* the phase (b).

In figure 6.17 measurement profiles of a steel sphere obtained with the two methods are compared. The measurement *via* frequency estimation shows significant ripple errors, while the ripples are not visible using the phase method. However, for high-sloped surfaces, fringe order errors begin to appear. Fringe order determination error correction has been reported by Ghim et al. [91] for CSI and similar improvements may be possible in WSI. The erroneous fringe order determination could be attributed to surface gradient-dependent effects due to the finite objective lens numerical aperture (NA) and optical aberrations [92]. The measurements reported here are designed to show the level of improvement with the new method and they do account for all the effect on the measurement uncertainty of all the instrument's various metrological characteristics [139], [196].

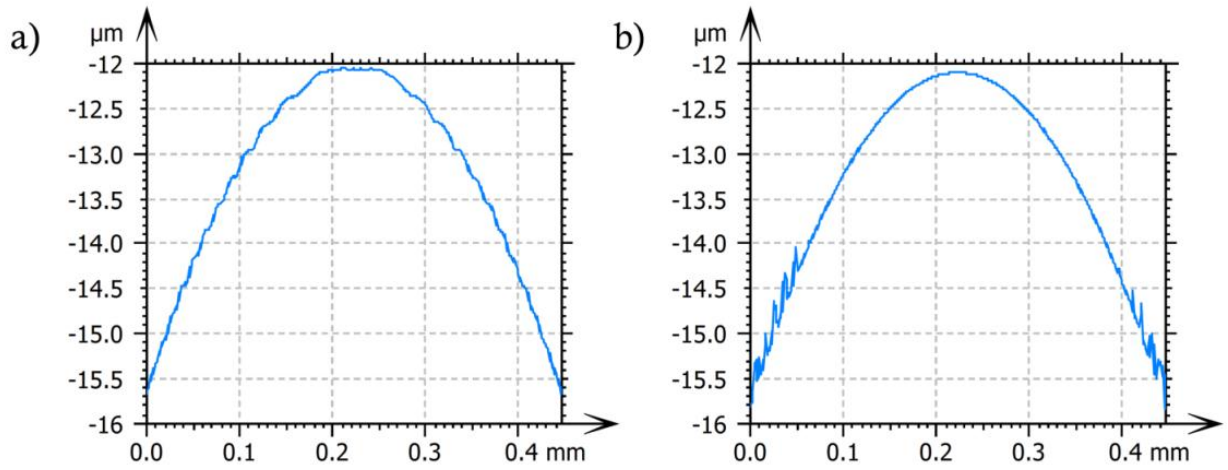

Figure 6.17. Profile of steel sphere measurements *via* estimation of the frequency (a) and the phase (b).

6.2.3 Phase WSI Conclusion

It has been shown that it is possible to combine the fringe frequency and phase information acquired in WSI to obtain absolute measurement of heights with repeatability comparable with PSI and CSI. The possible sources of error are included and their effects have been discussed. An analytical model has been described that allows the calculation of the minimum achievable variance (CRB) in the estimation of height from phase and frequency in the presence of Gaussian additive noise, showing a theoretical improvement of the measurement repeatability by a factor of approximately ten, which is in agreement with the experiments. Moreover, the method is also shown to reduce the vertical axis non-linearity by a factor of ten.

By implementing this method, the useful dynamic range of WSI can effectively be extended and comparisons using practical measurement examples clearly show the achieved performance improvements. Coupled with the increased measurement speed offered by WSI, this method broadens the potential applications of the technique for high-speed metrology at the nanoscale.

6.3 Summary

In this chapter two algorithms improvement for the WSI instrument have been described. The two algorithms are complementary, *i.e.* only one or both can be implemented. The Q-WSI algorithm allows measuring the *z*-position sign and therefore correctly distinguishing position associated with a positive or negative OPD. Additionally, the *z*-positions around the zero OPD are accessible if an initial estimation of the signal background is known. As a result, the measurement range is more than doubled with the drawback of reintroducing some mechanical scanning of the reference mirror. However, camera with a pixelated mask may avoid mechanical scans and provide multi-phase shifts in a single shot[192]. A description of the technique with a theoretical analysis of the sensitivity to additive noise and error due to signal not ideality has

also been reported. Real measurements have been reported which shows the doubled range and a reduced linearity deviation ($\pm$20 nm).

Another method to improve the performances of the WSI is by combining the fringe pattern frequency to resolve the fringe order and the phase to obtain the *z*-position. (phase WSI). A theoretical analysis of the sensitivity to additive noise is reported. Real measurement with the phase WSI algorithm shows measurement noise reduced by a factor of approximately 10, reaching the sub-nm range, and a linearity deviation also reduced by the same amount ($\pm$2 nm).

7 Conclusion and future research

The **Thesis Aim** was defined in Chapter 1 as:

"To establish traceability of surface topography measurements from a wavelength scanning interferometer".

Three **Thesis Objectives** were formulated as intermediate steps needed to fulfil the **Thesis Aim** or as strands of research that were successful.

7.1 Conclusion

The WSI instrument prototype was successfully built at University of Huddersfield and knowledge and experience acquired to continue the development of the technique at NPL (**Thesis objective 1**).

The MCs were evaluated according to draft international ISO standard and are summarised in table 7.1(**Thesis objective 2**) with other relevant WSI characteristics.

Measurement noise can be successfully estimated with two methods: subtraction or averaging.

The flatness deviation can be estimated by measuring a calibrated flat. In this specific WSI implementation, the flatness deviation estimation is influenced by measurement noise and *z*-axis non-linearity. Measurement noise can be reduced by averaging several measurements, thereby reducing the effect on the flatness estimation. The *z*-axis non-linearity is an error introduced by the fringe pattern processing algorithm. Despite reducing the effects of z-axis non-linearity by applying a window and avoid edge data from the demodulated phase, the non-linearity amplitude is comparable to the flatness deviation and therefore likely to affect its estimation.

The *z*-axis linearity coefficient (the maximum deviation from the best linear fit of the axis response) and the amplification factor are traditionally estimated with the SHS standard method. Alternate methods for the estimation of these two parameters have been proposed. The amplification factor can be estimated using the known wavelength of the light source, while the linearity coefficient can be estimated by measuring a tilted flat. It has been shown that the proposed method estimates the amplification factor with a lower uncertainty than the SHS method. Also, the proposed method provides more detailed information about the linearity deviation distribution in the instrument *z*-axis.

The lateral-axis amplification factor and linearity coefficient has been estimated by employing an ACG artefact. Two methods are compared: the reference grid method and the self-calibration method. The self-calibration method is not affected by error introduced in the alignment of the measured ACG with the reference measurement.

The full-width full-transmission lateral resolution can be estimated with an ASP artefact. The algorithm shows large “batwings” at the step height discontinuity, making estimation of reduced contrast lateral resolution, such as the lateral period limit, difficult. The measured MCs for the WSI prototype in table 7.1 lead to a standard uncertainty for a single value of height in the order of tens of nanometres for both objective lenses.

Table 7.1: WSI performance summary.

	Objective lens	2×	5×
***z* axis**	Measurement range	65 µm From -5 to -70 µm	30 µm From -5 to -35 µm
	Measurement noise (S-filter) (N_m)	7 nm (nesting index: 5 µm)	6 nm (nesting index: 10 µm)
	Flatness deviation (S-filter) (S_z)	26 nm (nesting index: 5 µm)	34 nm (nesting index: 10 µm)
	Amplification coefficient (α_z)	1.000 ±0.002	1.000 ±0.002
	Linearity deviation (l_z) MPE: Maximum permissible error RMSE: Root mean square error	≤80 nm (MPE) 16 nm (RMSE)	≤110 nm (MPE) 22 nm (RMSE)
Lateral axes	Field of view (FOV)	(1.717×1.243) mm	(0.686×0.497) mm
	Amplification coefficient (α_x , α_y)	*x:* 1.002 *y:* 0.997	*x:* 1.000 *y:* 0.997
	Linearity deviation (l_x, l_y)	1.21 µm	0.81 µm
	Width full height transmission (D_{LIM})	--	80-120 cycle/mm
Speed	Measurement (for 256 frames) + computing speed	1.2 + 1.5 seconds	1.2 + 1.5 seconds

Table 7.2 present a comparison of the MCs for WSI with other surface measuring topography instruments. The MCs of the WSI have smaller values than the MCs of the confocal instrument, apart for the measurement noise that has a comparable value, and therefore WSI measurements are associated with lower *z*-axis uncertainty than measurements executed with the confocal instrument. CSI instead shows lower MCs value than the WSI and therefore CSI measurement are associated with a lower uncertainty than WSI. The main advantage of the WSI with respect to the confocal and CSI technique is the measurement speed at the expenses of a fixed measurement range set by the objective numerical aperture. The main contribution to the uncertainty for WSI measurement is the *z*-axis linearity, which is an error introduced by the fringe processing algorithm. Research efforts have therefore been devoted to finding a suitable algorithm with reduced non-linearity effects. The algorithm improvements described in section 6 reduces the measurement noise and the linearity deviation by an order of magnitude, and therefore to values comparable or smaller than the CSI technique, whilst preserving the same measurement speed and doubling the measurement range in the QWSI case.

Table 7.2. Comparison of MCs relative to the *z*-axis across calibrated instruments. The CSI measuring speed has been calculated as the time needed to scan vertically 70 µm, with a step size of 80 nm and a camera of 200 fps for a fair comparison.

	Instrument name	**Confocal**		**CSI**		**WSI**		**Phase QWSI**	
	Objective lens	20×	50×	20×	50×	2×	5×	2×	5×
***z*-axis MCs**	Measurement Noise /nm	4.1	1.4	0.17	0.34	7	6	0.6	0.6
	Residual Flatness /nm	162	27	1.6	2.2	26	34	--	--
	Amplification coefficient	1.000	1.000	1.000	1.000	1.000	1.000	1.000	1.000
	Linearity deviation /nm	19	18	7	7	16	22	2	2
Additional specs	Measurement range / µm	2000		2200		70	30	140	60
	Measurement speed / seconds	10		4.4		1.2		1.2	

Two algorithm improvements have been presented in section 6: Q-WSI and phase WSI.

The Q-WSI technique consists in recording two fringe patterns in quadrature. This solution reduces the MPE by approximately half. Another advantage of the Q-WSI mode is to distinguish between positive and negative OPD and to measure around the zero OPD position, which doubles the vertical range of the instrument. For the 2× and 5× objective lenses, the measurement range increases to 140 µm and 70 µm, respectively (**Thesis objective 3**). The main disadvantage of this mode is that it reintroduces some mechanical shift of the reference mirror. However, commercially available cameras with a pixelated array on the camera sensor are capable of recording four different phase shifts (more than the two required for the Q-WSI) in a single shot [192]; alternatively, multiple cameras can be employed [193].

The phase-WSI technique is another proposed solution which greatly improves the WSI performance. By estimating the frequency and the phase of the fringe pattern it is possible to resolve the fringe order and estimate the *z*-position with reduced noise and with smaller non-linearity. Both noise and non-linearity are reduced by an order of magnitude. The achieved noise is the sub-nanometres range and the non-linearity amplitude reaches the few nanometres, therefore a MPE of the same order of magnitude (**Thesis Objective 3**).

7.2 Future research

Future work is required to recalibrate the WSI instrument with the Q-WSI and phase WSI algorithms. In particular a linear phase demodulation algorithm for the specific need of the WSI technique needs to be designed. Linear PSI algorithms are specific to a single known frequency of the fringe pattern. Iterative PSI algorithms could provide the best frequency and phase estimation performance, reducing measurement noise, linearity deviation and sensitivity to high-frequency vibrations. Implementation of the Q-WSI and phase WSI techniques and algorithms need to be implemented in parallel on the GPU to fully extend the WSI measurement uncertainty characterisation to these techniques.

The estimation of the flatness map is affected by noise and non-linearity of the vertical axis. The proposed techniques greatly reduce the measurement noise and the non-linearity amplitude therefore opening the possibility for a more accurate estimation of the flatness map, and possibility to study the effect of the defocus aberration on the flatness map and eventually correct for it.

Further research is required to characterise the WSI response as a function of the surface spatial frequency. In general, measurement noise increases for surfaces with large slopes since the exit pupil is not entirely filled with light. The same applies for rough surfaces: scattered light decreases the light collected by the objective lens, reducing the intensity of the interference signal. Recent research elaborated an uncertainty model for CSI as a function of tilt, NA and surface roughness [197]. Furthermore, two additional MCs are likely to be introduced by the ISO standard committee: maximum measurable slope and surface fidelity [198].

A complete characterisation of the optics response as a function of the surface spatial frequencies, *i.e.* the OTF, is possible for CSI instruments [179] and similar concept is applicable for WSI.

Design of long depth of focus objective lenses [199] has been reported in the literature: the WSI technique may extend its measurement capabilities to high NA objective lens with an extended depth of focus.

A CMOS camera with a phase shifts pixelated array would allow implementing the Q-WSI technique without the need to move the reference mirror, therefore keeping the advantages of speed and no mechanical moving parts.

Another possible development is to increase further the measurement speed. In the WSI instrument object of this thesis the measurement speed is limited by the frame rate of the CCD camera. CMOS or sCMOS [200] (scientific CMOS) cameras may be a solution to increase the measurement speed. Both CMOS and sCMOS cameras have higher frame rate, which means reduced exposure time. Reduced exposure time coupled with the lower light sensitivity of CMOS

sensor would lead to increased measurement noise. To compensate for the increased measurement noise due to faster measurement, a high-power light source can be employed.

Reduction of the measurement speed has to be coupled with reduction of the computation time. Optimisation of the parallel phase demodulation algorithms on the GPU and/or FPGA can push forward the computing speed. Ultimately a sCMOS sensor with embedded FPGA for on-chip computation would provide the lowest latency.

Appendix A

Interference of light

Interferometric techniques are methods to measure displacement by exploiting the wave nature of light. Light as an electromagnetic wave which is fully described by Maxwell's equations. In a homogenous medium, the electromagnetic field propagates as a transverse wave whose electric and magnetic field satisfies the wave equation:

$$\nabla^2 u(\boldsymbol{r},t) - \frac{1}{c^2}\frac{\partial^2 u(\boldsymbol{r},t)}{\partial t^2} = 0 \tag{7.2.1}$$

where ∇^2 is the Laplacian operator, u is the electric or magnetic field, c is the propagation speed of the wave, $\boldsymbol{r} = (x, y, z)$ are the spatial coordinates and t is time. In an homogenous, transparent medium the propagation speed is equal to $c = \frac{c_0}{n}$ where n is the refractive index of that medium and c_0 is the the speed of light in free space. A possible solution of the electric field in equation (7.2.1) is a monochromatic wave:

$$E(\boldsymbol{r},t) = E_0(\boldsymbol{r})\cos(\omega t + \varphi(\boldsymbol{r})) \tag{7.2.2}$$

where $E_0(\boldsymbol{r})$ and $\varphi(\boldsymbol{r})$ are the amplitude and phase wavefront of the monochromatic wavefunction and ω is the angular frequency (rad/s). The monochromatic wavefunction is usually written in complex form which also satisfy the wave equation and it will simplify the algebra later on:

$$E_c(\boldsymbol{r},t) = E_0(\boldsymbol{r})\mathrm{e}^{j\omega t}\mathrm{e}^{j\varphi(\boldsymbol{r})}. \tag{7.2.3}$$

In practice, any measurement of the electric field is taken over many cycles of the time dependent term due to the time response of the detector. What is actually measured is the average of the time dependent term. As an example for light in the visible at 600 nm the oscillating period is approximately 2 fs (500 THz), faster than any available detector. Therefore the complex field is usually written omitting the temporal term:

$$E_c(\boldsymbol{r},t) = E_0(\boldsymbol{r})\mathrm{e}^{j\varphi(\boldsymbol{r})}. \tag{7.2.4}$$

The intensity of an electric field may be shown to be related to the complex amplitude as:

$$I(\boldsymbol{r}) \cong |E_0(\boldsymbol{r})|^2 \tag{7.2.5}$$

due to the averaging over several cycles.

Interference occurs when two waves occupy the same points in space. The resulting field is the sum of the individual fields:

$$E_0(\boldsymbol{r}) = E_1(\boldsymbol{r}) + E_2(\boldsymbol{r}) \tag{7.2.6}$$

and the intensity of the two fields can be written as:

$$I_0(\boldsymbol{r}) = |E_0(\boldsymbol{r})|^2 = E_0(\boldsymbol{r})\, E_0(\boldsymbol{r})^* \tag{7.2.7}$$

where $E_0(\boldsymbol{r})^*$ is the complex conjugate of the complex field. Combining equation (7.2.6) and equation (7.2.7) and dropping the spatial dependency for clarity, the resulting intensity is:

$$I_0(\boldsymbol{r}) = |E_1|^2 + |E_2|^2 + E_1\, {E_0}^* + [E_1\, {E_0}^*]^* = |E_1|^2 + |E_2|^2 + 2Re[E_1\, {E_0}^*] \tag{7.2.8}$$

where *Re* is the real part of the complex field. In the case of two monochromatic waves of same frequency and phase φ_1 and φ_2 the intensity becomes:

$$I_0 = I_1 + I_2 + 2\sqrt{I_1 I_2}\, \cos(\varphi_1 - \varphi_2) \tag{7.2.9}$$

where I_1 and I_2 are the intensities of the fields E_1 and E_2 are defined as in equation (7.2.5). The observed intensity resulting from the sum of two fields with same frequency and different phase is composed by two constant terms corresponding to the intensity of the two fields and a term proportional to the cosine of the phase difference between the fields.

Coherence

When evaluating the interference between two waves it is important to introduce the idea of coherence. The coherence is a measure of the statistical relationship between points of a wave over time and space. In order to observe interference there must be some degree of coherence or correlation between the phases of the interfering wave.

For example let's consider the superposition of several waves having random phases and for simplicity equal amplitudes. For N waves, each with a phase φ_n the superposition is the sum of the complex fields:

$$E_T(\boldsymbol{r}) = \sum_{n=1}^{N} E_n(\boldsymbol{r}) = \sum_{n=1}^{N} a(\boldsymbol{r}) e^{j\varphi_n(\boldsymbol{r})} \tag{7.2.10}$$

and the resulting intensity is:

$$I_T(\boldsymbol{r}) = |E_T(\boldsymbol{r})|^2 = E_T(\boldsymbol{r})\, E_T(\boldsymbol{r})^* = [a(\boldsymbol{r})]^2 \sum_{n=1}^{N} e^{j\varphi_n(\boldsymbol{r})} \sum_{n=1}^{N} e^{-j\varphi_n(\boldsymbol{r})}. \tag{7.2.11}$$

The double summation gives a result in the form of:

$$I_T(\boldsymbol{r}) = a^2(1 + e^{j(\varphi_1 - \varphi_2)} + e^{-j(\varphi_1 - \varphi_2)} + 1 \ldots) \tag{7.2.12}$$

where the spatial dependency has been dropped for clarity. By using the trigonometric identity $\cos(\varphi) = \frac{1}{2}(e^{j\varphi} + e^{-j\varphi})$ equation (7.2.12) becomes:

$$I_T = a^2(N + 2\cos(\varphi_1 - \varphi_2) + \cdots). \tag{7.2.13}$$

If N is large the contribution of the cosines averages out and the observed intensity becomes:

$$I_T = a^2 N \tag{7.2.14}$$

i.e. the sum of the time averaged intensities. Therefore, in the case of field superposition with random phases the interference is not observable due to the intensities averaging. To observe the interference, some correlation or coherence between the phases has to be present.

The light coherence can be separated into two types: temporal and spatial coherence. The degree of coherence of light is described statistically by the use of the correlation function, *i.e.* a measure of the similarity of two waves as a function of the shift between them.

Temporal coherence

The autocorrelation function of the complex wave-function is defined as:

$$G(\tau) = \lim_{T\to\infty} \frac{1}{2T} \int_{-T}^{T} E^*(t)E(t+\tau)\, dt = < E^*(t)E(t+\tau) > \tag{7.2.15}$$

where the spatial dependency is excluded for brevity and the assumption that the complex field is stationary, *i.e.* its statistical properties do not change over time is made. The function $G(\tau)$ is called the temporal autocorrelation function and its maximum is always found to be at $G(0)$. It is useful to define the complex degree of temporal coherence by normalising equation (7.2.15) so its maximum value does not exceed unity:

$$g(\tau) = \frac{G(\tau)}{G(0)} = \frac{<E^*(t)E(t+\tau)>}{<E^*(t)E(t)>}. \tag{7.2.16}$$

If $g(\tau)$ decays monotonically on either side of its peak value, the coherence time is defined as the time for which the complex degree of temporal coherence drops by a prescribed amount. From the point of view of interferometry, the coherence length is more often used because the time delay is introduced by changing the optical path length in the instrument. The coherence length is related to the coherence time by:

$$l_c = \frac{c}{n}\tau_c \tag{7.2.17}$$

where c is the speed of light in vacuum, n is the refractive index of the medium in which the wave is travelling and τ_c is the coherence time.

The temporal coherence of light is related to its power spectral density (PSD) due to application of the Weiner-Khinchin theorem. The Wiener-Khinchin theorem states that the PSD of a stationary process is equal to the Fourier transform of its autocorrelation function:

$$S(\omega) = \int_{-\infty}^{+\infty} G(\tau) e^{j\omega\tau} d\tau. \tag{7.2.18}$$

Therefore, there is an inverse relationship between the width of the PSD and the coherence time of an optical wave. Waves with a larger PSD (for instance white light sources) have shorter coherence time and thus shorter coherence length. On the other hand, waves with narrower PSD (*e.g.* laser) have longer coherence time and length.

Spatial coherence

To describe the spatial coherence of a wave, the spatial dependence needs to be reintroduced. The mutual coherence function can be defined as:

$$G(\boldsymbol{r_1}, \boldsymbol{r_2}, \tau) = < E^*(\boldsymbol{r_1}, t) E(\boldsymbol{r_2}, t + \tau) > \tag{7.2.19}$$

and in its normalised form is the complex degree of coherence:

$$g(\boldsymbol{r_1}, \boldsymbol{r_2}, \tau) = \frac{G(\boldsymbol{r_1}, \boldsymbol{r_2}, \tau)}{[I(\boldsymbol{r_1}) I(\boldsymbol{r_2})]^{\frac{1}{2}}} \tag{7.2.20}$$

whose absolute magnitude is bounded between zero and unity.

For the case where $\boldsymbol{r_1} = \boldsymbol{r_2}$, the complex degree of coherence becomes the complex degree of temporal coherence as in equation (7.2.16). The spatial coherence may be considered by examining the complex degree of coherence for a certain time delay, usually $\tau = 0$. If the light is monochromatic, the complex degree of temporal coherence reduces to the harmonic function:

$$G(\boldsymbol{r_1}, \boldsymbol{r_2}, \tau) = G(\boldsymbol{r_1}, \boldsymbol{r_2}) e^{jk\tau}. \tag{7.2.21}$$

By substituting equation (7.2.21) in equation (7.2.20) and dropping the temporal dependence, it is possible to define the complex degree of spatial coherence as

$$g(\boldsymbol{r_1}, \boldsymbol{r_2}) = \frac{G(\boldsymbol{r_1}, \boldsymbol{r_2})}{[I(\boldsymbol{r_1}) I(\boldsymbol{r_2})]^{\frac{1}{2}}}. \tag{7.2.22}$$

The coherence area in a plane is given by a fixed drop in the value of the function $|g(\boldsymbol{r_1}, \boldsymbol{r_2})|$ with the distance on the plane $|\boldsymbol{r_1} - \boldsymbol{r_2}|$.

The coherence area is important when considering the waves passing through apertures. For examples, if a light wave passes through a pinhole smaller than its coherence area at that point, spatial coherence is imparted upon the wave.

Coherence of two waves

The concepts of temporal and spatial coherence introduced in the previous sections can be applied to describe the coherence of the superposition of two waves, and therefore, the cross-correlation is used as opposed to the auto-correlation. Two waves with complex wave-function $E_1(\boldsymbol{r}, t)$ and $E_2(\boldsymbol{r}, t)$ have a cross-correlation function G_{12} defined as

$$G_{12}(\boldsymbol{r_1}, \boldsymbol{r_2}, \tau) = < {E_1}^*(\boldsymbol{r_1}, t) E_2(\boldsymbol{r_2}, t+\tau) > \tag{7.2.23}$$

and by normalising the cross correlation function, the complex degree of coherence is given by

$$g_{12}(\boldsymbol{r_1}, \boldsymbol{r_2}, \tau) = \frac{G_{12}(\boldsymbol{r_1}, \boldsymbol{r_2}, \tau)}{[I_1(\boldsymbol{r_1})\, I_2(\boldsymbol{r_2})]^{\frac{1}{2}}} \tag{7.2.24}$$

where the intensities $I_1(\boldsymbol{r})$ and $I_2(\boldsymbol{r})$ are the time average of the squared magnitude of the field. The intensity of two waves interfering at the same point location $\boldsymbol{r}$ can be written as in equation (7.2.8) explicating the time average of the intensities,

$$I = < |E_1|^2 > + < |E_2|^2 > + < {E_1}^* E_2 > + < {E_2}^* E_1 >. \tag{7.2.25}$$

The last two terms in Equation (7.2.25) are the cross-correlation of the complex field and its conjugate and, therefore,

$$I = I_1 + I_2 + G_{12} + {G_{12}}^* = I_1 + I_2 + 2\, Re\{G_{12}\}. \tag{7.2.26}$$

The complex degree of coherence in equation (7.2.24) can be substituted into equation (7.2.26) to obtain

$$I = I_1 + I_2 + 2\sqrt{I_1 I_2}\, Re\{g_{12}\} \tag{7.2.27}$$

and in its final form

$$I = I_1 + I_2 + 2\sqrt{I_1 I_2}\, |g_{12}| \cos\varphi \tag{7.2.28}$$

which is similar to equation (7.2.9) with the difference that the interference term is modulated by the magnitude of the degree of coherence of the two waves. The interference intensity is therefore a sinusoidal pattern that is a function of the phase difference between the two interfering waves. The case where two electric fields with the same frequency interfere is called homodyne interference.

The case where the two fields do not have the same frequency it is called heterodyne interference. In this case the magnitude of the complex degree of coherence can be shown to be

$$g_{12} = e^{j\varphi} e^{j\,\delta\omega t} \tag{7.2.29}$$

where $\delta\omega$ is the difference of pulsation of the two fields $\delta\omega = \omega_1 - \omega_2$ and φ the phase difference. By substituting equation (7.2.29) in equation (7.2.28) it is obtained

$$I = I_1 + I_2 + 2\sqrt{I_1 I_2}\cos(\delta\omega\, t + \varphi) \tag{7.2.30}$$

In the heterodyne case, therefore, the fringe visibility is not a constant but oscillates in time with a frequency equal to the frequency difference between the two fields and with a phase equal to the phase difference between the two fields.

Displacement measuring interferometry

In displacement measuring interferometry (DMI) two interfering light beams are employed to measure the displacement of moving object or heights variation across a surface. In all interference-based measuring instruments the beam reflected from the surface to measure, also called the measurement beam, is combined with a beam reflected from a known surface, the reference beam, to observe interference fringes and calculate the phase shift between the two beams.

Different optical setups are possible to observe interference fringes and some are shown in figure 7.0.1. The light from the source is split by the beam splitter and the two beam reflected by the reference and the object mirror. The reference and measurement beams travel different optical length along the interferometers reference and measurement arms. The beams are then recombined and the interference signal intensity measured depends on the phase difference according to equation (7.2.28).

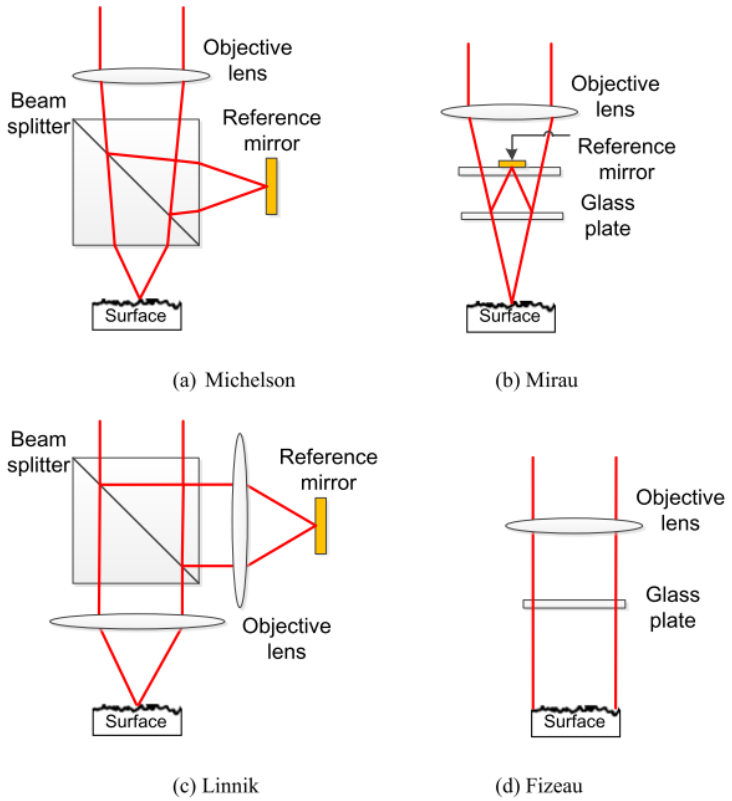

Figure 7.0.1. Interferometer configurations (from [3]).

The phase difference between the two beams is related to the optical path difference, as

$$\varphi = kn\,2d_2 - kn\,2d_1 = kn\,2L \tag{7.2.31}$$

where $k = {}^{2\pi}/_{\lambda}$ is the wavenumber of the light, n is the refractive index of the medium where the light travels, and d_2 and d_1 the physical distance of the mirrors from the beam splitter. The displacement of the object mirror is therefore proportional to the phase difference as:

$$L = \frac{\varphi}{k\,n\,2}. \tag{7.2.32}$$

Many possible different optical setup and interferometer variation are possible to accomplish a specific metrological task. A complete description of all the possibilities is not the aim of this chapter but only the instruments and techniques relevant to surface measurements are discussed. For further insight on interferometric techniques see [105], [201]–[203].

Interferometric techniques for surface topography measurement combine a classical microscope imaging instrument with an interferometer setup. The light from a sample to measure, with an unknown phase or wavefront, interferes with the light coming from a reference sample and therefore with a fixed phase or a known wavefront. The interference between the two waves creates an interference pattern on the camera, which can be processed to retrieve the surface topography.

Appendix B

Window phase demodulation optimisation code (section 4.1)

```
clc
clear all
close all

%% scan params
StartHeight = 5; % in um
EndHeight = 7; % in um
Height = linspace(StartHeight,EndHeight,(EndHeight-StartHeight)*1000)';
%height vector in micrometer
Wavelength = [0.692882 0.587747 ]; %start and end wavelengths in micrometer
N =256; %number of frames
PhaseEdgesToDrop = N/32*0;
%% signal params
DC = 1;
AC = 1;
SNR=60;% SNR in Db
Noise = AC/sqrt(2*10^(SNR/10));%
%% derived params
WaveNumbers = linspace (1/Wavelength(1),1/Wavelength(2), N )';
Dimension = '\mum';
%% save parameters
PathName =  '';
FileName = PathName;
%% analysis
WinName = [' Rectangular' ; ' Gaussian   ';' Hann       '; ' Hamming
';];
WinName = cellstr(WinName);

for i = 1:length(Height)
    Signal = DC + AC * sin ( 4 * pi * Height(i) * WaveNumbers) + Noise *
randn(N,1);

    index = 1;
    Win(:,index) = rectwin(N);
    [Rect_FFT, Freqs, Rect_Phase, Rect_FittedPhase,
ExtractedHeight(i,index), HeightError(i,index)] =
phase_extractor_DifferentWindow(Signal , WaveNumbers, Dimension ,
Win(:,index), WinName(index), Height(i) ,PhaseEdgesToDrop, 0 , PathName );

    index = 2;
    Win(:,index) = gausswin(N,1.75);
    [Gauss_FFT, Gauss_Freqs, Gauss_Phase, Gauss_FittedPhase,
ExtractedHeight(i,index),HeightError(i,index)] =
phase_extractor_DifferentWindow(Signal , WaveNumbers, Dimension ,
Win(:,index), WinName(index), Height(i),PhaseEdgesToDrop, 0 ,PathName);

    index = 3;
    Win(:,index) = hann(N,'periodic');
    [Hann_FFT, Hann_Freqs, Hann_Phase, Hann_FittedPhase,
ExtractedHeight(i,index),HeightError(i,index)] =
phase_extractor_DifferentWindow(Signal , WaveNumbers, Dimension ,
Win(:,index), WinName(index), Height(i),PhaseEdgesToDrop, 0,PathName );

    index = 4;
    Win(:,index) = hamming(N,'periodic');
```

```
    % WinName(index) = ' Hamming'
    [Hamm_FFT, Hamm_Freqs, Hamm_Phase, Hamm_FittedPhase,
ExtractedHeight(i,index),HeightError(i,index)] =
phase_extractor_DifferentWindow(Signal , WaveNumbers, Dimension ,
Win(:,index), WinName(index), Height(i),PhaseEdgesToDrop, 0,PathName);
end
MaxError = max(abs(HeightError));
RMSError = sqrt(mean((HeightError).^2));

%% plot results
h(1) = figure('units','normalized','outerposition',[0 0 1 1]);
hold on
NumOfPlot=index;
LineW=2;
PlotFontSize = 20;
AxisFontSize= 20;
plot(Height,HeightError(:,1),'b','LineWidth',LineW);
plot(Height,HeightError(:,2),'r','LineWidth',LineW);
plot(Height,HeightError(:,3),'g','LineWidth',LineW);
plot(Height,HeightError(:,4),'Color',[0.75,0,0.75],'LineWidth',LineW);
set(gca,'FontSize',AxisFontSize)
hold off
xlabel(strcat('Nominal height [', Dimension, ']'
),'FontSize',AxisFontSize,'FontWeight','bold');
ylabel (strcat('Height error [',Dimension
,']'),'FontSize',AxisFontSize,'FontWeight','bold');
FirstLine = char(strcat ('Heights errors with N =', int2str(N), ' frames
for heights range [', int2str(Height(1)),'-', int2str(Height(end)),']
',Dimension ));
SecondLine = char(strcat('Percentage of dropped edge phase points for
fitting:', num2str(PhaseEdgesToDrop/N*2*100),' % (i.e.
',num2str(PhaseEdgesToDrop*2),' points )' ));
ThridLine = char(strcat('Max error magnitude in the range: ',
num2str(MaxError) ,' ' ,Dimension ));
FourthLine = char(strcat('RMSE in the range: ', num2str(RMSError) ));
title({FirstLine ; SecondLine; ThridLine; FourthLine});
legend(WinName,'FontSize',AxisFontSize,'FontWeight','bold');
grid on
hold off
legend('Rectangular','Gaussian','Hann','Hamming','Location','Best');

%% Saving section. UNCOMMENT TO SAVE GRAPHS
PathName = uigetdir
if length(PathName)~=0
    RangeStr = strcat('Range', num2str(StartHeight),'_',
num2str(EndHeight));
    PhasePointsStr = strcat('PercDrop',num2str(2*PhaseEdgesToDrop/N*100));
    %     h=figure(1);
    FileName = strcat(PathName,'\Error', RangeStr,PhasePointsStr);
    SaveFigPngEps( FileName , gcf );
else FileName = PathName;
end

%% select and display details of some heights calculation
[SelectedHeight,SelectedError] = ginput;
% SelectedHeight = 6.9403;
DisplayData = 1;

for i=1:length(SelectedHeight)
```

```
    [SelectedNominalHeight(i),SelectedNominalHeight_index(i)]= findvalues(
Height , SelectedHeight(i));
    Signal = DC + AC * sin ( 4 * pi * SelectedNominalHeight(i) *
WaveNumbers) + Noise * randn(N,1);
    index=1;
    phase_extractor_DifferentWindow(Signal , WaveNumbers, Dimension ,
Win(:,index), WinName(index), SelectedNominalHeight(i) ,PhaseEdgesToDrop,
DisplayData,FileName );
    index=2;
    phase_extractor_DifferentWindow(Signal , WaveNumbers, Dimension ,
Win(:,index), WinName(index), SelectedNominalHeight(i) ,PhaseEdgesToDrop,
DisplayData, FileName );
    index=3;
    phase_extractor_DifferentWindow(Signal , WaveNumbers, Dimension ,
Win(:,index), WinName(index), SelectedNominalHeight(i) ,PhaseEdgesToDrop,
DisplayData, FileName );
    index=4;
    phase_extractor_DifferentWindow(Signal , WaveNumbers, Dimension ,
Win(:,index), WinName(index), SelectedNominalHeight(i) ,PhaseEdgesToDrop,
DisplayData, FileName );
end
```

```
function [ FFT, Freqs, Phase, FittedPhase, Height , HeightError] =
phase_extractor_DifferentWindow( YDataIn , XDataIn, XDim , Window ,
WindowName, RealHeight,PhaseEdgesToDrop,DisplayData,PathName )
%frequency_extractor: Extract the frequency of a sinusoidal signal from the
%slope of the fitted unwrapped phase
%
% Input:

% YDataIn : sinsoidal signal amplitude vector
% XDataIn: x axis value (MUST be same length of the YDataIn)
% XDim: string with the dimension of the x axis (time, wavenumber or
whatever)
% Window: Window data to be used before FFT
% WindowName: string with name of the window
% RealHeight: height of the generated signal for comparison
% PhaseEdgesToDrop: phase edges points to drop for the fitting (increase
precision and SNR sensitivuty?)
% DisplayData: bool value. If equal 1 the plots of the currect calculation
%               are displayed
%

% Output:

% FFT: FFT of windowed data
% Freqs: frequencies values
% Phase: extracted unwrapped phase
% FittedPhase: fitted phase
% ExtractedFreq : phase slope
%

%% calculate params
N = length(XDataIn); %length of data in
Fs = N  / (XDataIn(end)- XDataIn(1)); %data in sampling frequency
```

```
%% remove the DC by removing the mean value
YDataIn = YDataIn - mean(YDataIn);

%% windowing of YdataIn
% win = window(WindowType , N);
YDataInWindowed = YDataIn .* Window;

%% calculate FFT of and scaled frequencies vector
FFTwindowed = fft(YDataInWindowed)/N;
FFT = fftshift(fft(YDataIn)/N);
FFTwin = fftshift(fft(Window)/N);

%filter the spectrum
if (strcmp(WindowName ,cellstr(' Rectangular')))
    CutLow = 2 ;
elseif (strcmp(WindowName , cellstr(' Gaussian   ')))
    CutLow = 3;
elseif (strcmp(WindowName , cellstr(' Hann       ')))
    CutLow = 3;
elseif (strcmp(WindowName , cellstr( ' Hamming    ')))
    CutLow = 3;
elseif (strcmp(WindowName , cellstr(' Blackman   ')))
    CutLow = 4;
else
    CutLow = 2;
end

CutHigh = N/2+1;
filteredFFT = zeros(length(XDataIn),1);
filteredFFT(CutLow:CutHigh) = FFTwindowed(CutLow:CutHigh); %select only
half spectrum to extract the phase later
NormFreqs = linspace(-0.5,0.5,length(XDataIn)); %normalised frequencies
Freqs = Fs .* NormFreqs'/2; % scaled frequencies value (show the calculated
height)
%shift fft for display
FFTwindowed = fftshift(FFTwindowed);
%calculate the phase shift of the Window function by itself
filteredFFTWin = zeros(N,1);
filteredFFTWin(CutLow:CutHigh) = FFTwin(CutLow:CutHigh); %select only half
spectrum to extract the phase later

%% Calculate IFFT
IFFT = ifft(filteredFFT);
WinIFFT = ifft(filteredFFTWin);

%% extract and unwrap the phase
WrappedPhase = angle(IFFT);
Phase = unwrap(WrappedPhase);
WinWrappedPhase = angle(WinIFFT);
WinPhase = unwrap(WinWrappedPhase); % phase change of the window

%% phase fitting with edges removed
FittinPolynomDegree = 1;
p = polyfit(XDataIn(PhaseEdgesToDrop+1:end-PhaseEdgesToDrop),
Phase(PhaseEdgesToDrop+1: end - PhaseEdgesToDrop), FittinPolynomDegree);
FittedPhase = polyval(p,XDataIn);

%text to write on the plot
Px= poly2sym(p);
LinearFitString = sym2str(Px,'L2S','k','*');
```

```
ExtractedFreq = p(end-1);

%% calculate height
Height = ExtractedFreq/4/pi;
HeightError = RealHeight - Height;

%% plots

if ( DisplayData == 1 )

    LineW=2;
    PlotFontSize = 20;
    AxisFontSize= 20;
    hfig = figure;
    set(hfig,'Units', 'Normalized', 'OuterPosition', [0 0 1 1]); % plot
with figure at full screen

    subplot(2,2,1)
    plot(XDataIn,YDataIn,'g',XDataIn, Window,'r',XDataIn,YDataInWindowed,
'b');
    xlabel(strcat('Wavenumber [',XDim ,'^{-1}]')); ylabel('Intensity
[a.u.]');
    legend('Original','Window','Windowed');
    title(strcat('Signal: ','original and after windowing with ',
WindowName)); % %, WindowType

    subplot(2,2,2)
    MagFFT = 20*log10(abs(FFT )); maxMagFFT = max(MagFFT);minMagFFT =
min(MagFFT);
    plot(Freqs , MagFFT,'g',Freqs ,20*log10(abs(FFTwin )), 'r' ,Freqs
,log(abs(FFTwindowed )),'b');
    xlabel(strcat('Scaled frequency [',XDim,'] (i.e. height)'));
ylabel('Intensity [dB]');
    ylim([minMagFFT maxMagFFT + 3]);
    legend('Signal','Window','Windowed signal');
    title(strcat('FFT magnitude'));% of signal with ', WindowName,
'window'));

    subplot(2,2,4)
    plot(Freqs , unwrap(angle(FFT )), 'g',Freqs , unwrap(angle(FFTwin )),
'r' ,Freqs , unwrap(angle(FFTwindowed )),'b');
    xlabel(strcat('Scaled frequency [',XDim,'] (i.e. height)'));
ylabel('Phase [rad]');
    legend('Signal','Window','Windowed signal');
    title(strcat('Phase'));% of signal with ', WindowName, 'window'));

    subplot(2,2,3)
    FirstLine = char(strcat('Phase for ', WindowName ));
    SecondLine = char(strcat('Nominal heigth: ', num2str(RealHeight), XDim
)) ;
    ThirdLine = char(strcat('Calculated height: ', num2str(Height) , XDim
));
    plot(XDataIn, Phase,'b',XDataIn, FittedPhase,'g');
    xlabel(strcat('Wavenumber [',XDim ,'^{-1}]'));
    ylabel('Phase [rad]');

    hold on
    if (PhaseEdgesToDrop ~= 0 ) % if some phase edges are dropped before
the fitting highlight them
```

```
        plot( XDataIn(1:PhaseEdgesToDrop) ,Phase(1:PhaseEdgesToDrop), 'ro')
        plot( XDataIn(end +1 - PhaseEdgesToDrop : end) ,Phase(end +1 -
PhaseEdgesToDrop : end), 'ro')% mark the phase data dropped for the fitting
    end
    hold off


    legend('Extracted','Fitted', 'Dropped Data','Dropped Data', 'Window
Phase','Location','NorthWest')%'Fitting Weight Function',
    title({FirstLine;SecondLine ;ThirdLine });

    %plot phase and fitted phase by itself
    WaveNumbers = XDataIn;
    h = Height;
    Unit = XDim;
    hPhase  = figure('units','normalized','outerposition',[0 0 1 1]);
    plot(WaveNumbers , Phase,'b',WaveNumbers ,
FittedPhase,'g','LineWidth',LineW)
    hold on
    if (PhaseEdgesToDrop ~= 0 ) % if some phase edges are dropped before
the fitting highlight them
        plot( XDataIn(1:PhaseEdgesToDrop) ,Phase(1:PhaseEdgesToDrop),
'ro','LineWidth',LineW)
        plot( XDataIn(end +1 - PhaseEdgesToDrop : end) ,Phase(end +1 -
PhaseEdgesToDrop : end), 'ro','LineWidth',LineW)% mark the phase data
dropped for the fitting
    end
    hold off
    FirstLine = char(strcat('Phase for ',WindowName));
    SecondLine = char(strcat('Nominal heigth: ', num2str(RealHeight), XDim
)) ;
    ThirdLine = char(strcat('Calculated height: ', num2str(Height) , XDim
));
    title({FirstLine;SecondLine ;ThirdLine })
    xlabel(['Wavenumber [' Unit '^{-1}]'] ,
'FontSize',AxisFontSize,'FontWeight','bold');
    xlim([WaveNumbers(1) WaveNumbers(end)]);
    ylabel('Phase(rad)','FontSize',AxisFontSize,'FontWeight','bold');
    set(gca,'FontSize',AxisFontSize)

    legend('Extracted','Fitted','Dropped Data','Dropped
Data','FontSize',PlotFontSize,'FontWeight','bold','Location','North');

text(WaveNumbers(length(WaveNumbers)/2.56),FittedPhase(length(FittedPhase)/
8),strcat('\phi(k)=',LinearFitString,''),...
        'FontSize',PlotFontSize)

    %plot derivatives of extracted nad fitted phase
    DiffPhase = diff(Phase(PhaseEdgesToDrop+1: end - PhaseEdgesToDrop))*
Fs;

    DiffFittedPhase = diff(FittedPhase(PhaseEdgesToDrop+1: end -
PhaseEdgesToDrop))* Fs;

    figure('units','normalized','outerposition',[0 0 1 1])
    plot(XDataIn(PhaseEdgesToDrop+1:end-PhaseEdgesToDrop-1),
DiffPhase,'LineWidth',LineW );
    hold on
    plot(XDataIn(PhaseEdgesToDrop+1:end-PhaseEdgesToDrop-1),
DiffFittedPhase ,'g','LineWidth',LineW);
```

```
    hold off

legend('Extracted','Fitted','FontSize',PlotFontSize,'FontWeight','bold','Lo
cation','South');
    FirstLine = char(strcat('Phase derivative for ',WindowName));
    title({FirstLine;})
    xlabel(strcat('Wavenumber [',XDim ,'^{-
1}]'),'FontSize',PlotFontSize,'FontWeight','bold');
    xlim([WaveNumbers(1) WaveNumbers(end)]);
    ylabel(strcat('Phase derivative
[rad*',XDim,']'),'FontSize',PlotFontSize,'FontWeight','bold');
    set(gca,'FontSize',AxisFontSize)
    hPhaseDerivative = gcf;

    %save the plots as file
    if length(PathName)~=0
        FileName = strcat(PathName,char(WindowName));
        SaveFigPngEps( strcat(FileName,'Phase' ) , hPhase );
        SaveFigPngEps( strcat(FileName,'PhaseDerivative' ) ,
hPhaseDerivative);
    end
end
end
```

Publication

Refereed Journal Papers

Giuseppe Moschetti, Alistair Forbes, Richard K. Leach, Xiang Jiang, and Daniel O'Connor, "**Quadrature wavelength scanning interferometry**," Appl. Opt. 55, 5332-5340 (2016)

Giuseppe Moschetti, Alistair Forbes, Richard K Leach, Xiang Jiang, and Daniel O'Connor, "**Phase and fringe order determination in wavelength scanning interferometry**," Opt. Express 24, 8997-9012 (2016)

Refereed Conference Papers

Moschetti, Giuseppe, Muhamedsalih, Hussam, Jiang, Xiang , Leach, Richard K. And Connor, Daniel (2015) ***Extending the measurement range for wavelength scanning interferometry.*** Paper presented at: Precision Interferometric Metrology, ASPE 2015 Summer Topical Meeting. 7-10 July 2015, Golden, Colorado, USA.

Moschetti, Giuseppe, Muhamedsalih, Hussam,O Connor, Daniel, Jiang, Xiang and Leach, Richard K. (2015) ***Vertical axis non-linearities in wavelength scanning interferometry.*** Paper presented at: Laser Metrology and Machine Performance XI, EUSPEN LAMDAMAP 2015. 17-18 March 2015, Huddersfield, UK.

Non-refereed Conference papers

Moschetti, Giuseppe (2013), ***Development of on-line interferometric metrology techniques for high dynamic range surface measurement.*** Poster session presented at: Computing and Engineering Annual Researchers' Conference 2013 (CEARC'13), University of Huddersfield, Huddersfield, UK.

References

[1] J. Fahlteich, C. Steiner, M. Top, D. Wynands, T. Wanski, S. Mogck, E. Kucukpinar, S. Amberg-Schwwab, C. Boeffel, and N. Schiller, "Roll-to-Roll Manufacturing of Functional Substrates and Encapsulation Films for Organic Electronics : Technologies and Challenges," *Sid 2015 Dig.*, pp. 106–110, 2015.

[2] X. Jiang, K. Wang, F. Gao, and H. Muhamedsalih, "Fast surface measurement using wavelength scanning interferometry with compensation of environmental noise," *Appl. Opt.*, vol. 49, no. 15, pp. 2903–2909, May 2010.

[3] H. M. Muhamedsalih, "Investigation of wavelength scanning interferometry for embedded metrology.," University of Huddersfield, 2013.

[4] Nanomend, "Enhanced in-line detection, cleaning and repair of nano-scale defects," *NanoMend is funded by the EU FP7 programme*. [Online]. Available: http://nanomend.eu/. [Accessed: 12-Nov-2015].

[5] L. Blunt, M. Elrawemi, L. Blunt, and H. Muhamedsalih, "Implementation of in Process Surface Metrology for R2R Flexible PV Barrier Films Implementation of in Process Surface Metrology for R2R Flexible PV Barrier Films," *Int. J. Autom. Technol.*, vol. 9, no. 3, p. 312, 2015.

[6] D. J. Whitehouse, "Surface metrology," *Meas. Sci. Technol.*, vol. 8, no. 9, pp. 955–972, 1999.

[7] R. Leach, A. Weckenmann, J. Coupland, and W. Hartmann, "Interpreting the probe-surface interaction of surface measuring instruments, or what is a surface?," *Surf. Topogr. Metrol. Prop.*, vol. 2, no. 3, p. 35001, Jul. 2014.

[8] Geneva: International Organization for Standardization, "ISO 14406:2010 Geometrical product specifications (GPS) — Extraction," 2010.

[9] R. Young, "The Topografiner: An Instrument for Measuring Surface Microtopography," *Rev. Sci. Instrum.*, vol. 43, no. 7, p. 999, 1972.

[10] E. Merzbacher, "The early history of quantum tunneling," *Phys. Today*, pp. 44–49, 2002.

[11] J. G. Simmons, "Generalized Formula for the Electric Tunnel Effect between Similar Electrodes Separated by a Thin Insulating Film," *J. Appl. Phys.*, vol. 34, no. 6, pp. 1793–1803, 1963.

[12] H.-U. Danzebrink, L. Koenders, G. Wilkening, a Yacoot, and H. Kunzmann, "Advances in scanning force microscopy for dimensional metrology," *CIRP Ann. - Manuf. Technol.*, vol. 55, no. 2, pp. 841–878, 2006.

[13] H. J. Butt, B. Cappella, and M. Kappl, "Force measurements with the atomic force microscope: Technique, interpretation and applications," *Surf. Sci. Rep.*, vol. 59, no. 1–6, pp. 1–152, 2005.

[14] S. Rosén, T. R. Thomas, and B.-G. Rosén, "The Stedman diagram revisited," *Surf. Topogr. Metrol. Prop.*, vol. 2, no. 1, p. 14005, 2013.

[15] M. Stedman, "Basis for comparing the performance of surface-measuring machines," *Precis. Eng.*, vol. 9, no. 3, pp. 149–152, Jul. 1987.

[16] X. Jiang, P. J. Scott, D. J. Whitehouse, and L. Blunt, "Paradigm shifts in surface metrology. Part II. The current shift," *Proc. R. Soc. A*, vol. 463, no. 2085, pp. 2071–2099, 2007.

[17] P. De Groot, "Principles of interference microscopy for the measurement of surface topography," *Adv. Opt. Photonics*, vol. 7, pp. 1–65, 2015.

[18] F. Helmli, "Focus Variation Instruments," in *Optical Measurement of Surface Topography SE - 7*, R. Leach, Ed. Springer Berlin Heidelberg, 2011, pp. 131–166.

[19] Geneva: International Organization for Standardization, "ISO 25178-606:2015 Geometrical product specification (GPS) — Surface texture: Areal Part 606: Nominal characteristics of non- contact (focus variation) instruments," 2015.

[20] "Alicona InfiniteFocus," 2015. [Online]. Available: http://www.alicona.co.uk/home/fileadmin/alicona/pdfs/Alicona_InfiniteFocusG5_Optical_micro_coordinate_and_surface_finish_measurement_in_one_system_EN.pdf. [Accessed: 01-Dec-2015].

[21] M. Minsky, "Microscopy Apparatus," 1961.

[22] R. Artigas, “Optical Measurement of Surface Topography,” R. Leach, Ed. Berlin, Heidelberg: Springer Berlin Heidelberg, 2011, pp. 237–286.
[23] G. Q. Xiao, T. R. Corle, and G. S. Kino, “Real-time confocal scanning optical microscope,” *Appl. Phys. Lett.*, vol. 53, no. 8, pp. 716–718, 1988.
[24] M. D. Egger, R. Galambos, M. Hadravsky, and M. Petran, “Tandem-scanning reflected-light microscope.,” *J. Opt. Soc. Am.*, vol. 58, no. 5, pp. 661–664, 1968.
[25] P. J. Verveer, Q. S. Hanley, P. W. Verbeek, L. J. Van Vliet, and T. M. Jovin, “Theory of confocal fluorescence imaging in the programmable array microscope (PAM),” *J. Microsc.*, vol. 189, no. 3, pp. 192–198, 1998.
[26] F. Blateyron, “Chromatic Confocal Microscopy,” in *Optical Measurement of Surface Topography SE - 5*, R. Leach, Ed. Springer Berlin Heidelberg, 2011, pp. 71–106.
[27] Micro-Epsilon, “Confocal Chromatic Displacement sensor,” 2015.
[28] Polytec Limited, “Chromatic Confocal Point Sensors,” 2015. [Online]. Available: http://www.polytec-ltd.co.uk/fileadmin/user_uploads/Products/Surface_Metrology/TopSens/OM_BR_TMS-TopSens_2012_09_1000_E.pdf. [Accessed: 02-Dec-2015].
[29] Stilsa, “Confocal Chromatic Sensors,” 2015. [Online]. Available: http://www.stilsa.com/catalog2/pdf/STILSA_Initial_CCS_CHR.pdf. [Accessed: 02-Dec-2015].
[30] Micro-Epsilon, “Confocal Chromatic measurement system,” 2015. [Online]. Available: http://www.micro-epsilon.com/download/products/cat--confocalDT--en.pdf. [Accessed: 02-Dec-2015].
[31] Nanovea, “Chromatic Confocal,” 2015. [Online]. Available: http://nanovea.com/wp-content/themes/wp-nanovea/brochures/profilers.pdf. [Accessed: 02-Dec-2015].
[32] Geneva: International Organization for Standardization, “ISO 25178-602:2010 Geometrical product specifications (GPS) — Surface texture: Areal Part 602: Nominal characteristics of non-contact (confocal chromatic probe) instruments,” 2013.
[33] W. Lyda, M. Gronle, D. Fleischle, F. Mauch, and W. Osten, “Advantages of chromatic-confocal spectral interferometry in comparison to chromatic confocal microscopy,” *Meas. Sci. Technol.*, vol. 23, no. 5, p. 54009, May 2012.
[34] D. GABOR, “A New Microscopic Principle,” *Nature*, vol. 161, no. 4098. pp. 777–778, 1948.
[35] S. Seebacher, W. Osten, and W. P. O. Jueptner, “Measuring shape and deformation of small objects using digital holography,” *Proc. SPIE 3479, Laser Interferom. IX Appl.*, vol. 3479, no. 0, pp. 104–115, 1998.
[36] W. Osten, A. Faridian, P. Gao, K. Körner, D. Naik, G. Pedrini, A. K. Singh, M. Takeda, and M. Wilke, “Recent advances in digital holography,” *Appl. Opt.*, vol. 53, no. 27, p. G44, 2014.
[37] T. Colomb and J. Kühn, “Digital Holographic Microscopy,” in *Optical Measurement of Surface Topography SE - 10*, R. Leach, Ed. Springer Berlin Heidelberg, 2011, pp. 209–235.
[38] E. N. Leith and J. Upatnieks, “Reconstructed Wavefronts and Communication Theory,” *J. Opt. Soc. Am.*, vol. 52, no. 10, p. 1123, 1962.
[39] E. Cuche, P. Marquet, and C. Depeursinge, “Simultaneous amplitude-contrast and quantitative phase-contrast microscopy by numerical reconstruction of Fresnel off-axis holograms.,” *Appl. Opt.*, vol. 38, no. 34, pp. 6994–7001, 1999.
[40] U. Schnars and W. Juptner, “Digital recording and numerical reconstruction of holograms,” *Meas. Sci. Technol.*, vol. 13, p. 17, 2002.
[41] Lyncee tec, “HOLOGRAPHIC MEMS ANALYZER,” 2015. [Online]. Available: http://www.lynceetec.com/holographic-mems-analyzer/#3. [Accessed: 02-Nov-2015].
[42] Lyncee tec, “DHM - T series,” 2015. .
[43] J. Kühn, F. Charrière, T. Colomb, E. Cuche, F. Montfort, Y. Emery, P. Marquet, and C. Depeursinge, “Axial sub-nanometer accuracy in digital holographic microscopy,” *Meas. Sci. Technol.*, vol. 19, no. 7, p. 74007, 2008.
[44] M. K. Kim, “Principles and techniques of digital holographic microscopy,” *J. Photonics Energy*, p. 18005, 2010.
[45] P. J. de Groot, “Coherence scanning interferometry,” in *Optical measurement of surface*

topography SE-9, R. K. Leach, Ed. Springer Berlin Heidelberg, 2011, pp. 167–186.
[46] Piotr Szwaykowsky, "MInimization of vibration induced errors using a geometrical approach to phase shifting interferometry," in *ASPE Precision Interferometric Metrology*, 2015.
[47] D. Malacara, *Optical Shop Testing*, Third ed. ^. Wiley, 2007.
[48] M. Servin, J. C. Estrada, and J. A. Quiroga, "The general theory of phase shifting algorithms.," *Opt. Express*, vol. 17, pp. 21867–21881, 2009.
[49] J. A. N. Buytaert and J. J. J. Dirckx, "Study of the performance of 84 phase-shifting algorithms for interferometry," *J. Opt.*, vol. 40, no. 3, pp. 114–131, Sep. 2011.
[50] P. de Groot, "Derivation of algorithms for phase-shifting interferometry using the concept of a data-sampling window.," *Appl. Opt.*, vol. 34, no. 22, pp. 4723–30, Aug. 1995.
[51] J. Schmit and K. Creath, "Window function influence on phase error in phase-shifting algorithms.," *Appl. Opt.*, vol. 35, no. 28, pp. 5642–9, Oct. 1996.
[52] J. Harris, "On then Use of Windows with the Discrete for Harmonic Analysis Fourier Transform," *Proc. IEEEIEEE*, vol. 66, no. 1, p. 51, 1978.
[53] K. G. Larkin and B. F. Oreb, "Design and assessment of symmetrical phase-shifting algorithms," *J. Opt. Soc. Am. A*, vol. 9, no. 10, p. 1740, 1992.
[54] M. Servin and J. C. Estrada, "Analysis and synthesis of phase shifting algorithms based on linear systems theory," *Opt. Lasers Eng.*, vol. 50, no. 8, pp. 1009–1014, 2012.
[55] J. C. Estrada, M. Servin, and J. a Quiroga, "A self-tuning phase-shifting algorithm for interferometry.," *Opt. Express*, vol. 18, no. 3, pp. 2632–8, Feb. 2010.
[56] M. Servin and A. Gonzalez, "Linear analysis of the 4-step Carré phase shifting algorithm : spectrum , signal-to-noise ratio , and harmonics response," vol. 21881, pp. 10692–10697, 2011.
[57] a. González, M. Servin, J. C. Estrada, and H. C. Rosu, "N-Step Linear Phase-Shifting Algorithms With Optimum Signal To Noise Phase Demodulation," *J. Mod. Opt.*, vol. 58, no. January 2013, pp. 1278–1284, 2011.
[58] P. J. de Groot, J. C. Dainty, and L. Deck, "New algorithms and error analysis for sinusoidal phase shifting interferometry," *Proc. SPIE*, p. 70630K–70630K–14, 2008.
[59] P. J. De Groot, "Vibration in phase-shifting interferometry," *J. Opt. Soc. Am. A*, vol. 12, no. 2, pp. 354–366, 1995.
[60] P. J. de Groot and L. L. Deck, "Numerical simulations of vibration in phase-shifting interferometry.," *Appl. Opt.*, vol. 35, no. 13, pp. 2172–8, 1996.
[61] L. L. Deck, "Suppressing phase errors from vibration in phase-shifting interferometry.," *Appl. Opt.*, vol. 48, no. 20, pp. 3948–3960, 2009.
[62] K. Hibino, B. F. Oreb, D. I. Farrant, and K. G. Larkin, "Phase-shifting algorithms for nonlinear and spatially nonuniform phase shifts," *J. Opt. Soc. Am. A*, vol. 14, no. 4, p. 918, 1997.
[63] Y. Ishii and R. Onodera, "Phase-extraction algorithm in laser-diode phase-shifting interferometry.," *Opt. Lett.*, vol. 20, no. 18, pp. 1883–5, Sep. 1995.
[64] M. Servin, J. C. Estrada, J. a Quiroga, J. F. Mosiño, and M. Cywiak, "Noise in phase shifting interferometry.," *Opt. Express*, vol. 17, no. 11, pp. 8789–8794, 2009.
[65] A. Dubois, "Effects of phase change on reflection in phase-measuring interference microscopy.," *Appl. Opt.*, vol. 43, no. 7, pp. 1503–7, Mar. 2004.
[66] P. J. de Groot, "Correlated errors in phase-shifting laser Fizeau interferometry," *Appl. Opt.*, vol. 53, no. 19, p. 4334, Jun. 2014.
[67] P. Groot, "Phase-shift calibration errors in interferometers with spherical Fizeau cavities.," *Appl. Opt.*, vol. 34, no. 16, pp. 2856–2863, 1995.
[68] G. A. Ayubi, C. D. Perciante, J. L. Flores, J. M. Di Martino, and J. A. Ferrari, "Generation of phase-shifting algorithms with N arbitrarily spaced phase-steps," no. 2, 2014.
[69] P. de Groot, "Design of error-compensating algorithms for sinusoidal phase shifting interferometry.," *Appl. Opt.*, vol. 48, pp. 6788–6796, 2009.
[70] L. L. Deck, "Model-based phase shifting interferometry," *Appl. Opt.*, vol. 53, no. 21, pp. 4628–4636, 2014.

[71] K. Freischlad, “Sub-angstrom surface metrology with a virtual reference interferometer,” *Proc. SPIE*, vol. 8943, no. 84930B, 2012.
[72] U. P. Kumar, B. Bhaduri, M. P. Kothiyal, and N. K. Mohan, “Two-wavelength micro-interferometry for 3-D surface profiling,” *Opt. Lasers Eng.*, vol. 47, no. 2, pp. 223–229, Feb. 2009.
[73] P. deGroot, E. O. Soc, S. P. O. I. Engineers, E. Commiss, D. G. S. R. Communities, and Dev, “101-Frame Algorithm for Phase Shifting Interferometry,” *Conf. Opt. Insp. Micromeasurements II*, vol. 3098, pp. 283–292, 1997.
[74] T. Dresel, G. Häusler, and H. Venzke, “Three-dimensional sensing of rough surfaces by coherence radar.,” *Appl. Opt.*, vol. 31, no. 7, pp. 919–925, 1992.
[75] a F. Fercher, K. Mengedoht, and W. Werner, “Eye-length measurement by interferometry with partially coherent light.,” *Opt. Lett.*, vol. 13, no. 3, pp. 186–188, 1988.
[76] D. Huang, E. Swanson, C. Lin, J. Schuman, W. Stinson, W. Chang, M. Hee, T. Flotte, K. Gregory, C. Puliafito, and A. Et, “Optical coherence tomography,” *Science*. 1991.
[77] P. J. Caber, “Interferometric profiler for rough surfaces,” *Appl. Opt.*, vol. 32, no. 19, pp. 3438–3441, Jul. 1993.
[78] L. Deck and P. De Groot, “High-speed noncontact profiler based on scanning white-light interferometry,” *Appl. Opt.*, vol. 33, no. 31, pp. 7334–7338, Nov. 1994.
[79] C. Ai and E. L. Novak, “Centroid approach for estimating modulation peak in broad-bandwidth interferometry,” 5,633,715, 1997.
[80] S. S. Chim and G. S. Kino, “Three-dimensional image realization in interference microscopy.,” *Appl. Opt.*, vol. 31, no. 14, pp. 2550–3, 1992.
[81] K. G. Larkin, “Efficient nonlinear algorithm for envelope detection in white light interferometry,” *J. Opt. Soc. Am. A*, vol. 13, no. 4, pp. 832–843, Apr. 1996.
[82] P. De Groot, “9 Coherence Scanning Interferometry.”
[83] P. De Groot, X. C. De Lega, J. Kramer, and M. Turzhitsky, “Determination of Fringe Order in White-Light Interference Microscopy,” *Appl. Opt.*, vol. 41, no. 22, pp. 4571–4578, Aug. 2002.
[84] A. Harasaki, J. Schmit, and J. C. Wyant, “Improved vertical-scanning interferometry,” *Appl. Opt.*, vol. 39, no. 13, pp. 2107–15, May 2000.
[85] M. Fleischer, R. Windecker, and H. J. Tiziani, “Theoretical Limits of Scanning White-Light Interferometry Signal Evaluation Algorithms,” *Appl. Opt.*, vol. 40, no. 17, pp. 2815–2820, Jun. 2001.
[86] P. Pavliček and O. Hýbl, “White-light interferometry on rough surfaces---measurement uncertainty caused by noise,” *Appl. Opt.*, vol. 51, no. 4, pp. 465–473, Feb. 2012.
[87] A. Harasaki and J. C. Wyant, “Fringe Modulation Skewing Effect in White-Light Vertical Scanning Interferometry,” *Appl. Opt.*, vol. 39, no. 13, pp. 2101–2106, May 2000.
[88] F. Gao, R. K. Leach, J. Petzing, and J. M. Coupland, “Surface measurement errors using commercial scanning white light interferometers,” *Meas. Sci. Technol.*, vol. 19, no. 1, p. 15303, 2008.
[89] P. Lehmann, P. Kühnhold, and W. Xie, “Reduction of chromatic aberration influences in vertical scanning white-light interferometry,” *Meas. Sci. Technol.*, vol. 25, no. 6, p. 65203, 2014.
[90] A. Pförtner and J. Schwider, “Dispersion Error in White-Light Linnik Interferometers and its Implications for Evaluation Procedures,” *Appl. Opt.*, vol. 40, no. 34, pp. 6223–6228, Dec. 2001.
[91] Y.-S. Ghim and A. Davies, “Complete fringe order determination in scanning white-light interferometry using a Fourier-based technique,” *Appl. Opt.*, vol. 51, no. 12, pp. 1922–1928, Apr. 2012.
[92] R. Mandal, J. Coupland, R. Leach, and D. Mansfield, “Coherence scanning interferometry: measurement and correction of three-dimensional transfer and point-spread characteristics,” *Appl. Opt.*, vol. 53, no. 8, p. 1554, Mar. 2014.
[93] P. de Groot and X. C. de Lega, “Signal Modeling for Low-Coherence Height-Scanning Interference Microscopy,” *Appl. Opt.*, vol. 43, no. 25, pp. 4821–4830, Sep. 2004.

[94] W. K. Chong, X. Li, and Y. C. Soh, “Harnessing spectral property of dual wavelength white LED to improve vertical scanning interferometry.,” *Appl. Opt.*, vol. 52, no. 19, pp. 4652–62, Jul. 2013.
[95] S. Tereschenko, P. Lehmann, P. Gollor, and P. Kuehnhold, “Robust vertical scanning white-light interferometry in close-to-machine applications,” no. 0, p. 95250Q, 2015.
[96] 4D Technology, “Product.” [Online]. Available: http://www.4dtechnology.com/products/index.php. [Accessed: 05-Dec-2015].
[97] S.-W. Kim and G.-H. Kim, “Thickness-Profile Measurement of Transparent Thin-Film Layers by White-Light Scanning Interferometry,” *Appl. Opt.*, vol. 38, no. 28, pp. 5968–5973, Oct. 1999.
[98] M. Roy, I. Cooper, P. Moore, C. Sheppard, and P. Hariharan, “White-light interference microscopy: effects of multiple reflections within a surface film.,” *Opt. Express*, vol. 13, no. 1, pp. 164–70, Jan. 2005.
[99] Geneva: International Organization for Standardization, “ISO 25178-604:2013 Geometrical product specifications (GPS) — Surface texture: Areal Part 604: Nominal characteristics of non- contact (coherence scanning interferometry) instruments,” 2013.
[100] Z. Corporation, “3D Optical Surface Profilers,” 2015. [Online]. Available: http://www.zygo.com/?/met/profilers/. [Accessed: 04-Nov-2015].
[101] Taylor Hobson, “Non-contact Profilers,” *2015*. [Online]. Available: http://www.taylor-hobson.com/products/23/109.html. [Accessed: 04-Nov-2015].
[102] P. de Groot and L. Deck, “Three-dimensional imaging by sub-Nyquist sampling of white-light interferograms,” *Opt. Lett.*, vol. 18, no. 17, pp. 1462–1464, 1993.
[103] M. Suematsu and M. Takeda, “Wavelength-shift interferometry for distance measurements using the Fourier transform technique for fringe analysis.,” *Appl. Opt.*, vol. 30, no. 28, pp. 4046–55, Oct. 1991.
[104] H. Kikuta, K. Iwata, and R. Nagata, “Distance measurement by the wavelength shift of laser diode light.,” *Appl. Opt.*, vol. 25, no. Ld, p. 2976, 1986.
[105] V. Badami and P. De Groot, *Displacement measuring interferometry*. Taylor & Francis, 2013.
[106] A. Yamamoto, C.-C. Kuo, K. Sunouchi, S. Wada, I. Yamaguchi, and H. Tashiro, “Surface Shape Measurement by Wavelength Scanning Interferometry Using an Electronically Tuned Ti:sapphire Laser,” *Opt. Rev.*, vol. 8, no. 1, pp. 59–63, 2001.
[107] H. Muhamedsalih, F. Gao, and X. Jiang, “Comparison study of algorithms and accuracy in the wavelength scanning interferometry.,” *Appl. Opt.*, vol. 51, no. 36, pp. 8854–62, Dec. 2012.
[108] M. Takeda, H. Ina, and S. Kobayashi, “Fourier-transform method of fringe-pattern analysis for computer-based topography and interferometry,” *J. Opt. Soc. Am.*, vol. 72, no. 1, p. 156, Jan. 1982.
[109] Y. Zhang, Y. Bai, J. Xu, W. Xu, and Y. Zhou, “Effective improvement of depth resolution and reduction of ripple error in depth-resolved wavenumber-scanning interferometry,” vol. 66, pp. 58–63, 2015.
[110] G. Barwood, P. Gill, and W. Rowley, “Laser diodes for length determination using swept-frequency interferometry,” *Meas. Sci. Technol.*, vol. 4, pp. 988–994, 1993.
[111] Y. Ishii, “Wavelength-Tunable Laser-Diode Interferometer,” *Opt. Rev.*, vol. 6, no. 4, pp. 273–283, 1999.
[112] G. P. Barwood, P. Gill, and W. R. C. Rowley, “High-accuracy length metrology using multiple-stage swept-frequency interferometry with laser diodes,” *Meas. Sci. Technol.*, vol. 9, pp. 1036–1041, 1999.
[113] A. Davila, J. M. Huntley, C. Pallikarakis, P. D. Ruiz, and J. M. Coupland, “Wavelength scanning interferometry using a Ti:Sapphire laser with wide tuning range,” *Opt. Lasers Eng.*, vol. 50, no. 8, pp. 1089–1096, 2012.
[114] L. Perret and P. Pfeiffer, “Sinusoidal nonlinearity in wavelength-sweeping interferometry.,” *Appl. Opt.*, vol. 46, no. 33, pp. 8074–8079, 2007.
[115] H. J. Yang, S. Nyberg, and K. Riles, “High-precision absolute distance measurement using

dual-laser frequency scanned interferometry under realistic conditions," *Nucl. Instruments Methods Phys. Res. Sect. A Accel. Spectrometers, Detect. Assoc. Equip.*, vol. 575, no. 3, pp. 395–401, 2007.
[116] M. Vannoni, A. Sordini, and G. Molesini, "He–Ne laser wavelength-shifting interferometry," *Opt. Commun.*, vol. 283, no. 24, pp. 5169–5172, 2010.
[117] J. Thiel, T. Pfeifer, and M. Hartmann, "Interferometric measurement of absolute distances of up to 40 m," *Measurement*, vol. 16, pp. 1–6, 1995.
[118] J. A. Stone, A. Stejskal, and L. Howard, "Absolute interferometry with a 670-nm external cavity diode laser.," *Appl. Opt.*, vol. 38, no. 28, pp. 5981–94, 1999.
[119] S.-H. Lu, J.-H. Chen, C.-F. Kao, Y.-P. Lan, and L.-C. Chang, "Determining large step heights using zero-order interference fringe identification and an external cavity diode laser," *Opt. Commun.*, vol. 259, no. 1, pp. 14–18, 2006.
[120] F. Gao, H. Muhamedsalih, and X. Jiang, "Surface and thickness measurement of a transparent film using wavelength scanning interferometry.," *Opt. Express*, vol. 20, no. 19, pp. 21450–6, Sep. 2012.
[121] P. De Groot, "Measurement of transparent plates with wavelength-tuned phase-shifting interferometry.," *Appl. Opt.*, vol. 39, no. 16, pp. 2658–63, Jun. 2000.
[122] P. D. Ruiz, Y. Zhou, J. M. Huntley, and R. D. Wildman, "Depth-resolved whole-field displacement measurement using wavelength scanning interferometry," *J. Opt. A Pure Appl. Opt.*, vol. 6, no. 7, p. 679, 2004.
[123] Zygo Corporation, "Verifire™ MST," 2015. [Online]. Available: http://www.zygo.com/?/met/interferometers/verifire/mst/. [Accessed: 01-Jan-2015].
[124] Y.-S. Ghim, A. Suratkar, and A. Davies, "Reflectometry-based wavelength scanning interferometry for thickness measurements of very thin wafers.," *Opt. Express*, vol. 18, no. 7, pp. 6522–9, 2010.
[125] J. M. Schmitt, "Optical Coherence Tomography: A review," *IEEE J. Sel. Top. Quantum Elect.*, vol. 5, no. 4, pp. 1205–1215, 1999.
[126] R. Su, M. Kirillin, E. W. Chang, E. Sergeeva, S. H. Yun, and L. Mattsson, "Perspectives of mid-infrared optical coherence tomography for inspection and micrometrology of industrial ceramics," *Opt. Express*, vol. 22, no. 13, pp. 15804–15819, 2014.
[127] M. Wojtkowski, "High-speed optical coherence tomography: basics and applications.," *Appl. Opt.*, vol. 49, no. 16, pp. D30–D61, 2010.
[128] Y. Yan, Z. Ding, L. Wang, C. Wang, and Y. Shen, "High-sensitive quantitative phase imaging with averaged spectral domain phase microscopy," *Opt. Express*, vol. 303, no. November, pp. 21–24, 2013.
[129] M. T. Tsai, Y. J. Lee, Y. C. Yao, C. Y. Kung, F. Y. Chang, and J. Der Lee, "Quantitative phase imaging with swept-source optical coherence tomography for optical measurement of nanostructures," *IEEE Photonics Technol. Lett.*, vol. 24, no. 8, pp. 640–642, 2012.
[130] J. Xu and R. Stroud, *Acousto-optic devices: principles, design, and applications*. Wiley, 1992.
[131] J. Ward, C. N. Pannell, E. S. Wachman, and W. Seale, "Applications of acousto-optic devices for spectral imaging systems," 2012.
[132] E. G. Bucher and J. W. Carnahan, "Characterization of an Acousto-optic Tunable Filter and Use in Visible Spectrophotometry," *Appl. Spectrosc.*, vol. 53, no. 5, pp. 603–611, 1999.
[133] H. Muhamedsalih, "Investigation of Wavelength Scanning Interferometry for Embedded Metrology," University of Huddersfield, 2013.
[134] "International vocabulary of metrology – Basic and general concepts and associated terms (VIM)," 2012.
[135] Olympus, "Lext OLS4100," 2015.
[136] Taylor Hobson, "CCI HD Optical profiler," *2015*. [Online]. Available: http://www.taylor-hobson.com/uploads/downloads/products/CCI_HD_Lowres_EN.pdf. [Accessed: 09-Nov-2015].
[137] BIPM, IEC, IFCC, ISO, IUPAC, IUPAP, and OIML, "Guide to the Expression of Uncertainty in Measurement," *Bureau International des Poids et Mesures JCGM 100*, no. October. 2012.

[138] J. Seewig, M. Eifler, and G. Wiora, “Unambiguous evaluation of a chirp measurement standard,” *Surf. Topogr. Metrol. Prop.*, vol. 2, no. 4, p. 45003, 2014.
[139] R. K. Leach, “Is one step height enough,” in *Proceedings of ASPE*, 2015, no. October.
[140] P. Giacomo, “News from the BIPM,” *Metrologia*, vol. 20, no. 1, pp. 25–30, 1984.
[141] R. K. Leach, C. L. Giusca, and P. Rubert, “A single set of material measures for the calibration of areal surface topography measuring instruments : the NPL Areal Bento Box.”
[142] R. K. Leach, C. L. Giusca, and K. Naoi, “Development and characterization of a new instrument for the traceable measurement of areal surface texture,” *Meas. Sci. Technol.*, vol. 20, no. 12, p. 125102, Dec. 2009.
[143] C. L. Giusca, R. K. Leach, and A. B. Forbes, “A virtual machine-based uncertainty evaluation for a traceable areal surface texture measuring instrument,” *Measurement*, vol. 44, no. 5, pp. 988–993, Jun. 2011.
[144] R. K. Leach, “Traceable measurement of surface texture at the National Physical Laboratory using NanoSurf IV,” *Meas. Sci. Technol.*, pp. 1162–1172, 2000.
[145] C. L. Giusca, R. K. Leach, F. Helary, T. Gutauskas, and L. Nimishakavi, “Calibration of the scales of areal surface topography-measuring instruments: part 1. Measurement noise and residual flatness,” *Meas. Sci. Technol.*, vol. 23, no. 3, p. 35008, Mar. 2012.
[146] C. L. Giusca, R. K. Leach, and F. Helery, “Calibration of the scales of areal surface topography measuring instruments: part 2. Amplification, linearity and squareness,” *Meas. Sci. Technol.*, vol. 23, no. 6, p. 65005, Jun. 2012.
[147] C. L. Giusca and R. K. Leach, “Calibration of the scales of areal surface topography measuring instruments: part 3. Resolution,” *Meas. Sci. Technol.*, vol. 24, no. 10, p. 105010, Oct. 2013.
[148] R. Felder, “Practical realization of the definition of the metre, including recommended radiations of other optical frequency standards (2003),” *Metrologia*, vol. 40, no. 4, pp. 103–133, 2003.
[149] C. Giusca, “Development of a traceability route for areal surface texture measurements,” 2014.
[150] NPL, “Good practice guide.” [Online]. Available: http://www.npl.co.uk/publications/guides/dimensional-good-practice-guides. [Accessed: 11-Nov-2015].
[151] C. L. Giusca, J. D. Claverley, W. Sun, R. K. Leach, F. Helmli, and M. P. J. Chavigner, “Practical estimation of measurement noise and flatness deviation on focus variation microscopes,” *CIRP Ann. - Manuf. Technol.*, vol. 63, no. 1, pp. 545–548, 2014.
[152] H. Haitjema, “Uncertainty in measurement of surface topography,” *Surf. Topogr. Metrol. Prop.*, vol. 3, no. 3, p. 35004, 2015.
[153] K. Irie, a E. McKinnon, K. Unsworth, and I. M. Woodhead, “A model for measurement of noise in CCD digital-video cameras,” *Meas. Sci. Technol.*, vol. 19, no. 4, p. 45207, Apr. 2008.
[154] A. J. Jerri, “The Shannon Sampling Theorem-Its Various Extensions and Applications: A Tutorial Review,” *Proc. IEEE*, vol. 65, no. 11, pp. 1565–1596, 1977.
[155] H. D. Luke, “The Origins of the Sampling theorem,” *IEEE Commun. Mag.*, vol. 1, no. April, pp. 106–108, 1999.
[156] A. Koehler, “New method of Illumination for phomicrographical purposes,” *J. R. Microsc. Soc.*, vol. 14, pp. 261–262, 1894.
[157] K. Creath and J. C. Wyant, “Absolute measurement of surface roughness.,” *Appl. Opt.*, vol. 29, no. 26, pp. 3823–3827, 1990.
[158] Geneva: International Organization for Standardization, “ISO 25178-3:2012 Geometrical product specifications (GPS) — Surface texture: Areal Part 3: Specification operators,” 2014.
[159] Geneva: International Organization for Standardization, “ISO 25178-601:2010 Surface texture. Areal. Nominal characteristics of contact (stylus) instruments,” 2010.
[160] “NPL Areal Calibration set,” 2014. [Online]. Available:

http://www.npl.co.uk/upload/pdf/areal-calibration-set.pdf.
[161] B. F. Alexander, "Elimination of systematic error in subpixel," *Opt. Eng.*, vol. 30, no. 9, 1991.
[162] Geneva: International Organization for Standardization, "ISO 5436-1:2001 Geometrical Product Specifications (GPS) -- Surface texture: Profile method; Measurement standards -- Part 1: Material measures," 2001.
[163] P. De Groot, J. Beverage, Z. Corporation, and L. B. Road, "Calibration of the amplification coefficient in interference microscopy by means of a wavelength standard," in *SPIE optical metrology*, 2015, no. June.
[164] J. F. Biegen, "Calibration requirements for Mirau and Linnik microscope interferometers.," *Appl. Opt.*, vol. 28, no. 11, pp. 1972–1974, 1989.
[165] C. L. Giusca and R. K. Leach, "Good Practice Guide No . 127 Calibration of the metrological characteristics of Coherence Scanning Interferometers (CSI) and Phase Shifting Interferometers (PSI) Measurement Good Practice Guide No . 127 Calibration of the metrological characteristics," 2013.
[166] A. Henning, C. Giusca, A. Forbes, I. Smith, R. Leach, J. Coupland, and R. Mandal, "Correction for lateral distortion in coherence scanning interferometry," *CIRP Ann. - Manuf. Technol.*, vol. 62, no. 1, pp. 547–550, Jan. 2013.
[167] A. B. Forbes, "Efficient Algorithms for Structured Self-Calibration Problems," in *Algorithms For Approximation IV. Proceedings of the 2001 International Symposium*, 2001, vol. 1, no. 3, pp. 1–5.
[168] Lord Rayleigh, "XV. On the theory of optical images, with special reference to the microscope," *London, Edinburgh, Dublin Philos. Mag. J. Sci.*, vol. 42.255, pp. 167–195, 1896.
[169] R. Barakat and E. Levin, "Application of Apodization to Increase Two-Point Resolution by the Sparrow Criterion. I. Coherent Illumination," *J. Opt. Soc. Am.*, vol. 53, no. 2, p. 274, 1963.
[170] R. Barakat and E. Levin, "Application of Apodization to Increase Two-Point Resolution by the Sparrow Criterion. II. Incoherent Illumination," *J. Opt. Soc. Am.*, vol. 53, no. 2, pp. 274–282, 1963.
[171] E. Abbe, "Beiträge zur Theorie des Mikroskops und der mikroskopischen Wahrnehmung.," *Arch. für mikroskopische Anat. 9.1*, pp. 413–418, 1873.
[172] X. Colonna De Lega and P. de Groot, "Lateral resolution and instrument transfer function as criteria for selecting surface metrology instruments," *Imaging Appl. Opt. Tech. Pap.*, 2012.
[173] R. Leach, *Optical Measurement of Surface Topography*. Springer, 2011.
[174] G. Häusler and S. Ettl, "Limitations of Optical 3D Sensors," in *Optical Measurement of Surface Topography SE - 3*, R. Leach, Ed. Springer Berlin Heidelberg, 2011, pp. 23–48.
[175] P. de Groot and X. C. de Lega, "Interpreting interferometric height measurements using the instrument transfer function," in *SPIE*, 2005, vol. Proceeding, no. 30–37.
[176] M. R. Foreman, C. L. Giusca, J. M. Coupland, P. Török, and R. K. Leach, "Determination of the transfer function for optical surface topography measuring instruments—a review," *Meas. Sci. Technol.*, vol. 24, no. 5, p. 52001, May 2013.
[177] J. M. Coupland and J. Lobera, "Holography , tomography and 3D microscopy as linear filtering operations," *Meas. Sci. Technol.*, vol. 19, 2008.
[178] J. W. Goodman, *Introduction to Fourier Optics*, 2nd Editio. McGraw-Hill, 1996.
[179] J. Coupland, R. Mandal, K. Palodhi, and R. Leach, "Coherence scanning interferometry: linear theory of surface measurement," *Appl. Opt.*, vol. 52, no. 16, p. 3662, May 2013.
[180] R. Mandal, K. Palodhi, J. Coupland, R. Leach, and D. Mansfield, "Application of linear systems theory to characterize coherence scanning interferometry," in *SPIE*, 2012, vol. 8430, no. May, pp. 1–10.
[181] a. J. Henning, J. M. Huntley, and C. L. Giusca, "Obtaining the Transfer Function of optical instruments using large calibrated reference objects," *Opt. Express*, vol. 23, no. 13, p. 16617, 2015.

[182] I. Young, R. Zagers, and L. Van Vliet, "Depth-of-focus in microscopy," *Proc. …*, pp. 493–498, 1993.
[183] T. Doi, T. Vorburger, and P. Sullivan, "Effects of defocus and algorithm on optical step height calibration," *Precis. Eng.*, vol. 23, no. November 1998, pp. 135–143, 1999.
[184] a Fujii, H. Suzuki, and K. Yanagi, "Development of measurement standards for verifying functional performance of surface texture measuring instruments," *J. Phys. Conf. Ser.*, vol. 311, p. 12009, 2011.
[185] Geneva: International Organization for Standardization, "ISO 25178-70:2014 BSI Geometrical product specification (GPS) — Surface texture : Areal. Material measures," 2014.
[186] Joint Committee for Guides in Metrology (JCGM), "Evaluation of measurement data: Guide to the expression of uncertainty in measurement," no. September, 2008.
[187] F. Pavese and A. B. Forbes, *Data Modeling for Metrology and Testing in Measurement Science*. Birkhäuser Basel, 2008.
[188] D. C. Rife and R. R. Boorstyn, "Single-Tone Parameter Estimation from Discrete-Time Observations," *IEEE Trans. Inf. Theory*, vol. 20, no. 5, pp. 591–598, 1974.
[189] H. L. Van Trees and K. L. Bell, *Detection Estimation and Modulation Theory, Part I*, 2nd Ed.^n. Somerset, NJ, USA: John Wiley & Sons, 2013.
[190] G. Moschetti, H. Muhamedsalih, O. Connor, X. Jiang, and R. K. Leach, "Vertical axis non-linearities in wavelength scanning interferometry," in *11th International Conference and Exhibition on Laser Metrology, Machine Tool, CMM & Robotic Performance*, 2015, pp. 31–39.
[191] P. L. M. Heydemann, "Determination and correction of quadrature fringe measurement errors in interferometers," *Appl. Opt.*, vol. 20, no. 19, pp. 3382–3384, 1981.
[192] N. J. . Brock, J. E. Millerd, J. C. Wyant, and J. B. Hayes, "Pixelated phase-mask interferometer," 7,230,717 B2, 2007.
[193] A. Safrani and I. Abdulhalim, "Real-time phase shift interference microscopy.," *Opt. Lett.*, vol. 39, no. 17, pp. 5220–3, 2014.
[194] Y.-S. Ghim, A. Suratkar, A. Davies, and Y.-W. Lee, "Absolute thickness measurement of silicon wafer using wavelength scanning interferometer," *Proc. SPIE*, vol. 8133, no. 1, pp. 1–6, 2011.
[195] E. Peterson, "A Not-so-Characteristic Equation: the Art of Linear Algebra," pp. 1–15, 2007.
[196] P. J. De Groot, "Progress in the specification of optical instruments for the measurement of surface form and texture," *Proc. SPIE 9110, Dimens. Opt. Metrol. Insp. Pract. Appl. III*, vol. 9110, pp. 1–12, 2014.
[197] M. Liu, C. F. Cheung, M. Ren, and C.-H. Cheng, "Estimation of measurement uncertainty caused by surface gradient for a white light interferometer," *Appl. Opt.*, vol. 54, no. 29, pp. 8670–8677, 2015.
[198] R. K. Leach, "Is one step height enough ?," in *Proc. ASPE*, 2015, no. October.
[199] Vázquez-Villa, A., S. Delgado-Atencio, J. A., Vázquez-Montiel, J. Castro-Ramos, and M. Cunill-Rodríguez, "Aspheric lens to increase the depth of focus," *Opt. Lett.*, vol. 40, no. 12, pp. 2842–2845, 2015.
[200] J. M. Flores-Moreno, M. H. De la Torre I., M. S. Hernández-Montes, C. Pérez-López, and F. Mendoza S., "Interferometric comparison of the performance of a CMOS and sCMOS detector," *Proc. SPIE - Int. Soc. Opt. Eng.*, vol. 9660, no. 0, p. 96601A, 2015.
[201] N. Bobroff, "Recent advances in displacement measuring interferometry," *Meas. Sci. Technol.*, vol. 4, no. 9, pp. 907–926, 1999.
[202] M. Pisani, A. Yacoot, P. Balling, N. Bancone, C. Birlikseven, M. Çelik, J. Flügge, R. Hamid, P. Köchert, P. Kren, U. Kuetgens, A. Lassila, G. B. Picotto, E. Şahin, J. Seppä, M. Tedaldi, and C. Weichert, "Comparison of the performance of the next generation of optical interferometers," *Metrologia*, vol. 49, no. 4, pp. 455–467, 2012.
[203] P. de Groot, "Unusual techniques for absolute distance measurement," *Opt. Eng.*, vol. 40, no. 1, p. 28, 2001.